Electrocatalytic Water Splitting with Ruthenium Nanoparticles

Jordi Creus Casanovas

ADVERTIMENT. L'accés als continguts d'aquesta tesi doctoral i la seva utilització ha de respectar els drets de la persona autora. Pot ser utilitzada per a consulta o estudi personal, així com en activitats o materials d'investigació i docència en els termes establerts a l'art. 32 del Text Refós de la Llei de Propietat Intel·lectual (RDL 1/1996). Per altres utilitzacions es requereix l'autorització prèvia i expressa de la persona autora. En qualsevol cas, en la utilització dels seus continguts caldrà indicar de forma clara el nom i cognoms de la persona autora i el títol de la tesi doctoral. No s'autoritza la seva reproducció o altres formes d'explotació efectuades amb finalitats de lucre ni la seva comunicació pública des d'un lloc aliè al servei TDX. Tampoc s'autoritza la presentació del seu contingut en una finestra o marc aliè a TDX (framing). Aquesta reserva de drets afecta tant als continguts de la tesi com als seus resums i índexs.

ADVERTENCIA. El acceso a los contenidos de esta tesis doctoral y su utilización debe respetar los derechos de la persona autora. Puede ser utilizada para consulta o estudio personal, así como en actividades o materiales de investigación y docencia en los términos establecidos en el art. 32 del Texto Refundido de la Ley de Propiedad Intelectual (RDL 1/1996). Para otros usos se requiere la autorización previa y expresa de la persona autora. En cualquier caso, en la utilización de sus contenidos se deberá indicar de forma clara el nombre y apellidos de la persona autora y el título de la tesis doctoral. No se autoriza su reproducción u otras formas de explotación efectuadas con fines lucrativos ni su comunicación pública desde un sitio ajeno al servicio TDR. Tampoco se autoriza la presentación de su contenido en una ventana o marco ajeno a TDR (framing). Esta reserva de derechos afecta tanto al contenido de la tesis como a sus resúmenes e índices.

WARNING. The access to the contents of this doctoral thesis and its use must respect the rights of the author. It can be used for reference or private study, as well as research and learning activities or materials in the terms established by the 32nd article of the Spanish Consolidated Copyright Act (RDL 1/1996). Express and previous authorization of the author is required for any other uses. In any case, when using its content, full name of the author and title of the thesis must be clearly indicated. Reproduction or other forms of for profit use or public communication from outside TDX service is not allowed. Presentation of its content in a window or frame external to TDX (framing) is not authorized either. These rights affect both the content of the thesis and its abstracts and indexes.

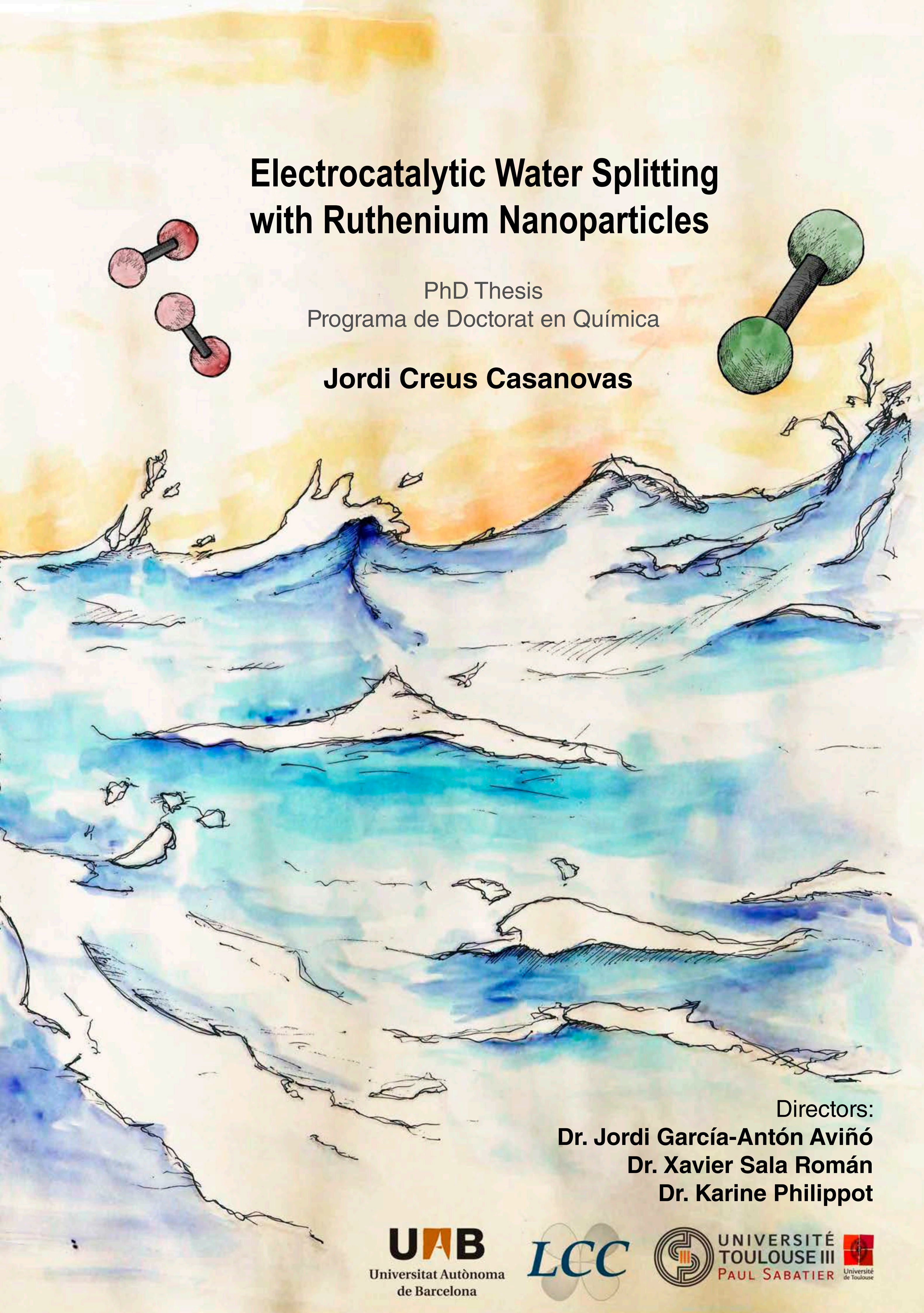

Electrocatalytic Water Splitting with Ruthenium Nanoparticles

PhD Thesis
Programa de Doctorat en Química

Jordi Creus Casanovas

Directors:
Dr. Jordi García-Antón Aviñó
Dr. Xavier Sala Román
Dr. Karine Philippot

UAB
Universitat Autònoma
de Barcelona

LCC

UNIVERSITÉ
TOULOUSE III
PAUL SABATIER

Université
de Toulouse

This PhD thesis was performed in the frame of a cotutelle agreement under the supervision of Dr. Xavier Sala and Dr. Jordi García-Antón from the Universitat Autònoma de Barcelona (UAB), and of Dr. Karine Philippot from the Laboratoire de Chimie de Coordination (LCC – CNRS) and Université Toulouse III – Paul Sabatier (UT3 – UPS).

THÈSE

En vue de l'obtention du

DOCTORAT DE L'UNIVERSITÉ DE TOULOUSE

Délivré par :

Université Toulouse 3 Paul Sabatier (UT3 Paul Sabatier)

Cotutelle internationale avec "Universitat Autònoma de Barcelona"

Présentée et soutenue par :
Jordi Creus Casanovas
le mercredi 11 juillet 2018

Titre :

Electrocatalytic Water Splitting with Ruthenium Nanoparticles

---

École doctorale et discipline ou spécialité :
ED SDM : Chimie organométallique de coordination - CO 043

Unité de recherche :
Laboratoire de Chimie de Coordination (LCC - CNRS)

Directeur/trice(s) de Thèse :
Dr. Karine PHILIPPOT: Directrice de Recherche (LCC- CNRS), Toulouse
Dr. Xavier SALA: Professor agregat (UAB), Barcelona

Jury :

Prof. Dr. Joan Carles BAYÓN (UAB) Barcelona
Prof. Dr. Philipp KURZ (Institut für Anorganische und Analytische Chemie) Freiburg
Prof. Dr. Daniel MASPOCH (ICN2 - BIST) Barcelona
Dr. Hynd REMITA (LCP - CNRS) Paris
Dr. Karine PHILIPPOT (LCC - CNRS) Toulouse

Universitat Autònoma de Barcelona

Electrocatalytic Water Splitting with Ruthenium Nanoparticles

Jordi Creus Casanovas

PhD Thesis

Programa de Doctorat en Química

Dr. Jordi García-Antón, Dr. Xavier Sala & Dr. Karine Philippot

Departament de Química

Facultat de Ciències

2018

Memòria presentada per aspirar al Grau de Doctor en Química per Jordi Creus Casanovas:

Jordi Creus Casanovas

Vist i plau

Dr. Jordi García-Antón	Dr. Xavier Sala	Dr. Karine Philippot
Departament de Química Facultat de Ciències Universitat Autònoma de Barcelona	Departament de Química Facultat de Ciències Universitat Autònoma de Barcelona	Laboratoire de Chimie de Coordination (LCC–CNRS) Université Toulouse III - Paul Sabatier (UPS)
		K Philippot

Bellaterra, 8 de Juny de 2018

Toulouse, May the 30th 2018

Acknowledgements

During these years working as a researcher, every time someone asked me how hard was doing the PhD, I always answered the same thing: “there are three points influencing your PhD-life: the labmates, the topic and the directors”. But I was so lucky in the three of them, that I can only say it was not hard at all.

First of all I would like to thank Dr. Xavier Sala and Dr. Jordi García-Antón to choose me as PhD student in the group barely knowing me before, and to Dr. Karine Philippot for accepting to do the cotutelle agreement and so let me being part of her group as well. It has been a pleasure for me being able to discuss with you all about chemistry (and about life from time to time), even sometimes the physical distance made it a little bit difficult to join us all together. Thanks for your patience, your helpful advises and your talks, always making me feel like a chemist.

This work couldn’t have been performed without the help of collaborators, technicians and researchers, providing ideas and tools for the understanding of the materials. I would like to thank all the people in the Servei d’Anàlisis Químic (in UAB) for their support, especially to Ignasi, Sandra and Esther for their kindness. From other sections, Prof. Dr. Santiago Suriñach for the TG analyses and discussions, Dr. Guillaume Sauthier for XPS analyses and fittings, Pau Nolis, Eva Monteagudo and all the people in the seRMN for NMR experiments and a lot of patience, and also Dr. Ángel Álvarez for XRD analyses. In Toulouse, Prof. Pierre Lecante for WAXS analyses, Dr. Yannick Coppel for NMR experiments and discussions, and Dr. Vincent Collière for helpful advises and teaching how to not destroy the TEM apparatus.

Being part of two research groups (or even three from time to time) gives you the chance of meeting a lot of people and so makes more difficult to count everyone who has been sharing with you a little bit of his time. I will start in Barcelona, thanking Dr. Roger Bofill and Dr. Lluís Escriche, who have always been there for help and fun. I would like to thank all the students that spend some time in SelOxCat, more specifically to Hai-Jie, Bing (and his Chinese sweets), Jonathan (and the time we shared in Toulouse), Marcos (for our electrochemical discussions and the good times with “Killer Hamsters”), Rosa (the SelOxCat mami), Nacho (“va-mos al centro!”), Laura (for the shared patience with the carbon fibers), Enrico (for distracting coffees in stressful times), Lluís (for his voley lessons), Lavinia (the fairly winner of our “pintxos” contest), Laia (our duck-daughter) and all the TFG/TFM students (Laia, Alex, Victor, Laura Punky, Miquel, Fernando, Hector, Elena, etc.). I would like to specially thank N♥ria, for her courage, motivation, her interest for learning and understanding, and always altruist manners. I am really happy you came here so we could meet and have fun together!

It is not obvious that the people surrounding you will be nice and friendly, but this is the case I experienced with the Inorganic people: we are now a communion! I want to thank Katia, Borràs, Solde, CruFran, Sele, Mario, Marc, Clara, Momo, Grumpy, Changyong, Dani l'amic invisible, Míriam, Merche, Dani Herrera, Dani Peral, Jose and all the students that have spent some time in this nice family. More specially, Quim and Glòria deserve a special acknowledgement, considering their support and friendship in the most stressful times.

Moving north to Toulouse, I would like to thank Dr. Catherine Amiens and Dr. Diana Ciuculescu, who have been always there for chemistry but also for life discussions. The first researchers I found in "Equipe L" have been very important in my scientific evolution on NPs, specially Tugce and LuisMi, which I am very grateful with, but also Marlène, Mahmud, Léa, Kais and Laize (I miss you). Also Roberto, always ready for watching football game, playing any sport, or most often, for drinking beer, but also a nice and helpful labmate and friend. As in UAB, in LCC there is also someone who has been very important during the thesis: the old Sam. It was nice to "move you" to Toulouse, to be able to discuss so much about our works, to share BBQs and beers. Congratulations for your nice Pablito to you and Elo, and very good luck in your future!

Going south again to the region of castells and calçots, Tarragona. If I got this PhD grant was because I was in the right place at the right time, and this was thanks to Prof. Dr. Antoni Llobet, who also gave me the opportunity to keep a collaboration that (I think) made me grow as chemist. In Llobet's group I met such nice people: Serena, Pablo, Sergi (and your patience as "commercial"), Laia, Lorenzo, Craig, Carolina (one of the nicest person I ever met) and Roc (my first advisor and scientific model).

I couldn't finish the "scientific acknowledgments" without thanking the people in URV, because it is also thanks to Prof. Dr. Carmen Claver and Dr. Cyril Godard that I am here today. But also the people in the lab, such as Toniu (a good friend, even lost on the mountain), Itzi (the most pleasant supervisor and model), Núria, Eli, Isma, Ana&Sasha, Olga, and of course Jessica, who encouraged me and whose steps I have tried to follow during all the PhD. Somehow you have been a model to me, also in chemistry.

Finally I want to thank the people who surrounded me out of the lab, generally less time than desired. On one side Ricard, Marc, Pau, Fàges & Fontde (the perfect flatmate). Also Marina, Laia and Torres. On another side, my mountain friends Bere, Conguito and Pau. Strange people that I met in Göttingen, David and Marc, people who I would never go out with. A special acknowledge to Uri, one of the friends that strongly supported me during this time, and the creator of the nice cover of this manuscript.

At last, I would like to acknowledge the 100% support in anything at any time, coming from my family. My parents, Domènec and Núria, my two best sisters Gisela and Laia, and the cutests nephew and nice I could ever have, Joel and Tània, as well as my brother-in-law and advisor Antonio.

The presence of you all has been important at some point of this 4-years period.

Finally, I would also like to thank Universitat Autònoma de Barcelona for the pre-doctoral PIF-UAB grant, the “Eurorégion Pyrénées-Méditerranée” and HC3A-GDRI for internship financial support:

UAB
Universitat Autònoma
de Barcelona

GDRI
HC3A
Groupement De Recherche International
Heteroelements and Coordination Chemistry:
from Concepts to Applications

GOBIERNO
DE ESPAÑA

MINISTERIO
DE ECONOMÍA
Y COMPETITIVIDAD

Euroregió Pirineus Mediterrània
Eurorégion Pyrénées-Méditerranée
Eurorregión Pirineos Mediterráneo

Abreviations

AC	Alternating Current
APS	Artificial Photosynthesis
b	Tafel slope [$mV\cdot dec^{-1}$]
C_{DL}	Double-Layer Capacitance [mF]
CF	Carbon Fibers
Ch.	Chapter
CNT	(Multi-Walled) Carbon Nanotubes
CVD	Chemical Vapor Deposition
DFT	Density Functional Theory
EA	Elemental Analysis
ECSA	ElectroChemically active Surface Area
EDX	Energy-dispersive X-ray spectroscopy
Eq.	Equation
FCV	Fuel Cell Vehicles
FTO	Fluorine-doped Tin Oxide electrode
GC	Glassy Carbon electrode
GHG	Green-House Gases
HEC	Hydrogen Evolution Catalyst
HER	Hydrogen Evolution Reaction
i	Current intensity [mA]
ICP	Inductive-Coupled Plasma
j	Current density [$mA\cdot cm^{-2}$]
j_0	Exchange Current Density [$mA\cdot cm^{-2}$]
MOF	Metal-Organic Framework
MWCNT	Multi-Walled Carbon Nanotubes
M-H	Metal-Hydride
NMR	Nuclear Magnetic Ressonance
NPs	Nanoparticles
O.D.	Outside Diameter

OEC	Oxygen Evolving Complex
OER	Oxygen Evolution Reaction
PBS	Phosphate Buffer Solution
PCET	Proton-Coupled Electron Transfer
PEM	Polymer Electrolyte Membrane
PMMA	Poly(Methyl MethAcrylate)
PS	Photosensitizer
PS-I/PS-II	Photosystem I-II
PVs	Photovoltaics
PVP	Polyvinylpyrrolidone
RDE	Rotating Disk Electrode
RDF	Radial Distribution Function
rds	Rate-Determining Step
Rub	Ruthenium black
SMR	Steam Methane Reforming
STAG	Stabilizing Agent
(HR)TEM	(High Resolution) Transmission Electron Microscopy
TGA	ThermoGravimetric Analysis
TMs	Transition Metals
UPD	Under-Potential Deposition
WAXS	Wide-Angle X-ray Scattering
WE	Water Electrolysis
WOC	Water Oxidation Catalyst
WS	Water Splitting
XPS	X-Ray Photoelectron Spectroscopy
XRD	X-Ray Diffraction spectroscopy
ē	Electron
η	Overpotential
η_0	Onset overpotential
η_{10}	Overpotential at j=10 mA·cm^{-2}

Table of Contents

1. General Introduction 1
    - 1.1 World Energy Outlook 3
    - 1.2 Solar Energy 5
    - 1.3 Hydrogen: Advantages & Disadvantages 6
        - 1.3.1 Hydrogen production 8
        - 1.3.2 Hydrogen storage & transport 11
    - 1.4 Artificial Photosynthesis vs. Natural Photosynthesis 12
    - 1.5 Water Splitting 14
        - 1.5.1 Oxygen Evolution Reaction 17
            - 1.5.1.1 Molecular complexes as WOCs 20
            - 1.5.1.2 Metallic nanoparticles as WOCs 24
        - 1.5.2 Hydrogen Evolution Reaction 28
            - 1.5.2.1 Molecular complexes as HECs 30
            - 1.5.2.2 Metallic nanoparticles as HECs 33
        - 1.5.3 Benchmarking of immobilized electrocatalysts 37
            - 1.5.3.1 Jaramillo's Methodology 38
            - 1.5.3.2 Copper Under-Potential Deposition 39
    - 1.6 Nanochemistry 40
        - 1.6.1 Stabilization of metal nanoparticles 42
        - 1.6.2 Synthesis of metal nanoparticles 43
        - 1.6.3 Organometallic approach for the synthesis of metal nanoparticles 44
        - 1.6.4 Characterization of metal nanoparticles 46
    - 1.7 References 47
2. Objectives 57
3. Colloidal Ruthenium Nanoparticles as Hydrogen Evolution Catalysts 61
    - 3.0 Preface 62
    - 3A Synthesis of a Porous Ru Nanomaterial and its Evaluation as HEC in Acidic and Neutral Conditions 65
        - 3A.1 Introduction 65
        - 3A.2 Synthesis & characterization of Ru-MeOH/THF porous nanomaterial 65
        - 3A.3 Electrocatalytic HER studies 67
        - 3A.4 Electrocatalytic performance benchmarking 71
        - 3A.5 Conclusions & perspectives 72
        - 3A.6 Experimental part 73

3A.7 References 76

3B Pyridine-Stabilized RuNPs: Synthesis, Characterization & HER Studies 79

3B.1 Introduction 79

3B.2 Synthesis & characterization of RuNPs stabilized with pyridine-based ligands 80

3B.2.1 TEM analysis 81

3B.2.2 ^{1}H-NMR studies with Ru-0.2PP 85

3B.2.3 Elemental composition 87

3B.2.4 Surface reactivity studies 90

3B.2.5 Study of the fate of the ligand 96

3B.2.6 Oxidation studies 101

3B.3 Electrocatalytic HER studies 111

3B.4 Conclusions & perspectives 115

3B.5 Experimental part 116

3B.6 References 120

3C Hydrogen Evolution Catalysis with Ru-0.2PP NPs: Study of the Fate of the NPs in Catalysis 123

3C.1 Introduction 123

3C.2 Synthesis & characterization of Ru1 123

3C.2.1 Ligand coordination studies through DFT calculations 126

3C.3 Electrocatalytic HER studies in 1 M H_2SO_4 130

3C.4 Electrocatalytic HER studies in 1 M NaOH 133

3C.5 Electrocatalytic performance comparison 135

3C.6 Conclusions & perspectives 139

3C.7 Experimental part 141

3C.8 References 144

4. Supported Ruthenium Nanoparticles on Carbon-based materials as Water Splitting Catalysts 147

4.0 Preface 148

4A Carbon Nanotube-supported RuNPs as Catalyst for Water Oxidation and Hydrogen Evolution reactions: Oxidation State-dependent Activity 151

4A.1 Introduction 151

4A.2 Synthesis & characterization of Ru@CNT and RuO_2@CNT 152

4A.3 Electrocatalytic HER studies 159

4A.4 Electrocatalytic OER studies 163

4A.5 Influence of the oxidation state of the NPs 166

4A.6 Conclusions & perspectives 167

4A.7 Experimental part 170

4A.8 References 173

4B Carbon Microfiber-Supported RuNPs as HECs: Stabilizing Effect of the Support & Surface Environment 177

4B.1 Introduction 177

4B.2 Synthesis & characterization of CF-supported RuNPs 178
4B.3 Electrocatalytic HER studies 182
4B.4 Conclusions & perspectives 191
4B.5 Experimental part 193
4B.6 References 196

5. General Conclusions & Perspectives 199

6. Annexes 205

Annex 1: Tables for Hydrogen Evolution Catalysts' Electrochemical Performance Benchmarking
Annex 2: *A porous Ru nanomaterial as an efficient electrocatalyst for the hydrogen evolution reaction under acidic and neutral conditions* (J. Creus *et al. Chem. Commun.* **2017**, *53*, 11713)
Annex 3: *A Million Turnover Molecular Anode for Catalytic Water Oxidation* (J. Creus *et al. Angew. Chem. Int. Ed.* **2016**, *55*, 15382)

1

General Introduction

This first chapter aims at providing to the readers the state of the art in the field of water splitting catalysis, as well as to report the motivation that focused our interest on this scientific challenge. The main aspects of the Oxygen and Hydrogen Evolution Reactions (OER and HER, respectively) will be displayed together with a general review on catalysts development and mechanistic understanding.

Recently, metal NPs proved to be efficient catalysts for the production of hydrogen from water. However, fundamental studies are still necessary in order to design more efficient nanocatalysts. In this line, the organometallic approach will be presented as a prominent tool for the synthesis of metal nanoparticles, which allows a control on their structural properties (e.g. surface environment, size, shape) and thus reactivity, being the method chosen for own studies in the other parts of this work.

1. General Introduction

1.1 World Energy Outlook

The huge increase on the population during the last century[1] (Figure 1a) as well as the establishing of the welfare state in 1st world countries as a basic lifestyle, have enhanced the energy demand (Figure 2a) and thus the need for the associated resources. Additionally, the great advances in technological, scientific and medical research are not only accomplishing their purpose, which is to facilitate people's everyday life, but are fundamentally creating a dependency of human being on energy-requiring devices. This statement is depicted on Figure 2a, where we can see how the energy consumption changed over the years.[2] This illustrates how the priorities have changed on 1st world population, to reach a more comfortable society following the colloquially called "minimum effort law".

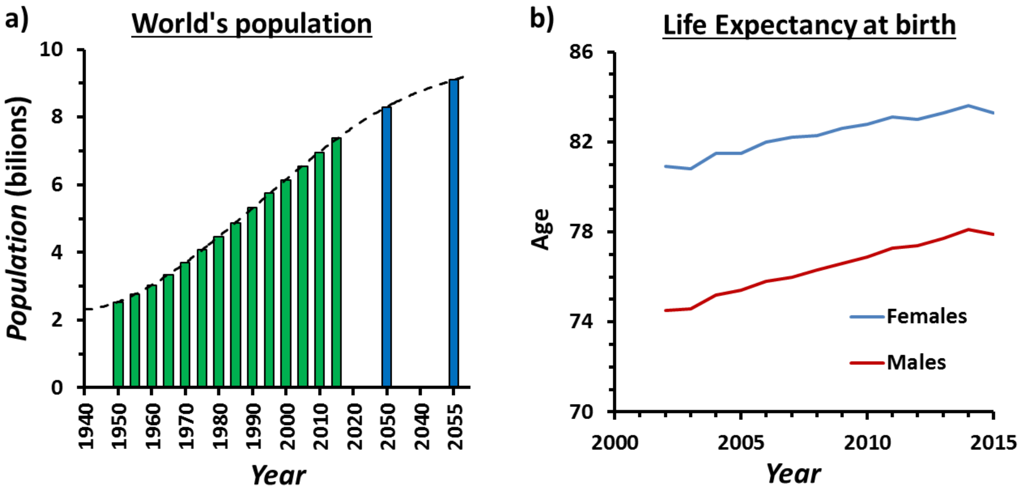

Figure 1. a) World's population increase over the last decades (green) and future perspectives (blue);[1] b) increase on the life expectancy at birth during the last 15 years.[3]

In fact, the advancement in medicine that is increasing the life expectancy in human beings (Figure 1b),[3] is of course promoting this aforementioned rise on the world citizens, affecting not only on the energy reservoirs for artificial devices, but most importantly on the availability of sufficient products for feeding the entire population.[4]

Besides the philosophical discussion on the changes of 1st-world-"civilized" society, there is a drawback to be solved, energetically speaking. Energy has largely been obtained by the combustion of fossil fuels as coal, oil or natural gas (Figure 2a), leading to two important problems: firstly, the main feedstocks are running out inducing an obvious increase on their price;[5] secondly, and with a greater significance in what Earth and human lifetimes concern, the use of these sources as energy precursors has dramatically increased the presence of greenhouse gases (GHG: $H_2O_{(g)}$, CO_2, CH_4, NO_X or O_3) in the atmosphere.[6] Ozone hole or global warming are some of the resulting effects of this massive GHG concentration, but derivative outcomes are also observed, like ocean level increase due to glaciers melting or animal migration due to temperature rising. Nonetheless, air pollution is the 4th risk factor for human health,[7] after high blood pressure, dietary risks and smoking; and SO_X, O_3 or NO_X are well-associated with a range of illness.

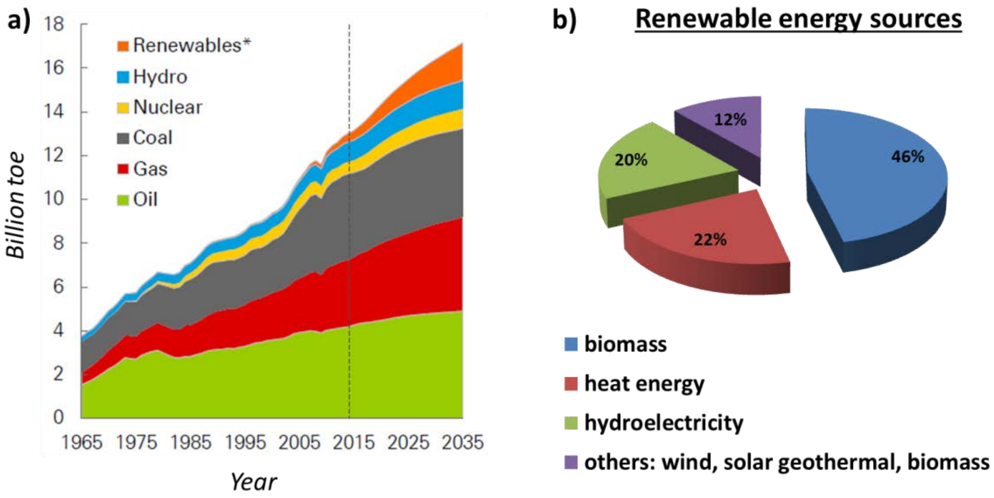

Figure 2. Left, world energy consumption by year in billion toe, divided in energy sources.[2] Right, percentage of energy obtained from the main renewable sources.[8]

Fortunately, the interest on replacing fossil fuels as energy sources, by more cleaner and renewable products that can be widely used without damaging the environment, is rising. Obviously, this concern is not shared with all the administrations, governs and of course companies, who prioritize the own success against to the common interest to keep a healthier world. Recent studies hypothesize that fossil fuels will remain supplying 75% of the energy demand on 2035, against 85% in 2015.[2] This means a slowing down on the increase of carbon emissions, even though a fall by around 30% by 2035 should be achieved to accomplish the goals set up in the “Paris agreement” by the United Nations.[9] As in 2015 only 3% of the overall consumed energy was coming from renewables,[2] an increase up to 10% as planned for 2035 would be a significant progress, even if still a small achievement.

The development of engines allowing the use of renewable energies has already reached a milestone: they start becoming cost-competitive in the countries where there is an obvious governmental support.[8] On the other hand, as depicted in Figure 2b, out of the 3% of power that is being supplied by renewables, 46% is coming from traditional biomass, 22% from heat energy (modern biomass, geothermal and solar heat), 20% from hydroelectricity and 12% is electricity from wind, solar, geothermal, and biomass.

1.2 Solar Energy

Among all renewable sources, sunlight energy is the most available one: more sunlight energy strikes the earth in 1 hour than all of the energy consumed on the planet in 1 year.[10] This means that a 0.02% of this solar energy would be enough to fulfil all human energy requirements. Additionally, all chemical and radioactive polluting by-products of so-called thermonuclear reactions taking place in the Sun are there retained, and only pure radiant energy is transmitted to the Earth.[11] The effective solar radiation reaching the whole surface of the Earth in one year (eliminating the backscattered and absorbed, which is around 46%), means approximately a solar power of 89,300 TW, nine times higher than the wind power (1000 TW) that is the second most powerful renewable source. This indicates that by using a 10% efficient device, on only 0.17% of the Earth's surface, we could achieve the current 15 TW of worldwide energy consumption.

However, this harvested energy needs to be harnessed in other forms such as fuels, chemicals or electricity. This implies to transform the charge formed by photon absorption into a vector of energy that can be later used. Nowadays, devices using sunlight can be divided in three main categories, as follows:

a) *Solar thermal systems*, which directly convert sunlight radiation into thermal energy for heating applications.
b) *Photovoltaics (PVs)* that transform the solar energy into electricity without the interface of a heating engine.
c) *Solar fuels,* namely the storage of the solar energy into the chemical bonds of molecules.

To achieve an alternative to fossil fuels using sunlight as energy source we need chemical products as vectors that, when consumed, release clean and environmentally friendly by-products. In this sense, in 1912, the photochemist G. Ciamician, who is considered as the father of solar panels, proposed a challenge:[12,13]

> "*to fix the solar energy through suitable photochemical reactions with new compounds that master the photochemical processes that hitherto have been the guarded secret of the plants*"

In summary, he proposed to use the sunlight energy and to store it into chemical bonds, as plants do for example with CO_2 fixation during the photosynthesis. This aims at energy transformation and storage into solar fuels.

This is the birth of the "Artificial Photosynthesis" (APS) concept, which will be further discussed in section 1.4. Briefly, it is a biomimetic process inspired by the principle of photosynthesis that plants apply for the energy storage. Through the photosystem II (PS-II), plants absorb the solar energy to break water molecules into O_2 and a gradient of protons (H^+) and electrons (ē). The released charged species go to the photosystem I (PS-I), where they act as reductive agents to achieve the energy storage as chemical bonds in carbohydrates. In the APS concept, the breaking of water molecules is achieved by means of the sunlight energy as well, but synthetic catalysts are required to perform the involved redox process, instead of the natural ones in plants. By this way, water becomes precursor of a fuel, which can either be a carbon-based one (from CO_2 reduction) or H_2.

Regarding more precisely the redox process involved when considering water as energy source, two products are obtained when breaking water molecules: O_2 and H_2. The H-H bond in the gaseous H_2 molecule is highly energetic.[14] Once initiated, its combustion in the presence of O_2 is straightaway and can be explosive in concentrations of 4-74%, following the reverse reaction:

$$2H_2 + O_2 \rightarrow 2H_2O \qquad \Delta H = -113.5\ Kcal \cdot mol^{-1} \qquad \text{Eq. 1}$$

As a consequence, the use of H_2 as a fuel is of high interest due to the high energy release in its combustion. However, its utilization can be dangerous as well as its transportation and storage is complex. In the following section, H_2 advantages and disadvantages as chemical energy vector will be discussed.

1.3 Hydrogen: Advantages & Disadvantages

Hydrogen as an element is the most abundant in the universe,[15] which at standard temperature and pressure (273.15 K, 10^5 Pa) is present as molecular H_2: a colorless, odorless, tasteless and highly combustible gas. It was first identified by H. Cavendish in 1766,[16] who named it as “inflammable air”. Some years later he found out that water was produced when this gas was combusted (Eq. 1). In 1783, A. Lavoisier proposed the name “hydrogen” to imply that it is a component of water (hydro). However, it was over one century before, in 1672, that R. Boyle produced it describing the synthetic reactions,[17] starting up from iron filings and diluted acids:

$$Fe + 2HX \rightarrow FeX_2 + H_2 \qquad \text{Eq. 2}$$

Despite the fact that in the Universe “H” is basically found in atomic or plasma states, in the Earth it exists as molecular H_2, even if it is a light gas that rapidly escapes from Earth’s gravity,[18] and in chemical compounds such as hydrocarbons and H_2O. H_2 is naturally produced by some bacteria and algae, and it is also a component in flatus.[19]

Several advantages strongly suggest H_2 as a promising alternative to fossil fuels:

1. It can be obtained from the most abundant chemical product on Earth, H_2O.

2. Its combustion leads to the only formation of steam and liquid H_2O, which is highly considerable from an environmental point of view.
3. It is nontoxic.
4. In fuel cells, the chemical energy of H-H bond gets directly transformed into electricity without any heat requirement and with enhanced efficiency, in contrast to other fuels.
5. The long-distance energy transmission is more economical than through high-voltage AC (alternating current) lines.

The comparison of the properties of H_2 with those of gasoline evidences the high capacity of this gas as a fuel:

Table 1. Comparison of H_2 properties with those of gasoline.[20]

	Properties					
Fuel	***Specific energy ($KWh\cdot Kg^{-1}$)***	***Energy density ($MJ\cdot dm^{-3}$)***	***Self-ignition temperature (K)***	***Flame propagation in air ($m\cdot s^{-1}$)***	***Explosion energy (Kg TNT$\cdot m^{-3}$)***	***Difussion coeficient in air ($cm^2\cdot s^{-1}$)***
H_2	33.33	9.17	858	0.02	2.02	0.61
Gasoline	12.4	34.2	498-774	0.40	44.22	0.05

Interestingly, hydrogen has a specific energy value 2.5 higher than gasoline, although its low energy density hampers its storage (further discussed in section 1.3.2). In terms of security, H_2 self-ignition starts at temperatures around 50% higher than gasoline (858 vs. 498-774 K), and its explosion energy is more than 20 times lower, stating it as a less dangerous alternative. Moreover, H_2 is a light gas that rapidly diffuses in air and it has no damaging healthy effect due to its non-toxicity, in contrast to gasoline.

Table 2. Comparison of energetic parameters of H_2 and typical molecules usable as fuels.[21] Gibs free energy ($\Delta G°$), theoretical thermodynamic potential ($E°_{theor}$), maxiumum potential ($E°_{max}$) and energy per mass density ($KWh\cdot Kg^{-1}$).

Fuel	H_2	*MeOH*	NH_3	N_2H_4	*HCOH*	*CO*	HCO_2H	CH_4	C_3H_8	*EtOH*
$\Delta G°$ ($Kcal\cdot mol^{-1}$)	-56.7	-166.8	-80.8	-143.9	-124.7	-61.6	-68.2	-195.5	-503.2	-341
$E°_{theor}$ (V)	1.23	1.21	1.17	1.56	1.35	1.33	1.48	1.06	1.08	1.15
$E°_{max}$ (V)	1.15	0.98	0.62	1.28	1.15	1.22	1.14	0.58	0.65	-
Specific Energy ($KWh\cdot Kg^{-1}$)	33.33	6.13	5.52	5.22	4.82	2.04	1.72	13.9	-	8

It is also worth to compare H_2 energy data with those of several products that can be used in fuel cells as energy vectors.[21] Doing so (Table 2), we notice that the specific energy of H_2 is not only higher than gasoline's one, but also than other fuels such as formic acid, MeOH or ammonia. Additionally, H_2 is the energy vector losing less energy on its combustion ($E°_{theor}$- $E°_{max}$).

In the following section, hydrogen production processes will be described, with the focus centered on the Water Electrolysis (WE) and the Steam Reforming of Methane (SMR) from natural gas. In terms of cost,[22] WE is highly advantageous given that water is renewable, cheaper and easier to obtain than petroleum or natural gas; however, the refining process increases the costs of its production up to similar rates than gasoline, as depicted in Figure 3.

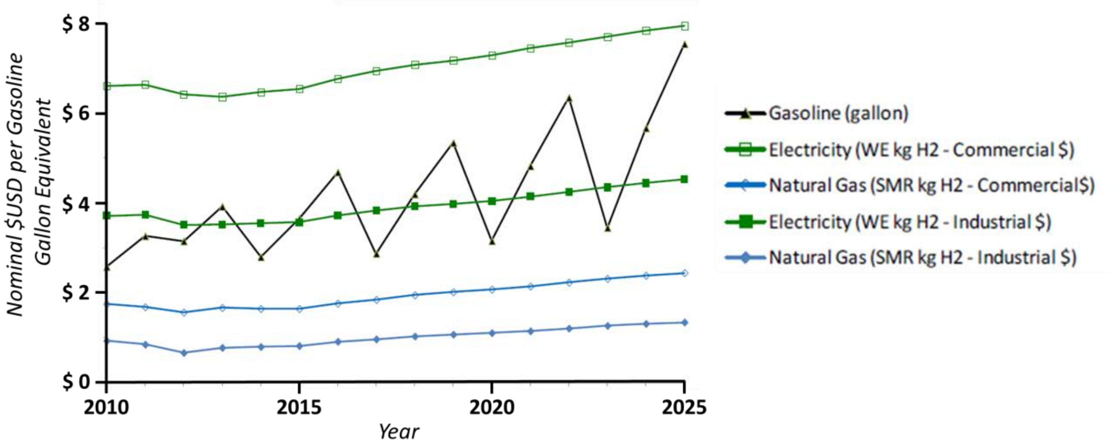

Figure 3. Past, present and future perspective on the cost of using H_2 instead of gasoline, published by *Air Products*.[22] Gasoline (black triangle), commercial electricity from WE (empty green square), industrial electricity from WE (filled green square), commercial natural gas from SMR (empty blue diamond) and industrial natural gas from SMR (filled blue diamond).

Consequently, it is important to consider not only the interest of H_2 as a fuel, but also the feasibility of its production, storage and transport. All these points will be briefly discussed in the following sections.

1.3.1 Hydrogen production

Nowadays, several processes are being used to produce H_2 starting up from various chemical compounds. The most important ones are briefly described hereafter.

Steam-reforming

Industrially, H_2 gas is mainly obtained by the Steam Reforming of Methane (SMR) or fossil fuel reforming from natural gas (95% of H_2 production in US in 2017).[23] SMR is an environmentally unfriendly process that consists in reacting gaseous water (steam) and CH_4 under high temperature and pressure (700-1100 °C, 20 atm.) to promote the H_2 formation as follows:

$$CH_4 + H_2O \rightarrow CO + 3H_2 \qquad \text{Eq. 3}$$

$$CO + H_2O \rightarrow CO_2 + H_2 \qquad \text{Eq. 4}$$

By this way, a well-known mixture called as “syngas” (synthesis gas) composed by H_2 and CO is obtained (Eq. 3). The formed CO can be reused in the “water-gas shift reaction” for further obtaining H_2 (see Eq. 4).

The main drawback of the steam reforming process for obtaining H_2 is the huge production of CO_2 as by-product, which is one of the green-house gases to be avoided in the atmosphere. In this sense, there is nowadays the aim of using a renewable source instead of naphta in the reforming process. Ethanol can be an alternative,[21,24] as it is easy to transport, biodegradable, has low toxicity and it can be easily decomposed in the presence of H_2O to form H_2 (Eq. 5):

$$C_2H_5OH + 3H_2O \rightarrow 2CO_2 + 6H_2 \qquad \text{Eq. 5}$$

EtOH can be produced from the sugar fermentation of biomass. Those carbohydrates are produced by natural plants from CO_2 and water. Considering that CO_2 is the only by-product of EtOH reforming, the latter is considered as a renewable fuel. Moreover, the efficiency of ethanol in the reforming process is higher than that of other carbon-based products with a reaction enthalpy of $\Delta H^0_{298} = 83.03\ \mathrm{Kcal \cdot mol^{-1}}$.

Thermochemical decomposition

Another typical method to produce H_2 consists on the thermal treatment of water to split it into O_2 and H_2. The Gibbs free energy of the water decomposition can be lowered down by increasing the temperature, becoming null at 4700 K.[25] However, the highest available temperature by a nuclear reactor is 1300 K which is far from the required heat for the single-step decomposition of water.

An alternative to circumvent this drawback is to realize the thermal splitting of water by a multi-step method. Metal-based two-step decomposition of water can be achieved at temperatures above 1273 K, involving the intermediate formation of a metal oxide, metal hydride or hydrogen halide. With the purpose to lower down even more the required temperature, a multi-step process can be used involving several reactions all of them having smaller energy barriers. For example, the following four-step procedure (Eq. 6-9) involves only one reaction with temperatures above 1000 K:

$$2H_2O_{(g)} + I_{2(g)} + SO_{2(g)} \rightarrow 2HI_{(g)} + H_2SO_{4(g)} \qquad \mathrm{T = 300\ K} \qquad \text{Eq. 6}$$

$$H_2SO_{4(g)} \rightarrow H_2O_{(g)} + SO_{2(g)} + 0.5O_{2(g)} \qquad \mathrm{T = 510\ K} \qquad \text{Eq. 7}$$

$$Ni_{(s)} + 2HI_{(g)} \rightarrow NiI_{2(s)} + H_{2(g)} \qquad \mathrm{T = 570\ K} \qquad \text{Eq. 8}$$

$$NiI_{2(s)} \rightarrow Ni_{2(s)} + I_{2(g)} \qquad \mathrm{T = 1070\ K} \qquad \text{Eq. 9}$$

Any thermochemical process aimed to be employed for the H_2 production requires these four steps: 1st, water decomposition or hydrolysis (Eq. 6) followed by the oxygen (Eq. 7) and hydrogen generation (Eq. 8), and ending up by the regeneration of any consumed intermediates (Eq. 9).

Water electrolysis

The electrochemical water splitting, or electrolysis of water, was discovered by W. Nicholson and A. Carlisle on 1800.[26] As its name announces, it consists in applying an electric potential onto a water-containing two-electrode cell, thus leading to the formation of O_2 and H_2 as the result of the splitting of water molecules (Eq. 10):

$$2H_2O \rightarrow 2H_2 + O_2 \qquad \Delta H = 113.5\ Kcal \cdot mol^{-1} \qquad \text{Eq. 10}$$

This breaking of water molecules is a non-favored reaction thermodynamically speaking and, as previously mentioned, the backward process is spontaneous at a wide range of concentrations (Eq. 1). Obviously, there is a dependency of the generation of the two gases formed (O_2 and H_2) on the applied potential at each electrode (cathode/anode). According to the Nernst equation, the required potentials (E^0 vs. NHE, for Eq- 11-12) for the anode to start oxidizing water and for the proton reduction at the cathode are:

$$E^0{}_{O_2/H_2O} = 1.229 - (0.059 \times pH) \qquad \text{Eq. 11}$$

$$E^0{}_{H^+/H_2O} = 0.000 - (0.059 \times pH) \qquad \text{Eq. 12}$$

As it can be deduced from the two equations, there is a clear dependency of the thermodynamic potential (E^0) for the production of O_2 and H_2 on the pH, graphically displayed in Figure 4.[25]

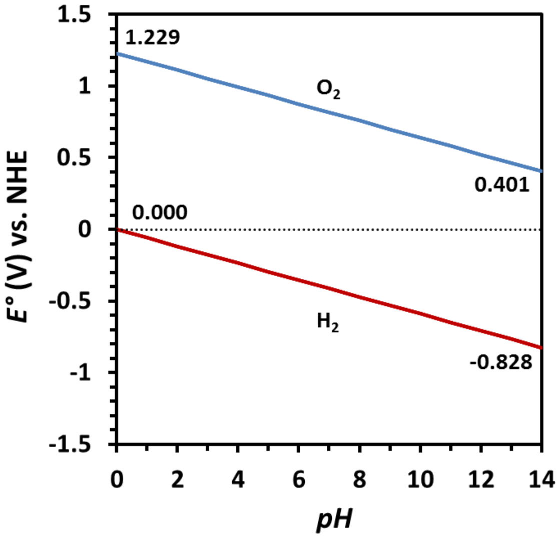

Figure 4. Graphical representation of the dependency of the thermodynamic potential (*E*° vs. NHE) of the O_2 and H_2 production from H_2O, depending on the pH.

In the case of the oxygen evolution reaction (OER), there is a potential decrease while the pH increases as the OER is favored under alkaline conditions. In contrast, for the cathodic hydrogen evolution reaction (HER), there is an increase on the required reductive potential at higher pH due to the smallest [H^+]. Moreover, there is an excess energy coming from electrochemical system resistance or water conductivity, which needs to be beaten and that is called overpotential (η). A catalyst is necessary to lowering down this energy in both semi-reactions. In "Nicholson & Carlisle"'s experiment, H_2 and O_2 bubbles appeared on two Pt-wires, which were used inside a sealed tube containing water, and powered with a voltaic pile, making a precedent for the use of Pt as electrocatalyst.

Currently, one commercial device to perform water electrolysis is the polymer electrolyte membrane (PEM) fuel cell.[27] In most of the PEM commercial systems, both the cathodic and anodic catalysts are based on Pt and Ir, which are scarce and highly-expensive metals that make them unsuitable for large-scale and industrial applications. As a consequence, there is still room for improvement in the development of electrodes and electrolytes with catalysts that are efficient, low-cost and that have long-term durability, based on more earth-abundant metals.[28]

The previously mentioned APS is a sunlight-assisted electrolysis of water, in which the energy comes from the sun irradiation instead of the electric power.

1.3.2 Hydrogen storage & transport

Hydrogen can be stored on the Earth in gas, liquid or solid (in chemical bonds or adsorbed) states. Gas and liquid storing have been used for a long time, but they have several disadvantages as follows:

- Liquid H_2 boils at around 20.3 K (-252.9 °C), which means that a high amount of energy is required to get liquated H_2.
- Cryogenic containers with temperature insulating are needed for the H_2 storage at so low temperatures, increasing the price of storing.
- Both liquid and compressed H_2 gas have lower energy density ($MJ \cdot dm^{-3}$) than hydrocarbon fuels. Thus, bigger tanks are required for having the same energy than with e.g. gasoline.

Given the drawbacks above mentioned, high density hydrogen storage is an issue for stationary and portable applications and remains significantly challenging for transportation. Carbon fiber is a material recently used for hydrogen containers, e.g. in fuel-cell vehicles (FCV), which enhances the tanks safety towards withstand crash, drop test, fire, and ballistic, as tested.[20] Alternative ways for storing H_2 in the solid state are being investigated, either under the form of chemical bonds in bigger molecules or metal complexes, or physically or chemically adsorbed onto solids' surfaces or within porous solids. For instance, H_2 can be stored under the form of metal hydride (M-H) species (Eq. 13-14):

$$M + \left(\frac{x}{2}\right) H_2 \rightarrow MH_x \qquad \text{Eq. 13}$$

$$M + \left(\frac{x}{2}\right) H_2O + \left(\frac{x}{2}\right) \bar{e} \rightarrow MH_x + \left(\frac{x}{2}\right) OH^- \qquad \text{Eq. 14}$$

Other possibilities are to physically store H_2 molecules into the cavities of three-dimensional molecular porous matrices.[20] Zeolites for example, allow hydrogen penetration in their pores at high temperatures.[29] By cooling down the material H_2 can be guested inside the pores, while reheating it releases H_2 back. However, very low storage capacity of 0.1-0.8 wt.% is achieved with zeolites. In Metal-Organic Frameworks (MOFs), both metal clusters and organic units can work as adsorption sites for H_2 molecules.[30] They are easy to synthesize and their physical properties can be tuned to achieve larger-diameter pores or change channel curvatures, to reach a storage capacity over 1-4 wt.%.

Chemical storage into liquid-phase compounds can be also considered, achieving good storage capacity of 8.9 wt.% for methanol, 15.1 wt.% for ammonia, and 13.2 wt.% for methylcyclohexane.[20] Aminoboranes (AB = NH_3-BH_3) are another alternative H_2-storing molecules thanks to their high hydrogen density (15.4 %) and low molecular weight (30.8 g·mol^{-1}).[31] The transition-metal catalyzed AB hydrolysis to obtain H_2 can be achieved under mild conditions, being able to generate three equivalents of H_2 per AB molecule (Eq. 15):

$$NH_3BH_3 + 2H_2O \xrightarrow[r.t.]{cat.} NH_4BO_2 + 3H_2 \qquad \text{Eq. 15}$$

Carbon-based materials are also promising for molecular H_2 storage because of their combined adsorption ability, high specific surface, pore microstructure, and low mass density.[32] Activated carbon,[32b] carbon fibers (CFs)[32c,d] and either Single-Walled Carbon NanoTubes (SWCNT) or Multi-Walled ones (MWCNT)[32e] are among carbon-based materials used as storage materials.

Although H_2 production, storage and transport methods are being investigated, there is still room for improvement to make H_2 a cost-effective alternative to carbon fuels.

1.4 Artifical Photosynthesis vs. Natural Photosynthesis

As previously mentioned, plants harvest solar energy in the PS-II[33] and use it to reduce CO_2 into carbohydrates by using water (Eq. 16-17):[13]

$$6H_2O + 6CO_2 + h\nu \rightarrow C_6H_{12}O_6 + 6O_2 \qquad E^0 = 1.24\ \mathrm{V} \qquad \text{Eq. 16}$$

$$2H_2O \rightarrow O_2 + 4H^+ + 4\bar{e} \qquad E^0 = 1.23\ \mathrm{V} \qquad \text{Eq. 17}$$

In other words, solar energy is being stored as chemical bonds in primary sugar molecules, such as glucose, that plants use as precursors for the formation of superior carbohydrates like cellulose. O_2 is formed as a byproduct, being the only waste product in this whole process that started around 3500 million years ago, and the responsible of guaranteeing the continuity of life in the Earth. In this way, plants are both, diminishing the CO_2 concentration in the atmosphere and producing the O_2 that life-being species require.

More specifically, water is oxidized on the oxygen evolving complex (OEC) by the Mn_4CaO_5 cluster,[34] using the sunlight energy harvested on the PS-II (see Figure 5). The Mn-cluster is capable of storing four oxidative charge equivalents, and the gradient of protons and electrons ($4H^+ + 4\bar{e}$) is transported to the PS-I, where it is used for the reduction of $NADP^+$ (nicotinamide adenine dinucleotide phosphate) to form the reduced form NADPH,[13] which is later on the responsible of fixing or reducing CO_2 in the Calvin cycle.

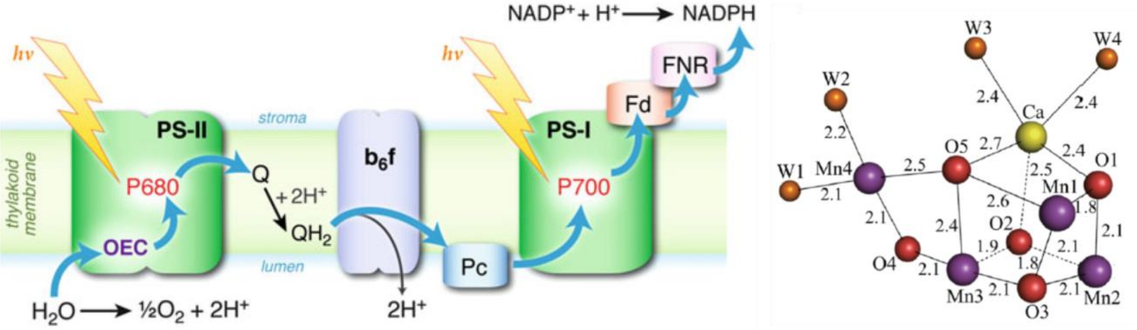

Figure 5. Left, photosynthetic electron-transfer chain of the thylakoid membrane;[35] right, Mn_4CaO_5 cluster in the OEC in the PS-II.[34]

This clean process has been for a long time a source of inspiration for scientists who try to find an alternative way to produce energy avoiding the use of C-based sources, and mimicking the natural photosynthetic pathway in plants. The splitting of water liberating "$4H^+ + 4\bar{e}$" follows the proton-coupled electron transfer (PCET) mechanism, that was described by T. J. Meyer *et al.* in 2004,[36] and which is of high importance for the rational development of water oxidation catalysts, as it will be later discussed.

The principle of artificial photosynthesis relies on the use of the released H^+ and $\bar{e}$ resulting from water oxidation, to produce at disposal molecules with high-energetic bonds. This means: a) CO_2-derivated carbohydrates (Eq. 18) or b) hydrogen (Eq. 19):

$$4H^+ + 4\bar{e} + CO_2 \rightarrow [CH_2O] + H_2O \qquad \text{Eq. 18}$$

$$4H^+ + 4\bar{e} \rightarrow 2H_2 \qquad \text{Eq. 19}$$

1.5 Water Splitting

Water splitting is known as a promising option to produce H_2 from the most available source in the Earth, H_2O (see Eq. 10 on page 10). The breaking of water into H_2 and O_2 gases is an energetically demanding process. It can also be named as water electrolysis, if the energy comes from an electronic device as it is the case on photovoltaic electrolyzer cells (PV/Electrolyzer, Figure 6a); or artificial photosynthesis, if the source of electrons is the direct sunlight irradiation, as in the mixed-colloid devices (Figure 6b).[37] However, systems that combine both techniques are of high interest, namely photoelectrochemical cells (PEC, Figure 6c). They take advantage of sunlight energy harvesting as inexorable source through photoactive species (photoanodes/photocathodes), instead of using expensive PV-devices. Further, alike PV-based systems, in PEC the two catalysts are placed in separated compartments and they can be present in homogeneous solution or immobilized onto the electrodes' surface.

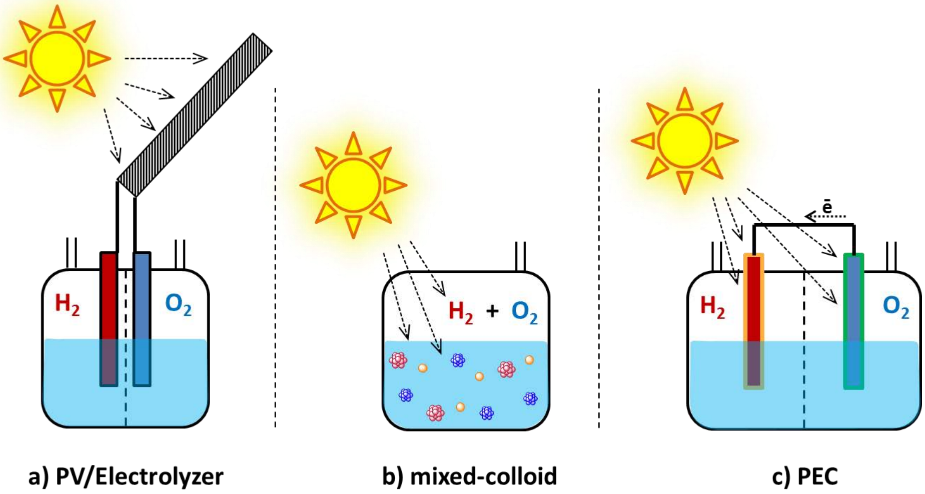

Figure 6. Schematic drawing of three different devices for the light driven water splitting process.

In plants chlorophyll is the antenna that harvests light. The light harvesting activates the OEC and its Mn-cluster leading to the breaking of water and O_2 formation (see Eq. 17 on page 13). In the APS, a photocatalyst (photosensitizer, semiconductor, etc.) is required to act as solar-energy absorbing species, as well as a Hydrogen Evolution Catalyst (HEC) or CO_2 reduction catalyst, and a Water Oxidation Catalyst (WOC). A photosensitizer (PS), as the well-known $[Ru(bpy)_3]^{2+}$ complex (**1** in Figure 7, left),[38] is a species that can work in a mixed-colloid device (e.g.) harvesting sunlight to provide the light-excited electron to the HEC, as shown in Figure 7 (right). The reduction catalyst is then able to reduce H^+ or CO_2 molecules, while on the same time, the oxidation catalyst gives an ē to reduce the PS^+ back to PS, being ready to oxidize water to O_2.

Also semiconducting materials (such as TiO_2, ZnO or CdS) can be simultaneously used as light-harvesting species and catalyst, e.g. in PEC devices. The first example was described by K. Honda and A. Fujishima in 1972:[39] they used TiO_2 as photoanode in connection with a Pt-based cathode, and, by irradiating UV-vis light, O_2 and H_2 bubbles respectively appeared on the surface of each electrode (Figure 7, bottom-left). If a PEC is used, both catalysts are activated through photoactive electrodes or species in each compartment, what enhances the efficiency of the whole device.

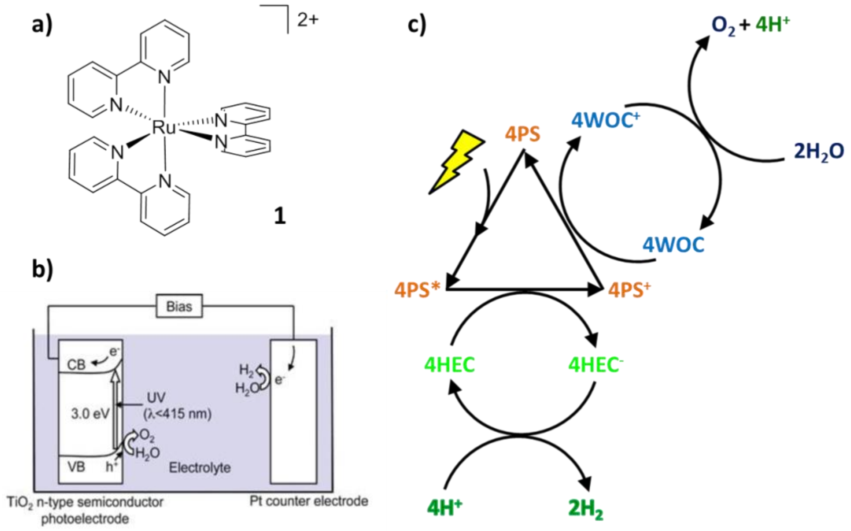

Figure 7. a) Photosensitive $[Ru(bpy)_3]^{2+}$ complex **1**; b), photoelectrochemical cell containing a TiO_2-photoactive anode and a Pt cathode, reported by Honda and Fujishima;[39] c) schematic representation of the electron transfer process in a photo-induced catalytic WS.

As previously introduced on page 11, potentials above the thermodynamic potential (1.23 V at pH=0) are required to oxidize water, as there are complex electron and ion transfer processes that slow down kinetics and make the reaction energetically inefficient.[40] This additional potential that is needed above the thermodynamic reaction potential ($E^0(O_2/H_2O)$ = -1.23 V and $E^0(H^+/H_2)$ = 0.00 V vs. RHE), is called overpotential (η). It derives from both chemical drawbacks and device set-up, as for example activation energy, species diffusion, electrodes and wires resistance, or bubble formation.

The role of the WOC is to lower down the activation barrier of the oxidative semi-reaction, and so to diminish the required overpotential to start forming O_2. The WOC can be an oxide material as first published by A. Coehn and M. Gläser in 1902,[41] or a molecular complex. Molecular complexes have recently been widely studied since the discovery of the ruthenium "blue dimer" by T. J. Meyer in 1982 (**2** in Figure 8).[42] Analogously, the HEC is needed to diminish the energy barrier for reducing protons (η), which is much lower than for the oxidative counterpart as it simply involves the formation of two H-H bonds (see section 1.5.2 for further details).

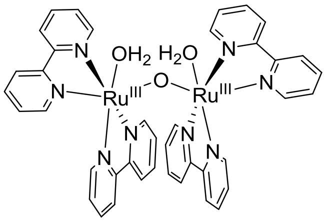

2

Figure 8. Structure of Meyer's "blue dimer" **2**.[42]

Considering that the general topic of this PhD work is the development of Ruthenium-based nano-sized species, to be used as catalysts for the WS process, from now on we will mainly focus on Ru-based catalysts for both, water oxidation and proton reduction reactions.

Before highlighting the literature data on WOCs and HECs, it is important to define two crucial concepts for the description and comparison of catalysts in general. The TurnOver Number (TON) of a catalyst (cat in Eq. 20) defines the number of times that the cat. is capable of performing the catalytic reaction (R→P in Eq. 20), and therefore how stable it is under the catalytic conditions. This can be easily calculated by dividing the number of moles of product ($n_{P(t=x)}$ in Eq. 21) formed at time t=x, by the number of moles of catalyst ($n_{cat.}$ in Eq. 20):

$$R \xrightarrow{cat} P \qquad \text{Eq. 20}$$

$$TON_{(t=x)} = \frac{n_{P(t=x)}}{n_{cat}} \qquad \text{Eq. 21}$$

$$TOF_{(t=x)}(s^{-1}) = \frac{TON_{(t=x)}}{x} = \frac{n_{P(t=x)}}{n_{cat} \cdot x} \qquad \text{Eq. 22}$$

The kinetic parameter generally used for catalyst benchmarking, is the TurnOver Frequency (TOF, [s^{-1}]). It corresponds to the TON value divided by a given period of time (t=x), for example the turnovers that a catalyst does per second (Eq. 22), corresponding to the velocity of the catalyst. Both parameters may change during catalytic experiments, depending on the catalyst stability, availability of substrates and/or reaction conditions.

Three other parameters that are key for the description and comparison of electrocatalysts are the onset overpotential (η_0), the overpotential at $|j|$ = 10 mA·cm^{-2} (η_{10}) and the Tafel slope (b):

- η_0 is referred to the electrochemical potential (respect to the thermodynamic E^0) at which the catalytic reaction starts, and it can be distinguished by a change on the current intensity (i) due to a Faradaic process, when performing voltammetry experiments.

- η_{10} is the potential (respect to the thermodynamic E^0) at which the system reaches a $|j|$ = 10 mA·cm^{-2}. This value is already normalized by the geometrical electrode surface area, so it allows the comparison between systems with similar loading and different surface areas, and it is generally accepted as the approximate current density expected for an integrated solar water-splitting device under 1 sun illumination operating at 10% solar-to-fuel efficiency.

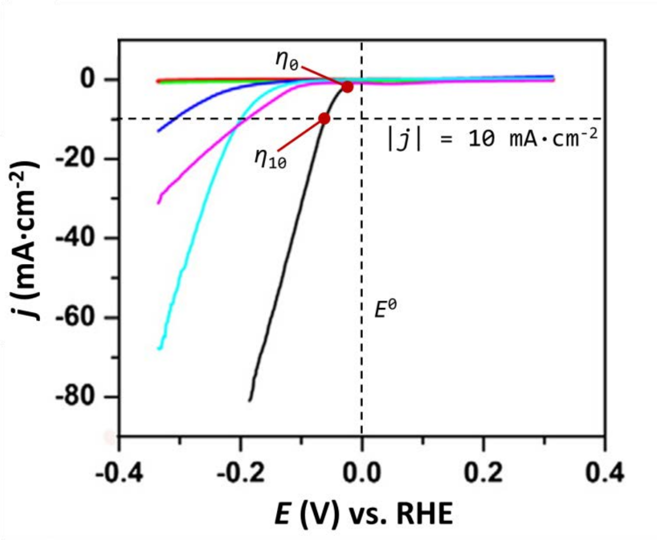

Figure 9. Typical polarization curves for HECs with η_0, η_{10} and E^0 parameters.

- The Tafel plot is the representation of the overpotential of an electrochemical system vs. the log of the current density (j). The equation ruling an electrocatlyst's curve is called the Tafel equation, and possesses an slope (b) which gives kinetic information on the rate determining step (rds) among the different reaction pathways (see specific information on the following OER/HER sections).

- Another interesting parameter can be deduced from the Tafel plot, which is informative of the catalyst activity: the exchange current density (j_0). It is defined as the obtained current in the absence of any faradaic process and at η_0; the higher j_0, the better the catalyst is considered. It can be obtained by resolving the Tafel equation for η = 0 mV, giving rise to the residual current of the catalytic system under non-faradaic conditions.

1.5.1 Oxygen Evolution Reaction

As previously mentioned, the OER is considered as the bottleneck for the development of water splitting devices. It is a complex reaction as it involves the extraction of 4 protons and 4 electrons from two water molecules, and an O=O double bond formation.[43] From a catalytic point of view, the Mn cluster of the PS-II system in natural PS is a model for the development of WOCs, as it collects the four hole equivalents produced by solar irradiation that are required for performing the oxidation of water. With regards to WO nanocatalysts, since the understanding of their catalytic mechanisms still supposes a significant challenge, the scientific community has paid great attention in the mechanisms arising in molecular WO complexes, with the aim of correlating their main steps onto solid systems. In this sense, the polypyridyl structure of the so-called "blue dimer" (Figure 8 in section 1.5) gave birth to a new family of water oxidizing Ru-compounds known as Ru-OH_2 polypyridyl complexes.[44,45] The study of the Ru-OH_2 polypyridyl family has permitted to elucidate the two most important processes in the oxygen evolution reaction: the Proton Coupled Electron Transfer (PCET) and the Oxygen-Oxygen bond formation.[46]

Proton-Coupled Electron Transfer (PCET)

An exhaustive study of Ru-OH_2 polypyridyl species through Cyclic Voltammetry (CV) and spectroscopic techniques enabled T. J. Meyer *et al.* to define the "Proton Coupled Electron Transfer" (PCET) mechanism.[36,47] They studied the different Ru oxidation states as well as the pKas of the aqua groups in each species, and observed that when an electron was removed from the $[Ru^{II}\text{-}OH_2]^{2+}$ species a proton was simultaneously lost. Hence, by the removal of $1H^+$ and 1ē or $2H^+$ and 2ē of the $[Ru^{II}\text{-}OH_2]^{2+}$ species (Eq. 23), three different metal oxidation states appeared to be stable:

$$[Ru^{II} - OH_2]^{2+} \xrightarrow{-H^+, -\bar{e}} [Ru^{III} - OH]^{2+} \xrightarrow{-H^+, -\bar{e}} [Ru^{IV} = O]^{2+} \qquad \text{Eq. 23}$$

This PCET process results from the increase in acidity of the aqua groups when the metal is oxidized. Therefore, the removal of an electron from the $[Ru^{II}\text{-}OH_2]^{2+}$ core induces the loss of a proton, leading to $[Ru^{III}\text{-}OH]^{2+}$ species which undergoes the same process to form $[Ru^{IV}{=}O]^{2+}$. This entity contains a more powerful electron donating oxygen group ($H_2O < OH^- < O^{2-}$), which better stabilizes high metal oxidation states. Consequently, redox potentials are lowered when PCET occurs, avoiding high energetic intermediates, as can be seen in Scheme 1:

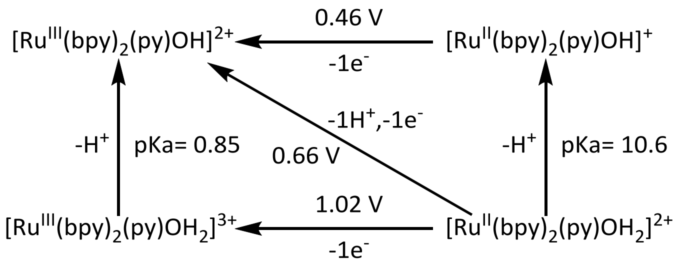
$[Ru^{III}(bpy)_2(py)OH]^{2+}$
0.46 V
-1e$^-$
$[Ru^{II}(bpy)_2(py)OH]^{+}$
-H$^+$
pKa= 0.85
-1H$^+$,-1e$^-$
0.66 V
-H$^+$
pKa= 10.6
1.02 V
$[Ru^{III}(bpy)_2(py)OH_2]^{3+}$
-1e$^-$
$[Ru^{II}(bpy)_2(py)OH_2]^{2+}$

Scheme 1. Acid-base redox potential diagram for Ru^{III}/Ru^{II} redox couples of $[Ru^{II}(bpy)_2(py)(OH_2)]^{2+}$. Potentials are given versus NHE.

PCET mechanism elucidation has been crucial not only for the understanding of Ru-OH_2 polypyridyl complexes reaction pathways, but also to contribute to the general knowledge of water oxidation mechanisms in the natural Mn-based OEC.

Oxygen-oxygen bond formation

After release of the necessary electrons and protons and the accumulation of the oxidative equivalents in the Ru^{IV}=O species, the O-O bond can be formed. Scheme 2 illustrates the two plausible mechanisms that have been experimentally proven by studying different molecular WOCs:[48,49]

1. **Water Nucleophilic Attack (WNA):** a water molecule attacks the M-O moiety of a highly oxidized metal.
2. **Intramolecular or Intermolecular pathway (I_2M):** two M-O centers merge to form a M-O-O-M peroxo moiety.

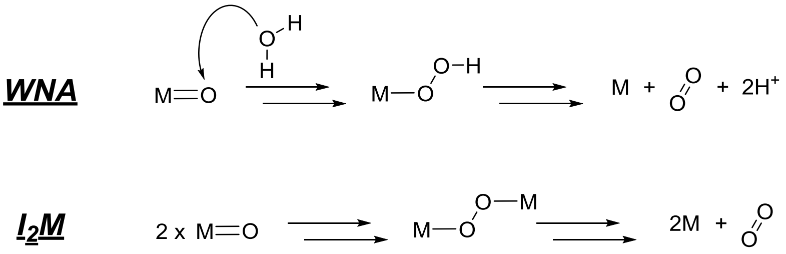

Scheme 2. Two plausible mechanisms for O-O bond formation with molecular WOCs.[50]

Both mechanisms have been observed depending on the catalyst nature and the reaction media. The most outstanding examples of water oxidation catalysts will be presented in the following section.

In the materials field, S. Trasatti *et al.* proposed a multi-step mechanism after studying as catalyst ternary metal oxides of $Ru_{0.3}Ti_{(0.7-x)}Ce_xO_2$ composition that catalyzed the OE reaction in acidic media.[51,52] Analogous to the homogeneous processes, the first step is the absorption of a hydroxide group (Eq. 24), followed by the formation of a metal-oxide species (Cat-O), either through a second electron transfer (Eq. 25) or a recombination step (Eq. 26):

a) $Cat_{(s)} + H_2O \rightarrow Cat - OH_{(ad)} + H^+ + \bar{e}$ Eq. 24

b) $Cat - OH_{(ad)} \rightarrow Cat - O_{(ad)} + H^+_{(aq)} + \bar{e}$ Eq. 25

b') $2Cat - OH_{(ad)} \rightarrow Cat - O_{(ad)} + Cat_{(s)} + H_2O$ Eq. 26

c) $2Cat - O_{(ad)} \rightarrow 2Cat_{(s)} + O_2$ Eq. 27

The last step, the O=O bond formation (Eq. 27), allows to regenerate the catalyst active species through a "I_2M"-like pathway.

As previously presented, from the Tafel equation of an electrocatalyst kinetic information on the catalyst performance can be obtained. In the particular case of heterogeneous OE catalysis, a Tafel slope (*b*) of 40 mV·dec^{-1} suggests a mechanism in which the second electron transfer (Eq. 25 or 26) is the rds, whereas a slope of 30 mV·dec^{-1} is characteristic for systems where the rds is the recombination reaction (Eq. 27).

1.5.1.1 Molecular complexes as WOCs

Among the state-of-the-art of molecular catalysts as WOCs, first-raw transition metals (TMs) such as Co, Cu, Mn and Fe are the most frequently earth-abundant metals object of study.[48-61] Mn is particularly interesting due to its role in natural photosynthesis, but also because of its high abundance. R. H. Crabtree, G. W. Brudvig *et al.* described in 1999 the first dinuclear Mn complex, $[H_2O(terpy)Mn(O)_2Mn(terpy)OH_2](NO_3)_3$ (terpy is 2,2':6',2"-terpyridine), capable of oxidizing water into molecular dioxygen (**3** in Figure 10).[53] Later on several studies reported no impressive activities and the decomposition of the sacrificial oxidant as secondary reaction.[54] B. Åkermark *et al.* could diminish the required overpotentials of dinuclear Mn-based complexes by using imidazole and carboxylate groups on the ligands, making the catalytic system compatible with the sacrificial oxidants.[55]

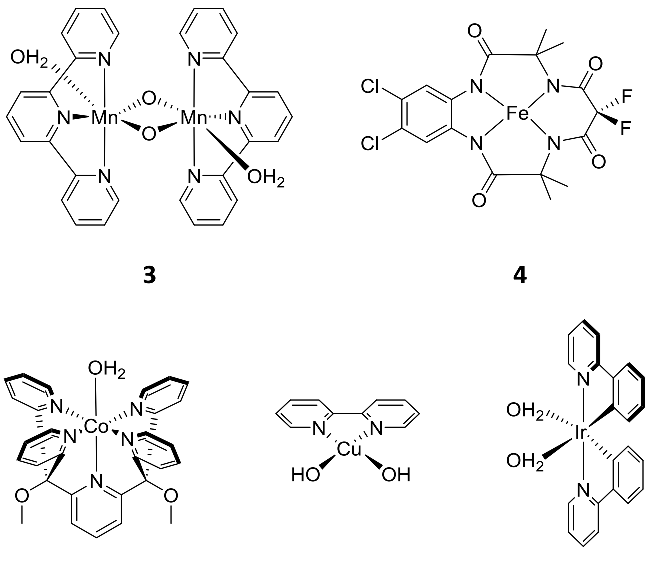

3 **4**

5 **6** **7**

Figure 10. Some TM-based molecular complexes as WOCs: $[H_2O(terpy)Mn(O)_2Mn(terpy)OH_2](NO_3)_3$ (**3**), Fe^{III}-TAML (**4**), $[Co(Py5)(OH_2)](ClO_4)_2$ (**5**), $[(bpy)Cu(\mu\text{-}OH)]_2^{2+}$ (**6**), and $[Ir(ppy)_2(H_2O)_2]^+$ (**7**).

Similar to Mn, Fe is highly abundant and has low toxicity, being thus a feasible option for OER.[56] S. Berhnard *et al.* reported in 2010 the first family of Fe complexes able to catalyze the OE (Fe^{III}-TAML, **4** in Figure 10), followed by J. Lloret-Fillol, M. Costas *et al.*[57]

Again, the stability under the oxidative conditions was doubtable in some cases,[58] achieving the formation of FeO_x species.

General knowledge on molecular Co-based OEC has rapidly evolved since C. P. Berlinguette's first published in 2011 the $[Co(Py5)(OH_2)](ClO_4)_2$ (Py5 = 2,6-(bis(bis-2-pyridyl)methoxymethane)pyridine) complex (**5** in Figure 10).[59] Good activities have been reported in other contributions,[60,61] but the nature of the real active species proved to be not molecular in some cases. Decomposition to nanoparticulated CoO_x or films has been observed,[62] thus stating the low stability of cobalt coordination compounds under OER conditions.

J. M. Mayer *et al.* described the first Cu-based complex as WOC $[(bpy)Cu(\mu\text{-}OH)]_2^{2+}$ (**6** in Figure 10), which at high pH values formed a dinuclear active species.[63] From this point, T. J. Meyer,[64] A. Llobet[65] and G. W. Brudvig,[66] among others, described several Cu-based homogeneous catalysts.

On the second and third row of the periodic table, low-abundant Ir-based complexes have attracted much attention as molecular WOCs. S. Bernhard described in 2008 the first family of Ir-complexes bearing cyclometalated phenylpyridine ligands, such as $[Ir(ppy)_2(H_2O)_2]^+$ (**7**) in Figure 10,[67] which showed OE activity for several days. R. H. Crabtree and M. Albretch also contributed on the development of Ir-based complexes containing pentamethylcyclopentadienyl (Cp*) and carbene-type ligands, respectively.[68] However, the stability of such molecular compounds and thus the nature of the active species are not evident due to ligand oxidation under the strong oxidative conditions,[69] and formation of active IrO_x species was observed.[70]

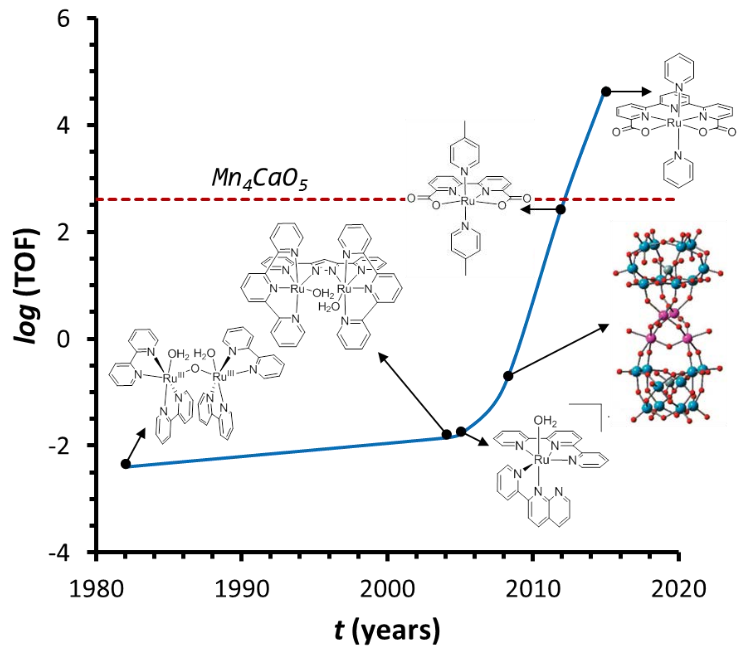

Figure 11. General plot on the report of new WOCs over the time and their increased catalytic activity in log(TOF) compared to the OEC from PS-I. The catalysts are shown in Figure 12 (**8**-**12**).

Polypyridyl-stabilized Ru molecular complexes were the center of intensive studies and improvements on the development of homogeneous water oxidation catalysis, due to both the electronic properties that polypyridyl ligands offer and their stability under catalytic reaction conditions. A proper way to analyze the progress over the years on the development of WOCs is to compare the increase of the TOF values (Figure 11).

According to that, a long time was necessary to develop a catalyst with activity values as high as the naturally occurring system (Figure 11). Blue dimer's TOF (0.004 s^{-1}) and TON (13.2) are much lower than the Mn cluster ones (TOF = 100-400 s^{-1}).[71] Until A. Llobet *et al.* reported in 2004 a ruthenium dimer containing a trpy and Hbpp ligands (2,2':6',6"-terpyridine; 2,2'-(1H-pyrazole-3,5-diyl)dipyridine, **8** in Figure 12), no great improvement has been achieved in terms of catalyst efficiency while this one reached higher TON (512) and TOF values (0.014 s^{-1}) than the "blue dimer".[72,73] At that time, it was believed that a dinuclear complex was mechanistically required for achieving the O-O bond formation,[74] but R. P. Thummel (2005)[75] and T. J. Meyer (2008)[76], among others, proved that mononuclear metallic complexes (**9**,**10** and **11**, respectively) could also work as WOCs.[74] Furthermore, M. Bonchio and C. L. Hill simultaneously published a family of Ru-POM (polyoxometallates) complexes mimicking the natural occurring Mn cluster,[61] such as the fast and water-soluble PW_9O_{34} with a tetraruthenium active core (**12** in Figure 12), which exhibited 4.5 TON/s rate.[77,78]

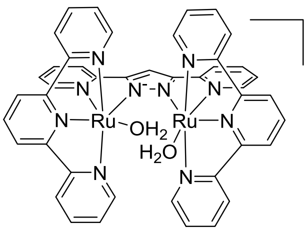

8

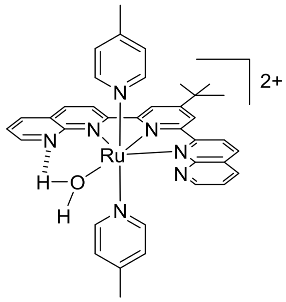

9

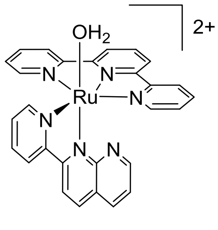

10

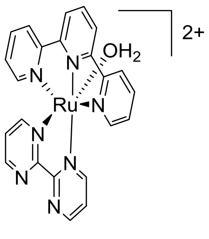

11

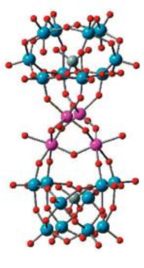

12

Figure 12. Structure of Llobet's dinuclear $[Ru^{II}_2(bpp)(trpy)_2(H_2O)_2]^{3+}$ (**8**), Thummel's $[Ru^{II}(tnp)(Me\text{-}py)_2(H_2O)]^{2+}$ (**9**) and $[Ru^{II}(trpy)(pynap)(H_2O)]^{2+}$ (**10**), Meyer's $[Ru(trpy)(bpm(OH_2)]^{2+}$ (**11**), and Bonchio's Ru_4-POM (**12**).

One step forward on the development of active WOCs and the rational design for mechanistic understanding of the molecular oxidation of water are the recent studies made by L. Sun and A. Llobet with a new family of mononuclear ruthenium complexes.[79,80] The incorporation of a dianionic ligand (main characteristic of this new family), 2,2’-bipyridine-6,6’-dicarboxylic acid (**13**, bda^{2-}) or 6,6'-dicarbonixilate-[2,2':6’,2”-terpyridyl] (**14**, tda^{2-}), provides an electronically richer metal center, in which this negatively charged equatorial ligand decreases the necessary overpotential for accessing higher oxidation states to oxidize water (**15** in Figure 13).[81] Thus, complex **15** from the Ru-bda family could produce oxygen with TON up to 55000 in an extremely short time lapse, leading to a TOF value of 300 s^{-1}. These numbers narrow the difference between the Mn cluster at OEC in PS-II and human designed catalysts (Figure 11). For Ru-bda complexes, an I$_2$M intermolecular mechanism for the O-O bond formation was detected by UV-vis spectroscopy through dimerization of two ruthenium centers.[79,80a,82]

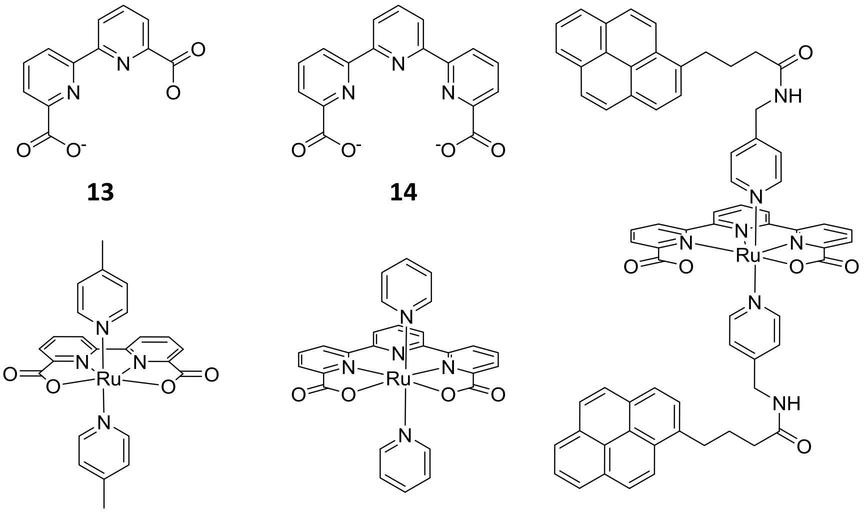

13

14

15

16

17

Figure 13. Structure of ligands bda^{2-} (**13**) and tda^{2-} (**14**) and their complexes [Ru(bda)(4-pic)$_2$] (**15**), [Ru(tda)(Py)$_2$] (**16**) and [Ru(tda)(Py-Pyr)$_2$] (**17**).

More impressive is still the performance of the Ru-tda-based complex, such as complex **16** in Figure 13. In this case, initial 7-coordination geometry is observed on the Ru center without the presence of any H$_2$O molecules in the coordination sphere.[83] This is crucial as the carboxylates play a double role: besides facilitating the oxidation of the metal towards higher oxidation states due to its anionic ability, after the coordination of a water molecule they act as acidic groups for the PCET, removing protons for the formation of the Ru^{V}=O active species. Ru-tda family complexes can reach up to 50000 s^{-1} TOF values depending on the nature of the axial ligands, and being the more active WOCs published so far (Figure 11). This improvement on the catalytic activity is attributed to the richer electron density of the metal coordination sphere, which at the same time creates also steric hindrance, leaving aside the I_2M mechanism as a feasible option.

The fact that Ru-tda complexes follow the WNA pathway, and so do not require the approach of two catalyst molecules for the O-O bond formation, allows their anchoring onto solid supports without altering their catalytic performance and avoiding side reactions as complex decomposition.[84] When I_2M is the main O-O bond formation pathway, e.g. with Ru-bda complexes,[85] the immobilization of the catalyst hinders the approach of two complex molecules, facilitating those side reactions. π-Stacking interactions between pyrene-based ligands and CNTs is a plausible choice for molecular catalyst immobilization, as demonstrated with Ru(tda)$(py\text{-}Pyr)_2$ complex **17** in Figure 13,[84a] which enables the preparation of photoactive materials for the light-driven oxidation of water.[84b]

These results open a new door towards the construction of molecular anodes for the OER, in which the proper rational design of ligands will permit to tune the mechanistic pathway of the catalytic reaction. Further, the immobilization of the active species in an efficient manner is a way to maintain the catalytic active species stable and to allow their recycling.

1.5.1.2 Metallic nanoparticles as WOCs

As previously mentioned, it is well-known since the publication of A. Coehn and M. Glässer in 1902 that metal-oxide materials can also catalyze oxygen evolution from water.[41] For the development of new catalytic materials, maximizing the number of surface active sites is of paramount importance and, therefore, systems at the nanoscale, with large surface area to volume ratios, present obvious advantages. Contrarily to traditional electrolyzers, that work in basic condition, proton exchange membrane (PEM) for WS systems operate in acidic media and provide numerous performance advantages that convert them in ideal devices for the delocalized storage of renewable electricity at the small scale.[86] IrO_x species are widely used in Proton Exchange Membrane Water Electrolyzer (PEMWE),[87,52] but their prohibitive conditions (expensive and scarce)[88] prevent them to be applied in large-scale industrial applications.

RuO_2 has been widely used as WOC after P. A. Christensen *et al.* first published in 1988 the photochemical performance of a rutile-structured RuO_2 in oxidizing water.[89] Recently, J. Rossmeisl *et al.* attributed this high catalytic performance to the average binding energy of surface bonded oxygen species (found as activity-controlling parameter) through thermochemical density functional theory (DFT)-based OER calculations, as represented in the volcano type activity plot (Figure 14), which correlates the overpotential of a series of MO_X-based WOCs with their M-O binding energy.[90]

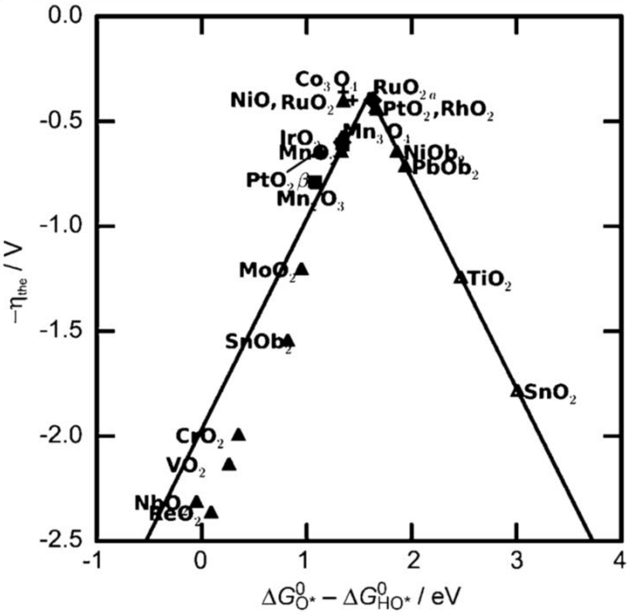

Figure 14. Volcano-type plot of the correlation between MO_x-WOCs activity (expressed as overpotential) and their metal-oxygen binding standard free energies based on DFT-calculations.[90]

A recent contribution of I. E. L. Stephens, I. Chorkendorff *et al.* constitutes the state-of-the-art work to discuss the factors that influence the activity and stability of Ru-based NPs in OER.[86] Ru^0/RuO_2 NPs (2-9 nm) prepared through magnetron sputtering were tested with thermally oxidized RuO_2. The former turned out to be more active than the oxidized material, but it immediately corrodes to form soluble RuO_4, therefore losing the activity as WOC, as already observed for other systems based on metallic Ru.[91a,90] OER mass activity, specific activity (0.32 mA·cm^{-2} at η = 0.25 V) and TOF data (0.1-1.0 s^{-1} for η = 0.22-0.27 V) for the RuO_2 system resulted one order of magnitude higher than those found for any other NP in acidic media, which is attributed to the clean surfaces provided by this preparative method. This is particularly clear when the performance of this system is compared with the chemically prepared 6 nm RuO_2-NPs reported by Y. Shao-Horn *et al.*[92] of similar size and crystallinity but clearly lower specific activities (0.182 mA·cm^{-2} at η = 0.30 V), although being in basic media.

Metallic Ru stability issues under OER acidic conditions were also observed by P. Strasser *et al.* when they compared the electrocatalytic OER activity and stability of Ru, Ir and Pt NPs with that of their corresponding bulk counterparts.[91c] Even if Ru^0-NPs show the best initial specific activity, important passivation and corrosion are observed from the first CV scan given that RuO_4 forms at potentials close to those needed for OER.

In basic media (1 M NaOH), high current densities at relatively low overpotentials (η = 0.35 V) have also been reported by J. C. Peters, T. F. Jaramillo *et al.* when benchmarking a commercial RuO_2 as well as a wide set of nanoparticulate metals.[93] However, when the specific current densities are calculated by taking into account the electrocatalytic (ECSA) or BET (Brunauer-Emmett-Teller) surface areas, the obtained values drastically decrease, underperforming other transition metal oxides such as NiO, $NiCoO_2$ or Mn_3O_4.

B. Lim *et al.* published the inferior efficiency of hydrous RuO_2 of low crystallinity with regards to that of a crystalline counterpart prepared by annealing of the former at 400 °C (η_{10} is 123 mV lower for the latter).[91a] The inverse trend is reported by M. Han *et al.* when analyzing metallic RuNPs of different crystallinity.[94] The better performance of amorphous RuNPs in this case (η_0 50-60 mV lower) is attributed to the higher number of coordinately unsaturated available surface sites. This trend better correlates with the general results observed for other transition-metal oxides and from those described for RuO_2 thin films.[95]

Decomposition of molecular complexes into nanosized materials is barely reported for Ru-based catalysts, contrasting with other TMs. This is in agreement with the intrinsic stability of Ru molecular WOCs that contain robust ligands. However, when using ligands with easily oxidizable organic groups,[96] CO_2 generation has been observed. This implies that massive ligand degradation occurs concomitant with the formation of O_2, thus pointing to the formation of RuO_2 as the final active species rather than the initial molecular complex. A particularly interesting example of ligand degradation is the case of the Ru-bda complex (Figure 15a) when anchored onto a glassy carbon surface (for further details see section 1.5.1.1).[85] Although this catalyst is extremely robust in homogeneous phase, under its immobilized form it cannot undergo dimerization due to restricted mobility, resulting in ligand degradation and the formation of highly active RuO_2-NPs (j = 1.5 mA·cm^{-2} at η = 283 mV, Figure 15b).

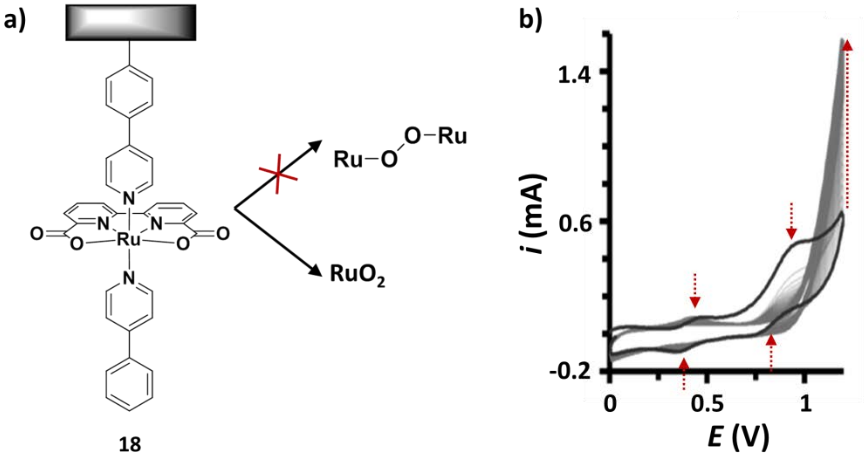

Figure 15. a) Ru-bda@GC complex structure (**18**) and degradation under catalytic conditions. b) Repetitive cyclic voltammograms (50 cycles) for GC-supported Ru-bda at pH=7 up to 1.20 V. The black solid line corresponds to the first cycle whereas the rest are drawn in gray.

T. Ren *et al.* reported the embedding of pre-formed 1.6 nm RuO_2 NPs into mesoporous silica (SBA-15),[91d] displaying higher TOF than any other related particles in SiO_2 ($TOF_{max} = 0.27\ s^{-1}$) and a TON > 200 after 15 cycles. This high activity relays on the pore-confinement effect in SBA-15, which prevents crystal growth during annealing and thus allows obtaining a metal oxide of small size, low crystallinity and high surface area. This hypothesis is in agreement with the reduced activity reported by D. W. Bruce *et al.* for similar RuO_2 NPs embedded in a MCM-41 mesoporous silica with very small pore diameter (2.7 nm, $TOF_{max} = 0.038\ s^{-1}$).[91e] Probably, the small pores size blocks the access of active surface area. Low TON and TOF values (10 and 0.006 s^{-1}, respectively) have been also recently reported by E. V. Johnston *et al.* with subnanometric RuO_2 NPs embedded into a pyridine-functionalized siliceous mesocellular foam (MCF) arising from $RuCl_3$ impregnation, reduction with $NaBH_4$ and air oxidation of the Ru^0-NPs formed.[97] Finally, it is also worth mentioning the work of A. Mills *et al.* about the photoreduction of RuO_4^{2-} to yield RuO_2 NPs of 2-3 nm with TiO_2 as dopant in a one-pot reaction.[98] When triggered by Ce^{IV}, the system shows remarkable stability but a moderate TOF of *ca.* 0.02 s^{-1}.

M. V. Martinez-Huerta *et al.* reported an electrochemically-triggered system where the support/electrode has a key role for the described performance.[99] The catalytic system is composed of bimetallic (Pt_3Ru) NPs supported onto titanium carbonitride (TiCN). While the expected role of Pt is merely affecting the final Ru %wt. in the sample, enhanced activity and stability of the supported Ru/RuO_2 catalyst under OER conditions are observed. Both effects are attributed to the TiCN support that prevents the catalyst aggregation and dissolution.

Although the $[Ru(bpy)_3]^{2+}$ complex has been commonly employed for the photocatalytic evaluation of Ru-based NPs in OER,[91,94,100] the use of semiconducting materials as light-harvesters has been also reported.[91b] T. Ren *et al.* photocatalytically evaluated the RuO_2@SBA-15 system of 2nd generation with a better dispersion of the catalyst, which showed O_2 yields > 90%, with a TOF value of $6.6\cdot10^{-3}\ s^{-1}$.[100] This system outperforms many other transition metal oxides and previous RuO_2 systems reported to date, probably due to the pores of the SBA-15 support, which allow the efficient interaction between the catalyst and the PS. The photocatalytic evaluation of the MCF-based system of E. V. Johnston *et al.* (*vide supra*),[97] in a similar OER configuration, led to a TON of 4 and a three times lower TOF of $2.2\cdot10^{-2}\ s^{-1}$.

A different approach aiming at facilitating ē-transfers between the RuO_2 catalyst and the PS was described by R. Yoshida *et al.*[101] The reported hydrogel system closely arranges pre-formed RuO_2 NPs and a $[Ru(bpy)_3]^{2+}$-derivative by means of both electrostatic interactions between polar groups and steric confinement within a polymeric matrix, which produces O_2 under visible light irradiation. Finally, the n-semiconductor TaON has been doped with RuO_2 NPs of different sizes arising from the calcination of $[(NH_4)_2RuCl_6]$ at different temperatures.[91b] Under visible light irradiation the doped system outperforms bare TaON, highlighting the higher efficiency of RuO_2 as OER catalyst.

1.5.2 Hydrogen Evolution Reaction

The reduction of protons is a simpler process than the O_2 evolution reaction. In contrast to the oxidative process where four H-O bonds have to be broken and an O=O double bond formed, HER involves the formation of two H-H bonds by the reduction of two H^+ groups. This divergence is evidenced with the overpotentials that catalysts require in each semi-reaction, in general being < 100 mV for HECs and > 200 mV for WOCs.

Pt-group metals are the most used for HER, being Pt itself the most active metal in reducing protons. Thus, there is a huge interest in replacing it, due to its scarcity and resulting prohibitive price. However, WS-devices containing a proton exchange membrane work better at acidic pH, making most of the first-raw metal-based species unsuitable given their low stability under these conditions.

After studying the mechanistic insights on published catalysts based on natural products, V. Artero *et al.* stated that an efficient catalyst for the reduction of protons should possess the following features:[102]

- A redox-active species (usually d-block transition metals) capable to be oxidized or reduced at moderate potentials.
- An available coordination site for the M-H bond formation, either with an easy-to-exchange labile ligand (through ligand reductive elimination) or a vacant position.
- A basic group (often called proton relay) which assists the M-H bond formation and facilitates the PCET process by capture and deliver of protons to the vicinity of the reactive center.

Mechanistic studies on molecular proton reduction are multitudinous, going through a M-H bond formation preceded by a metal reduction. The mechanism has been described, for example, for Co-based complexes both experimentally and theoretically. It can go through a homolytic pathway by the interaction of two Co^{X}-H species to form two $Co^{(X-1)}$ groups (bold arrows, Scheme 3), or by the heterolytic pathway by the reaction of a Co^{X}-H with a H^+ in solution, thus recovering the Co^{X} species (dashed arrows, Scheme 3).[103]

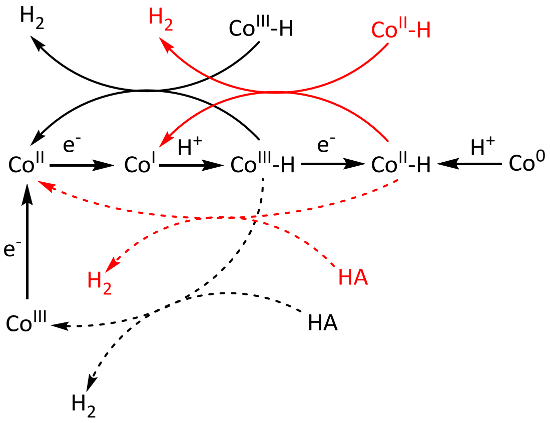

Scheme 3. HER mechanism proposal by H. B. Grey a *et al.* for the [(triphos)CoIII(H)$_2$]$^+$ (triphos, 1,1,1-tris(diphenylphosphinomethyl)ethane) complex through hemolytic (bold) and heterolytic (dashed) pathways.[103]

In nanomaterials HER has been described to occur through two different reaction pathways, namely Volmer-Heyrovsky or Volmer-Tafel. The followed steps are represented in Scheme 4 and hereafter described (Eq. 28-30):[104]

Volmer: $$Cat_{(s)} + H^+_{(aq)} + \bar{e} \rightarrow Cat - H_{(ad)} \qquad \text{Eq. 28}$$

Heyrovsky: $$Cat - H_{(ad)} + H^+_{(aq)} + \bar{e} \rightarrow H_{2(s)} + Cat_{(s)} \qquad \text{Eq. 29}$$

Tafel: $$2Cat - H_{(ad)} \rightarrow H_{2(s)} + 2Cat_{(s)} \qquad \text{Eq. 30}$$

The Volmer step (Eq. 28) is the adsorption of one proton onto the catalyst surface, and is common for all the HEC. It is considered as a PCET-step on the surface of the catalyst, and is alternatively called discharge reaction. The desorption step can either go through the electrodesorption of the adsorbed hydride with an H$^+$ in solution (Heyrovsky, Eq. 29), which is also a PCET process (analogous to WNA in OER); or the recombination of two metal-hydride groups (M-H), from a unique particle or from two different ones (Tafel, Eq. 30, analogous to I$_2$M in OER).

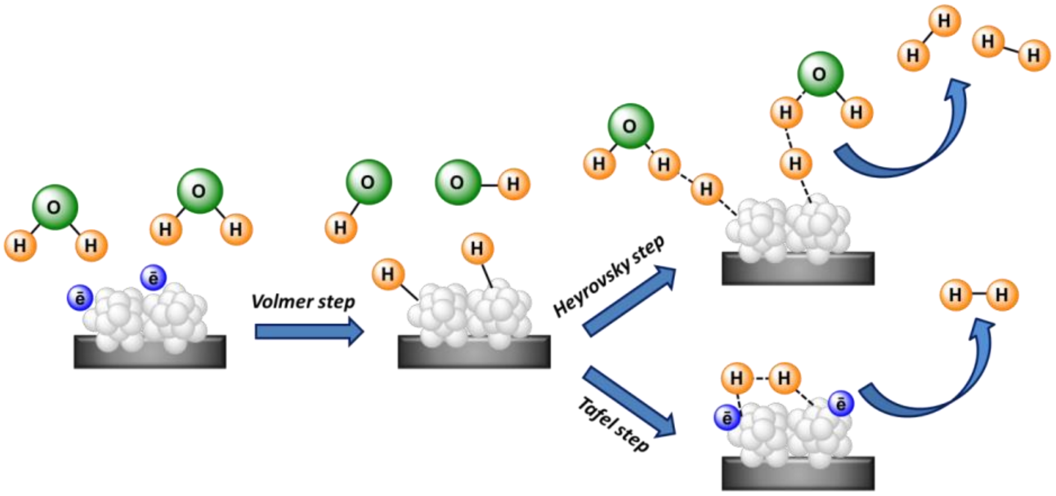

Scheme 4. Representation of the three steps involved on the HER mechanism on materials as catalysts.

Thermodynamically, electrocatalysts are ruled by the Nernst equation, which allows to calculate the thermodynamic potentials as $E^0(H^+/H_2) = 0.00 - (0.059 \times pH)$. However, electrocatalysts require higher energies than the thermodynamic equilibrium potential due to kinetic drawbacks. This additional energy is called overpotential (η), and is the difference between E^0 and the potential at which the catalytic reaction starts. The catalyst has to overcome this barrier, being considered as good HECs the ones reaching remarkable activities at $\eta \leq 100$ mV. HER kinetics follows the Butler-Volmer equation (Eq. 31), which evidences that there is a strong dependency on the electrochemical potential:[105]

$$j = j_0[-e^{-\frac{\alpha nF\eta}{RT}} + e^{(1-\alpha)\frac{nF\eta}{RT}}] \qquad \text{Eq. 31}$$

where j is the current density, j_0 is the exchange current density, α is the charge transfer coefficient, n=1 is the number of electrons transferred, F is the Faraday constant, R is the ideal gas constant, and T is the temperature. At a low overpotential close to the equilibrium potential (η = 0.05V), the equation is simplified and a linear correlation between η and j is observed (Eq. 32). However, at higher η values, the linear relationship appears between η and log(j) (Eq. 33 and 34):

$$\eta = (\frac{RT}{nFj_0})j \qquad \text{Eq. 32}$$

$$\eta = a + b \cdot log(j) = -\left(\frac{2.3RT}{\alpha nF}\right) logj_0 + (\frac{2.3RT}{\alpha nF})logj \qquad \text{Eq. 33}$$

$$b = \frac{2.3RT}{\alpha nF} \qquad \text{Eq. 34}$$

As previously presented, the graphical representation of η vs. log(j) is called the Tafel plot, with the slope of the equation plotting the curve equal to b (Eq. 34), named as Tafel slope. The equation gives kinetic information about the catalyst and its rate determining step (rds), even though complete information on the reaction mechanism is hard to elucidate. The rds of the general hydrogen evolution reaction depends on the binding energy of the M-H bond. In acidic conditions, if the rds of the reaction is the Volmer step, a typical Tafel slope (b) of ≈120 $mV\cdot dec^{-1}$ is obtained. However, if the rds is the Heyrovsky or the Tafel step, characteristic slopes of ≈40 $mV\cdot dec^{-1}$ or ≈30 $mV\cdot dec^{-1}$ are observed, respectively.

1.5.2.1 Molecular complexes as HECs

There are several examples of first-row earth-abundant metal-based catalysts that are active for the reduction of protons.[106] For instance, bio-inspired [FeFe] (**19**) and [NiFe] - hydrogenases (**20**)[107] have already been described (Figure 16). Also, iron-based porphyrins (**21**) have attracted the attention of the scientific community,[108] being Fe one of the most earth-abundant metals and also highly present in natural reactions. In fact, Co[109] and Ni[110] porphyrins have also been reported as HECs. In fact Co[111] has been used in several molecular complexes such as polypyridinic-based ones, cobaloximes[112] or diamine-dioxine [Co^{II}(DO)(DOH)pnX$_2$] (**22**, Figure 16),[113] among others.

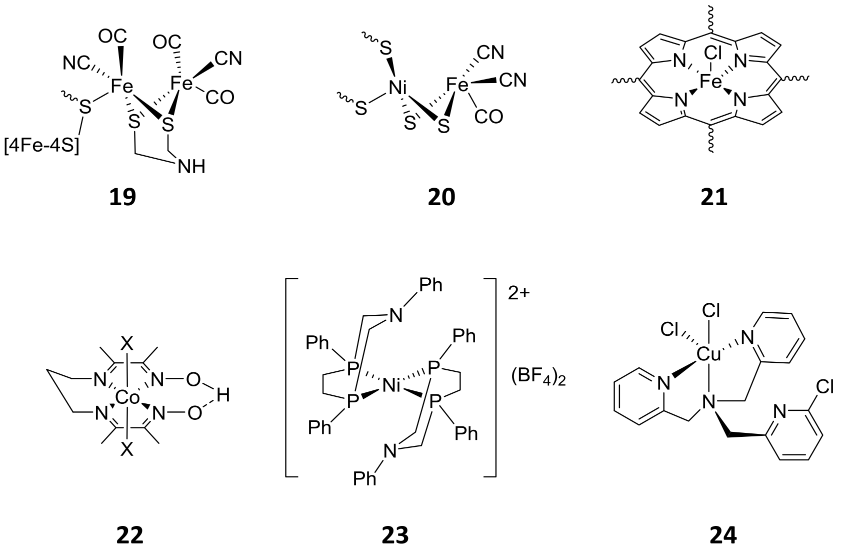

Figure 16. Earth-abundant metal-based complexes as HECs: [Fe-Fe]-hydrogenase (**19**),[107] [Ni-Fe]-hydrogenase (**20**),[107] Fe-based porphyrin (**21**),[108] [Co^{III}(DO)(DOH)pnX$_2$] (**22**),[113] [Ni(P$_2^{Ph}$N^{Ph})$_2$](BF$_4$)$_2$ (**23**) [114] and [Cu(Cl-TMA)Cl$_2$] (**24**).[115a]

Ni(II) bis(diphosphine) complexes, among other types, have been shown to be active towards the reduction of protons as well, with [Ni(P$_2^{Ph}$N^{Ph})$_2$](BF$_4$)$_2$ described by D. L. DuBois *et al.* (**23**, Figure 16) reaching higher TOFs than [FeFe]-hydrogenase enzymes due to the pendant amine, which acts as an effective proton relay.[114]

Cu, as Fe, has also been a widely studied alternative as it is earth-abundant and low-cost. The best electrocatalytic performances have been achieved by the corrole-based [(Cor)Cu^{III}]^0 complex published by R. Cao *et al.*[115a] Nonetheless, [Cu(Cl-TMPA)Cl$_2$] (**24**, Figure 16) has also been studied in electrochemical systems (by X . Wang *et al.*),[115b] and it has also shown photocatalytic activity stating Cu as a good choice for light-driven HER devices.

Manganese is particularly attractive due to its abundance and low safety concern, as stated by the European Medicine Agency. Both mono- and dinuclear Mn complexes have been recently reported as active HECs.[116] Also, Mo-based complexes with polypyridine chelating ligands have been described as HECs by J. R. Long and C. J. Chang.[117] Pyridine-based ligands are particularly attractive due to the roughness of the aromatic structure against hydrogenation, but also because of their strong σ-donation and π-backbonding interactions, which stabilize low metal oxidation states, crucial for catalytic hydrogen evolution.

The M-H bond energy plays a key role in proton reduction catalysis given that a high M-H binding energy eases the adsorption of hydrogen but hardens the H_2 desorption. On the other hand a low M-H binding energy results in the opposite effect (Figure 17). Platinum is at the center of the volcano plot for proton reduction catalysts since it possess the optimum M-H binding energy, which is neither too low nor too high.[118] However, M-H strength also depends on the coordination sphere of the metal, highlighting the importance of the right ligand design for correctly tuning the complex catalytic performance. Ruthenium presents a slightly weaker M-H bond compared to Pt, which hardly decreases the HER efficiency.[119]

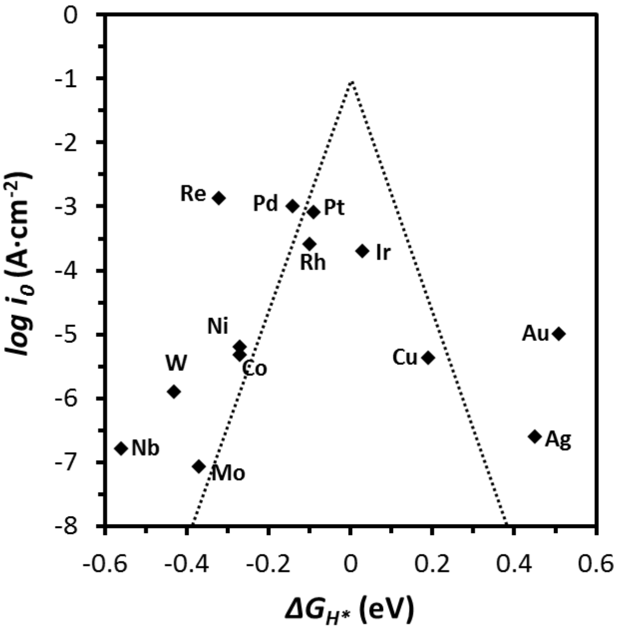

Figure 17. Volcano plot correlating the experimentally measured exchange current, log(i_0), as a function of the free Gibbs energy for H absorption ($\Delta G_{H^*} = \Delta E_H + 0.24$ eV). Plot adapted from ref. 118.

In molecular electrocatalysis, Ru complexes appeared not to be appropriate candidates for proton reduction catalysis. Several groups tried to use Ru complexes, but their decomposition was observed onto the electrode surface. T. Abe *et al.* demonstrated in 2000 that a Ru-based complex ($[(NH_3)_5Ru^{III}\text{-O-}Ru^{IV}(NH_3)_4\text{-O-}Ru^{III}(NH_3)_5]Cl_6$) (**25**) was able to catalyze HER, but only after a few electrochemical cycles it lost its reversibility (Figure 18a), presumably forming zero-valent species on the surface of the electrode, which were not molecular anymore.[120]

R. P. Thummel and E. Fujita employed their complexes previously used as WOCs (**26** in Figure 18)[75a] in HER.[121a] They observed some activity with these complexes, reaching current intensities of 90 µA at $E \approx 1.36$ V in an organic:acid mixture solution. Similarly, T. J. Meyer published that the $[Ru(tpy)(bpy)X]^{2+}$ complex (**27** in Figure 18, X = solvent, H) was capable of reducing protons with an i = 80 µA at $E \approx 1.5$ V vs. NHE.[121b]

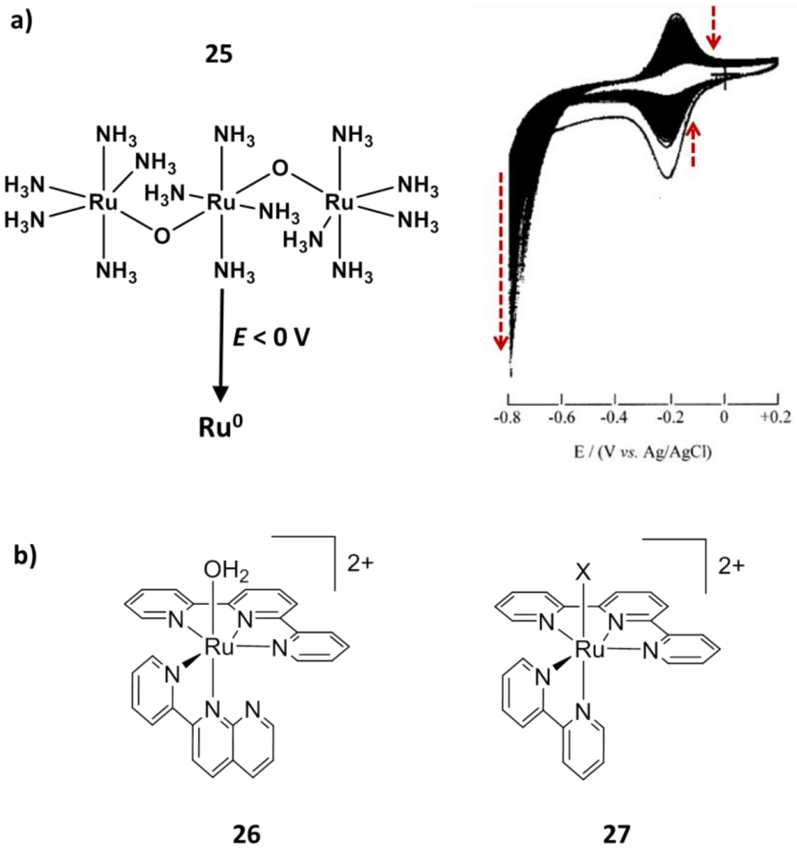

Figure 18. Abe's Ru-based complex (**23**) and electrochemical decomposition upon HER conditions with simultaneous reductive current increasing.[120] Thummel and Fujita (top, **24**)[121a] and Meyer (down, **25**)[121b] Ru-based molecular complexes tested as HEC.

Hence, the low HER performances of the Ru-based molecular complexes were not encouraging for those willing to substitute the expensive Pt by Ru as metallic center in coordination compounds as HECs.

1.5.2.2 Metallic nanoparticles as HECs

Concerning Ru-based nanomaterials capable of reducing protons to H_2, the literature is neither more extensive than with homogeneous catalysts. The use of Ru-electrocatalysts at the nanoscale for HER is a very recent field, with most of the papers published in the 2016-18 period. They are mainly based on RuNPs dispersed or supported onto C-based N-doped materials. One of the most important parameters controlling the HE activity of a Ru-based nanocatalyst is the oxidation state of the particles of the catalytic material: in general, metallic Ru is claimed to be the responsible in reducing protons, but a few isolated examples report on catalysts made of Ru^0/RuO_2 mixtures or RuO_2, that are also available to conduct HER. The following part will mainly focus on Ru metal systems, highlighting the most outstanding materials.

Analogously to WOCs, it has been common to test the catalysts on the surface of a GC electrode. For instance, V. Horvat-Radošević *et al.* published a catalytic system made of Ru^0-nanomaterial of ca. 100 nm in size, that were synthesized by electroreduction of $(NH_4)_2RuCl_6$ onto the GC surface.[122] The obtained hybrid material was tested in a 0.5 M H_2SO_4 solution, giving η_0 = 50 mV and η_{10} = 90mV. In a similar synthetic methodology but starting from another Ru precursor, $RuCl_3{\cdot}xH_2O$,[123] O. Joo *et al.* reported a film composed by 80-90 nm sized NPs with a η_0 = 30 mV, lower than in the previous paper, but a higher η_{10} > 380 mV. None of the two publications provide information on the stability of the catalyst.

Another synthetic possibility, highly explored in the recent years, is to pre-synthesize stabilized RuNPs onto a carbon-based matrix (e.g. carbon nitride, doped graphene, hollow carbon spheres, etc.) and deposit them afterwards onto the GC surface. J. Baek *et al.* reported RuNPs onto a nitrogenated holey two-dimensional carbon structure (Figure 19a), $Ru@C_2N$,[119] which are active and stable in both acidic and alkaline pH, showing one of the best performances for Ru-based HE-nanocatalysts, with η_0 = 9.5 mV and η_{10} = 22 mV at acidic pH, very close to the state-of-the-art Pt performance. Very interestingly, in this paper they experimentally estimate the number of active sites of the hybrid system by the Cu UnderPotential Deposition method (UPD), that will be further detailed in the following section, and which allows a normalization of the activity for benchmarking purposes.[124] With an analogous synthetic methodology, T. Adschiri *et al.* prepared 2-5 nm NPs onto graphene-layered carbon (GLC, Figure 19d), which when deposited onto RDE-GC started reducing protons at η_0 close to 0 mV, reaching $j = -10\ mA{\cdot}cm^{-2}$ at only 35 mV.[125]

Similarly R. K. Shervedani *et al.* described a synthetic S-doped graphene as a support for 35 nm RuNPs *in-situ* obtained by electroreduction.[126] When drop-casted onto GC, the hybrid material showed marked activity with a η_0 = 65 mV and η_{10} = 80 mV, being stable after 500 cycles. In another study by C. Liu *et al.*,[127] 4 nm RuNPs were encapsulated in a C-based core-shell material being surrounded by N,P-codoped carbon in a 30 nm hollow structure ($RuP_x@NPC$, Figure 19b). The supporting material is believed to prevent particles aggregation and tune the electronic structure of the particles, giving catalytic activities of η_0 = 0 mV and η_{10} = 51 mV and good stability with only slight current degradation after 10h.

M. Shao *et al.* published a study on RuNPs of ca. 42.9 nm supported onto Si nanowires, a material obtained by simple impregnation of the support in a $RuCl_3$ solution.[128] Despite that the system on GC showed worse η_0 = 150 mV and η_{10} = 200 mV than the same RuNPs in absence of the Si-based support (η_0 = 110 mV and η_{10} = 185 mV), they observed an enhancement of the stability under catalytic conditions, with limited agglomeration of the particles. A. M. Önal *et al.* published a 4 nm Ru^0/CeO_2 catalyst with different Ru loadings, what controls the specific activity of the hybrid system, with the catalyst containing 1.86% Ru achieving a small η_{10} = 47 mV and a $TOF_{27mV} = 0.8\ s^{-1}$,[129] and which is completely stable after 10000 catalytic cycles.

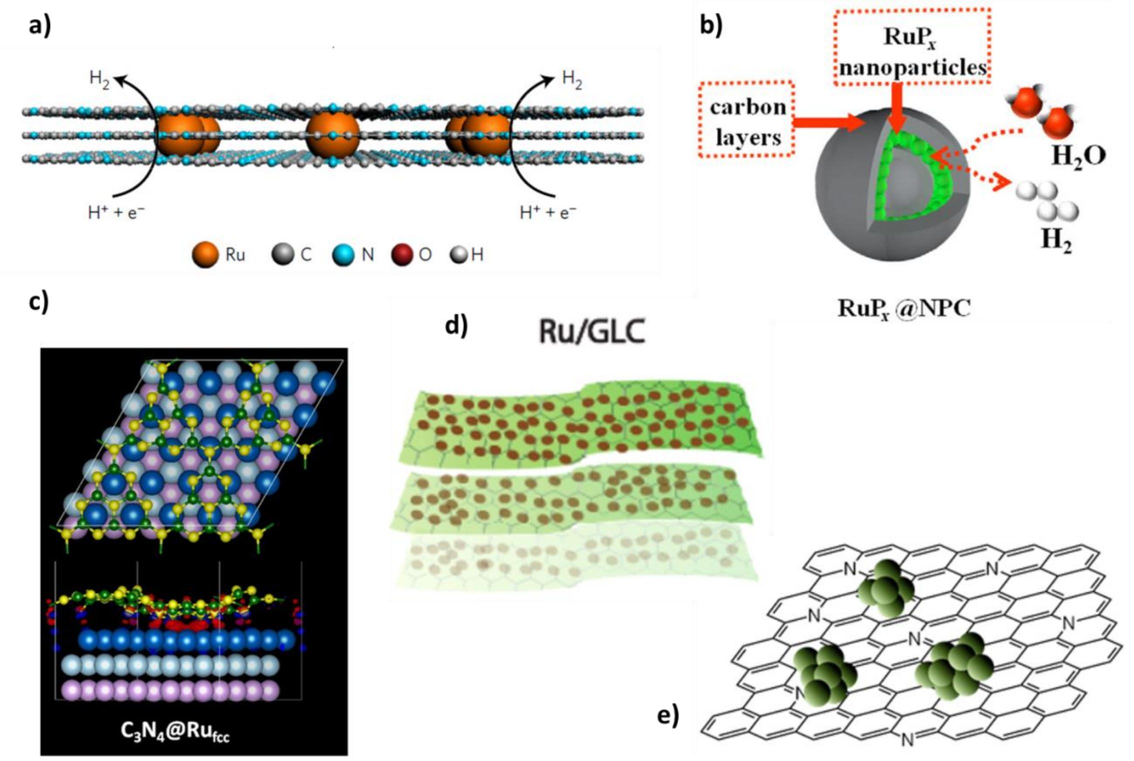

Figure 19. Ru-based nanosystems as HECs: a) Baek's Ru@C_2N,[119] b) Liu's RuP_x@NPC, [127] c) Qiao's Ru/C_3N_4/C,[131] d) Adschiri's Ru@GLC[125] and e) Tour's Ru-NG750.[130]

In comparison to Baek's Ru@C_2N system,[119] which is active also under alkaline pH with η_{10} = 17 mV and high TOFs (0.76 s^{-1} (25 mV) and 1.66 s^{-1} (50 mV)), J. M. Tour[130] presented a catalytic system made of 6 nm Ru^0-nanoclusters deposited onto N-doped graphene (Ru-NG750, Figure 19e) which is unstable under acidic conditions, but that presents a variable catalytic activity at 1 M KOH depending on the reducing thermal treatment temperature and exhibits a very small η_{10} = 8 mV, with a medium TOF_{100mV} = 0.35 s^{-1}. S. Qiao *et al.* prepared an anomalously fcc-structured 2 nm Ru catalyst on graphitic carbon nitride supported onto carbon,[131] named Ru/C_3N_4/C, and drop-casted onto a GC. The system has a very high activity as HEC in basic conditions, with η_0 = 15-20 mV and η_{10} = 79 mV, due to the atypical Ru structure, which might be induced by the *g*-C_3N_4 support (Figure 19c). The RuP_x@NPC material described by C. Liu showed also interesting results (η_{10} = 74 mV) when tested under alkaline conditions.[127]

It is worth noting that RuO_2 has also been reported as a good HEC. This suggests a change of the oxidation state at its surface due to the reductive conditions applied, which may favor the formation of a Ru-H bond. Indeed, H. You in 2003[132] and H. Zhang in 2010[133] both described an activation of RuO_2, suggesting an increase of the number of active sites, through the formation of metallic Ru. Also L. A. Näslund observed the same trend in a recent work,[134] and demonstrated the formation of a $RuO(OH)_2$ by XPS analysis at different reduction times. B. Lim reported hydrous RuO_2 NPs (size < 5 nm) capable to catalyze the reduction of protons under alkaline conditions with $\eta_0 \approx 25$ mV and $\eta_{10} = 60$ mV, but without any description on the oxidation state modification.[91a] As mentioned in section 1.5.1.2 (M-NPs as WOCs), an annealed crystalline-RuO_2 sample obtained from this hydrous-RuO_2 was good in oxidizing water, what allowed them to prepare an efficient tandem cell with both catalysts on the cathode and anode, respectively. As a curiosity, S. Barman *et al.* described a bifunctional catalyst made of RuO_2-nanowires supported onto carbon nitride (RuO_2-NWs@g-CN),[135] which was able to catalyze both HER and OER with good-to-moderate activities and high stabilities at acidic and basic pHs.

2D Ru^0-nanosheets reported by Peng and *et al.*[136] showed remarkable catalytic results as HEC onto GC electrode supports with $\eta_0 \approx 0$ mV and $\eta_{10} = 20$ mV at $j_m = 10$ mA·mg^{-1} (j_m = mass activity). The interesting feature of this system is that RuO_2 is being formed when Ru^0-nanosheets are oxidized under heat, which is active towards OER. The use of both Ru^0 and RuO_2 permits the construction of a durable cell with good performances in water splitting.

S. Fukuzumi *et al.* studied photocatalytic HER using PVP-stabilized RuNPs (PVP = polyvinylpyrrolidone) as HEC, and described the optimal conditions for this system (Figure 20).[137] One of the main objectives of their work was to use basic media for the reductive reaction, since OER is thermodynamically more favorable under this condition. The main conclusions they reached were:

- An optimal catalyst concentration was found to be 12.5 mg·L^{-1}, not observing an increase on the reaction rate at higher concentrations, presumably due to light dispersion and opacity when more material is present in the reaction medium.
- Even though at acidic pH HER is favored due to increased H^+ concentration, this system barely diminishes its catalytic rate at pH ranging from 4.5-10, dropping off to very low values only at pH = 11.
- An activity-size dependency was observed when testing NPs of different sizes. On the one hand, small NPs present higher negative charge density, easing the hydrogen-atom association step but hindering the proton reduction process. On the other hand, larger NPs ease the proton reduction process but hinder the hydrogen-atom association step. The best results were obtained with particles of intermediate size, namely 4.1 nm sized NPs.
- Electron transfer between species in a colloidal solution was not optimal when using RuNPs as catalyst with typical PS (e.g. $[Ru(bpy)_3]^{2+}$). The use of 2-phenyl-4-(1-naphthyl)-quinolinium ion ($QuPh^+$-NA) as co-PS seemed to be crucial for enhancing the electron transfer to the particles.

- The use of MO_X-based materials (SiO_2, TiO_2, CeO_2, etc.) as supports for RuNPs enhanced the reaction rate and stability of the materials.[138]

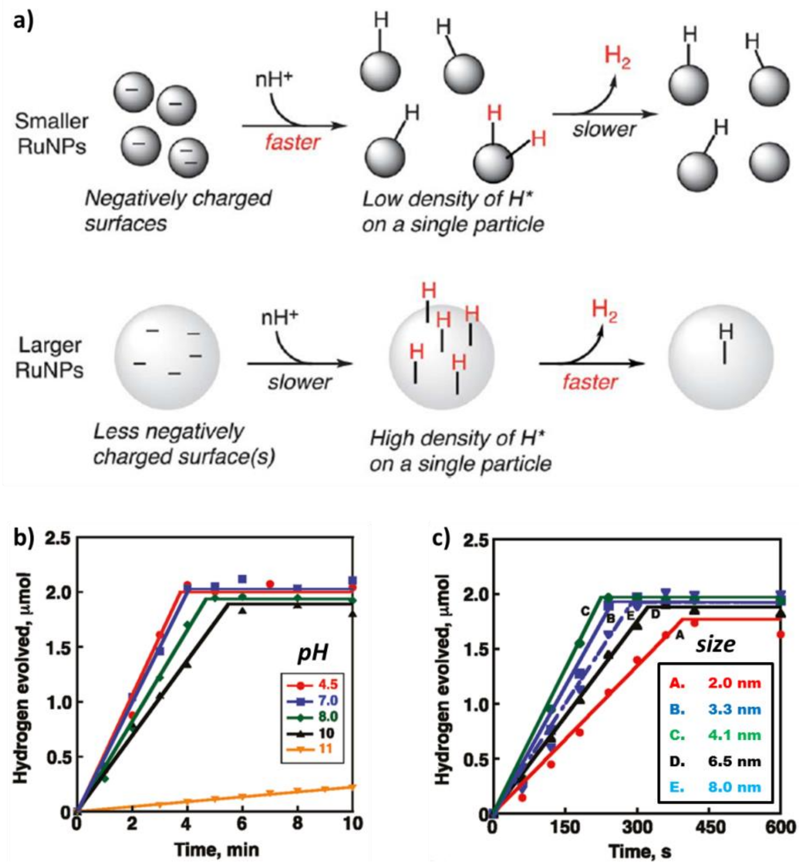

Figure 20. a) Mechanistic scheme for the hydrogen-evolving reaction catalyzed by RuNPs: size effect on the reaction rate for the "hydrogen-atom association" and "proton reduction" steps; b) time courses of hydrogen evolution under photoirradiation, rate dependency on pH and c) particle size. Figure adapted from references 137-138.

1.5.3 Benchmarking of immobilized electrocatalysts

The main difficulty when looking at the data at our disposal on nanoparticulated systems or materials for comparative purposes is the wide range of conditions that are used for the catalytic experiments. Catalyst loading, pH-media, particle size/surface, etc. may all affect catalysis, in both OE and HE reactions. There is a requirement of normalizing the activity in order to compare a series of catalysts in spite of the different conditions employed. This normalization can be done by metal percentage, number of active sites, electrochemically active surface area, or any other feasible quantification. To reach this objective, two valuable methods have been reported (among others) in order to benchmark the electrocatalytic performance of different catalysts.

The first method, reported by T. F. Jaramillo *et al.*, is based on the approximate calculation of double-layer capacitance (C_{DL}) of a deposited catalyst onto an electrode, which allows obtaining a modified electrochemical active surface area (ECSA), and thus the normalization of the catalytic current by this area.[139] The second one is a bit more precise and consists on the deposition of Cu^0 onto the active sites of the material through an electroreduction process of a Cu^{2+}-salt, and the consecutive oxidation, which is of course proportional to the amount of deposited Cu and thus, to the number of active sites. [119,124]

1.5.3.1 Jaramillo's benchmarking methodology

T. F. Jaramillo *et al.* described a methodology that allows normalizing the vast electrochemical data nowadays on WOCs and HECs independently of the metal used on each case.[139] This methodology basically consists on precise steps and reaction conditions, importantly focused on referencing the results by the real electrode active area, and on choosing benchmarking parameters that allow a fast and easy evaluation of the intrinsic activity and stability of the system.

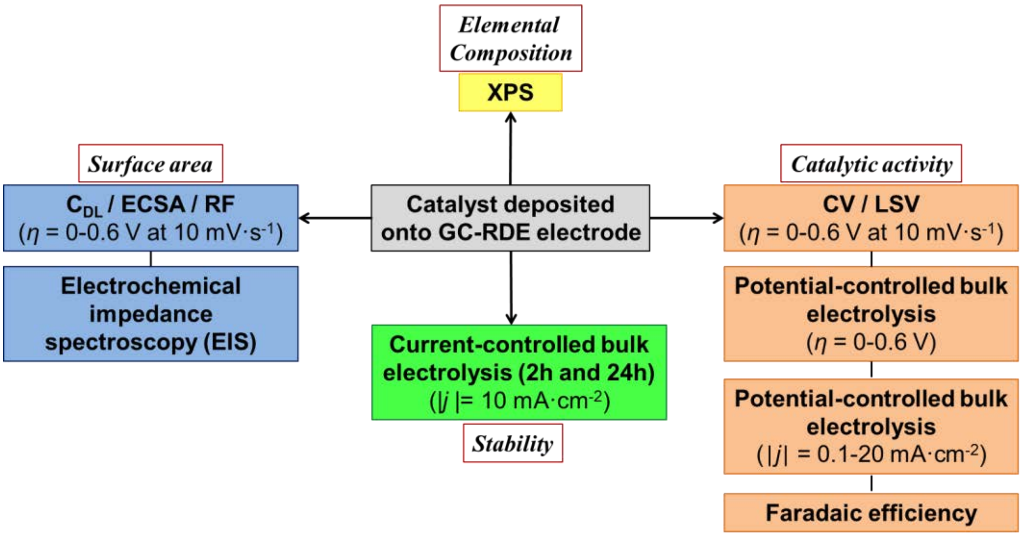
Elemental Composition
XPS
Surface area
C_DL / ECSA / RF
(η = 0-0.6 V at 10 mV·s⁻¹)
Electrochemical impedance spectroscopy (EIS)
Catalyst deposited onto GC-RDE electrode
Current-controlled bulk electrolysis (2h and 24h)
(|j |= 10 mA·cm⁻²)
Stability
Catalytic activity
CV / LSV
(η = 0-0.6 V at 10 mV·s⁻¹)
Potential-controlled bulk electrolysis
(η = 0-0.6 V)
Potential-controlled bulk electrolysis
(|j| = 0.1-20 mA·cm⁻²)
Faradaic efficiency

Scheme 5. Different steps proposed for catalyst electrocatalytic activity benchmarking in Jaramillo's methodology.

The main points are summarized below and in Scheme 5:

1. Use of RDE-GC as non-catalytic conductive material.
2. Working in 1 M NaOH and 1 M H_2SO_4.
3. Estimation of Electrochemically Active Surface Area (ECSA) and Roughness Factor (RF) from double-layer capacitance (C_{DL}) measurements in non-faradaic regions (see Experimental part in Chapter 3A for an example of C_{DL}, ECSA and RF estimation).

4. Normalization of activity (*i* or *j*) by ECSA/RF: $j_S = \frac{j}{RF} = \frac{i}{S*ECSA}$
5. Controlled current electrolysis at $|j|$ = 10 mA·cm^{-2}, the approximate current density expected for an integrated solar water-splitting device under 1 sun illumination operating at 10% solar-to-fuels efficiency.
6. Change on the η_{10} before and after 2h-electrolysis at $|j|$ = 10 mA·cm^{-2}.
7. 24h-stability test.
8. Faradaic efficiency calculation.

In addition, they suggest the use of X-Ray Photoelectron Spectroscopy (XPS) for elemental composition determination, and Electrochemical Impedance Spectroscopy (EIS) as a complementary technique for surface area calculation (ECSA). To sum everything up, all the data can be collected in one single graph, giving an idea of the activity, stability and active area at a glance (Figure 21). Thus, the best catalysts should appear at the left corner of the graph, and the closer to the diagonal the more stable they are after 2h electrolysis.

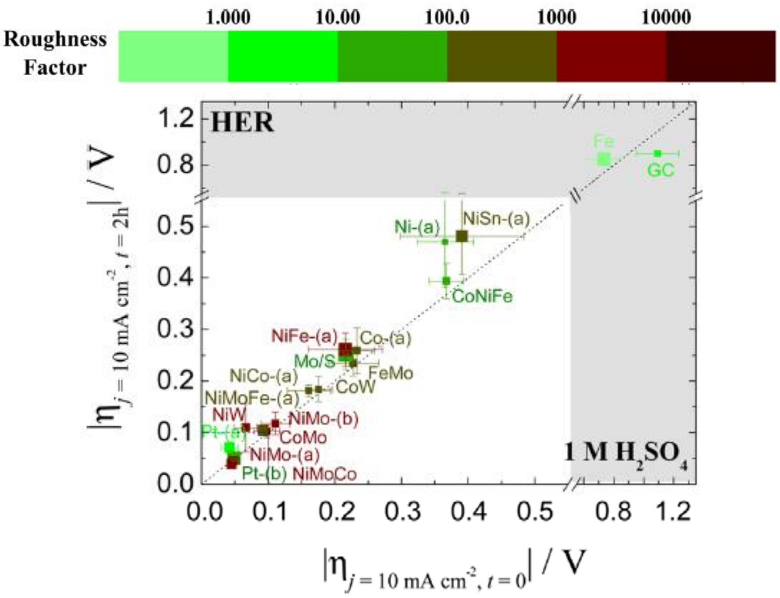

Figure 21. Plot of activity, stability and RF for HER catalysts in 1M H_2SO_4. Image adapted from ref. 139b.

1.5.3.2 Copper Under-Potential Deposition

Underpotential deposition (UPD) is an electrochemical process that consists in the reductive deposition of a metal at potentials less reductive than the equilibrium potential of this metal. This is possible because if a reductive species is present on an electrode (M^0), it can electroreduce a metal ion A^+ at a more positive potential than it would occur without the presence of M^0. Thus, a M-A deposition is achieved, whereas A-A (bulk formation) would take place in the absence of M^0.[124]

If we consider a Ru material, Cu is an ideal metal for performing UPD, as Cu and Ru atoms have similar atomic radii as well as Pt (Cu: 0.128 nm; Ru: 0.134 nm; Pt: 0.138 nm). Experimentally, the method consists in 2 steps as follows:

1. First, the Cu-UPD potential value needs to be found (Eq. 35, E_{UPD}), which will depend on the supported metal and the catalyst itself (surface environment, reductive power, etc.). Also different experiment times need to be checked, to ensure complete active sites (Ru_{ae}) coverage. For doing so, similar conditions to Kucernak's paper (ref. 124) have been used (5 mL of a 5 mM $CuSO_4$ solution in 1 M H_2SO_4), and these parameters can be modified as required. It is important to work in an accurate way, since E_{UPD} and the bulk Cu deposition potential can be close enough to get a mixture of deposited species.

$$Ru_{ae} + Cu^{2+} \xrightarrow{E_{UPD}} Ru_{ae} - Cu_{\text{UPD}} \qquad \text{Eq. 35}$$

2. Second, once the UPD is done under the optimized conditions (see Eq. 35), a sweep voltammetry has to be performed in a fresh solution (1 M H_2SO_4) without any Cu trace. If only UPD is achieved, an oxidative wave will appear at potentials barely more positive than E_{UPD}, corresponding to the oxidation of deposited Cu^0 back to Cu^{2+} (Eq. 36). The area under this wave (Q_{Cu}, Coulombs) will be proportional to the number of active sites, which can be calculated as shown in Eq. 37. However, if the equilibrium potential is reached during the reduction process, two overlapped waves will appear in the oxidation step corresponding to both deposited species. This will hinder the active sites calculation.

$$Cu_{\text{UPD}} \rightarrow Cu^{2+} + 2\bar{e} \qquad \text{Eq. 36}$$

$$n(mol) = \frac{Q_{Cu}}{2F} \qquad \text{Eq. 37}$$

$$TOF(s^{-1}) = \frac{i}{2Fn} = \frac{i}{Q_{Cu}} \qquad \text{Eq. 38}$$

(*i* is the current intensity on a LSV measurement, F is the Faradaic constant, and *n* the number of active sites obtained by the UPD method)

This procedure allows the direct calculation of the kinetic parameter TOF (Eq. 38), by simply dividing current values (*i*) in a voltammetric measurement by Q_{Cu}.

1.6 Nanochemistry

The use of metal (M) and metal-oxide (MO_X) nanoparticles (NPs) has been widely increasing in the last decades due to their intrinsic properties and the extensive fields and applications where they can be used.[140] It is currently considered that nanomaterials are those materials that possess at least one dimension (1D) ranging from 1-100 nm (Figure 22), while for NPs the three dimensions are within the nanometrc scale, being formed by several metal atoms.

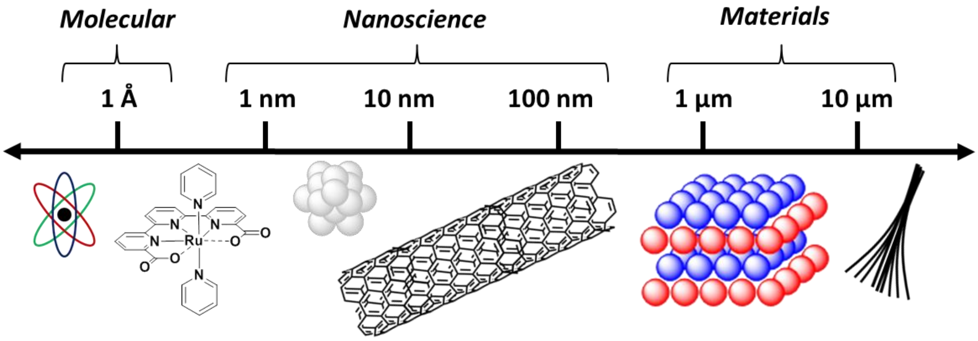

Figure 22. Metric scale involving species under nanometric size and up to micrometric materials: atom, molecular coordination complex, nanoparticle, carbon nanotube, crystalline material, carbon micro-fibers.

In catalysis, NPs are in the frontier between homogeneous and heterogeneous catalysts, as they display properties from both families.[141] In homogeneous catalysis, the reactants and the catalyst are in the same phase, ensuring a good interaction but a difficult recovery of the catalytic species. Each entity acts as an active site, allowing the understanding of the mechanistic pathways and providing high activities and stabilities. On the other hand, heterogeneous catalysts are in different phase than reactants (normally rugged solid catalysts vs. gas/solution reactants) permitting the easy recovery and recycling of the catalysts. They require high surface areas for achieving high active sites' population, and there can be different active sites acting in alternative ways, what hinders the mechanistic understanding and the selectivity of the process. NPs can present different selectivity by tuning their surface composition, and on the other side, they can be deposited onto solid supports to be recycled and reused. Ru-based NPs have been used in a wide set of catalytic reactions, such as aryl hydrogenation,[142] methanol oxidation,[143] Heck and Suzuki reactions,[144] CO oxidation,[145] or Fischer-Tropsch,[146] among others.

Depending on the properties of the NPs homogeneous dispersions can be obtained, first called by T. Graham as colloidal suspensions,[147] considering as colloids those compounds that have a very slow and non-crystalline precipitation. A wide range of NPs are described in the literature as the result of intensive work made by the scientific community, playing with synthesis methods, stabilizing agents, etc. as it will be shortly summarized hereafter.

1.6.1 Stabilization of metal nanoparticles

The existence of small NPs is only kinetically favored, being the formation of the bulk material the thermodynamically stable process.[148] The use of stabilizing agents (STAG) allows: 1st, to stop the nucleation process during the synthesis, obtaining a range of sizes, shapes and dispersions by using different molecules; 2nd, to limit the aggregation of NPs keeping their intrinsic properties; and 3rd, to make the NPs dispersible in different conditions depending on the nature of the STAG.[149] Two main stabilization ways are described:

- *Steric stabilization,* which is a repulsive interaction happening between organic moieties from molecules present on the surface of two different particles (see Figure 23a). This prevents the interaction between different particles, and thus, the agglomeration to form the bulk material.

- *Electrostatic stabilization,* which involves the presence of ionic species, creating an electric double layer surrounding the NPs that get electrostatically repulsed by the other stabilized particles (see Figure 23b).[150]

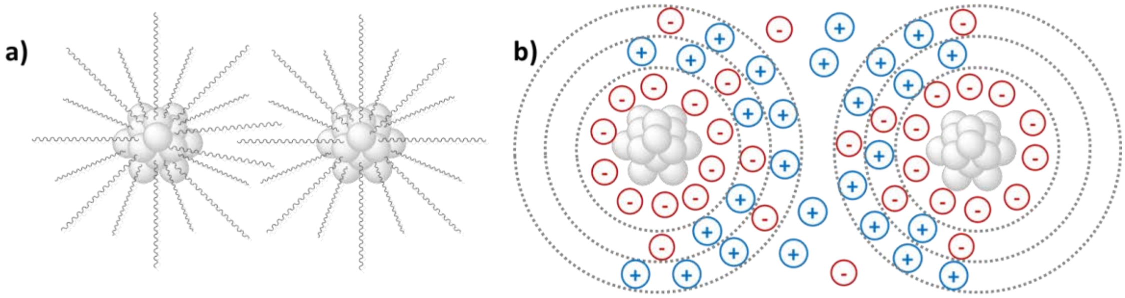

Figure 23. Illustrative representation of a) steric stabilization and b) electrostatic stabilization modes.

The use of an appropriate stabilizing agent is of paramount importance, as the nature of the stabilizer can completely shift both the physical properties and chemical interactions of the particles and the other molecules in the catalytic reactions. A wide range of molecules can act as stabilizers for metal-based NPs. One well-known example is the use of polymers,[149] which lead to steric interactions due to their long polymeric chains, as well as playing a role on the solubility of the NPs due to their polar/apolar properties. Polyvinylpyrrolidone (PVP) has been widely used as STAG.[151] Also surfactants, micelles and microemulsions can create a confined environment around the particles, controlling the NPs growth and preventing them from the interaction with other particles or nucleating species.

Ionic liquids have been widely studied as NPs' stabilizers having an interesting behavior as they can do both, steric and electrostatic stabilization,[152] namely "electro-steric" interactions. Additionally, they play a double role as they can act both as stabilizer and as reaction media. Molecules containing an electron-donor moiety can be also employed as stabilizing agents. In this sense, organic ligands like those used to build metallic complexes such as phosphines, carbenes, amines, pyridines or thiols have been reported to allow the formation of stable NPs.[153] Small molecules as CO or NH_3, or even solvents like 1-heptanol or other alcohols have been also described for that purpose.[154]

1.6.2 Synthesis of metal-NPs

There are several synthetic methods that allow the generation of nanoparticles, offering different advantages/disadvantages in key parameters as size, shape, dispersion, surface control or oxidation state. Those methodologies are classified in two main categories:[150]

- The physical methods (*top-down*), consist on the subdivision of large metallic structures by using physical or mechanical energy. The main drawback is the lack of control of the final structure, obtaining irregular nanocrystals with no uniformity on the size or shape.
- The chemical methods (*bottom-up*), are based on the growth or nucleation of small units as atoms, molecules or clusters, by means of chemical reactions. This approach is less effective in terms of quantitative production than the previous one, but it allows an extensive control on the reaction conditions permitting the tuning of the size, surface and dispersion of the particles, in other words, it offers better defined NPs.

Most of the strategies used for the synthesis of metal-based NPs are from the second category, and the main methods are as follows:

a) **Chemical reduction of transition-metal salts.** It is the most common method for the production of NPs and it involves the chemical reduction of an oxidized transition metal salt to a zero-valent naked atom.[155] The atomic unit starts nucleating with other metallic atoms until forming a stable nucleus. This method allows the reproducible formation of monodispersed particles or clusters. There are advantages of using salts, such as the ease to deal with their solubility in water or organic solvents, thus allowing the use of a wide range of STAG. However, the main disadvantage of this procedure is the remaining counter-ions, both from the precursor and the reducing agent, which are difficult to eliminate and can end up coordinated on the surface of the particles, tuning their reactivity or selectivity.

b) **Thermal, photochemical or sonochemical decomposition.** In this case, the use of temperature, light or ultrasound radiation promotes the decomposition of a metal complex, allowing obtaining big amounts of particles without the use of further reagents, but with a poor control on the size and shape of the NPs.

c) **Chemical vapor deposition (CVD).**[156] As its name defines, this process consists on the evaporation of relatively volatile metallic precursors under reduced pressure, and the subsequent condensation of the metal atoms at low temperatures and in presence of organic solvents in gaseous phase, which act as STAG. Once again, the lack of control on the size and shape of the formed NPs makes the method disadvantageous.

d) **Electrochemical reduction.** This method[157] consists on the applying of a negative potential to a NPs' precursor. It is advantageous as there are no remaining secondary products from the reducing agents or salts, and the colloidal product is easy to isolate as a precipitate or deposited onto the electrode (electrodeposition).

Besides those different methods the decomposition of an organometallic or a metal-organic complex as metal source, has proven to be a very efficient and versatile method to have at disposal well-defined NPs. It is called the organometallic approach, and will be more deeply described in the following section.

1.6.3 Organometallic approach for the synthesis of metal-NPs

The organometallic approach was first described by B. Chaudret *et al.* in the early 90s'.[158] It consists of the decomposition of an organometallic precursor, preferentially under H_2 atmosphere thus liberating naked metal atoms and volatile by-products (Scheme 6). The released metal atoms start nucleating to form a nucleus and the presence of a stabilizing agent can control the particles' growth to form a nanosized material. The role of the STAG is to interact with the surface of the particles during the synthetic procedure, to reach a stable material and limit a further growth under those synthetic conditions.

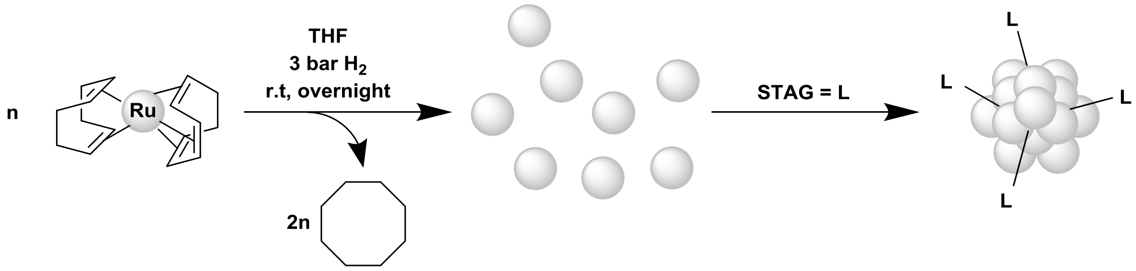

Scheme 6. Schemcatic representation of the organometallic approach for the synthesis of Ru^0-NPs.

The rational experiment design allows a control on the size of the NPs, either by changing the reaction conditions (temperature, pressure, concentration, etc.), the ratio between the stabilizing agent and the metallic source, or by replacing the STAG itself, being the last parameter crucial. Each molecule will have different coordination properties, interacting at a different synthesis time and in a different way with the NPs' surface, what will finally have influence not only on the size, dispersion and structure of the product, but most importantly on its performance as catalysts. Some important features of the organometallic methodology are:

- ✓ No salts are used, avoiding the presence of coordinated ions.
- ✓ Mild conditions can be applied as low temperature and pressure, so no specific requirements are needed.
- ✓ No by-products are formed, just the decomposed organic material and the STAG excess, which are easy to remove by solubility/precipitation techniques. The use of olefinic groups leads to alkanes formation, very easy to remove by simple evaporation.
- ✓ Control of the oxidation state, which under the inert conditions used during the synthesis, can be preserved.
- ✓ Reproducibility.

There are some drawbacks to mention as well:

- × Synthetic precursors are not always commercially available, meaning in some cases a time-consuming preparation.
- × The use of organic solvents instead of water as reaction media, although some possibilities exist to circumvent this problem, like the use of a water-soluble precursor or the use of amphiphilic ligands that allow the redispersion of the obtained NPs in water.
- × Zero-valent metallic particles are obtained, which are very reactive under air and so oxidation may be hard to control.

Moreover, as an interesting aspect, the methodology allows the addition of a support in the reaction media. In this way, the nanomaterials can be directly synthesized on the surface of another material, as for example CNTs,[159] silica,[160] MOFs,[161] etc. The approach opens as well the possibility of preparing bimetallic systems, using as "nucleation center" as-synthesized NPs of one specific metal, during the synthesis with a second organometallic precursor, or by decomposing simultaneously two metal precursors.[162]

1.6.4 Characterization of metal-based NPs

Several techniques are used to characterize nanosized materials, from their size, morphology and structure, to oxidation state or surface environment. Elemental analysis (EA), Inductive-Coupled Plasma (ICP), Infrared spectroscopy (IR) or solution/solid state Nuclear Magnetic Ressonance (NMR), are common techniques which can be applied for nanomaterials. Hereafter, a short summary on more specific characterization techniques that have been used during this PhD thesis is given, mainly focused on the application and information obtained from each analysis.

Transmission Electron Microscopy (TEM) and High Resolution TEM (HRTEM). TEM & HRTEM are microscopic techniques that allow obtaining at low and high resolution, respectively, visual information as size distribution, dispersion on solid support or morphology.[163] Practically, it consists on the applying of an electron beam in high-vacuum conditions to the sample, which is deposited onto a carbon-covered copper grid; the detection of the transmitted electrons allows magnifying and focusing the image onto a screen or a Charge-Coupled Device (CCD) camera. The sample needs to contrast against the support to be able to differentiate one to each other, and there are some limitations related for example with the high energy of the electron beam or with the use of magnetic particles. High-resolution microscopes can be equipped with a device allowing the analysis of generated X-Ray by the Energy-dispersive X-Ray spectroscopy (EDX), providing information on the elements present on a specific region, in addition of information on the structure and oxidation state of the NPs.

Wide-Angle X-Ray Scattering (WAXS). WAXS is an X-Ray diffraction technique that analyzes the scattering at wide angles, which as Bragg's law describes, are caused by small crystalline structures or subnanometer-sized ones.[164] Thus, WAXS gives information on the crystalline structure/s of small NPs, reporting also interatomic distances (crystalline domains). The radial distribution function (RDF) is obtained by the Fourier transform of the intensity, providing a distribution of the metal-metal bonds inside an assembly of nanoparticles, being well-defined when homogeneous crystalline NPs are analyzed.

Thermogravimetric Analysis (TGA). TGA is based on the change on a sample weight by decomposition or evaporation of species due to heat application.[165] It requires a precision balance and a high-temperature furnace that allows increase the temperature with a controlled rate (°C/min). Different species might have a different thermal stability leading to change of the weight loss slope at different temperatures, proportional to the weight of the species. This technique is very useful for determining loading of species on supports or organic percentage on a metal-organic material.

X-Ray Photoelectron Spectroscopy (XPS). XPS is a technique based on the analysis of X-Ray photoexcited superficial electrons that gives information on the nature of the atoms as well as the oxidation state. The peak position is indicative of the chemical composition of the sample, while the intensity gives information on the abundance of the species, being dependent on each element and oxidation state.

1.7 References

1 M. Roser, E. Ortiz-Ospina, *OurWorldInData* **2017** [Online] https://ourworldindata.org/world-population-growth/ (accessed Oct 6 2017).

2 BP Energy Outlook **2017**, BP Global.

3 The EU in the world, World Population Prospects 2017, United Nations, Eurostat statistic explained, **2016**.

4 D. Meadows, J. Randers, D. Meadows. A Synopsis: Limits to Growth: The 30-Year Update, **1972**.

5 P. E. Hodgson, *Modern Age* **2008**, *3*, 238-246.

6 "IPCC AR4 SYR Appendix Glossary" , Retrieved 14 December **2008**.

7 Energy and air pollution, World Energy Outlook Special Report 2016, International Energy Agency (IEA).

8 Energy and climate change, World Energy Outlook Special Report 2015, International Energy Agency (IEA).

9 "Paris Agreement". United Nations Treaty Collection. 8 July 2016.

10 L. Hammarström, S. Hammes-Schiffer, *Acc. Chem. Res.* **2009**, *42*, 1859-1860.

11 B. Viswanathan, *Fuel Cells*, Energy Sources, Fundamentals of Chemical Conversion Processes and Applications. Elseiver, **2017**, Chapter 7, 139-147.

12 G. Ciamician, *Science* **1912**, *36*, 385-394.

13 D. G. Nocera, *Acc. Chem. Res.* **2012**, *45*, 767-776.

14 N. S. Lewis, *Nature* **2001**, *414*, 589-590.

15 D. Palmer, *Hydrogen in the Universe*, 1997, NASA. Retrieved 5 February **2008**.

16 H. Cavendish, *Philosophical Transactions* **1766**, *56*, 141-184.

17 R .Boyle, "Tracts written by the Honourable Robert Boyle containing new experiments, touching the relation betwixt flame and air..." London, **1672**.

18 M. Dresselhaus, **2003** "Basic Research Needs for the Hydrogen Economy". Argonne National Laboratory, U.S. Department of Energy, Office of Science Laboratory. Retrieved 5 February **2008**.

19 W. H. Berger, **2007** "The Future of Methane". University of California, San Diego. Retrieved 12 February 2008.

20 B. Viswanathan, *Hydrogen Storage*, Energy Sources, Fundamentals of Chemical Conversion Processes and Applications. Elseiver, **2017**, Chapter 10, 185-212.

21 B. Viswanathan, *Fuel Cells*, Energy Sources, Fundamentals of Chemical Conversion Processes and Applications. Elseiver, **2017**, Chapter 14, 329-356.

22 DOE Hydrogen and Fuel Cell Technical Advisory Committee, Brian Bonner, **2013**, Air products.

23 J. R. Rostrup-Nielsen, *Catal. Rev.: Sci. Eng.* **2004**, *46*, 247-270.

---

24 L. Tartakovsky, A. Mosyak, Y. Zvirin, *Int. J. Energy Res*. **2013**, *37*, 259-267.

25 B. Viswanathan, *Hydrogen as an Energy carrer*, Energy Sources, Fundamentals of Chemical Conversion Processes and Applications. Elseiver, **2017**, Chapter 9, 161-183.

26 S. Trasatti, *J. Electroanal. Chem.* **1999**, *476*, 90-91.

27 M. Carmo, D. L. Fritz, J. Mergel, D. Stolten, *Int. J. Hydrogen Energy* **2013**, *38*, 4901-4934.

28 X. Li, X. Hao, A. Abudula, G. Guan, *J. Mater. Chem.* **2016**, *4*, 11973-12000.

29 a) M. H. Kowsaria, S. Naderlou, *Microporous Mesoporous Mater.* **2017**, *240*, 39-49; b) P. Roy, N. Das, *Ultrason. Sonochem.* **2017**, *36*, 466-473.

30 a) N. Bimbo, W. Xu, J. E. Sharpe, V. P. Ting, T. J. Mays, *Mater. Des.* **2016**, *89*, 1086-1094; b) Y. Liu, J. Lu, J. Yang, Y. Zhang, J. Wang, C. Li, L. Xia, *Mater. Lett.* **2018**, *214*, 91-94.

31 M. Zahmakiran, S. Ozkär, *Top. Catal.* **2013**, *56*, 1171-1183.

32 a) H. M. Lee, Y. J. Heo, K. H. An, S. C. Jung, D. C. Chung, S. J. Park, B. J. Kim*, Int. J. Hydrogen Energy* **2018**, *43,* 5894-5902; b) L. Luo, T. Chen, W. Zhao, M. Fan, *BioResources* **2017**, *12*, 6237-6250; c) N. Thaweelap, P. Thongtana, C. Sitthiwet, S. Thiangviriya, P. Eiamlamai, R. Utke, *Int. J. Hydrogen Energy* **2017**, *42*, 24915-24926; d) A. Yadava, N. Verma, *Int. J. Hydrogen Energy* **2017**, *42*, 27139-27153; e) R. S. Rajauraa, S. Srivastavaa, P. K. Sharmab, S. Mathurb, R. Shrivastavac, S. S. Sharmad, Y. K. Vijay, *Nano-Structures & Nano-Objects* **2018**, *14*, 57-65.

33 J. Kargul, J. Barber. Structure and Function of Photosynthetic Reaction Centres in *Molecular Solar Fuels.* T. J. Wydrzynski, W. Hillier (Eds.), RSC, **2011**, *5*, 107-142.

34 Y. Umena, K. Kawakami, J. R. Shen, N. Kamiya, *Nature* **2011**, *473*, 55-61.

35 V. Krewald, M. Retegan, D. A. Pantazis, Principles of Natural Photosynthesis in *Solar enery for* fuels. H. Tüysüz, C. K. Chan (Eds.), Springer Cham, *Top. Curr. Chem.* **2016**, *371*, 23-48.

36 J. M. Mayer, *Annu. Rev. Phys. Chem.* **2004**, *55*, 363-390.

37 a) A. C. Nielander, M. R. Shaner, K, M. Papadantonakis, S. A. Francis, N. S. Lewis, *Energy Environ. Sci.* **2015**, *8*, 16-25; b) J. R. McKone, N. S. Lewis, H. B. Gray, *Chem. Mater.* **2014**, *26*, 407-414; c) D. M. Fabian, S. Hu, N. Singh, F. A. Houle, T. Hisatomi, K. Domen, F. E. Osterlohf, S. Ardo, *Energy Environ. Sci.* **2015**, *8*, 2825-2850.

38 D. Hong, Y. Yamada, T. Nagatomi, Y. Takai, S. Fukuzumi, *J. Am. Chem. Soc.* **2012**, *134*, 19572-19575.

39 A. Fujishima, K. Honda, *Nature* **1972**, *238*, 37-38.

40 M. Bajdich, M. Garcia-Mota, A. Vojvodic, J. K. Nørskov, A. T. Bell, *J. Am. Chem. Soc.* **2013**, *135*, 13521-13530.

41 A. Coehn, M. Gläser, *Z. Anorg. Chem.* **1902**, *33*, 9-24.

42 S. W. Gersten, G. J. Samuels, T. J. Meyer, *J. Am. Chem. Soc.* **1982**, *104*, 4029-4030.

43 X. Sala, S. Maji, R. Bofill, J. García-Antón, L. Escriche, A. Llobet, *Acc. Chem. Res.* **2014**, *47*, 504-516.

44 X. Sala, I. Romero, M. Rodriguez, L. Escriche, A. Llobet, *Angew. Chem.* **2009**, *121*, 2882-2893.

45 a) J. A. Gilbert, D. S. Eggleston, W. R. Murphy Jr., D. A. Geselowitz, S. W. Gersten, D. J. Hodgson, T. J. Meyer*, J. Am. Chem. Soc.* **1985**, *107*, 3855-3864; b) K. J. Takeuchi, M. S. Thompson, D. W. Pipes, T. Meyer, *J. Inorg. Chem.* **1984**, *23*, 1845-1851.

46 a) F. Liu, J. J. Concepcion, J. W. Jurss, T. Cardolaccia, J. L. Templeton, T. J. Meyer, *Inorg. Chem.* **2008**, *47*, 1727-1752; b) D. Moonshiram, J. W. Jurss, J. J. Concepcion, T. Zakharova, I.

Alperovich, T. J. Meyer, Y. Pushkar, *J. Am. Chem. Soc.* **2012**, *134*, 4625-4636; c) J. W. Jurss, J. J. Concepcion, J. M. Butler, K. M. Omberg, L. M. Baraldo, D. G. Thompson, E. L. Lebeau, B. Hornstein, J. R. Schoonover, H. Jude, J. D. Thompson, D. M. Dattelbaum, R. C. Rocha, J. L. Templeton, T. J. Meyer, *Inorg. Chem.* **2012**, *51*, 1345-1358; d) J. A. Stull, R. D. Britt, J. L. McHale, F. J. Knorr, S. V. Lymar, J. K. Hurst*, J. Am. Chem. Soc.* **2012**, *134*, 19973-19976; e) J. K. Hurst, J. L. Cape, A. E. Clark, S. Das, C. Qin, *Inorg. Chem.* **2008**, *47*, 1753-1764.

47 B. A. Moyer, T. J. Meyer, *J. Am. Chem. Soc.* **1978**, *100*, 3601-3603.

48 a) S. Romain, F. Bozoglian, X. Sala, A. Llobet, *J. Am. Chem. Soc.* **2009**, *131*, 2768-2769; b) F. Bozoglian, S. Romain, M. Z. Ertem, T. K. Todorova, C. Sens, J. Mola, M. Rodriguez, I. Romero, J. Benet-Buchholz, X. Fontrodona, C. J. Cramer, L. Gagliardi, A. Llobet, *J. Am. Chem. Soc.* **2009**, *131*, 15176-15187.

49 J. J. Concepcion, M. K. Tsai, J. T. Muckerman, T. J. Meyer*, J. Am. Chem. Soc.* **2010**, *132*, 1545-1557.

50 S. Romain, L. Vigara, A. Llobet, *Acc. Chem. Res.* **2009**, *42*, 1944-1953.

51 L. A. De Faria, J. F. C. Boodts, S. Trasatti, *J. Appl. Electrochem.* **1996**, *26*, 1195-1199.

52 E. Antolini, *ACS Catal.* **2014**, *4*, 1426-1440.

53 J. Limburg, J. S. Vrettos, L. M. Liable-Sands, A. L. Rheingold, R. H. Crabtree, G. W. Brudvig, *Science* **1999**, *283*, 1524-1527.

54 a) J. Limburg, J. S. Vrettos, H. Y. Chen, J. C. de Paula, R. H. Crabtree, G. W. Brudvig, *J. Am. Chem. Soc.* **2001**, *123*, 423-430; b) C. W. Cady, K. E. Shinopoulos, R. H. Crabtree, G. W. Brudvig, *Dalton Trans.* **2010**, *39*, 3985-3989; c) P. Kurz, G. Berggren, M. F. Anderlund, S. Styring, *Dalton Trans.* **2007**, *0*, 4258-4261; d) G. Berggren, A. Thapper, P. Huang, P. Kurz, L. Eriksson, S. Styring, M. F. Anderlund, *Dalton Trans.* **2009**, *0*, 10044-10054; e) G. Berggren, A. Thapper, P. Huang, L. Eriksson, S. Styring, M. F. Anderlund, *Inorg. Chem.* **2011**, *50*, 3425-3430; f) K. J. Young, M. K. Takase, G. W. Brudvig, *Inorg. Chem.* **2013**, *52*, 7615-7622.

55 a) E. A. Karlsson, B.-L. Lee, T. Åkermark, E. V. Johnston, M. D. Kärkäs, J. Sun, Ö. Hansson, J. E. Bäckvall, B. Åkermark, *Angew. Chem., Int. Ed.* **2011**, *50*, 11715-11718; b) W. A. A. Arafa, M. D. Kärkäs, B. L. Lee, T. Åkermark, R. Z. Liao, H. M. Berends, J. Messinger, P. E. M. Siegbahn, B. Åkermark, *Phys. Chem. Chem. Phys.* **2014**, *16*, 11950-11964.

56 W. C. Ellis, N. D. McDaniel, S. Bernhard, T. J. Collins, *J. Am. Chem. Soc.* **2010**, *132*, 10990-10991.

57 J. L.Fillol, Z. Cordolà, I. Garcia-Bosch, L. Gómez, J. J. Pla, M. Costas, *Nat. Chem.* **2011**, *3*, 807-813.

58 D. Hong, S. Mandal, Y. Yamada, Y-M. Lee, W. Nam, A. Llobet, S. Fukuzumi, *Inorg. Chem.* **2013**, *52*, 9522-9531.

59 D. L. Wasylenko, C. Ganesamoorthy, J. Borau-Garcia, C. P. Berlinguette, *Chem. Commun.* **2011**, *47*, 4249-4251.

60 a) D. K. Dogutan, R. McGuire Jr., D. G. Nocera, *J. Am. Chem. Soc.* **2011**, *133*, 9178-9180; b) T. NakazonoA. R. , Parent, K. Sakai, *Chem. Commun.* **2013**, *49*, 6325-6327; c) E. Pizzolato, M. Natali, B. Posocco, A. Montellano López, I. Bazzan, M. Di Valentin, P. Galloni, V. Conte, M. Bonchio, F. Scandola, A. Sartorel, *Chem. Commun.* **2013**, *49*, 9941-9943; d) Q. Yin, J. M. Tan, C. Besson, Y. V. Geletii, D. G. Musaev, A. E. Kuznetsov, Z. Luo, K. I. Hardcastle, C. L. Hill, *Science* **2010**, *328*, 342-345.

---

61 a) A. Sartorel, M. Carraro, G. Scorrano, Z. R. De, S. Geremia, N. D. McDaniel, S. Bernhard, M. Bonchio, *J. Am. Chem. Soc.* **2008**, *130*, 5006-5007; b) Y. V. Geletii, B. Botar, P. Kogerler, D. A. Hillesheim, D. G. Musaev, C. L. Hill, *Angew. Chem. Int. Ed.* **2008**, *47*, 3896-3899.

62 a) Q. Daniel, R. B. Ambre, B. Zhang, B. Philippe, H. Chen, F. Li, K. Fan, S. Ahmadi, H. Rensmo, L. Sun, *ACS Catal.* **2017**, *7*, 1143-1149; b) J. J. Stracke, R. G. Finke, *ACS Catal.* **2013**, *3*, 1209-1219.

63 S. M. Barnett, K. I. Goldberg, J. M. Mayer, *Nat. Chem.* **2012**, *4*, 498-502.

64 M. T. Zhang, Z. Chen, P. Kang, T. J. Meyer, *J. Am. Chem. Soc.* **2013**, *135*, 2048-2051.

65 a) P. Garrido-Barros, I. Funes-Ardoiz, S. Drouet, J. Benet-Buchholz, F. Maseras, A. Llobet, *J. Am. Chem. Soc.* **2015**, *137*, 6758-6761; b) P. Garrido-Barros, C. Gimbert-Suriñach, D. Moonshiram, A. Picon, P. Monge, V. S. Batista, A. Llobet, *J. Am. Chem. Soc.* **2017**, *139*, 12907-12910.

66 C. W. Cady, R. H. Crabtree, G. W. Brudvig, *Coord. Chem. Rev.* **2008**, *252*, 444-455.

67 N. D. McDaniel, F. J. Coughlin, L. L. Tinker, S. Bernhard, *J. Am. Chem. Soc.* **2008**, *130*, 210-217.

68 a) J. F. Hull, D. Balcells, J. D. Blakemore, C. D. Incarvito, O. Eisenstein, G. W. Brudvig, R. H. Crabtree, *J. Am. Chem. Soc.* **2009**, *131*, 8730-8731; b) R. Lalrempuia, N. D. McDaniel, H. Müller-Bunz, S. Bernhard, M. Albrecht, *Angew, Chem. Int. Ed.* **2010**, *49*, 9765-9768.

69 A. Savini, P. Belanzoni, G. Bellachioma, C. Zuccaccia, D. Zuccaccia, A. Macchoini, *Green. Chem.* **2011**, *13*, 3360-3374.

70 a) J. D. Blakemorem, N. D. Schley, G. W. Olack, C. D. Incarvito, G. W. Brudvig, R. H. Crabtree, *Chem. Sci.* **2011**, *2*, 94-98; b) U. Hintermair, S. W. Sheenhan, A. R. Parent, D. H. Ess, D. T. Richens, P. H. Vaccaro, G. W. Brudvig, R. H. Crabtree, *J. Am. Chem. Soc.* **2013**, *135*, 10837-1051; c) L. S. Sharninghausen, S. B. Sinha, D. Y. Shopov, B. Choi, B. Q. Mercado, X. Roy, D. Balcells, G. W. Brudvig, R. H. Crabtree, *J. Am. Chem. Soc.* **2016**, *138*, 15917-15926.

71 G. C. Dismukes, R. Brimblecombe, G. A. N. Felton, R. S. Pryadun, J. E. Sheats, L. Spiccia, G. F. Swiegers, *Acc. Chem. Res.* **2009**, *42*, 1935-1943.

72 P. Garrido-Barros, C. Gimbert-Suriñach, R. Matheu, X. Sala, A. Llobet, *Chem Soc. Rev.* **2017**, *46*, 6088-6098.

73 C. Sens, I. Romero, M. Rodriguez, A. Llobet, T. Parella, J. Benet-Buchholz, *J. Am. Chem. Soc.* **2004**, *126*, 7798-7799.

74 a) D. J. Wasylenko, R. D. Palmer, C. P. Berlinguette, *Chem. Commun.* **2013**, *49*, 218-227; b) A. Sartorel, M. Bonchio, S. Campagna, F. Scandola, *Chem. Soc. Rev.* **2013**, *42*, 2262-2280; c) S. A. Cook, A. S. Borovik, *Nat. Chem.* **2013**, *5*, 259-260.

75 a) R. Zong, R. P. Thummel, *J. Am. Chem. Soc.* **2005**, *127*, 12802-12803; b) H.-W. Tseng, R. Zong, J. T. Muckerman, R. Thummel, *Inorg. Chem.* **2008**, *47*, 11763-11773; c) D. E. Polyansky, J. T. Muckerman, J. Rochford, R. Zong, R. P. Thummel, E. Fujita, *J. Am. Chem. Soc.* **2011**, *133*, 14649-14665.

76 J. J. Concepcion, J. W. Jurss, J. L. Templeton, T. J. Meyer, *J. Am. Chem. Soc.* **2008**, *130*, 16462-16463.

77 S. Piccinin, A. Sartorel, G. Aquilanti, A. Goldoni, M. Bonchio, S. Fabris, *PNAS* **2013**, *110*, 4917-4922.

78 Q. Yin, T. Jeffrey Miles, C. Besson, G. Musaev, E. K. Aleksey, Z. Luo, I. H. Ken, L. H. Craig, *Science* **2010**, *328*, 342-345.

79 L. Duan, F. Bozoglian, S. Mandal, B. Stewart, T. Privalov, A. Llobet, L. Sun, *Nat. Chem.* **2012**, *4*, 418-423.

80 a) L. Duan, A. Fischer, Y. Xu, L. Sun, *J. Am. Chem. Soc.* **2009**, *131*, 10397-10399; b) L. Duan, C. M. Araujo, M. S. G. Ahlquist, L. Sun, *PNAS* **2012**, *109*, 15584-15588; c) Y. Jiang, F. Li, B. Zhang, X. Li, X. Wang, F. Huang, L. Sun, *Angew. Chem. Int. Ed.* **2013**, *52*, 3398-3401.

81 a) L. Duan, Y. Xu, M. Gorlov, L. Tong, S. Andersson, L. Sun, *Chem. Eur. J.* **2010**, *16*, 4659-4668; b) J. An, L. Duan, L. Sun, *Faraday Discuss. Chem. Soc.* **2012**, *155*, 267-275.

82 J. Nyhlen, L. Duan, B. Aakermark, L. Sun, T. Privalov, *Angew. Chem. Int. Ed.* **2010**, *49*, 1773-1777.

83 a) R. Matheu, M. Z. Ertem, J. Benet-Buchholz, E. Coronado, V. S. Batista, X. Sala, A. Llobet, *J. Am. Chem. Soc.* **2015**, *137*, 10786-10795; b) R. Matheu, M. Z. Ertem, C. Gimbert-Suriñach, J. Benet-Buchholz, X. Sala, A. Llobet, *ACS Catal.* **2017**, *7*, 6525-6532.

84 a) J. Creus, R. Matheu, I. Peñafiel, D. Moonshiram, P. Blondeau, J. Benet-Buchholz, J. García-Antón, X. Sala, C. Godard, A. Llobet, *Angew. Chem. Int. Ed.* **2016**, *55*, 15382-15386; b) R. Matheu, I. A. Moreno-Hernandez, X. Sala, H. B. Gray, B. S. Brunschwig, A. Llobet, N. S. Lewis, *J. Am. Chem. Soc.* **2017**, *139*, 11345-11348.

85 R. Matheu, L. Francàs, P. Chernev, M. Z. Ertem, V. S. Batista, M. Haumann, X. Sala, A. Llobet, *ACS Catal.* **2015**, *5*, 3422-3429.

86 E. A. Paoli, F. Masini, R. Frydenal, D. Deiana, C. Schlaup, M. Malizia, T. W. Hansen, S. Horch, I. E. L. Stephens, I. Chorkendorff, *Chem. Sci.* **2015**, *6*, 190-196.

87 M. Carmo, D. L. Fritz, I. Mergel, D. Stolten, *Int. J. Hydrogen Energy* **2013**, *38*, 4901-4934.

88 a) D. Chandra, D. Takama, T. Masaki, T. Sato, N. Abe, T. Togashi, M. Kurihara, K. Saito, T. Yui, M. Yagi, *ACS Catal.* **2016**, *6*, 3946-3954; b) T. Kuwabara, E. Tomita, S. Sakita, D. Hasegawa, K. Sone, M. Yagi, *J. Phys. Chem. C* **2008**, *112*, 3774-3779; c) T. Nakagawa, C. A. Beasley, R. W. Murray, *J. Phys. Chem. C* **2009**, *113*, 12958-12961; d) Y. X. Zhao, N. M. Vargas-Barbosa, E. A. Hernandez-Pagan, T. E. Mallouk, *Small* **2011**, *7*, 2087-2093; e) F. Song, X. L. Hu, *Nat. Commun.* **2014**, *5*, 4477-4485.

89 a) A. Harriman, I. J. Pickering, J. M. Thomas, P. A. Christensen, *J. Chem. Soc., Faraday Trans. 1* **1988**, *84*, 2795-2806; b) H. Over, *Chem. Rev.* **2012**, *112*, 3356-3426.

90 I. C. Man, H. Y. Su, F. Calle-Vallejo, H. A. Hansen, J. I. Martínez, N. G. Inoglu, J. Kitchin, T. F. Jaramillo, J. K. Nørskov, J. Rossmeisl, *ChemCatChem* **2011**, *3*, 1159-1165.

91 a) J. Lee, S. A. S. Shah, P. J. Yoo, B. Lim, *Chem. Phys. Lett.* **2017**, *673*, 89-92; b) K. Maeda, R. Abe, K. Domen, *J. Phys. Chem. C* **2011**, *115*, 3057-3064; c) T. Reier, M. Oezaslan, P. Strasser, *ACS Catal.* **2012**, *2*, 1765-1772; d) Y. Zhang, T. Ren, *Chem. Commun.* **2012**, *48*, 11005-11007; e) N. C. King, C. Dickinson, W. Zhou, D. W. Bruce, *Dalton Trans.* **2005**, *0*, 1027-1032.

92 K. A. Stoerzinger, L. Qiao, M. D. Biegalski, Y. Shao-horn, *J. Phys. Chem. Lett.* **2014**, *5*, 1636-1641.

93 S. Jung, C. C. L. McCrory, I. M. Ferrer, J. C. Peters, T. F. Jaramillo, *J. Mater. Chem. A* **2016**, *4*, 3068-3076.

94 S. Y. Tee, C. J. J. Lee, S. S. Dinachali, S. C. Lai, E.L. Williams, H. K. Luo, D. Chi, T. S. A. Hor, M. Y. Han, *Nanotechnology* **2015**, *26*, 415401-415407.

95 E. Tsuji, A. Imanishi, K. Fukui, Y. Nakato, *Electrochim. Acta* **2011**, *56*, 2009-2016.

---

96 a) L. Francàs, X. Sala, J. Benet-Buchholz, L. Escriche, A. Llobet, *ChemSusChem* **2009**, *2*, 321-329; b) A. C. Sander, A. Schober, S. Dechert, F. Meyer, *Eur. J. Inorg. Chem.* **2015**, *26*, 4348-4353; c) B. Radaram, J. A. Ivie, W. M. Singh, R. M. Grudzient, J. H. Reibenspies, C. E. Webster, X. Zhao, *Inorg. Chem.* **2011**, *50*, 10564-10571.

97 K. P. J. Gustafson, A. Shatskiy, O. Verho, M.D. Kärkäs, B. Schluschass, C. Tai, B. Åkermark, J. Bäckvall, E. V. Johnston, *Catal. Sci. Technol.* **2017**, *7*, 293-299.

98 A. Mills, P. A. Duckmanton, J. Reglinski, *Chem. Commun.* **2010**, *46*, 2397-2398.

99 M. Roca-Ayats, E. Herreros, G. García, M. A. Peña, M. V. Martínez-Huerta, *Appl. Catal. B Environ.* **2016**, *183*, 53-60.

100 Y. Zhang, E. C. Judkins, D. R. McMillin, D. Mehta, T. Ren, *ACS Catal.* **2013**, *3*, 2474-2478.

101 K. Okeyoshi, R. Yoshida, *Adv. Funct. Mater.* **2010**, *20*, 708-714.

102 N. Coutard, N. Kaeffer, V. Artero, *Chem. Commun* **2016**, *52*, 13728-13748.

103 a) J. R. McKone, S. C. Marinescu, B. S. Brunschwig, J. R. Winkler, H. B. Gray, *Chem. Sci.* **2014**, *5*, 865-878; b) A. C. Marr, D. J. E. Spencer, M. Schroder, *Coord. Chem. Rev.* **2001**, *219*, 1055-1074.

104 T. Shinagawa, A. T. Garcia-Esparza, K. Takanabe, *Sci. Rep.* **2015**, *5*, Article nº 13801; B. E. Conway, B. V. Tilak, *Electrochim. Acta* **2002**, *47*, 3571-3594.

105 M. Zeng, Y. Li, *J. Mater. Chem. A* **2015**, *3*, 14942-14962.

106 a) S. Fukuzumi, Y. Lee, W. Nam, *Coord. Chem. Rev.* **2018**, *355*, 54-73; b) H. Lei, H. Fang, Y. Han, W. Lai, X. Fu, R. Cao, *ACS Catal.* **2015**, *5*, 5145-5153; b) V. Fourmond, P. A. Jacques, M. Fontecave, V. Artero, *Inorg. Chem.* **2010**, *49,* 10338-10347.

107 a) W. Lubitz, H. Ogata, O. Rudiger, E. Reijerse, *Chem. Rev.* **2014**, *114*, 4081-4148; b) J. C. Fontecilla-Camps, A. Volbeda, C. Cavazza, Y. Nicolet, *Chem. Rev.* **2007**, *107*, 4273-4303.

108 a) I. Bhugun, D. Lexa, J. M. Savéant, *J. Am. Chem. Soc.* **1996**, *118*, 3982-3983; b) D. J. Graham, D. G. Nocera, *Organometallics* **2014**, *33*, 4994-5001.

109 a) R. M. Kellett, T. G. Spiro, *Inorg. Chem.* **1985**, *24*, 2373-2377; b) C. H. Lee, D. K. Dogutan, D. G. Nocera, *J. Am. Chem. Soc.* **2011**, *133*, 8775-8777; c) B. B. Beyene, S. B. Mane, C. H. Hung, *Chem. Commun.* **2015**, *51*, 15067-15070.

110 D. K. Bediako, B. H. Solis, D. K. Dogutan, M. M. Roubelakis, A. G. Maher, C. H. Lee, M. B. Chambers, S. Hammes-Schiffer, D. G. Nocera, *Proc. Natl. Acad. Sci. U. S. A.* **2014**, *111*, 15001-15006.

111 a) N. Queyriaux, R. T. Jane, J. Massin, V. Artero, M. Chavarot-Kerlidou, *Coord. Chem. Rev.* **2015**, *304-305*, 3-19; b) Y. Sun, J. P. Bigi, N. A. Piro, M. L. Tang, J. R. Long, C. J. Chang, *J. Am. Chem. Soc.* **2011**, *133*, 9212-9215; c) M. Guttentag, A. Rodenberg, C. Bachmann, A. Senn, P. Hamm, R. Alberto, *Dalton Trans.* **2013**, *42*, 334-337; d) A. Rodenberg, M. Orazietti, B. Probst, C. Bachmann, R. Alberto, K. K. Baldridge, P. Hamm, *Inorg. Chem.* **2015**, *54*, 646-657; e) W. M. Singh, T. Baine, S. Kudo, S. Tian, X. A. Ma, H. Zhou, N. J. De Yonker, T. C. Pham, J. C. Bollinger, D. L. Baker, B. Yan, C. E. Webster, X. Zhao, *Angew. Chem. Int. Ed.* **2012**, *51*, 5941-5944; f) L. Tong, R. Zong, R. P. Thummel, *J. Am. Chem. Soc.* **2014**, *136*, 4881-4884; g) D. Z. Zee, T. Chantarojsiri, J. R. Long, C. J. Chang, *Acc. Chem. Res.* **2015**, *48*, 2027-2036.

112 a) J. L. Dempsey, B. S. Brunschwig, J. R. Winkler, H. B. Gray, *Acc. Chem. Res.* **2009**, *42*, 1995-2004; b) V. Artero, M. Chavarot-Kerlidou, M. Fontecave, *Angew. Chem. Int. Ed.* **2011**, *50*, 7238-7266.

---

113 a) A. Bhattacharjee, E. S. Andreiadis, M. Chavarot-Kerlidou, M. Fontecave, M. J. Field, V. Artero, *Chem. Eur. J.* **2013**, *19*, 15166-15174; b) N. Kaeffer, M. Chavarot-Kerlidou, V. Artero, *Acc. Chem. Res.* **2015**, *48*, 1286-1295; c) J. Willkomm, N. M. Muresan, E. Reisner, *Chem. Sci.* **2015**, *6*, 2727-2736; d) C. C. McCrory, C. Uyeda, J. C. Peters, *J. Am. Chem. Soc.* **2012**, *134*, 3164-3170.

114 a) M. L. Helm, M. P. Stewart, R. M. Bullock, M. R. DuBois, D. L. DuBois, *Science* **2011**, *333*, 863-866; b) M. Frey, *ChemBioChem* **2002**, *3*, 153-160.

115 a) H. Lei, H. Fang, Y. Han, W. Lai, X. Fu, R. Cao, *ACS Catal.* **2015**, *5*, 5145-5153; b) J. Wang, C. Li, Q. Zhou, W. Wang, Y. Hou, B. Zhang, X. Wang, *Dalton Trans.* **2016**, *45*, 5439-5443.

116 a) M. D. Sampson, C. P. Kubiak, *Inorg. Chem.* **2015**, *54*, 6674-6676; b) K. Hou, H. T. Poh, W. Y. Fan, *Chem. Commun.* **2014**, *50,* 6630-6632; c) K. Hou, S. J. L. Lauw, R. D. Webster, W. Y. Fan, *RSC Adv.* **2015** *5,* 39303-39309; d) D. A. Valyaeva, G. Lavignea, N. Lugan, *Coord. Chem. Rev.* **2016**, *308*, 191-235.

117 a) H. I. Karunadasa, C. J. Chang, J. R. Long, *Nature* **2010**, *464*, 1329-1333; b) H. I. Karunadasa, E. Montalvo, Y. Sun, M. Majda, J. R. Long, C. J. Chang, *Science* **2012**, *335*, 698-702.

118 J. K. Nørskov, T. Bligaard, A. Logadottir, J. R. Kitchin, J. G. Chen, S. Pandelov, U. Stimming, *J. Electrochem. Soc.* **2005**, *152*, J23-J26.

119 J. Mahmood, F. Li, S. Jung, M. S. Okyay, I. Ahmad, S. Kim, N. Park, H. Y. Jeong, J. Baek, *Nature Nanotech.* **2017**, *12*, 441-446.

120 T. Abe, T. Goto, K. Ohzeki, M. Kaneko, *Electrochim. Acta* **2000**, *45*, 4009-4014.

121 a) J. L. Boyer, D. E. Polyansky, D. J. Szalda, R. Zong, R. P. Thummel, E. Fujita, *Angew. Chem. Int. Ed.* **2011**, *50*, 12600-12604; b) Z. Chen, C. R. K. Glasson, P. L. Holland, T. J. Meyer, *Phys. Chem. Chem. Phys.* **2013**, *15*, 9503-9507.

122 K. Magdić, K. Kvastek, V. Horvat-Radošević, *Electrochim. Acta* **2015**, *167*, 455-469.

123 G. Rahman, S. A. Mian, A. H. A. Shah, O. S. Joo*, J. Appl. Electrochem.* **2016**, *46*, 459-468.

124 C. L. Gree, A. Kucernak, *J. Phys. Chem. B* **2002**, *106*, 1036-1047.

125 Z. Chen, J. Lu, Y. Ai, Y. Ji, T. Adschiri, L. Wan, *ACS Appl. Mater. Interfaces* **2016**, *8*, 35132-35137.

126 R. K. Shervedani, A. Amini, *Carbon* **2015**, *93*, 762-773.

127 J. Q. Chi, W. K. Gao, J. H. Lin, B. Dong, K. L. Yan, J. F. Qin, B. Liu, Y. M. Chai, C. G. Liu, *ChemSusChem* **2018**, *11*, 743-752.

128 L. Zhu, Q. Cai, F. Liao, M. Shengb, B. Wub, M. Shao, *Electrochem. Commun.* **2015**, *52,* 29-33.

129 E. Demir, S. Akbayrak, A. M. Önal, S. Özkar, *ACS Appl. Mater. Interfaces* **2018**, *10*, 6299-6308.

130 R. Ye, Y. Liu, Z. Peng, T. Wang, A. S. Jalilov, B. I. Yakobson, S. H. Wei, J. M. Tour, *ACS Appl. Mater. Interfaces* **2017**, *9*, 3785-3791.

131 Y. Zheng, Y. Jiao, Y. Zhu, L. H. Li, Y. Han, Y. Chen, M. Jaroniec, S. Qiao, *J. Am. Chem. Soc.* **2016**, *138*, 16174-16181.

132 T. E. Lister, Y. V. Tolmachev, Y. Chu, W. G. Cullen, H. You, R. Yonco, Z. Nagy*, J. Electroanal. Chem.* **2003**, *554/555*, 71-76.

133 J. Cheng, H. Zhang, H. Ma, H. Zhong, Y. Zou, *Electrchim. Acta* **2010**, *55*, 1855-1861.

134 L. Å. Näslund, Á. S. Ingason, S. Holmin, J. Rosen, *J. Phys. Chem. C* **2014**, *118*, 15315-15323.

---

135 T. Bhowmik, M. K. Kundu, S. Barman, *ACS Appl. Mater. Interfaces* **2016**, *8*, 28678-28688.

136 X. Kong, K. Xu, C. Zhang, J. Dai, S. N. Oliaee, L. Li, X. Zeng, C. Wu, Z. Peng, *ACS Catal.* **2016**, *6*, 1487-1492.

137 a) Y. Yamada, T. Miyahigashi, H. Kotani, K. Okubo, S. Fukuzumi, *J. Am. Chem. Soc.* **2011**, *133*, 16136-16145; b) S. Fukuzumi, Y. Yamada, *J. Mater. Chem.* **2012**, *22*, 24284-24296.

138 Y. Yamada, S. Shikano, S. Fukuzumi, *J. Phys. Chem. C* **2013**, *117*, 13143-13152.

139 a) C. C. K. McCrory, S. Jung, J. C. Peters, T. F. Jaramillo, *J. Am. Chem. Soc.* **2013**, *135*, 16977-16987; b) C. C. K. McCrory, S. Jung, I. M. Ferrer, S. M. Chatman, J. C. Peters, T. F. Jaramillo, *J. Am. Chem. Soc.* **2015**, *137*, 4347-4357.

140 G. Schmid, in *Nanoparticles: From Theory to Application*, Ed Wiley-VCH, Germany, **2004**, *1*, ch.2, 4-44.

141 a) R. H. Crabtree, E. F. Peris, in *Química Organometálica de los Metales de Transición*, Publicaciones de la Universitat Jaume I, Castellón, **1997**; b) R. Whyman, in *Applied Organometallic Chemistry and Catalysis*, Oxford University Press, Oxford, **2001**.

142 a) M. Guerrero, Y. Coppel, N. T. T. Chau, A. Roucoux, A. Denicourt-Nowicki, E. Monflier, H. Bricout, P. Lecante, K. Philippot, *ChemCatChem* **2013**, *5*, 3802-3811; b) E. Bresó-Femenia, B. Chaudret, S. Castillón, *Catal. Sci. Technol.* **2015**, *5*, 2741-2751; c) X. Cui, A. Surkus, K. Junge, C. Topf, J. Radnik, C. Kreyenschulte, M. Beller, *Nature Communications* **2016**, *7*, Article number: 11326; d) Y. Morioka, A. Matsuoka, K. Binder, B. R. Knappett, A. E. H. Wheatley, H. Naka, *Catal. Sci. Technol.* **2016**, *6*, 5801-5805; e) A. D. Dwivedi, R. K. Rai, K. Gupta, S. K. Sin, *ChemCatChem* **2017**, *9*, 1930-1938.

143 Y. Lin, X. C. Clive, H. Yen, C. M. Wai, *Langmuir* **2005**, *21*, 11474-11479.

144 Y. Na, S. Park, S. B. Han, H. Han, S. Ko, S. Chang, *J. Am. Chem. Soc.* **2004**, *126*, 250-258.

145 S. H. Joo, J. Y. Park, J. R. Renzas, D. R. Butcher, W. Huang, G. A. Somorjai, *Nano Lett.* **2010**, *10*, 2709-2713.

146 J. Kang, K. Cheng, L. Zhang, Q. Zhang, J. Ding, W. Hua, Y. Lou, Q. Zhai, Y. Wang, *Angew. Chem. Int. Ed.* **2011**, *50*, 5200-5203.

147 T. Graham, *Phil. Trans. R. Soc. Lon.* **1861**, *151*, 183-224.

148 J. D. Aiken, R. G. Finke, *J. Mol. Catal. A: Chem.* **1999**, *145*, 1-44.

149 D. Astruc, F. Lu, J. R. Aranzaes, *Angew. Chem. Int. Ed.* **2005**, *44*, 7852-7872.

150 A. Roucoux, J. Schulz, H. Patin, *Chem. Rev.* **2002**, *102*, 3757-3778.

151 a) J. Osuna, D. De Caro, C. Amiens, B. Chaudret, E. Snoeck, M. Respaud, JM. Broto, A. Fert, *J. Phys. Chem.* **1996**, *100*, 14571-14574; b) T. Ayvalı, P. Lecante, P. Fazzini, A. Gillet, K. Philippot, B. Chaudret, *MRS Proceedings* **2014**, *1675*, 157-162.

152 a) J. Dupont, G. S. Fonseca, A. P. Umpierre, P. F. P. Fichtner, S. R. Teixiera, *J. Am. Chem. Soc.* **2002**, *124*, 4228-4229; b) J. D. Scholten, B. Caroline Leal, J. Dupont, *ACS Catal.* **2012**, *2*, 184-200.

153 a) C. Amiens, D. Ciuculescu-Pradines, K. Philippot, *Coord. Chem. Rev.* **2016**, *308*, 409-432; b) C. Pan, K. Pelzer, K. Philippot, B. Chaudret, F. Dassenoy, P. Lecante, M.-J. Casanove, *J. Am. Chem. Soc.* **2001**, *123*, 7584-7593; c) P. Lara, K. Philippot, B. Chaudret, *ChemCatChem* **2013**, *5*, 28-45.

154 K. Pelzer, K. Philippot, B. Chaudret, *Z. Phys. Chem.* **2003**, *217*, 1539-1547.

---

155 H. Bönemman, G. Braun, W. Brijoux, R. Brinkmann, A. Schulze, K. Seevogel, K. Siepen, *J. Organomet. Chem.* **1996**, *520*, 143-162.

156 F. W. S. Benfield, M. Green, J. S. Odgen, D. J. Young, *J. Chem. Soc. Chem. Commun.* **1973**, 866-867.

157 M. T. Reetz, W. Heilbig, *J. Am. Chem. Soc.* **1994**, *116*, 7401-7402.

158 K. Philippot *et al.* in *Ruthenium in catalysis* **2014**, C. Bruneau and P.H. Dixneuf (Eds), Wiley VCH, Weinheim, **2014**, *Top. Organomet. Chem.* **2014**, *48*, 319

159 E. Castillejos, P. Debouttière, L. Roiban, A. Solhy, V. Martinez, Y. Kihn, O. Ersen, K. Philippot, B. Chaudret, P. Serp, *Angew. Chem. Int. Ed.* **2009**, *48*, 2529-2533.

160 J. Llop Castelbou, K. C. Szeto, W. Barakat, N. Merle, C. Godard, M. Taoufik, C. Claver, *Chem. Commun.* **2017**, *53*, 3261-3264.

161 F. Schröder, D. Esken, M. Cokoja, M. W. E. van den Berg, O. I. Lebedev, G. V. Tendeloo, B. Walaszek, G. Buntkowsky, H. H. Limbach, B. Chaudret, R. A. Fischer, *J. Am. Chem. Soc.* **2008**, *130*, 6119-6130.

162 T. Ayvalı, P. F. Fazzini, P. Lecante, A. Mayoral, K. Philippot, B. Chaudret, *Dalton Trans.* **2017**, *46*, 15070-15079.

163 a) R. M. Axet, K. Philippot, B. Chaudret, M. Cabié, S. Giorgio, C. R. Henry, *Small* **2011**, *7*, 235-241; b) G. H. Woehrle, J. E. Hutchison, S. Özkar, R. G. Finke, *Turk. J. Chem.* **2006**, 30, 1-13.

164 S. G. Podorov, N. N. Faleev, K. M. Pavlov, D. M. Paganin, S. A. Stepanov, E. Förster, *J. App-. Crystallogr.* **2006**, *39*, 652-655.

165 A. W. Coats, J. P. Redfern, *Analyst* **1963**, *88*, 906-924.

2

Objectives

After presenting the state of the art on the field of hydrogen production by the splitting of water and the preparation and characterization of metal nanoparticles, several ideas come to our mind as possible targets in order to gain knowledge on the two semi-reactions involved in the process of water splitting into O_2 and H_2, namely the Oxygen Evolution (OER) and the Hydrogen Evolution (HER) Reactions. Thus, the core of this PhD project is based on the development of novel Ru-based nanoparticles, either metal oxide or metallic nanoparticle systems, to be used as catalysts for the oxidation of water into O_2 and the subsequent reduction of the released protons to H_2.

First, some general objectives will be presented, which will be later on divided into specific projects.

2. Objectives

In view of the state of the art previously presented, several options appear of interest to gain knowledge in the field of the production of hydrogen by the catalysis of water splitting. This field of catalysis is a challenging topic given the issues met in the process of water decomposition into O_2 and H_2, in particular for the first semi-reaction involved, namely the oxidation of water, where effective and stable catalysts based on earth-abundant and cheap species still need to be developed. If the second reaction seems easier to achieve thanks to the discovering of efficient catalysts (mainly of Pt), cheaper catalytic systems are required to make the whole process economically more accessible.

Thus, given the recent results published in the development of catalysts under the form of nanomaterials for the water splitting process, the main objectives of this PhD work are as follows:

1. Develop nano-sized catalysts for the OE and HE reactions.
2. Study the characteristics of the catalytically active species to understand which of them rule their catalytic performance. Control the parameters such as surface environment, oxidation state, physical structure, or species evolution under catalytic conditions, leaning on the organometallic approach as synthetic methodology.
3. Based on this knowledge, rationally design new catalysts with enhanced activities and stabilities by tuning the aforementioned catalyst’s properties.

More specifically, the following points have been the guidelines of this PhD thesis project:

1. Synthesize and characterize Ru^0-NPs stabilized with different ligands by following the organometallic synthesis approach. Study the effect of the synthetic conditions onto the final nanomaterials, modifying parameters such as the ligand/metal ratio. Investigate the stability of the particles in several reaction conditions related with the catalysis, like air exposure or contact with aqueous solutions, and the influence of temperature on their characteristics.
2. Obtain RuNPs supported onto rugged materials, either by immobilization of pre-formed NPs or by *in-situ* generation of the particles onto the supporting material. Investigate the effect of the support onto the formation, stabilization and catalytic properties of the NPs, employing different materials as supports

like carbon nanotubes or carbon fibers or by previously modifying the supports with new functionalities.

3. Study the oxidation of pre-synthesized RuNPs that are supported or not, into RuO_2 ones with the aim to find reaction conditions enabling to control this step in order to maintain at maximum as possible the nanoparticle characteristics in terms of size and surface environment.

4. Test Ru^0 and RuO_2-based nanomaterials towards the OER and HER. Study their stability during the catalytic process in terms of size and surface state. Unravel the role of the stabilizing ligands used for the synthesis of the particles on the catalytic performance. Apprehend which conditions favor the catalytic reactions to mechanistically understand how the reactions go through.

5. Compare the different performances in OE and HE catalysis to connect the properties of the catalysts with the displayed activities, finding correlations between them, in order to open new perspectives.

For achieving these targets, the organometallic approach has been employed as synthetic methodology, given the level of control it allows for the characteristics of the NPs, as described in Chapter 1. Ruthenium has been chosen as the active metal, because it already exhibited high activity for the target catalysis but also because it is only scarcely used in HER although it is more abundant than platinum. Moreover, previous knowledge acquired on the interest of Ru-based NPs prepared by the organometallic method in catalysis, appeared as a great advantage to perform an investigation of the structure-properties relationships.

The catalytic performance of the materials has been evaluated in electrochemical set-up's, being that the easiest and most comprehensive way to evaluate the catalysts. However, the aim is to further test them into photoelectrochemical devices.

3

Colloidal Ruthenium Nanoparticles as Hydrogen Evolution Catalysts

In this first experimental chapter, the synthesis of RuNPs by the organometallic approach in the presence of different stabilizing agents is described (MeOH/THF in 3A, pyridine-based ligands in 3B, and 4-phenylpyridine in 3C). Their characterization by using complementary techniques such as TEM-HRTEM, WAXS, XPS, NMR, EA, ICP or TGA, is presented with the aim to precisely define their intrinsic composition. Once deposited onto glassy carbon electrodes, they have been evaluated as catalysts for HER, and compared with the state-of-the-art nanomaterials. These studies have allowed to shed some light on the key parameters of the proton reduction catalysis.

3.0 Preface

As previously mentioned in the general introduction, H_2 can be produced from water through the Water Splitting (WS) process which involves two successive semi-reactions, namely Oxygen Evolution and Hydrogen Evolution reactions (OER and HER, respectively).[1] Electrochemically, these two reactions need to be catalyzed to make the whole process efficient, meaning operating at low overpotential and in fast kinetic conditions. The discovery of highly effective and stable electrocatalysts is thus extremely desired for both reactions. Regarding HER, among the various catalysts tested, Pt-based ones are considered as the best systems for this reaction.[2,3] However, the prohibitive price and scarcity of platinum make it unsuitable for large scale commercial application. Therefore, the development of efficient and cheaper species that could operate at low overpotentials with a high stability is extremely required.

Whereas ruthenium has been one of the most studied transition metals to develop catalysts for the OER showing high electrocatalytic activity, the performance of this metal for the HER had not been much investigated.[4] However, in the last few years, several works described Ru-based nanomaterials as efficient Hydrogen Evolution Catalysts (HECs) either in acidic or alkaline conditions.[5,6,7] For instance, Z. Peng *et al.* reported the preparation and electrocatalytic performance in the HER of two-dimensional Ru nanostructures.[6] The observed improved kinetics of this system when compared to Ru black powder is attributed to the greater specific area of the former due to its 2D structure. This hypothesis is supported by the fact that materials possessing a large surface area should display more active sites. The use of such materials seems thus to be a promising strategy to enhance the catalytic activity.

The best performing Ru-systems are composite materials made of RuNPs embedded into carbon matrices that strongly affect their catalytic behavior and do not permit to finely tune the active sites. The followed synthetic protocols lead to barely defined structures, disabling a proper correlation between the characteristics of the nanospecies and their catalytic properties even if it is a key-point to optimize a catalytic reaction. The design of finely controlled metal NPs should offer interesting perspectives to better understand the crucial parameters to develop nanostructured catalysts with increased performance, both in terms of efficiency and stability.

This chapter is splitted into three main sections. The first one (section 3A) concerns the facile synthesis of porous Ru nanoparticles that display a high surface area, which was shown to be fundamental for the enhancement on the catalytic HER. Section 3B, reports fundamental studies on RuNPs stabilized by pyridine-based ligands, and their catalytic activity towards the H_2 evolution is compared with that of different Ru-based systems previously synthesized in our group. In the last section (3C), the use of 4-phenylpyridine ligand as stabilizing agent enables the formation of very small RuNPs

(1.5 nm), which exhibit HER activities similar to that of Pt and of the best Ru-based systems reported so far.

3A. Synthesis of a Porous Ru Nanomaterial and its Evaluation as HEC in Acidic and Neutral Conditions

3A.1 Introduction

The use of materials with high surface area can be highly advantageous in electrocatalysis. Very recently, porous assemblies of Pd nanoparticles have been reported as an efficient catalyst for both HER and Oxygen Reduction Reaction (ORR).[8] This Pd nanomaterial exhibited high electrocatalytic activity for the HER with a low overpotential of ca. 80 mV at a current density of 100 mA·cm^{-2}, a small Tafel slope of 30 mV·dec^{-1} and a long-term stability for at least 1000 consecutive cyclic voltammograms. However, notwithstanding its high catalytic performance, palladium is not a cheaper alternative to platinum catalysts since it is in the same order of price. Other metals such as Ni, Co, Mo or Pt have been studied as nanostructured systems with interesting activities (see Tables A1-4 in the Annex part).

On the basis of the above mentioned results with Pd and of the possibilities offered by the organometallic approach to achieve nanostructured materials having a clean surface and high surface area as especially demonstrated for Ru,[9] we decided to evaluate the catalytic performance in HER of Ru nanomaterials derived from an organometallic precursor. We first focused on a Ru nanomaterial which displays a porous morphology combined with a clean and reactive metal surface as shown previously in gas-phase hydrogenation catalysis.[10] Moreover, its synthesis is very simple and achieved in mild conditions.[11] As it will be seen later on, this Ru nanomaterial proved to be a very effective HER catalyst, exhibiting high electrocatalytic performance and excellent durability under both acidic and neutral conditions.

3A.2 Synthesis & characterization of Ru-MeOH/THF porous nanomaterial

The Ru nanomaterial object of this study, and hereafter named as **Ru-MeOH/THF**, was easily prepared by decomposition of the [Ru(cod)(cot)] (cod = 1,5-cyclooctadiene; cot = 1,3,5-cyclooctatriene) organometallic precursor under a H_2 atmosphere (3 bar) in a MeOH/THF (5/95 in volume) solvent mixture in the absence of any other stabilizers.[11] In this way, a dark brown colloidal solution was obtained. Methanol and tetrahydrofuran act here as both solvents and stabilizing agents, being the MeOH/THF ratio essential for controlling the characteristics of the final material as size, shape and composition.

TEM/HRTEM (transmission electron microscopy at low and high resolution) analysis of the crude colloidal solution revealed the presence of nano-sized but quite big particles of ca. 21 ± 2 nm mean size, which are composed by very small NPs (Figure 1a,b,d). As visible in Figure 1b, these particles display a sponge-like morphology due to their multi-NPs composition, and a well-crystallized character (Figure 1e). The Fast Fourier Transformation (FFT, Figure 1f) of the HRTEM images (Figure 1d and e) indicate the presence of interplanar distances of 0.234, 0.203 and 0.158 nm corresponding to the crystalline (100), (101) and (102) planes of the hexagonal close-packed (hcp) structure of bulk Ru, respectively. The porous and polycrystalline aspect of the particles is attributed to an aggregation phenomenon of smaller individual particles during the synthesis process due to the composition of the reaction medium, particularly the absence of a strong stabilizer.

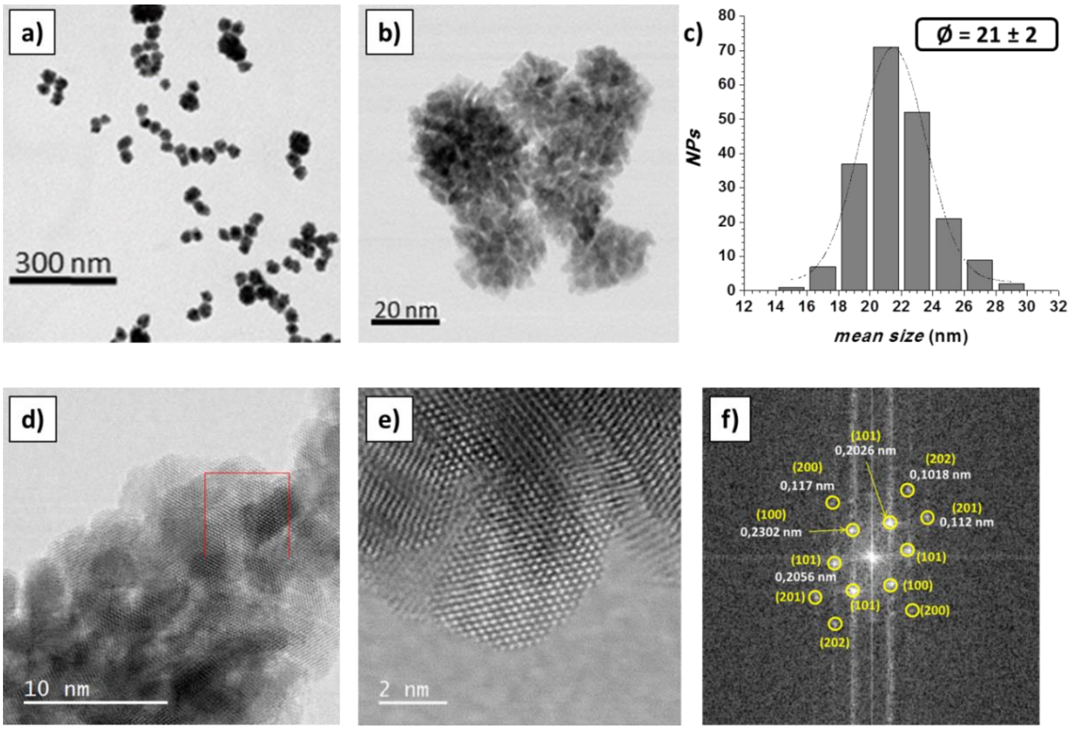

Figure 1. TEM images (a and b), corresponding size histogram (c), HRTEM images (d and e) and diffraction pattern (f) of **Ru-MeOH/THF** nanomaterial.

Nevertheless, the obtained colloidal solution is stable for a long period of time and the evaporation of the solvents under vacuum allowed to obtain the Ru nanomaterial in the form of a black powder without further purification. Powder X-Ray Diffraction analysis (XRD, Figure 2a) confirmed that the Ru particles adopt the hcp crystalline structure. X-Ray Photoelectron Spectroscopy (XPS) of a powder sample permitted the identification of the surface chemical composition and valence states of the Ru atoms (Figure 2b). The results revealed the presence of both Ru^0 and RuO_2 by the shoulder present at 280.8 eV (RuO_2) observed close to the peak of Ru^0 at 279.9 eV, both typical for Ru-$3d_{5/2}$.[12] The presence of RuO_2 can be explained by the formation of an oxide passivation layer due to air exposure of the nanomaterial. The formation of such a thin superficial oxide layer has been previously observed.[11]

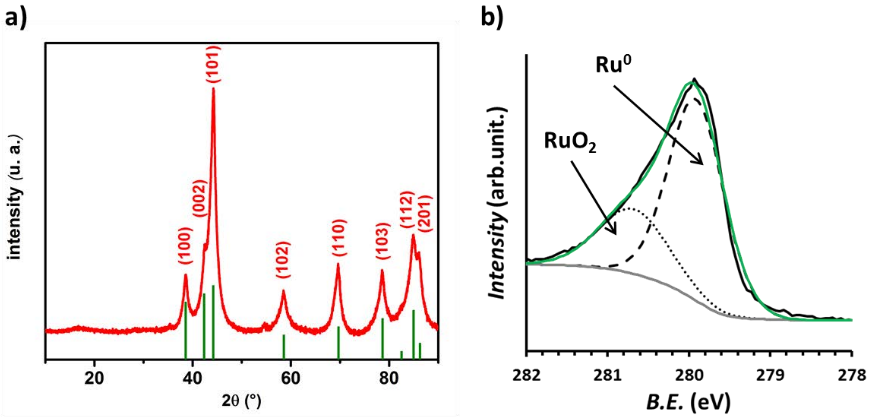

Figure 2. Powder a) XRD pattern (red) with Ru-hcp pattern (green) as reference, and b) powder XPS spectrum of **Ru-MeOH/THF** NPs.

3A.3 Electrocatalytic HER studies

The electrocatalytic activity of the **Ru-MeOH/THF** nanomaterial described above for the HER was first studied by linear sweep voltammetry (LSV) in 0.5 M H_2SO_4 solution. For that purpose, a dispersion of **Ru-MeOH/THF** was deposited onto a glassy carbon disk electrode (GC), leading to a supported system named as **Ru-GC**. The onset overpotential (η_0) and the overpotential required for achieving a $|j|$ = 10 mA·cm^{-2} (η_{10}), are distinctive values generally employed for electrocatalysts' comparison. More specifically, η_{10} corresponds to the approximate current density expected for a 10% efficient solar-to-fuel conversion photoelectrochemical cell under 1 Sun illumination.[1,13]

As shown in Figure 3a, **Ru-GC** displays an efficient catalytic activity with a low onset of $\eta_0 \approx 40$ mV and a $\eta_{10} = 83$ mV, which is a lower value than that measured for commercial Ru-black (Rub, $\eta_{10} = 94$ mV), but higher than the overpotential observed for the state-of-the-art Pt/C ($\eta_{10} = 58$ mV) catalyst. The long-term durability of our **Ru-GC** catalyst was studied by performing a current-controlled bulk electrolysis experiment for over 12 h (Figure 3b). At a current density of j = -10 mA·cm^{-2}, a stable overpotential was observed over the time of the experiment without important variation (i.e. 30 mV). This behavior is indicative of a good stability of the deposited **Ru-MeOH/THF** nanomaterial. The small overpotential increase is attributed to the formation of copious H_2 bubbles that block and inhibit the catalyst surface. In fact, as shown in the inset of Figure 3b, the polarization curves recorded before and after the bulk electrolysis perfectly overlay, providing evidence for the long-term stability of the **Ru-GC** catalyst.

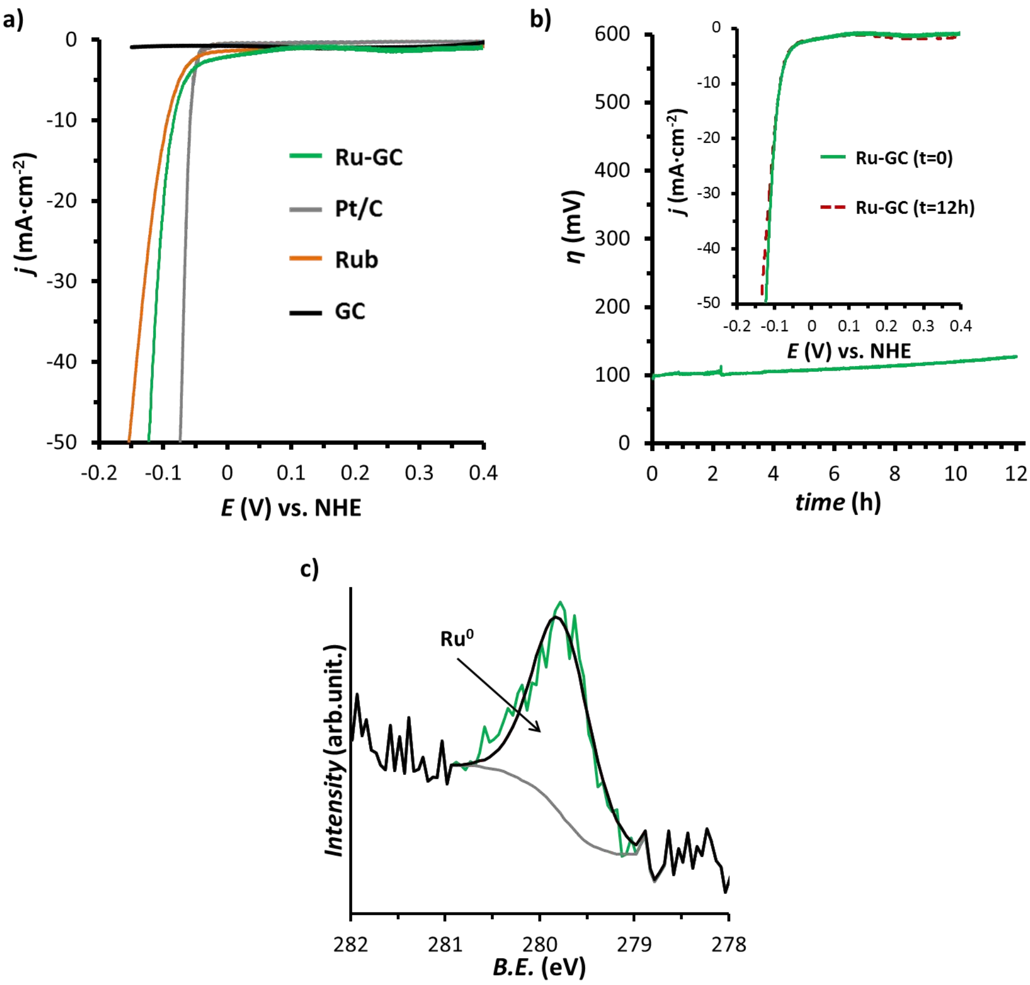

Figure 3. a) LSV curves of **Ru-GC** (green), Rub (orange), Pt/C (grey) and bare GC_d electrode (black) in 0.5 M H_2SO_4 solution at 10 mV·s^{-1}; b) current-controlled bulk electrolysis experiment of **Ru-GC** at *j* = -10 mA·cm^{-2} in 0.5 M H_2SO_4, without ohmic drop compensation. Inset, LSV curves of the initial **Ru-GC** (green) and after 12h bulk electrolysis experiment at *j* = -10 mA·cm^{-2} (dashed red) in 0.5 M H_2SO_4 solution at 10 mV·s^{-1}; c) XPS spectra of **Ru-GC** (green) after 15 min bulk electrolysis at *j* = -10 mA·cm^{-2} in 0.5 M H_2SO_4. Background (grey), metallic-Ru component (dashed black), envelop (bold).

To determine the nature of the catalytically active species, a XPS analysis was carried out after performing a current-controlled electrolysis at *j* = -10 mA·cm^{-2} for 15 min. The XPS data presented in Figure 3c, clearly reveal only one peak in the 3d core-level region at 279.8 eV, in contrast to the Ru^0/RuO_2 double-character of the **Ru-MeOH/THF** powder, suggesting Ru^0 to be the unique active species for the HER.

Tafel plot analysis allows evaluation of the rate determining step (rds) and therefore elucidation of the HER mechanism. As explained in the general introduction (Ch. 1), the HER process may occur following two different mechanisms each corresponding to a combination of two elementary steps. The first common step is the absorption of a hydride to form a Cat-H group (Volmer step), and it can be followed either by the Tafel step (recombination of two Cat-H species, Eq. 1) or the Heyrovsky (H_2 electrodesorption with a proton from the solution, Eq. 2):

$$2Cat - H_{(ad)} \rightarrow H_{2(s)} + 2Cat_{(s)} \qquad \text{Eq. 1}$$

$$Cat - H_{(ad)} + H^{+}_{(aq)} + \bar{e} \rightarrow H_{2(s)} + Cat_{(s)} \qquad \text{Eq. 2}$$

In our study, a Tafel slope of 46 mV·dec^{-1} has been determined from the low scan rate polarization curve performed with **Ru-GC** (Figure 4c). This value suggests that the HER follows the Volmer-Heyrovsky mechanism where the Heyrovsky step is the rds of the overall reaction.[14] The Tafel slope value is also an intrinsic parameter in the evaluation of the catalytic performance of electrocatalysts: 46 mV·dec^{-1} is a much lower value than that measured for commercial Ru black, namely 60 mV·dec^{-1}. This result indicates that our Ru nanomaterial presents superior kinetic performance.

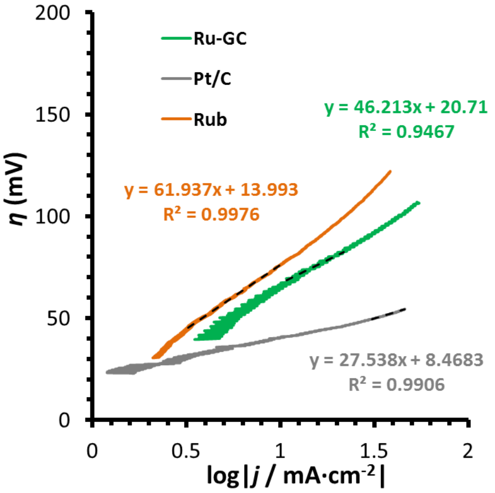

Figure 4. Tafel Plot of **Ru-GC** (green), Rub (orange) and Pt/C (grey) in 0.5 M H_2SO_4.

Another intrinsic electrochemical parameter from **Ru-GC** cathode can be subtracted from the Tafel equation. The exchange current density (j_0) is the obtained current in the absence of any faradaic process, namely at η_0. The higher this value is the better the catalyst is considered. **Ru-GC** has a j_0 = 0.36 mA·cm^{-2}, which is a good result compared to the best systems in the literature (see Table A3 in Annex1).

In order to evaluate the Faradaic yield of the **Ru-MeOH/THF** nanomaterial for the hydrogen production, a controlled potential electrolysis was performed at 50 mV vs. NHE in 0.5 M H_2SO_4 to a FTO-supported sample. The amount of H_2 produced over the time of the electrolysis was quantified by means of a Clark electrode, giving a nearly quantitative faradaic yield of 97% (Figure 5a), thus confirming that all the electrons used in the experiment were devoted to the reduction of H^+ to H_2. Additionally, the stable current measured over the time of the experiment provides evidence for the high stability of the catalytic activity of the nanomaterial (Figure 5b).

In the perspective study of investigating the **Ru-MeOH/THF** catalyst in a photocatalytic setup with a molecular photosensitizer, such as porphyrins or polypyridine ruthenium complexes which are used under neutral conditions,[15] electrocatalytic measurements were also performed at 0.1 M phosphate buffer solution (PBS).

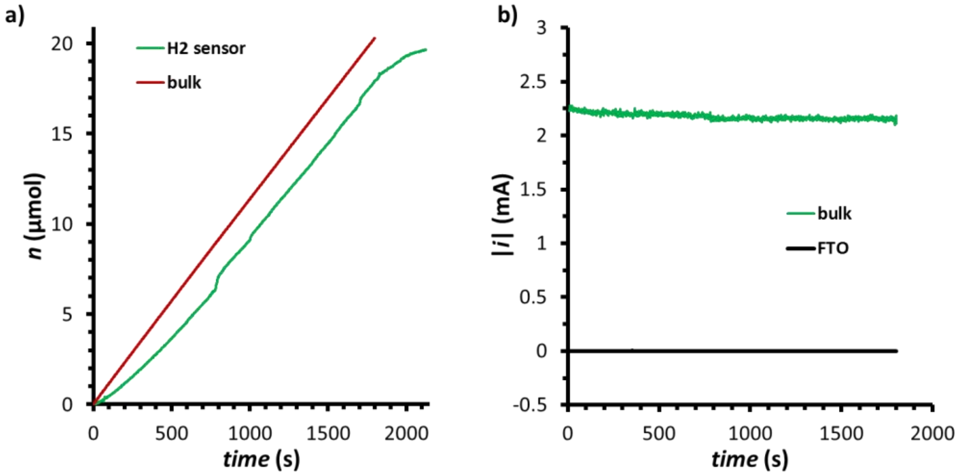

Figure 5. a) H_2 evolution profile measured by Clark electrode (green) compared to CPE (red); b) CPE of FTO-supported **Ru-MeOH/THF** onto (green) and bare FTO plate (black) in 0.5 M H_2SO_4 at 50 mV vs. NHE.

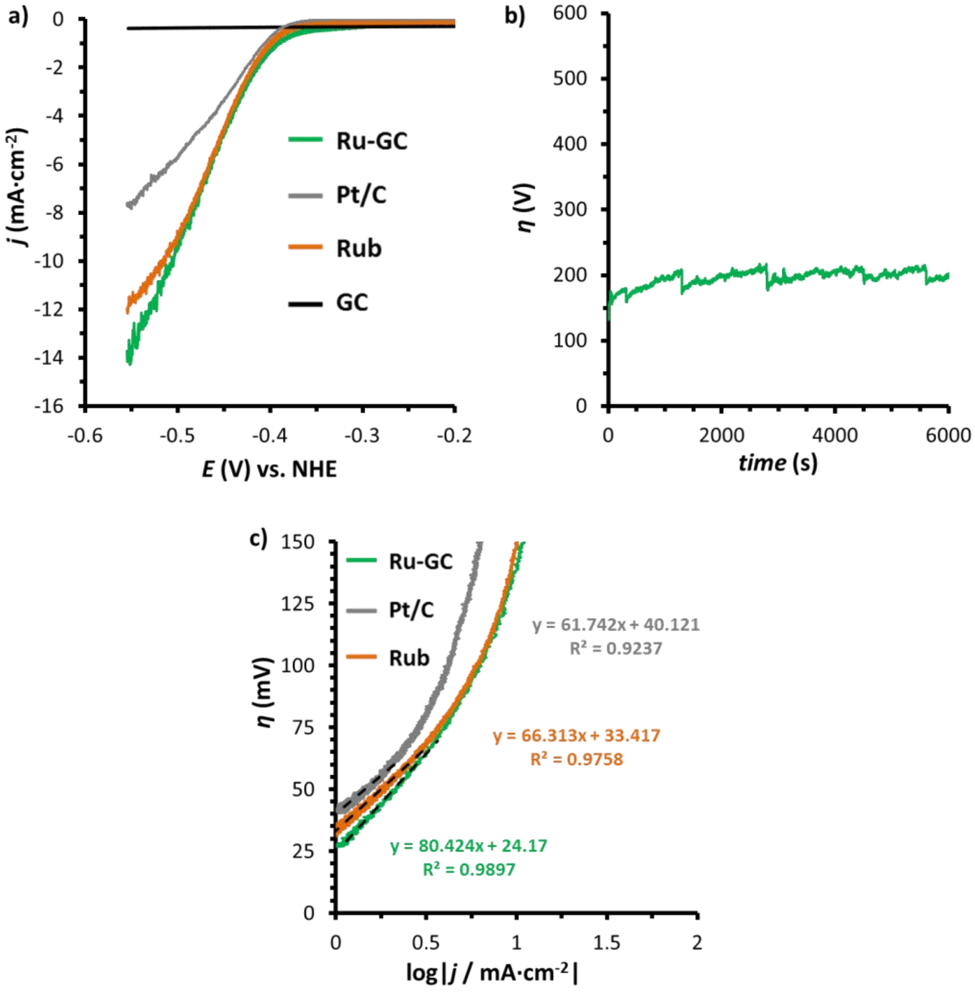

Figure 6. a) LSV curves of the **Ru-GC** (green), Rub (orange), Pt/C (grey) and bare GC_d (black) in 0.1 M PBS at 1 mV·s^{-1}; b) current-controlled bulk electrolysis of the **Ru-GC** at j = -10 mA·cm^{-2} in 0.1 M PBS, without ohmic-drop compensation; c) Tafel Plot of **Ru-GC** (green), Rub (orange) and Pt/C (grey) in 0.1 M PBS.

As shown in Figure 6a, it is worth noting that the **Ru-GC** catalyst also exhibits high electrocatalytic activity under these neutral conditions reaching a j = -10 mA·cm^{-2} at η_{10} of 83 mV. A current-controlled bulk electrolysis experiment performed at fixed j = -10 mA·cm^{-2} for almost 2 h demonstrated a stable catalytic activity (Figure 6b). A Tafel slope of 80 mV·dec^{-1} (Figure 6c) was determined in this case, which is higher than the corresponding value obtained in acidic solution, thus indicating slower kinetics for the HER under neutral than under acidic conditions, as expected.

3A.4 Electrocatalytic performance benchmarking

The electrocatalytic performance was further compared with other electrocatalysts following the benchmarking methodology published by T. F. Jaramillo *et al.*[3,16] First, from a current-controlled bulk electrolysis at j = -10 mA·cm^{-2} under acidic conditions, the corresponding η_{10} values at time t = 0 and t = 2h are reported in Table A3 (Annex 1) and plotted in Figure 7:

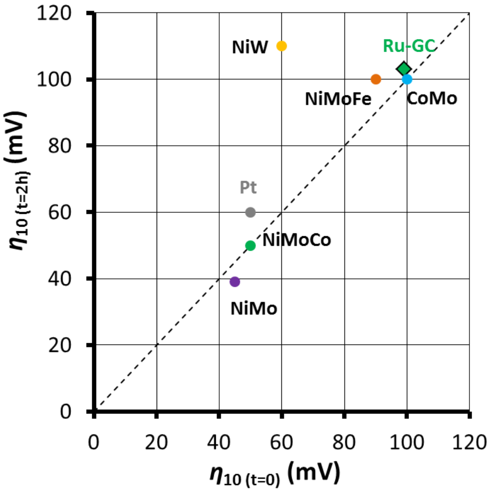

Figure 7. Graphical representation of electrocatalysts benchmarking comparison.

Following, the catalytically active surface area (ECSA) of the **Ru-GC** sample was estimated by a method based on cyclic voltammetry measurements (Figure 8b).[17] This gives direct access to the double layer capacitance (C_{DL}, Figure 8), which further permits the determination of the ECSA value by dividing C_{DL} by a general capacitance of 0.015 mF·cm^{-2}, for a catalyst-free carbon electrode under the same conditions. For better accuracy, the experiment was repeated three times, and an ECSA value of 45.2 cm^{2} was found leading to a roughness factor (RF) of 645 ± 87.

If we normalize these results by the Ru mass loading, a high value of 173.07 m^{2}·g^{-1} is obtained. In comparison to the value measured under the same conditions for Ru black used as a reference in this work, 72.60 m^{2}·g^{-1}, this result evidences that the **Ru-MeOH/THF** nanomaterial presents a very high electroactive surface area. It is also important to note that 173.07 $m^2 \cdot g^{-1}$ is a value higher than that reported by S. Liu *et al.* for the porous Pd material previously mentioned (0.36 $m^2 \cdot g^{-1}$).[8]

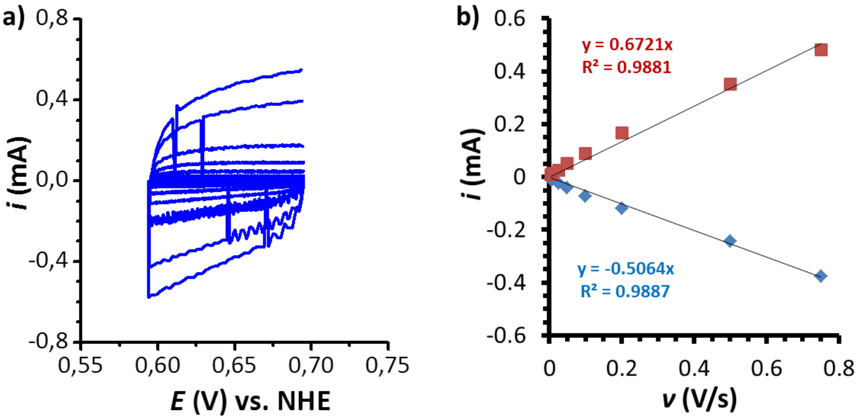

Figure 8. a) Representative multi CV experiment at different scan rates for C_{DL} determination in 0.5 M H_2SO_4; b) plot of current values at 0.65 V (vs. NHE) for the different scan rates, for C_{DL} determination.

As an alternative normalization method, the copper UnderPotential Deposition (UPD) has been applied to determine the number of active sites and to calculate the turnover frequency (TOF) (Figure 9a), as previously presented in section 1.5.3.2 in Chapter 1.[18] From the charge (*Q*, in coulombs [C]) under the Cu-UPD oxidation wave the active sites were quantified (18 nmol), allowing to calculate a TOF value of 0.87 s^{-1} at 100 mV of overpotential.

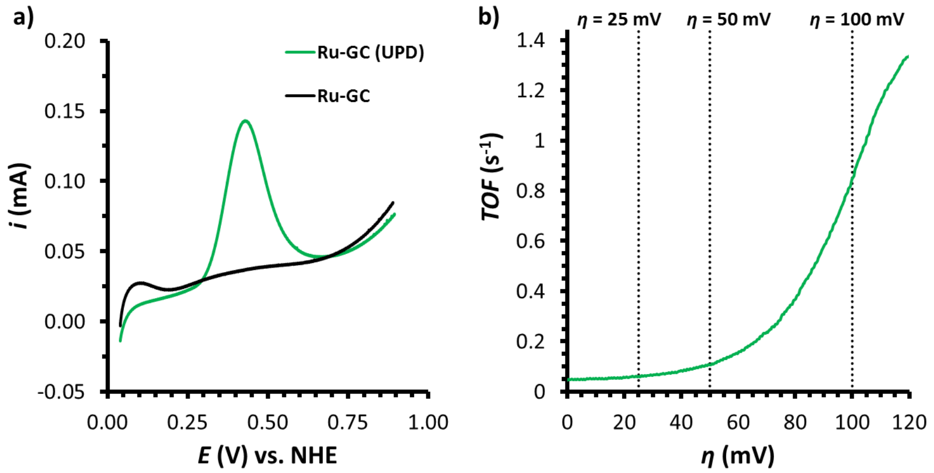

Figure 9. a) LSV curves of **Ru-GC** before (black) and after (green) Copper UPD in 0.5 M H_2SO_4; b) TOF vs. *η* (mV) plot of **Ru-GC** in 0.5 M H_2SO_4 solution. See Table A1 in Annex1 for comparison with the literature.

3A.5 Conclusions & perspectives

In this section, we have described the electrocatalytic performance of a porous Ru nanomaterial made of ca. 21 nm aggregates of small NPs in the HER, in both acidic and neutral conditions, and in comparison with commercial Ru black and Pt/C. This efficient electrocatalyst was easily prepared by the decomposition of an organometallic precursor under hydrogen using only a mixture of methanol and THF as stabilizers, which causes it to have a clean metal surface. Among the different characteristics determined in electrocatalysis, a low overpotential of 83 mV at a current density of j = -10 mA·cm^{-2} and an excellent durability up to 12h in 0.5 M H_2SO_4 were obtained. This remarkable behavior is attributed to the porous character of the nanomaterial coupled with the use of a mixture of solvents as stabilizers, which gives rise to a highly accessible metal surface as demonstrated by the high electrochemically active surface area measured, namely 173 m^2·g^{-1}.

Taking advantage of the synthetic methodology and the range of NPs that can be obtained by tuning the MeOH:THF solvent ratio,[11] as already published by our group, we envisage to study the catalytic performance of a series of NPs having different structural/size/agglomeration characteristics. These particles would be stabilized by the same agent all of them (MeOH:THF), but the different solvents ratio might allow to control the features of the colloids, altering the catalytic properties of the final material. This could suppose an important advance on the understanding of the catalytic pathways taking part on the surface of the particles, permitting a rational design of new active particles based on the gained knowledge in the stabilizing effect.

This work has been published in Chemical Communications in 2017 (A porous Ru nanomaterial as an efficient electrocatalyst for the hydrogen evolution reaction under acidic and neutral conditions, S. Drouet, J. Creus, V. Collière, C. Amiens, J. García-Antón, X. Sala, K. Philippot, Chem. Commun. ***2017****, 53, 11713-11716), and this publication is given in the Annex part.*

3A.6 Experimental part

Reagents. All operations for the synthesis of the **Ru-MeOH/THF** nanomaterial were carried out using standard Schlenk tubes, Fisher-Porter bottle techniques or in a glove-box (MBraun) under argon atmosphere. Solvents (THF and MeOH) were purified before use, by filtration on adequate column in a purification apparatus (MBraun) for THF and by distillation on magnesium for MeOH, and handled under argon atmosphere. Solvents were degassed before use according to a freeze-pump-thaw process. The ruthenium precursor, [Ru(cod)(cot)] was purchased from Nanomeps-Toulouse. Hydrogen gas (Alphagaz) was purchased from Air Liquide. High purity deionized water was obtained by passing distilled water through a nanopore Milli-Q water purification system.

Synthesis of Ru-MeOH/THF. 100 mg of [Ru(cod)(cot)] were dissolved under argon in a total volume of 100 mL of a MeOH/THF mixture (5:95) in a Fisher porter reactor inside a Glove-box. After pressurization of the reactor with 3 bar of H_2 at room temperature (r.t.), the initial yellow solution turned dark brown in a few minutes. A vigorous magnetic stirring and the H_2 pressure were maintained for 45 minutes. After this reaction time, the H_2 pressure was evacuated and a drop of the colloidal solution was deposited onto a carbon-covered copper grid for microscopy analysis. The Ru nanomaterial was isolated as a grey powder after simple evaporation to dryness under vacuum.

Characterization. The colloidal solution has been characterized by Transmission Electron Microscopy (TEM), High Resolution TEM (HRTEM) and the isolated solid by powder X-Ray Diffraction (XRD) and X-ay Photoelectron Spectroscopy (XPS).

Powder X-Ray Diffraction (XRD) measurements were performed with a PANalytical X'Pert Pro θ/θ diffractometer equipped with a X'Celerator detector using Cu radiation ($\lambda = 1.5418$ Å). The data were registered in the 2 θ range 2-90° with a step wise of 0.016° and a time by step equal to 1000s. Highscore software was used for data analysis.

Transmission Electron Microscopy (TEM) and High resolution TEM (HRTEM). Samples for TEM and HRTEM analyses were prepared by slow evaporation of a drop of the crude colloidal solution deposited onto a holey carbon-covered copper grid. Analyses were performed at the "Centre de Microcaractérisation Raymond Castaing" in Toulouse (UMS-CNRS 3623), on a MET JEOL JEM 1011 microscope operating at 100 kV with a resolution point of 0.45 nm and a JEOL JEM-ARM 200F microscope working at 200 kV with a resolution point lower of 0.19 nm, respectively. TEM allowed to evaluate the particle size, size distribution and morphology. Enlarged micrographs were used for treatment with ImageJ software to obtain a statistical size distribution and the nanoparticle mean diameter. FFT treatments of HRTEM images were carried out with Digital Micrograph Version 1.80.70 to determine the crystalline structure of the material. The analyses were done by assuming that the nanoparticles are spherical. Nanoparticle sizes are quoted as the mean diameter ± the standard deviation.

X-Ray Photoelectron Spectra (XPS) measurements were performed with a Phoibos 150 analyzer (SPECS GmbH, Berlin, Germany) in ultra-high vacuum conditions (base pressure $5E^{-10}$ mbar) with a monochromatic aluminium Kalpha X-Ray source (1486.74 eV). The energy resolution was measured by the FWHM of the Ag $3d^{5/2}$ peak for a sputtered silver foil was 0.62 eV.

Electrochemical measurements were performed using an Autolab (PGSTAT 302N) as potentiostat in a three-electrode configuration electrochemical cell. Glassy Carbon (GC) disk electrode coated with the catalyst material was used as working electrode (*S*

= 0.07 cm^{-2}), and a Pt wire and a $Hg/HgSO_4$ (K_2SO_4 sat.) were used as Counter (CE) and Reference electrodes (RE), respectively. GC disk electrode was carefully polished and ultrasonically rinsed for 10 min, both in ethanol and water. Both the CE and RE were rinsed with distilled water and dried with compressed air prior measurements.

Electrode Preparation: The modified GC electrode was prepared as follows: 2.5 mg of electrocatalyst was added into 100 μL of n-propanol, 2 μl of 5% Nafion and 398 μL of distilled water (Milli-Q). The mixture was ultra-sonicated for 10 min to obtain an ink. Then 5 μL of the ink were loaded onto the GC. The working electrode was then dried for 1h at r.t. All potentials were converted to NHE by adding a value of 0.645 V (reference value at 25°C). The current density was normalized over the geometric surface area of the electrode. The electrochemical studies for HER were conducted in 0.5 M H_2SO_4 (pH 0.3) solution and in 0.1 M phosphate buffer solution (pH 7) under argon, at 25°C and under continuous stirring.

Double-layer Capacitance (C_{DL}) and ElectroChemically active Surface Area (ECSA) determination. C_{DL} was estimated by CV. A non-Faradaic region was chosen from the LSV (typically a 0.1 V window about OCP), where no redox process takes place and all the measured current is due to double-layer charging. Based on this assumption, the charging current (i_c) can be calculated as the product of the electrochemical double-layer capacitance (C_{DL}) and the scan rate (v), as shown in Eq. 3:

$$i_c = vC_{DL} \qquad \text{Eq. 3}$$

Plotting i_c as a function of v yields a straight line with slope equal to C_{DL}. In this way, 8 different scan rates were used (5, 10, 25, 50, 75, 100, 250 and 500 mV/s), holding the working electrode at each potential vertex for 10 seconds prior to the next step. The ECSA was obtained by dividing the calculated capacitance by a tabulated value (Eq. 4, C_S = specific capacitance) that depends on the material used and solution (for C, in 1 M H_2SO_4 C_S=13-17 μF·cm^{-2}):

$$ECSA[cm^2] = \frac{C_{DL}}{C_S} \qquad \text{Eq. 4}$$

$$RF = \frac{ECSA}{S} \qquad \text{Eq. 5}$$

The Roughness Factor (RF) was calculated by dividing the ECSA by the geometrical surface area (S).

Copper UnderPotential Deposition (UPD). The UPD method was performed to determine the number of active sites. In an electrochemical cell, a controlled potential electrolysis was performed at 0.145 V vs. NHE for 100s in 0.5 M H_2SO_4 solution with 5 mM of $CuSO_4$. LSV were performed before and after the electrolysis in a free-copper solution (E_i = 0.04 V, E_f = 0.89 V, 10 mV/s). After the electrolysis, LSV exhibit a new wave devoted to the oxidation of deposited Cu at E = 0.41 V vs. NHE (Eq. 6). The number of active sites (n, Eq. 7) was calculated based on the UPD copper stripping charge (Q_{Cu}, Cu_{UPD}):

$$Cu_{\mathrm{UPD}} \rightarrow Cu^{2+} + 2\bar{e} \qquad \text{Eq. 6}$$

$$n = \frac{Q_{Cu}}{2F} \qquad \text{Eq. 7}$$

, where F is the Faraday constant (96485 C/mol).

TurnOver Frequency (TOF [s^{-1}]) was calculated as follows (Eq. 8):

$$TOF(s^{-1}) = \frac{I}{2Fn} = \frac{I}{Q_{Cu}} \qquad \text{Eq. 8}$$

, where *I* is the current intensity on the LSV measurement, F is the Faradaic constant, and *n* the number of active sites obtained by the UPD method. The factor 1/2 is based on the consideration that two electrons are required to form one hydrogen molecule from two protons ($2H^{+}+2\bar{e} \rightarrow H_2$).

3A.7 References

---

1 M. G. Walter, E. L. Warren, J. R. McKone, S. W. Boettcher, Q. Mi, E. A. Santori, N. S. Lewis, *Chem. Rev.* **2010**, *110*, 6446-6473.

2 S. Trasatti, *J. Electroanal. Chem. Interfacial Electrochem.* **1972**, *39*, 163-184.

3 C. C. McCrory, S. Jung, I. M. Ferrer, S. M. Chatman, J. C. Peters, T. F. Jaramillo, *J. Am. Chem. Soc.* **2015**, *137*, 4347-4357.

4 a) S. Fukuzumi, Y. Yamada, *J. Mater. Chem.* **2012**, *22*, 24284-24296; b) X. Li, X. Hao, A. Abudula, G. Guan, *J. Mater. Chem.* **2016**, *4*, 11973-12000; c) M. Zeng, Y. Li, *J. Mater. Chem. A*, **2015**, *3*, 14942-14962; d) M. Kuang, G. Zheng, *Small* **2016**, *12*, 5656-5675.

5 Z. Chen, J. Lu, Y. Ai, Y. Ji, T. Adschiri, L. Wan, *ACS Appl. Mater. Interfaces* **2016**, *8*, 35132-35137.

6 X. Kong, K. Xu, C. Zhang, J. Dai, S. Norooz Oliaee, L. Li, X. Zeng, C. Wu, Z. Peng, *ACS Catal.* **2016**, *6*, 1487-1492.

7 a) J. Mahmood, F. Li, S. M. Jung, M. S. Okyay, I. Ahmad, S. J. Kim, N. Park, H. Y. Jeong, J. B. Baek, *Nat. Nanotechnol.* **2017**, *12*, 441-446; b) Y. Zheng, Y. Jiao, Y. Zhu, L. H. Li, Y. Han, Y. Chen, M. Jaroniec, S. Z. Qiao, *J. Am. Chem. Soc.* **2016**, *138*, 16174-16181.

8 S. Liu, X. Mu, H. Duan, C. Chen, H. Zhang, *Eur. J. Inorg. Chem.* **2017**, 535-539.

9 a) K. P. in *Organometallic Ruthenium Nanoparticles and Catalysis*, P. Lignier, B. Chaudret, in *Ruthenium in catalysis* **2014**, C. Bruneau and P.H. Dixneuf (Eds), Wiley VCH, Weinheim, **2014**, *Top. Organomet. Chem.* **2014**, *48*, 319-370; b) C. Amiens, B. Chaudret, D. Ciuculescu-Pradines, V. Collière, K. Fajerwerg, P. Fau, M. Kahn, A. Maisonnat, K. Soulantica, K. Philippot, *New J. Chem.* **2013**, *37*, 3374-3401.

10 K. Pelzer, K. Philippot, B. Chaudret, W. Meyer-Zaika, G. Schmid, *Z. Anorg. Allg. Chem.* **2003**, *629*, 1217-1222.

11 K. Pelzer, O. Vidoni, K. Philippot, B. Chaudret, V. Colliere, *Adv. Funct. Mater.* **2003**, *13*, 118-126.

12 M. A. Ernst, W. G. Sloof, *Surf. Interface Anal.* **2008**, *40*, 334-337.

13 Y. Gorlin, T. F. Jaramillo, *J. Am. Chem. Soci.* **2010**, *132*, 13612-13614.

14 T. Shinagawa, A. T. Garcia-Esparza, K. Takanabe, *Sci. Rep.* **2015**, *5*, 13801-13821.

15 H. C. Chen, D. G. H. Hetterscheid, R. M. Williams, J. I. van der Vlugt, J. N. H. Reek, A. M. Brouwer, *Energy Environ. Sci.* **2015**, *8*, 975-982.

16 a) C. Fan, D. L. Piron, A. Sleb, P. Paradis, *J. Electrochem. Soc.* **1994**, *141*, 382-387; b) E. Navarro-Flores, Z. Chong, S. Omanovic, *J. Mol. Catal. A: Chem.* **2005**, *226*, 179-197; c) I. A. Raj, K. I. Vasu, *J. Appl. Electrochem.* **1992**, *22*, 471-477; d) C. Fan, D. L. Piron, P. Paradis, *Electrochim. Acta* **1994**, *39*, 2715-2722; e) I. A. Raj, K. I. Vasu, *J. Appl. Electrochem.* **1990**, *20*, 32-38.

17 S. Jung, C. C. L. McCrory, I. M. Ferrer, J. C. Peters, T. F. Jaramillo, *J. Mater. Chem. A* **2016**, *4*, 3068-3076.

18 C. L. Green, A. Kucernak, *J. Phys. Chem. B* **2002**, *106*, 1036-1047.

3B. Pyridine-Stabilized RuNPs: Synthesis, Characterization & HER Studies

3B.1 Introduction

As described in Chapter 1, the organometallic approach is a powerful method for obtaining small NPs with a narrow size distribution and a great surface control.[1] Apart from the metal precursor, the stabilizing agent (STAG) and the reaction conditions can influence the main characteristics of the obtained particles. By this way it is feasible to modify the NPs' properties by playing with ligands and/or reaction conditions in order to determine their effect on catalytic performance, and later on make correlations between NPs' structure and their catalytic activity.[2]

From literature data,[3] it is known that pyridine-based ligands have effective interaction with Ru in molecular complexes which allows assists NPs to reach high metal oxidation states through proton-coupled electron transfer (PCET) and prevents decomposition or degradation. Additionally, N-doped graphitic systems have shown to well stabilize Ru-based NPs, leading to some of the most active and rugged hydrogen evolution catalysts (HECs) in the literature.[4] Moreover, previous studies in the group allowed to provide RuNPs of ca. 1.3-nm in size and stabilized by 4-(4phenylpropyl)pyridine as the stabilizing ligand.[5] Deep NMR studies allowed elucidating the coordination mode of the ligand at the Ru surface and evidenced that the metallic particles are stabilized thanks to π-interactions with both aromatic groups (phenyl and pyridine). These results encouraged us to test other pyridine-based ligands for the synthesis of RuNPs with the aim to reach small, homogeneous-in-size and stable NPs.

More precisely, our main goal was to synthesize RuNPs with different characteristics, and to study how these changes interfere on the electrocatalytic performance of the particles when used as HECs and WOCs. For this purpose, two ligands were chosen, namely 4-phenylpyridine (**PP**) and 4'-(4-methylphenyl)-2,2':6',2"-terpyridine (**MPT**) (Figure 1). Using these two ligands as stabilizers, we could prepare new RuNPs and evaluate their interest as Ru metal-based catalysts for HER. Then we have tested different oxidation conditions to get a controlled oxidation of the RuNPs into RuO_2 ones for their evaluation in both HER[6] and OER[7] studies.

In the next parts, the synthesis and the characterization of RuNPs using the **MPT** and **PP** ligands will thus be described. The different essays performed in order to obtain RuO_2 NPs will be also described. Finally, preliminary tests on the HE catalysis will conclude the chapter, comparing the catalytic performances with those of other RuNPs stabilized with different molecules.

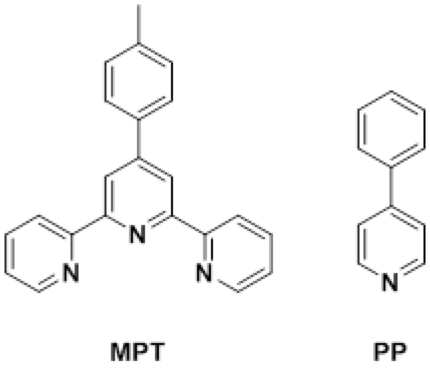

Figure 1. Ligands used as stabilizers in the synthesis of RuNPs: 4-phenylpyridine (**PP**) and 4’-(4-methylphenyl)-2,2’:6’,2”-terpyridine (**MPT**).

3B.2 Synthesis & characterization of RuNPs stabilized with pyridine-based ligands

The synthesis of the nanoparticles (NPs) was performed as previously described in Chapter 1 and 3A, using the same metal precursor, namely [Ru(cod)(cot)] (cod = 1,5-cyclooctadiene; cot = 1,3,5-cyclooctatriene) complex.[1] The decomposition of a THF-solution of [Ru(cod)(cot)] was achieved by reacting it with 3 bar H_2 overnight at room temperature (r.t., Scheme 1) in the presence of the chosen ligand among 4-phenylpyridine (**PP**) and 4’-(4-methylphenyl)-2,2’:6’,2”-terpyridine (**MPT**) (Figure 1). By this way, the initial yellow complex solution turned to a black colloidal suspension. After removing the excess H_2 and reducing the solution volume under vacuum, the formed RuNPs have been isolated by precipitation through addition of cold pentane followed by a filtration step.

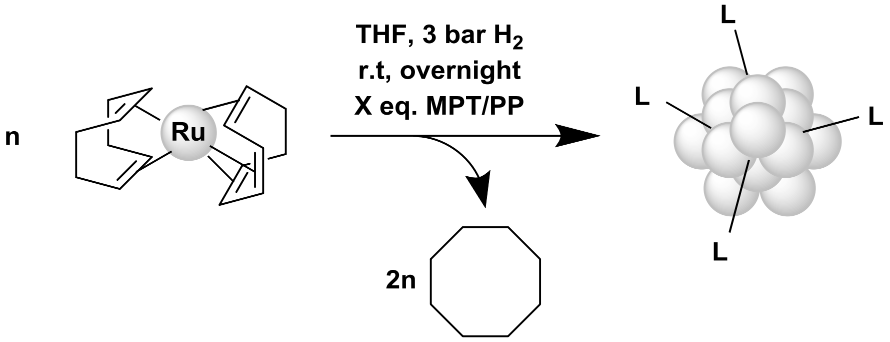

Scheme 1. Synthesis of RuNPs with X molar equivalents of **MPT**/**PP** ligands (L).

Three washings were then performed with pentane and under Ar in order to eliminate any rest of free ligand and get a purified black solid. The RuNPs could be obtained under the form of a solid after drying under vacuum. Those NPs, when directly exposed to air in solid-state, showed to burn spontaneously as a consequence of the accessible and highly reactive surface, as previously described with other RuNPs of similar sizes and stabilized with different ligands (see section 3B.2.6, method A).[1a] As the modification of the ligand-to-metal ratio (L/M) in the reaction medium can lead to a change on the particles' properties, e.g. mean size, shape, dispersion, solubility, stability, etc.,[8] we decided to apply different L/M ratios. The influence of this parameter on the characteristics of the particles was followed by transmission electron microscopy (TEM) analysis.

3B.2.1 TEM analysis

With the **MPT** ligand, different **MPT**/M ratios in the range 0.05 to 0.5 molar equivalent (equiv.) compared to the introduced Ru were then applied. Each synthesis was replicated for reproducibility issues. TEM analysis with grids prepared from both a crude colloidal solution and a re-dispersed sample after purification showed the same results. Thus, the latter were considered for comparison purpose, as summarized in Table 1. A small modification of the mean size and a strong change on the agglomeration were observed.

Table 1. TEM images of Ru-**MPT** NPs stabilized with different L/M ratios.

Ru-MPT (L/M ratio) Mean size (nm)	***TEM images***	***Observations***
Ru-0.05MPT 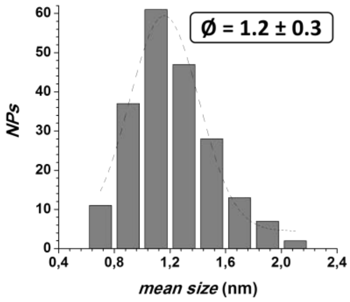 	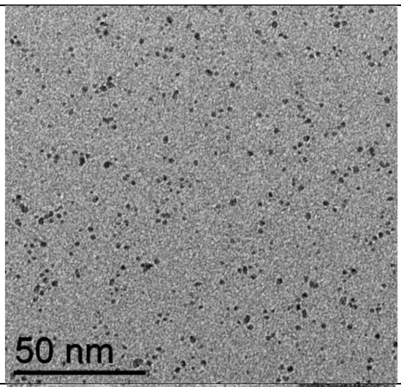 	Isolated and well-dispersed small NPs with a few agglomerated ones
Ru-0.1MPT 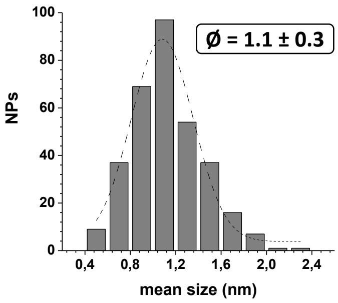 	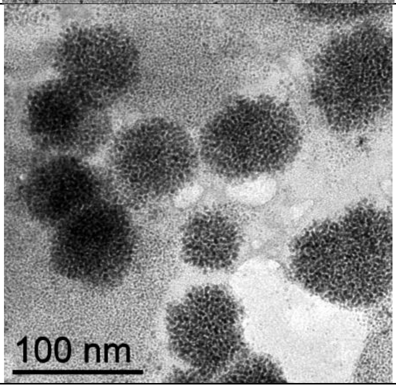 	Isolated small NPs with some aggregates made of individual small NPs

Ru-0.2MPT 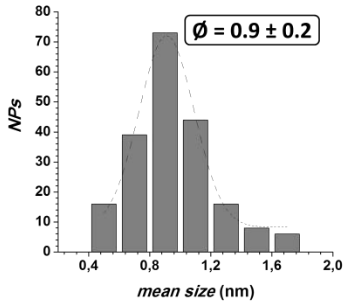 	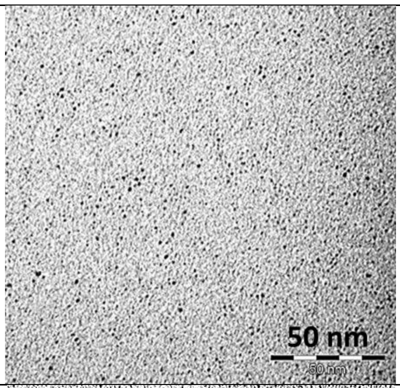 	Isolated and very small NPs with a few aggregates made of individual NPs (not shown here)
Ru-0.5MPT 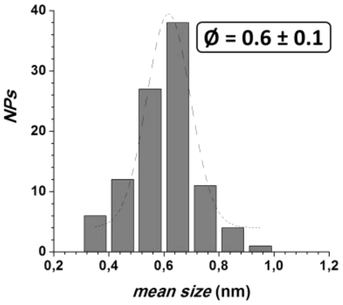 	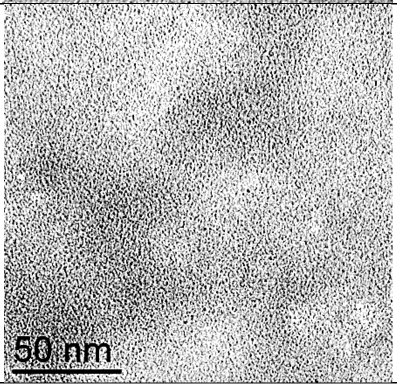 	Ultra small and NPs that are close to each other
Ru-1.0MPT	-	Formation of big agglomerates. No NPs observed

As can be observed on the TEM pictures, the application of high L/M ratios led to a decrease on the NPs' mean size, from ca. 1.2 nm in the case of 0.05 **MPT** equiv. to around 0.6 nm in the case of 0.5 equiv., very close to the limit of size measurement. Moreover, at high L/M ratios the particles appear more aggregated. A few concluding remarks can derive from these observations:

- ✓ First, even using a very low L/M ratio like 0.05, it allowed stabilizing small RuNPs of ca. 1.2 nm that are well dispersed. This result indicates that this ligand is very efficient in stabilizing RuNPs which can be explained by a strong coordination at the NP surface.
- ✓ Second, the use of higher L/M ratios than 0.05 led to a decrease in size of the NPs and even to the formation of ultra-small NPs of ca. 0.6 nm. This result shows that the quantity of **MPT** ligand present in the synthesis mixture has a strong influence on the growth of the NPs and the control of their size.
- ✓ Third, the agglomeration of NPs observed in the presence of an excess of ligand can be due to the aromaticity of the ligand. Indeed, one can expect **MPT** ligand to have π-like interactions with other capping ligand molecules surrounding other close NPs what can induce their agglomeration.
- ✓ Fourth, despite the agglomeration observed in the presence of high L/M ratio, the NPs remain individual. This indicates that the ligand capes well the particles

limiting their coalescence and keeping them separated to each other. This could be explained by an efficient stabilizing barrier around the NPs due to strong ligand interaction with the NP surface and/or surrounding ligands.

In contrast to these results, when utilizing the **PP** ligand, a different behavior has been observed. In that case, the L/M ratio has been changed in the range 0.1-1.0 equiv. (no 0.05 equiv. was tested since the particles dispersion was already good for higher L/M ratios). No substantial change neither on the particles' mean size nor on their agglomeration state has been observed whatever the quantity of ligand introduced for the synthesis of the particles (see table 2).

Table 2. TEM images of Ru-**PP** NPs stabilized with different L/M ratios.

<table>
<tr><th>Ru-PP (L/M ratio)
Mean size (nm)</th><th>TEM images</th><th>Observations</th></tr>
<tr><td>Ru-0.1PP
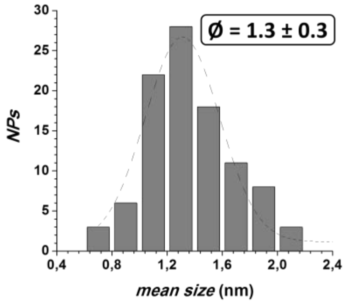 </td><td>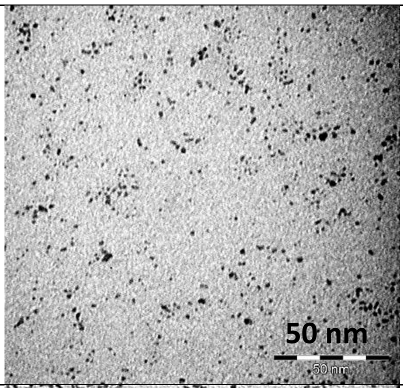 </td><td>Small and dispersed NPs, juxtaposed in packets of 2-3 in some cases</td></tr>
<tr><td>Ru-0.2PP
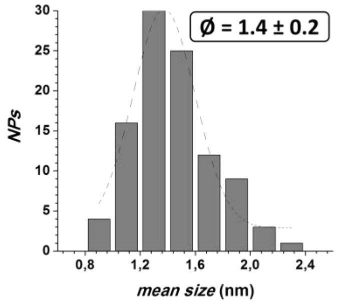 </td><td>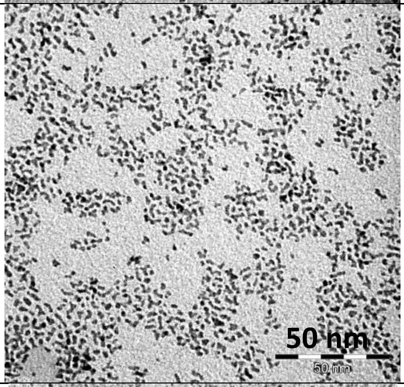 </td><td></td></tr>
<tr><td>Ru-0.5PP
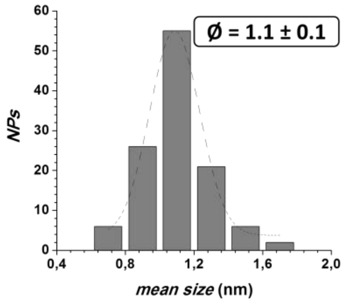 </td><td>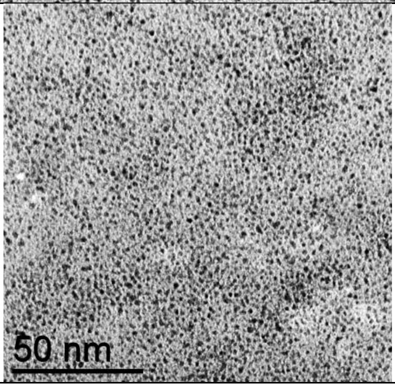 </td><td></td></tr>
</table>

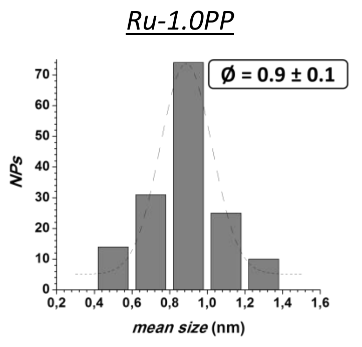

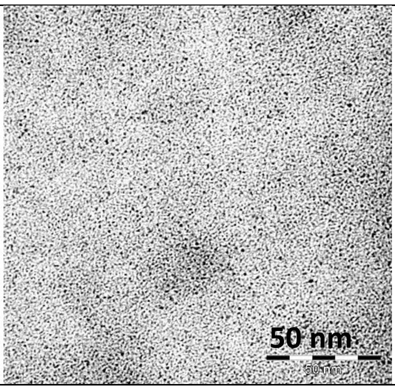

So, as can be noticed from the TEM images, small and well-dispersed RuNPs are formed in all cases. More precisely, mean sizes of ca. 1.3, 1.4, 1.1 and 0.9 have been measured for L/M ratios of 0.1, 0.2, 0.5 and 1.0, respectively. If focusing on the mean size values got for a L/M ratio between 0.1 and 0.5 for comparison purpose with the previous results obtained with the **MPT** ligand, it appears that higher **PP**/M ratios do not lead to a strong decrease on the NPs' mean size contrarily to what was observed with **MPT**. However, with the **PP** ligand, in all L/M ratios tested, the NPs are well-dispersed on the TEM grids and there are no big agglomerates of NPs, contrarily to the results with **MPT**. Only packets of 2-3 NPs close to each other are observed on some parts of the grids while agglomerates of individual NPs are formed when increasing the **MPT**/M ratio. These results indicate that the **PP** ligand is also very efficient in stabilizing RuNPs of small sizes. However the influence of the **PP** quantity on the control of the NPs' size seems more limited than in the case of **MPT** ligand. In addition, the **PP** ligand gives rise to a population of NPs that are very well-dispersed while they are more agglomerated with **MPT**.

The different stabilizing effects noticed between **MPT** and **PP** ligands can be due to different coordination mode / interaction strength or / and steric hindrance at the metal surface. We can expect that given its multi-pyridine structure, **MPT** ligand coordinates strongly to the surface of the NPs through σ-donation of pyridyl-N thus influencing the growth process. The **PP** ligand may interact differently and possibly more weakly, via a π-stacking mode involving the two rings, what does not change too much the NPs mean size regardless the L/M ratio. A similar trend was observed when studying the stabilization of Pd-NPs with pyrazole-derived ligands.[9] Moreover, the difference observed in terms of agglomeration, which is pronounced in the presence of a high concentration of **MPT** in contrast to **PP**, may be explained by the absence of strong interaction between capping ligands surrounding different NPs in the case of **PP**-stabilized NPs. This can support a different coordination mode of the ligands at NP surface.

From now on, the following studies will focus on **Ru-0.05MPT** and **Ru-0.2PP** samples, being the former the system that exhibited a better dispersion among all the **MPT**-stabilized samples. The second system has been chosen due to the good dispersion observed and reproducibility.

3B.2.2 ^{1}H-NMR studies with Ru-0.2PP NPs

NMR studies were carried out in order to shed some light on the coordination mode of the **PP** ligand at the surface of the RuNPs. **Ru-0.2PP** was chosen as system of study due to its higher activity in the electrocatalytic hydrogen evolution, as will be later on seen in section 3B.3. Furthermore, the study of **Ru-0.05MPT** sample is of interest to further understand the main differences on the ligand behavior between the two cases. Thus, the decomposition of the [Ru(cod)(cot)] in deuterated THF and in the presence of **PP** ligand (0.2 equiv.) and 3 bar H_2 (analogous to Scheme 1) has been followed by solution ^{1}H-NMR. Thus, an NMR tube was filled with a d^8-THF solution of [Ru(cod)(cot)] (10 mg in 0.7 mL) and PP ligand (1 mg; L/M ratio = 0.2) was added. ^{1}H-NMR spectrum of this mixture has been first recorded at 273 K without any H_2 in order to identify precisely the signals corresponding to the Ru precursor and the **PP** ligand and thus provide reference data (Figure 2). The low coordination of the cod-cot ligands of the Ru complex induces some mobility what explains the observation of the broadening of some signals.

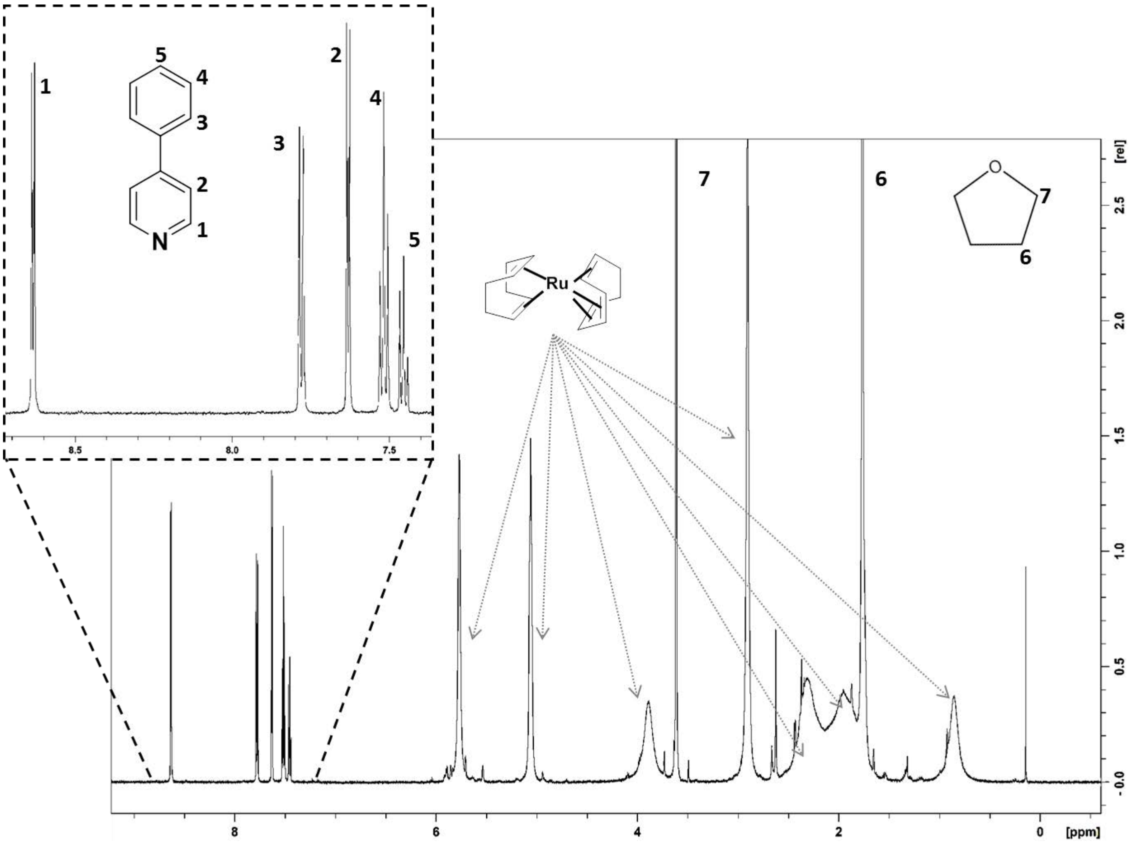

Figure 2. ^{1}H-NMR spectrum of the **PP**/[Ru(cod)(cot)] mixture in d^8-THF at 273 K before H_2 addition.

Further, the NMR tube has been pressurized with 3 bar of H_2, and the reaction mixture shacked to improve the dissolution of H_2 in the solution phase containing the Ru precursor and **PP** ligand. Figure 3 and Figure 4 report a series of ^{1}H-NMR spectra recorded at different reaction times. This allowed to follow the decomposition of the [Ru(cod)(cot)] precursor with time (Figure 3 B-E) until its total disappearance (Figure 3F, *t*=3 h).

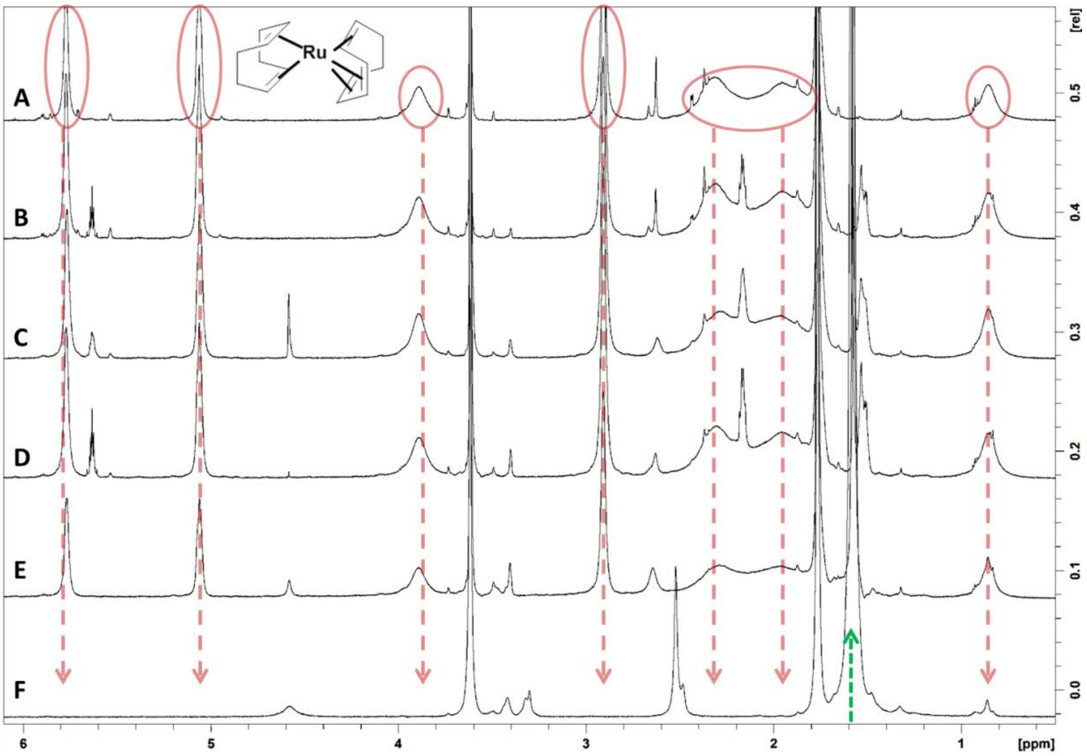

Figure 3. Aliphatic region of the NMR spectra recorded during the decomposition of [Ru(cod)(cot)] under H_2 in the presence of 0.2 equiv. of **PP** (d^8-THF; 273K) recorded at different reaction times: A) *t*=0, B) *t*=10 min, C) *t*=20 min, D) *t*=30 min E) *t*=60 min and F) *t*=3 h.

As can be observed, as soon as the signals corresponding to the cod and cot ligands from the Ru precursor started disappearing, a new signal emerged at 1.57 ppm that can be attributed to the formation of cyclooctane, as the result of the hydrogenation of cod and cot molecules. In parallel of this, a vanishing of the aromatic signals corresponding to the **PP** ligand was perceived (Figure 4). The signals attributed to the pyridyl group of the **PP** ligand were the first ones to disappear, followed by those of the phenyl group. Before their total disappearance, both the pyridyl and phenyl signals display a broadening which can be attributed to a Knight-shift effect, as the result of the proximity of the **PP** ligand to the NP surface. This derives from the local magnetic field created by the metallic atoms of Ru in the NPs formed. This evolved until a complete disappearance of the signals at the end of the reaction.

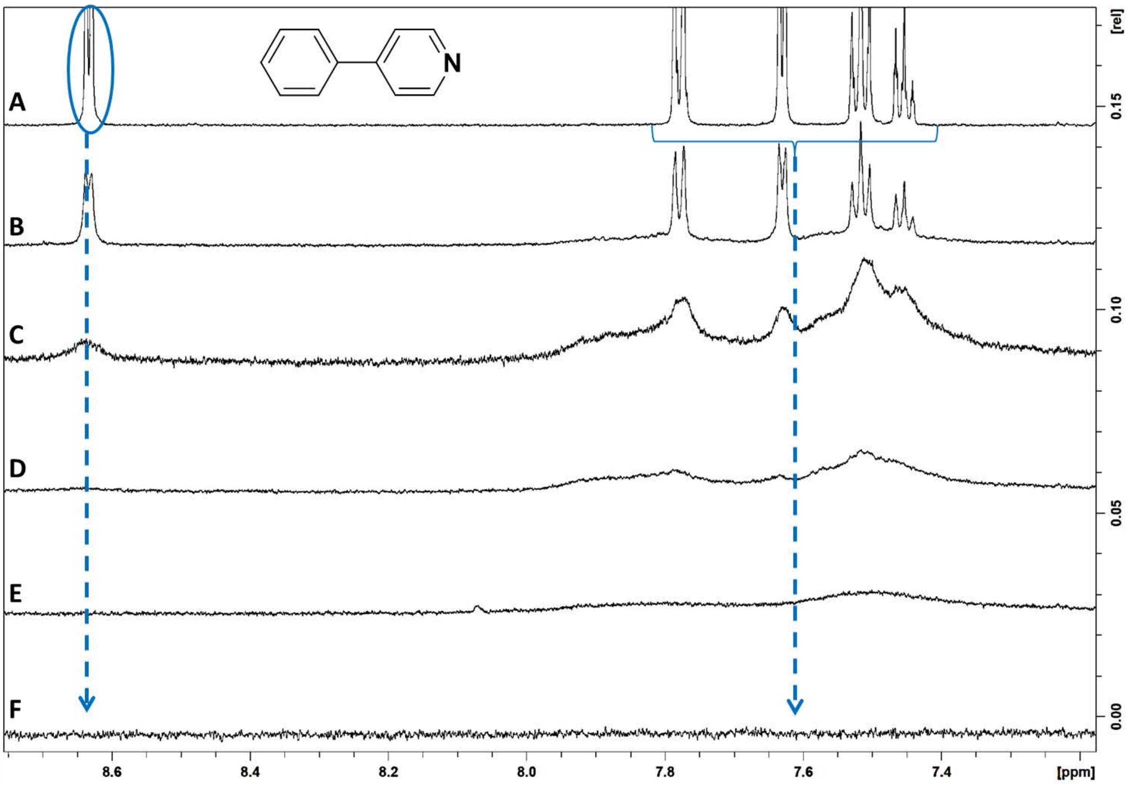

Figure 4. Aromatic region of the NMR spectra recorded during the decomposition of [Ru(cod)(cot)] under H_2 in the presence of 0.2 equiv. of **PP** (d^8-THF; 273K) recorded at different reaction times: A) *t*=0 , B) *t*=10 min, C) *t*=20 min, D) *t*=30 min E) *t*=60 min and F) *t*=3 h.

A similar phenomenon with the same order of disappearance of the signal groups (1st pyridyl, 2nd phenyl group signals) was previously observed when using 4-(4phenylpropyl)pyridine as stabilizing ligand for the synthesis of RuNPs and attributed to the initial coordination through the *N*-donor of the pyridyl group, followed by a π-stacking coordination by the two aromatic parts of the ligand.[5] The propyl chain contained in 4-(4phenylpropyl)pyridine allowing some degree of flexibility it can favor this type of stabilization in such small particles (1.3 nm). In the case of the **PP** ligand, although it is more rigid due to the absence of alkyl chain between the two aromatic parts, similar coordination properties at the NP surface can be expected. This seems to be confirmed by the ^{1}H-NMR results.

3B.2.3 Elemental composition

For the determination of the elemental composition of the **PP**-stabilized and **MPT**-stabilized RuNPs, two systems were selected, namely **Ru-0.2PP** and **Ru-0.05MPT**. This choice was governed by the fact that these samples display small, homogeneous and well-dispersed NPs as well as a very good synthetic reproducibility. Firstly, the purified **Ru-0.2PP** and **Ru-0.05MPT** samples were characterized by using elemental analysis (EA), inductively coupled plasma optical emission spectroscopy (ICP-OES) analysis and thermogravimetric analysis (TGA), in order to determine the final ligand-metal ratio in the purified NPs. The three analyses were replicated and for EA the average result was considered. ICP results exhibited a very low Ru content (ca. 20 wt%), in contrast to EA results where CHN analysis gave rise to only ca. 15-16 wt% of organics (leading thus by a calculation to 85-84 wt% of Ru). But it is important to note that a black residue attributed to undissolved Ru was always observed after the acidic digestion of the samples prior to ICP analysis. Such a phenomenon was already observed with other RuNPs from the group surrounded by an organic or inorganic matrix. Given the difficulties (in terms of values and reproducibility) met with the ICP data despite several measurements were performed in two different places, they were discarded, in favor of the elemental analysis results which were used to estimate the elemental composition of the RuNPs in compounds **Ru-0.2PP** and **Ru-0.05MPT**.

Besides the EA results (C,H,N contents), Table 3 contains estimated values (L/M, THF/M, H/M ratios and Ru content) further calculated on the basis of C,H,N results (see Experimental part for a typical calculation). Apart from the ligand used to stabilize the RuNPs, other coordinating molecules at the NP surface that can be expected are THF (used as synthesis solvent) and hydrides (due to the use of H_2 as decomposition gas). The amount of ligand (**PP** and **MPT**) was calculated based on the N wt.%. This was possible given the ligands are the only source of nitrogen in the reaction mixture for the NPs synthesis. Further, the corresponding C% and H% from the ligand were subtracted from the C and H contents determined by EA data. The remaining C wt.% was used to calculate the amount of THF present on the particles' surface (THF/M ratio), being the only remaining source of carbon present in solution (besides the ligand and the non-coordinating and volatile cyclooctane which was eliminated under vacuum). The remaining H wt.% was attributed to hydrides coordinated on the Ru atoms.

Table 3. C, H, N elemental analysis results obtained for **Ru-0.05MPT** and **Ru-0.2PP** samples. Ligand, THF and hydride ratios against metal, obtained from EA results.

	EA results				**Calculations performed**				
Sample	***N (%)***	***C (%)***	***H (%)***	***Total of CHN (%)***	***L/M***	***THF/M***	***H/M***	***Total of organics***	***M***
Ru-0.05MPT	1.72	13.69	1.26	16.66	0.06	0.09	0.11	17.62	82.37
Ru-0.2PP	1.16	12.49	1.28	14.93	0.11	0.04	0.38	15.45	84.55

The calculated ratios (L/M, THF/M, H/M) were divided by the Ru wt.% (M in Table 3) derived from the EA. As can be observed, for **Ru-0.05MPT,** the value L/M (0.06 molar eq.) calculated from the EA analysis results is very close to the L/M ratio (0.05 molar eq.) introduced for the synthesis of the particles . However, in the case of **Ru-0.2PP**, a much lower value is estimated from the EA (0.1 molar eq.) than the one utilized (0.2 molar eq.) for the synthesis. This difference can be explained by the fact that there is a low influence of the L/M ratio on the NPs characteristics, as previously noticed from the TEM analysis where the L/M ratio was observed to have a slight effect on the size of the particles. Given the small size of the NPs and the potential coordination of the **PP** ligand at the metal surface by interaction of the two aromatic rings and the consequent sterical hindrance, we can expect to have the coordination of a maximum quantity of ligand at the NP surface. This quantity could be close to the value of 0.1 molar eq. here determined. Such a low influence of the L/M ratio on the NPs characteristics was previously observed in the group using other ligands.[10]

TGA of **Ru-0.2PP** and **Ru-0.05MPT** samples was performed under N_2 flow, to avoid the oxidation of the particles during the thermal treatment, together with that of **PP** and **MPT** ligands for comparison purpose. The free ligands show a complete weight loss starting at ca. 180 and reaching the minimum at 200 and 350 °C for **PP** and **MPT** ligands, respectively. Concerning the analysis of the NPs, the continuous decrease from 50-150 °C is attributed to the presence of solvent in the sample, namely coordinated THF. Later on, in the 180-350 °C range, a total weight loss of around 18% and 15% has been observed for **Ru-0.05MPT** and **Ru-0.2PP**, respectively, which can be attributed to elimination of the organic part of the samples. The remaining mass percentage can thus be attributed to the Ru content, leading to 82% and 85% for **Ru-0.05MPT** and **Ru-0.2PP**, respectively.

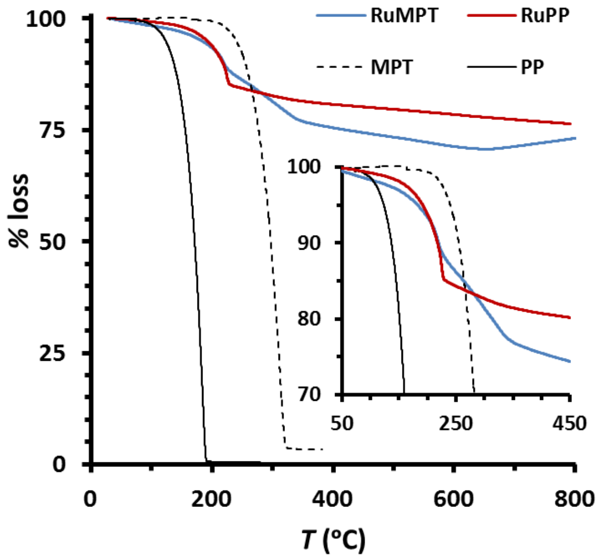

Figure 5. TG analysis of samples **Ru-0.05MPT** (blue) and **Ru-0.2PP** (red), and ligands **MPT** (dashed) and **PP** (bold).

In Table 4, Ru contents determined from TGA and EA analyses are compared for the two **Ru-0.2PP** and **Ru-0.05MPT** samples. Estimated values that correspond to the quantities of Ru precursor and ligand introduced for the synthesis of the particles (by approximating that all [Ru(cod)(cot)] and ligand completely reacted to form NPs), are also given for comparison purpose. As seen in Table 4, for **Ru-0.05MPT** estimated results and EA/TGA data are less different, than in the case of **Ru-0.2PP**: this could derive from the fact that not all the ligand introduced for the synthesis of the particles is coordinated to the NPs, and so the real Ru wt.% is higher than the estimated one, being this in harmony with the L/M ratios calculated from EA results in Table 3.

Table 4. Ru wt.% according to the synthetic conditions (Estimated) and to the EA and TGA results.

	Ru wt.%		
Sample	***Estimated***	***EA***	***TGA***
Ru-0.05MPT	86.19	82.37	82
Ru-0.2PP	76.46	84.55	85

3B.2.4 Surface reactivity studies

In order to get information on the surface state of the RuNPs, a few reactivity studies have been carried out, namely the coordination of CO molecules, the titration of surface hydrides and oxidation reactions.

Study of CO coordination at Ru NP surface

Due to its facile coordination on metal surfaces, CO can be used as a probe-molecule to study the surface state of metal NPs. This has been widely applied in the team with RuNPs by taking profit of the access to Fourier-transform infrared spectroscopy (FTIR / IR) and NMR techniques that Ru metal allows, in order to investigate the coordination of CO and get information on the coordination and mobility of stabilizing ligands or hydrides.[11]

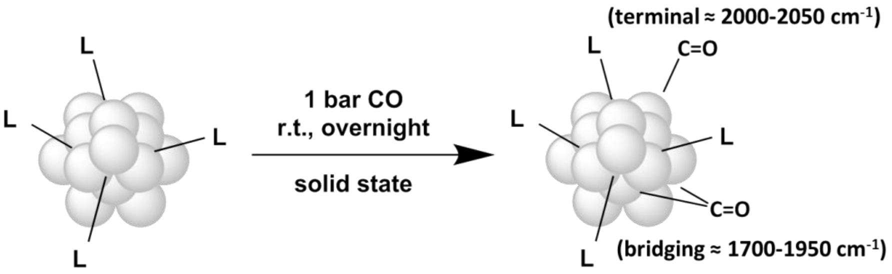

Scheme 2. Conditions for the reaction of CO at Ru nanoparticles' surface.

The coordination of CO at the surface of **Ru-0.05MPT** (1.2 ± 0.3 nm) and **Ru-0.2PP** (1.4 ± 0.2 nm) NPs was thus studied by FTIR spectroscopy. The powders obtained after the purification step of the NPs were exposed to 1 bar of CO overnight under stirring and at room temperature (Scheme 2). After this reaction time, KBr pellets were prepared with the RuNPs powders and IR spectra recorded, both inside the glovebox. The spectra before reaction with CO were also recorded in controlled atmosphere conditions together with those of the free **MPT** and **PP** ligands, for comparison purpose (Figure 6).

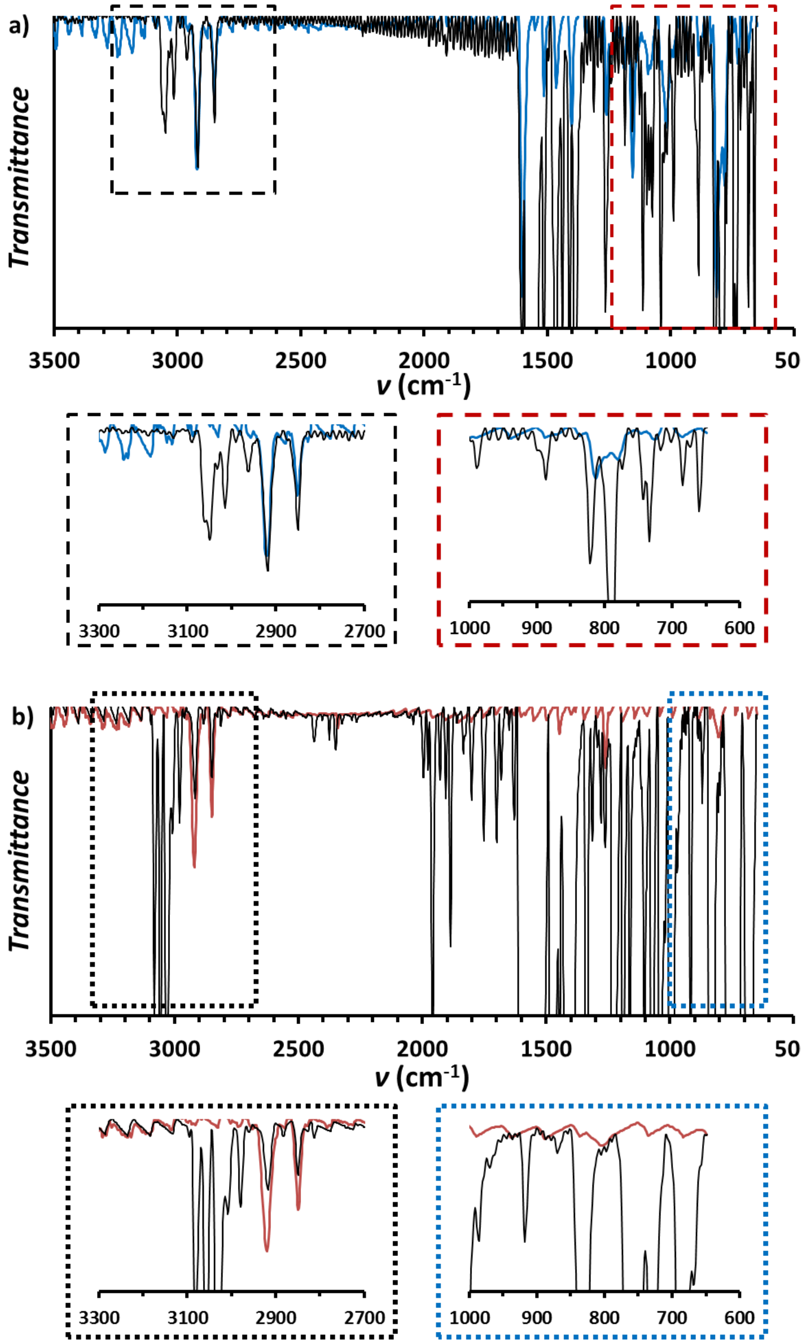

Figure 6. IR data of **MPT** ligand vs. **Ru-0.05MPT** NPs (top), and **PP** ligand vs. **Ru-0.2PP** NPs (bottom), and insets of the C-H stretching region (middle).The spectra corresponding to the NPs are in color.

As can be seen in Figure 6, FTIR data of the free organic ligands (**MPT** and **PP**) reveal two bands in the 2700-3000 cm^{-1} region. Those are typical from C-H stretching modes in alkane groups that might come from organic solvent (e.g. pentane) pollution present in the KBr, inside the glove-box or in the spectrometer. In addition, the other regions of the spectra are also contaminated, making difficult to attribute other aromatic signals from the ligand skeleton. The IR spectra of the NPs (**Ru-0.05MPT** and **Ru-0.2PP**), show the absence of vibration bands in the 3000-3300 cm^{-1} region, that are typical from aromatic C-H stretching vibrations, as well as the absence of C=C bands at 650-750 cm^{-1}. This loss of the aromatic signals could be attributed to a partial hydrogenation of the stabilizing ligands during the NP synthesis, given the known activity of RuNPs in catalyzing aromatic hydrogenation.[12] However, another reason could be the coordination of the ligand at the metal surface through π-stacking. Indeed, such a coordination of the ligand would induce a great proximity of all the aromatic protons to the metallic core, thus hindering the stretching vibrations or hiding the corresponding signals.

From previous works in the team, it is known that two types of signals corresponding to different Ru-CO coordination modes at the surface of the NP scan be observed: on one side, terminal CO at frequencies of 2000-2050 cm^{-1}, can be attributed to CO coordinated at particles' edges and apexes; on the other side, bridging CO between two or more metal atoms, at 1750-1950 cm^{-1}, is expected to coordinate on particles' faces.[13] These published data were taken as references to analyze the coordination of CO on the **Ru-0.05MPT** and **Ru-0.2PP** NPs' surface.

The FTIR spectra recorded after the reaction of the nanoparticles with 1 bar of CO overnight at room temperature, show in both cases (**Ru-0.05MPT** and **Ru-0.2PP**) new signals in the 1900-2400 cm^{-1} range (Figure 7a and b). A broad and intense signal at *ca.* 1950 cm^{-1} is particularly visible for **Ru-0.05MPT**. Such a signal has previously been reported as corresponding to CO coordination by the bridging mode on the faces of RuNPs. The sharpest signal visible at *ca.* 2040 cm^{-1} can be attributed to terminal CO coordinated onto edges and apexes. Finally there is a very small and sharp signal at ca. 2340 cm^{-1} which can be attributed to the coordination of CO_2.

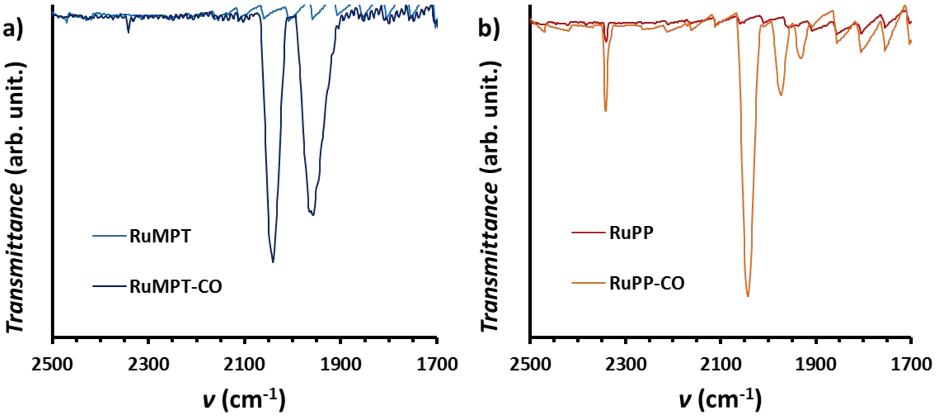

Figure 7. FTIR analysis of a) **Ru-0.05MPT** and b) **Ru-0.2PP** NPs before and after exposure to 1 bar CO overnight at room temperature.

In the case of **Ru-0.05MPT** system, the two CO signals detected at ca. 1950 and 2040 cm^{-1} have similar intensities. This may indicate that a similar quantity of free Ru sites are available on the NPs surface on apexes/edges and faces for coordinating CO and consequently, that **MPT** ligand occupies in a similar manner all the surface sites apexes/edges and faces. However, in the case of **Ru-0.2PP** system, the signal at ca. 1950 cm^{-1} is splitted into two smaller peaks at 1930 and 1975 cm^{-1}, both of them much less intensive than the terminal CO one. The presence of these two signals is attributed to two different bridging coordination modes, namely with three Ru atoms (at lower frequencies) or two Ru atoms, as previously reported by B. Chaudret *et al.*[14] The lower intensity of these two signals indicates that probably less faces are free on the surface of the particles to allow the coordination of CO in the bridging mode. From this we can deduce that the **PP** ligand probably occupies more efficiently the faces than the edges/apexes sites than **MPT** does. This can be explained by the smaller size of **PP** ligand compared to **MPT**, and its steric hindrance owing its rigidity. Other hypotheses could be the smaller size of the **Ru-0.05MPT** NPs where faces are probably slightly less developed and also the lower quantity of **MPT** ligand on the NP surface in contrast to **PP** one (L/M = 0.06 vs. 0.1 eq., respectively). Thus, the **PP** ligand may enable a more successful coverage of the particles' faces, as evidenced by the lower detection of bridging CO.

Study of the Oxidation state of RuNPs

Wide-Angle X-Ray Scattering (WAXS) technique was employed to determine the crystalline structure and the oxidation state of the metal in each **Ru-0.05MPT** and **Ru-0.2PP** samples. For this purpose 1 µm glass capillaries were filled with powders of NPs under argon atmosphere and sealed to avoid air entrance. The pattern observed for a purified sample of **Ru-0.05MPT** kept under argon atmosphere (Figure 8a), corresponds to hcp-metallic ruthenium. The peak detected at θ ≈ 4° can be explained by the presence of a few agglomerated NPs. The radial distribution function (RDF) is not regular and reflects a large size distribution. The maximum coherence length, that in fact corresponds to the longest Ru-Ru distances and consequently indicates the biggest crystalline domains, can be estimated to ca. 4.2 nm (Figure 8c, red). This value is quite different from the mean size determined by TEM analysis (1.2 ± 0.3 nm).

For the **Ru-0.2PP** system, hcp-metallic NPs were also observed (Figure 8b). In this case the RDF shows a coherence length of ca. 2.3 nm (Figure 8c). This size of crystalline domains is also larger than the mean size determined by TEM analysis, but less than for **Ru-0.05MPT** NPs. We can thus also estimate that a few larger NPs are present. Indeed, coherence length is a direct measurement of the maximum size of crystalline domains, and in case of size dispersion, the weight of larger NPs is quite high. Moreover the monotonous decrease profile of the distribution of distances (Figure 8b) is consistent with smaller sizes. These results indeed indicate a limited coalescence of small metallic NPs in the sample, it is however delicate to accurately evaluate the coalescence ratio of NPs without assumptions on their final shape.

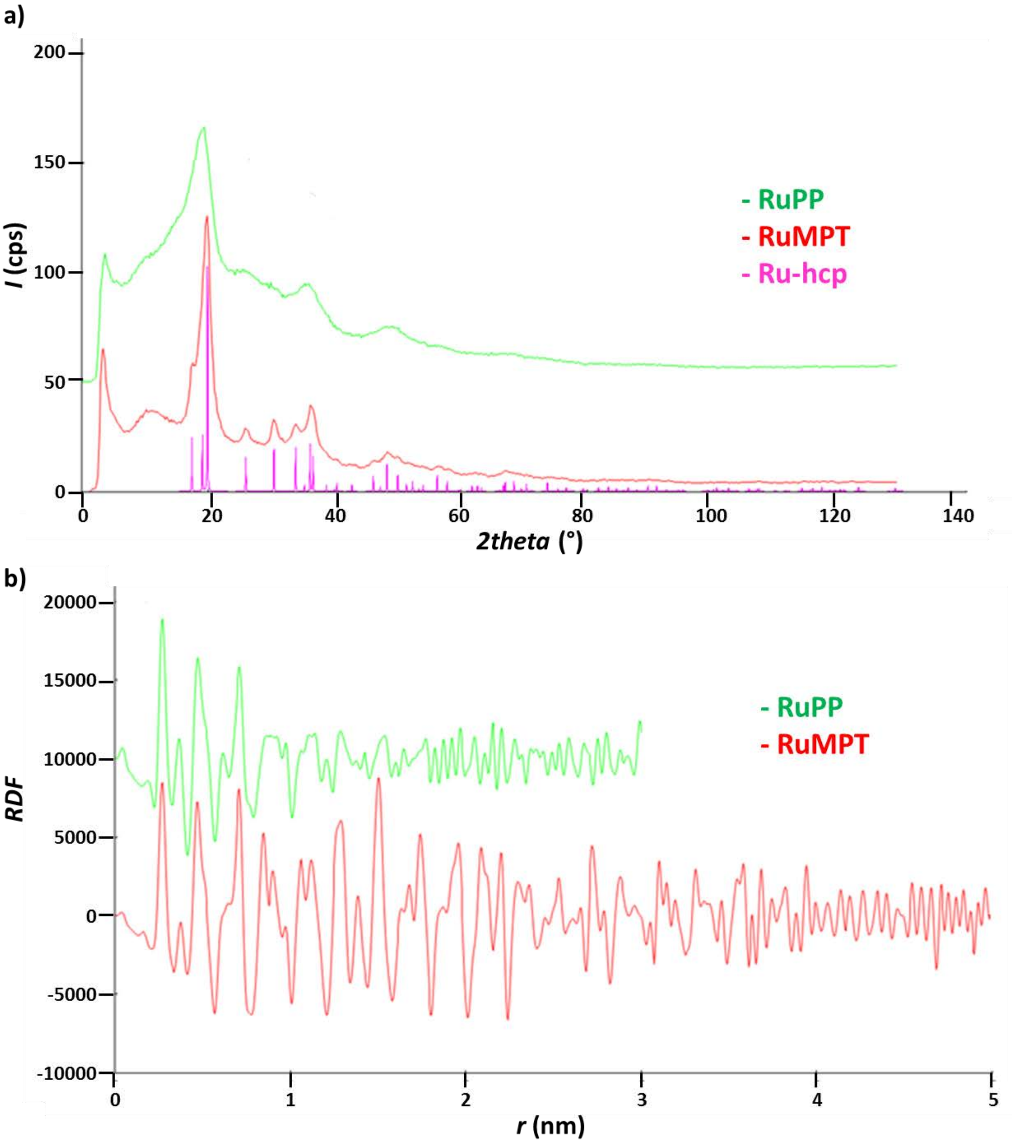

Figure 8. WAXS analysis with comparison with hcp Ru phase diagram of a) **Ru-0.2PP** and b) **Ru-0.05MPT** samples.and c) RDF (radial distribution frequency).

For the **Ru-0.2PP** system, hcp-metallic NPs were also observed (Figure 8b). In this case the RDF shows a coherence length of ca. 2.3 nm (Figure 8c). This size of crystalline domains is also larger than the mean size determined by TEM analysis, but less than for **Ru-0.05MPT** NPs. We can thus also estimate that a few larger NPs are present. Indeed, coherence length is a direct measurement of the maximum size of crystalline domains, and in case of size dispersion, the weight of larger NPs is quite high. Moreover the monotonous decrease profile of the distribution of distances (Figure 8b) is consistent with smaller sizes. These results indeed indicate a limited coalescence of small metallic NPs in the sample, it is however delicate to accurately evaluate the coalescence ratio of NPs without assumptions on their final shape.

Surface hydrides' titration

Due to the reaction conditions applied for the synthesis of the nanoparticles, namely the use of hydrogen gas to decompose the Ru precursor, the presence of hydrides at the nanoparticle surface can be expected (as estimated in the previous section 3B.2.3), in particular for Ru species since Ru is well-known to interact with hydrides. This has been demonstrated previously in the group for several systems of RuNPs using a simple titration method. This method is based on the hydrogenation of a simple olefin (norbornene) using a degassed colloidal solution of freshly prepared NPs without adding any extra hydrogen (Scheme 3). The hydrogenation of the olefin can take place only thanks to the hydrides present at the metal surface. The conversion of the olefin into corresponding alkane is followed by gas chromatography analysis which allows determining the necessary quantity of hydrogen atoms and subsequently the quantity of hydrides per metal surface atom.[15]

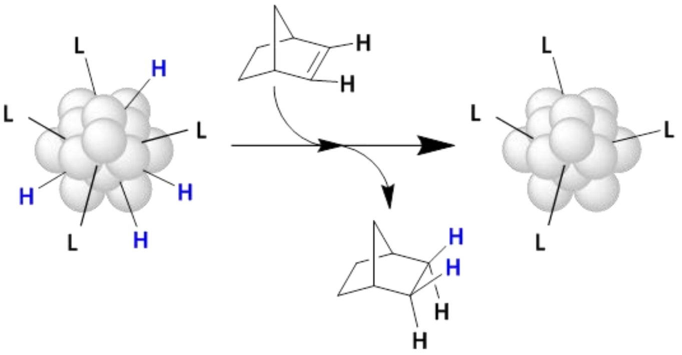

Scheme 3. Reaction scheme for the norbornene titration for hydride quantification.

This catalytic test was performed only with **Ru-0.2PP** sample. A freshly prepared crude colloidal suspension of **Ru-0.2PP** NPs was bubbled with argon several times to ensure complete removal of dissolved hydrogen. Then, 5 molar eq. of norbornene per Ru atom (90 mg, 1 mmol) were added to the reaction mixture, which was left at room temperature under vigorous stirring. After three days of reaction, an aliquot was taken for gas chromatography analysis in order to quantify the conversion of norbornene into norbornane. The conversion was estimated to be 6.4% which corresponds to 0.06 mmol of norbornane formed. This conversion leads to 0.12 mmol of hydrides titrated.

The quantity of Ru is based on the quantity of [Ru(cod)(cot)] complex introduced for the RuNPs synthesis and assuming a complete decomposition (Eq. 1). The total number of Ru atoms per NP (N_T) has been calculated from the NP mean size (Eq. 2):

$$60mg\text{"Ru"}\text{x}\frac{1mmolRu}{315.4mg} = 0.190mmolRu \qquad \text{Eq. 1}$$

$$N_T = \frac{dxN_AxV}{MW} = \frac{12.45x10^6x6.022x10^{23}x1.767x10^{-27}}{101.07} = 131\ atoms \qquad \text{Eq. 2}$$

Where *d* is the density of a Ru-atom (12.45 g·cm^{-3}) and *V* the volume ($V = (4/3)\pi R^2$, R=radius=(Ø/2)=(1.5/2) nm). The number of surface Ru atoms (N_S) has been calculated applying the rule of the magic number for close-shell clusters, which assumes that layers around a central atom are composed by [$10n^2+2$] atoms, being *n* the layer (*n* = 1, 2, 3, etc.) (see Table 5):

Table 5. Building of close-shell clusters following the rule of the magic number.

Shell (n)	***Atoms present in the core***	***Supplementary atoms in the shell (N_s) [$10n^2+2$]***	***Total number of atoms in the cluster (N_T)***	***% of Surface atoms (complete layers)***
1	1	12	13	92
2	13	42	55	76
3	55	92	147	62
4	147	162	309	52

Hence, for a NP of 131 Ru atoms, we can consider a total number of 55 atoms in the core (1+12+42) and thus 76 atoms in the upper layer (131-55) making it to be incomplete (76 out of 92). By this way around 58% of the Ru atoms are present at the NP surface. This corresponds thus to 0.110 mmol of Ru in the surface (total quantity of Ru square 0.58; 0.190*0.58 mmol). Given the conversion of norbornane determined by GC analysis, 0.12 mmol of hydrogen atoms are necessary which can be assumed to correspond to the quantity of hydrides present at the NP surface. By this way the number of hydride per surface Ru atom (Ru_{surf}) can be estimated to 1.1 H/Ru_{surf} (0.12/0.11). This value is very similar to previous results obtained in the group for other ligand-stabilized RuNPs,[15] such as 1.3 for Ru-PVP and Ru-HDA NPs or 1.1 for Ru-dppd nanoparticles.

This result clearly indicates that the surface of the **Ru-0.2PP** NPs is covered by hydrides. Considering the value of hydrides previously estimated from the EA data (section 3B.2.3), namely 0.38 H/Ru_{total}, and taking into account that only 58% of the atoms are on the surface we can calculate a H/Ru_{surf} ratio of 0.65 (0.38/0.58). This H/Ru_{surf} of 0.65 is almost the half of the titrated value (1.1 H/Ru_{surf}). This difference (which is quite important) can be explained by the fact that the titration test is performed using a crude colloidal solution, while EA on purified and prolonged drying under vacuum. We can thus consider that the loss of hydrides is reasonable although the quite important difference observed.

3B.2.5 Study on the fate of the ligand

RuNPs are known to be active catalysts for the hydrogenation of several molecules like simple olefins or arenes.[12] Taking into account that the synthesis of the particles is realized under hydrogen atmosphere (which makes the surface state of the particles cleaner due to hydrogenation of olefinic ligands from the precursor in cyclooctane), a legitim question about the fate of the ligand used as stabilizer arises: once the NPs are formed (which happens very rapidly as the [Ru(cod)(cot)] is quickly decomposed) in the presence of extra H_2, will the stabilizing ligand suffer any hydrogenation?

With the aim to get precise information on the nature of the ligand coordinated at the metal surface, experiments based on ligand exchange at the surface of pre-formed **Ru-0.2PP** NPs have been performed in order to identify the released molecules.

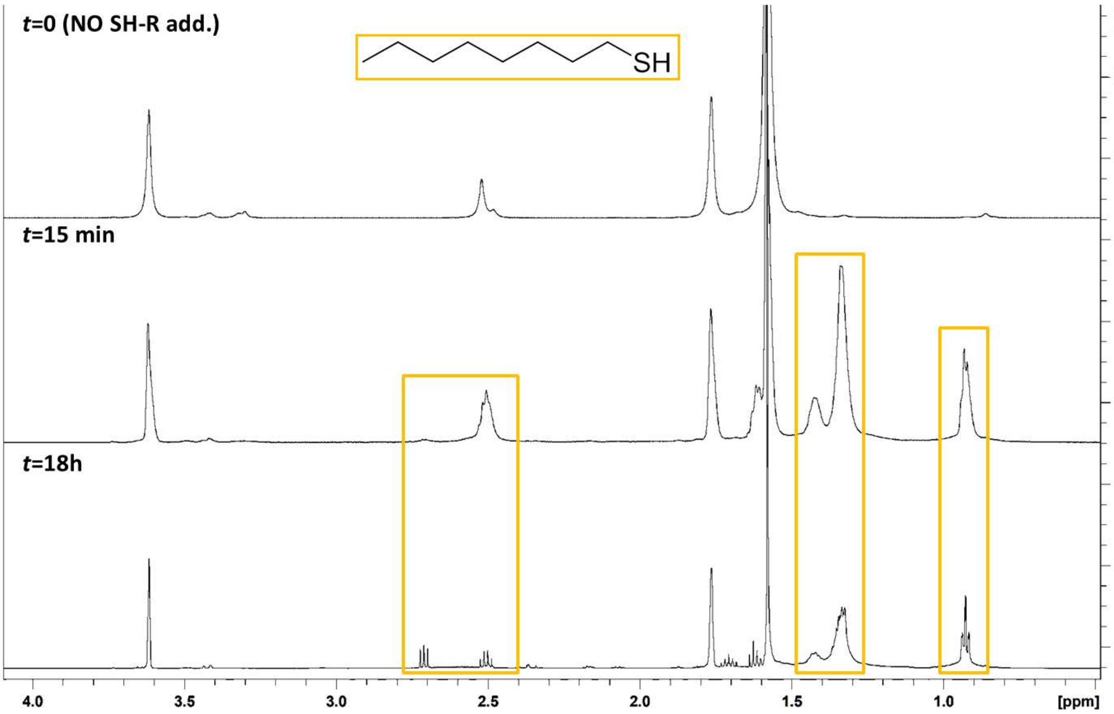

Figure 9. ^{1}H-NMR spectra (aliphatic region) in d^8-THF of the exchange experiment based on the addition of 1-octanethiol onto preformed **Ru-0.2PP** NPs at *t*=0 (before addition of thiol), *t*=15 min and *t*= 18 h.

For this purpose, ^{1}H-NMR studies have been carried out based on the addition of 1 molar equiv. of 1-octanethiol per Ru atom to a crude solution of pre-formed **Ru-0.2PP** NPs prepared into d^8-THF (Figure 9 and Figure 10). This high quantity of thiol was chosen in order to force the ligand exchange at Np surface. This process was inspired by previous results in the group where the benefit of the strong coordination of thiols at Ru surface was used to displace coordinated ligands.[5] The evolution of the reacting system has been followed by solution ^{1}H-NMR. Figure 9 shows a small decrease of the 1-octanethiol signals after 18h of reaction. It is important to note that there is a difference in terms of resolution between the spectra at *t*=15min and *t*=18h. This derives from the use of two different spectrometers: while in the first spectrum a 400 MHz NMR spectrometer was used, in the latter a 600 MHz was employed, to try to characterize the new appearing signals.

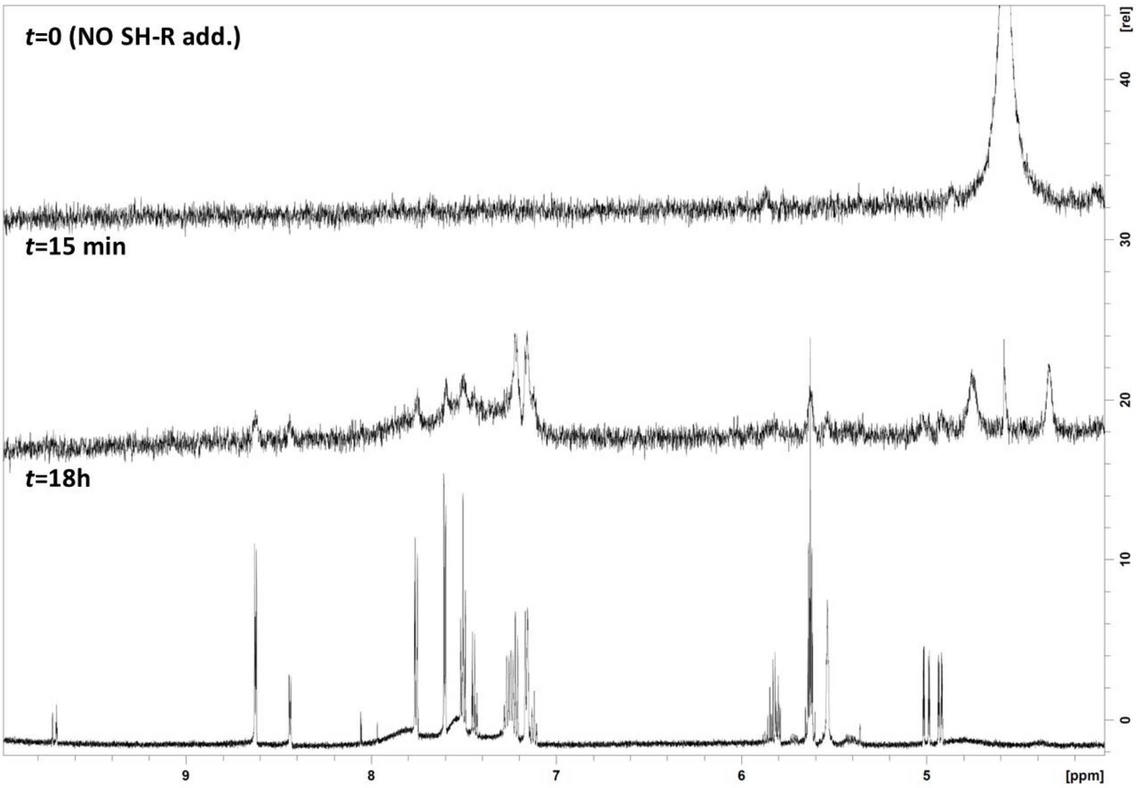

Figure 10. ^{1}H-NMR spectra (aromatic region) in d^8-THF of the exchange experiment based on the addition of 1-octanethiol onto preformed **Ru-0.2PP** NPs at *t*=0 (before addition of thiol), *t*=15 min and *t*= 18 h.

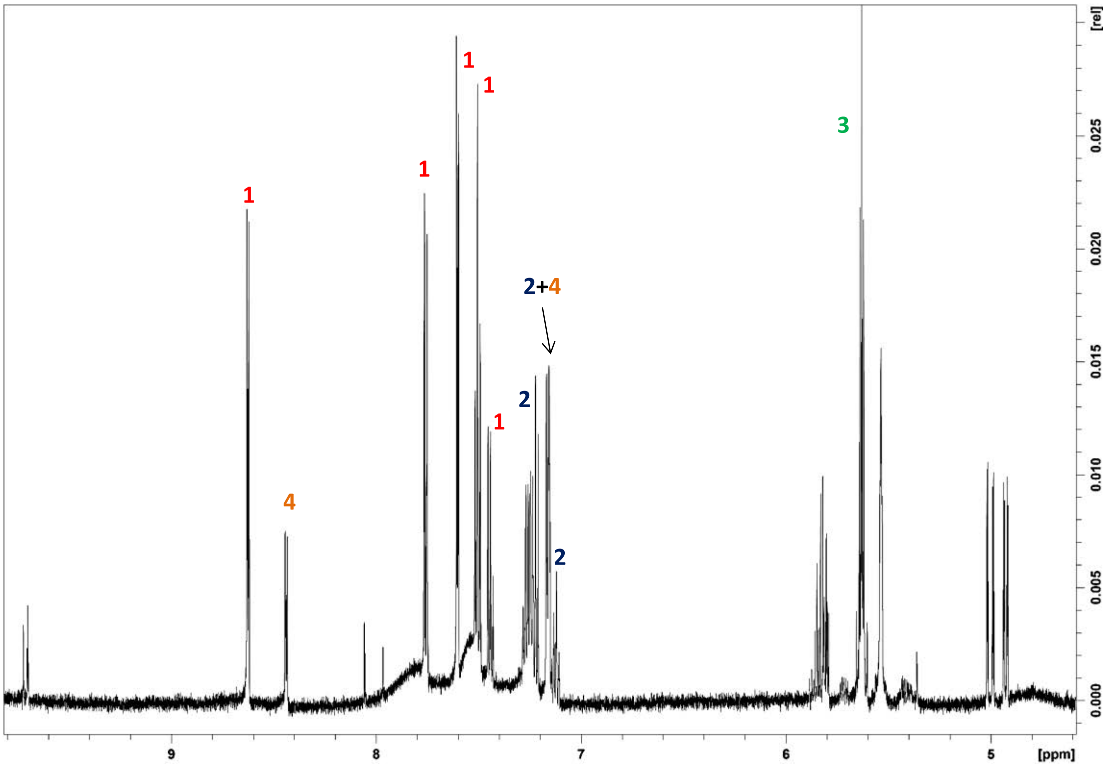

Figure 11. ^{1}H-NMR spectrum recorded after 18h of ligand exchange reaction and correlation to organic fragments as proposed in Figure 12.

In Figure 10, which shows a zoom of the aromatic part on the recorded ^{1}H-NMR spectra, it can be seen that 15 minutes after the thiol addition, signals are visible while it is not the case when measuring purified NPs in the absence of thiol (see Figure 10, *t*=0) as the result of the close proximity of the PP ligand with the metal surface. These aromatic signals can be attributed to **PP** ligand released in solution induced by the thiol coordination. However, not only the signals from the **PP** ligand are observed, but also other signals both in the aromatic and the alkyl parts of the spectra (Figure 11).

In order to identify more precisely which species have been released from the RuNPs' surface after coordination of the octanethiol, we tried to correlate the new signals observed with those of molecules that could result from the hydrogenation of the **PP** ligand but we were not able to attribute all the signals. Figure 12 shows a few potential molecules for which a good correlation with observed signals appeared. Species 2, 3 and 4 suggest that partial hydrogenation and/or C-C bond breaking of **PP** ligand may have occurred. However, it is important to underline that the signals of the **PP** ligand are also observed, together with broader peaks that correspond to **PP** ligand which is still coordinated because not completely released by the thiol exchange.

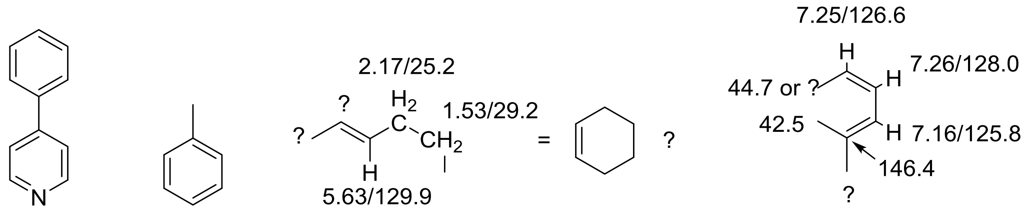

1 **2** **3** **4**

Figure 12. Possible structures that fit with the signals observed.

These results being not completely satisfying, the ligand substitution experiment was repeated by changing the conditions: first, 10 mg of purified **Ru-0.2PP** NPs were introduced in the NMR tube, to avoid cyclooctane signals disturbing; second, a thiol with a shorter alkyl chain was used, namely 1-pentanethiol (1 mol eq.), in order to decrease the number of aliphatic signals present in the spectra. An important remark is that these NPs were exposed to air before being re-dispersed in *d*^{8}-THF what, as previously mentioned and presented in the following section (3B.2.6), leaded to partial surface oxidation. The ^{1}-H NMR results are shown in Figure 13:

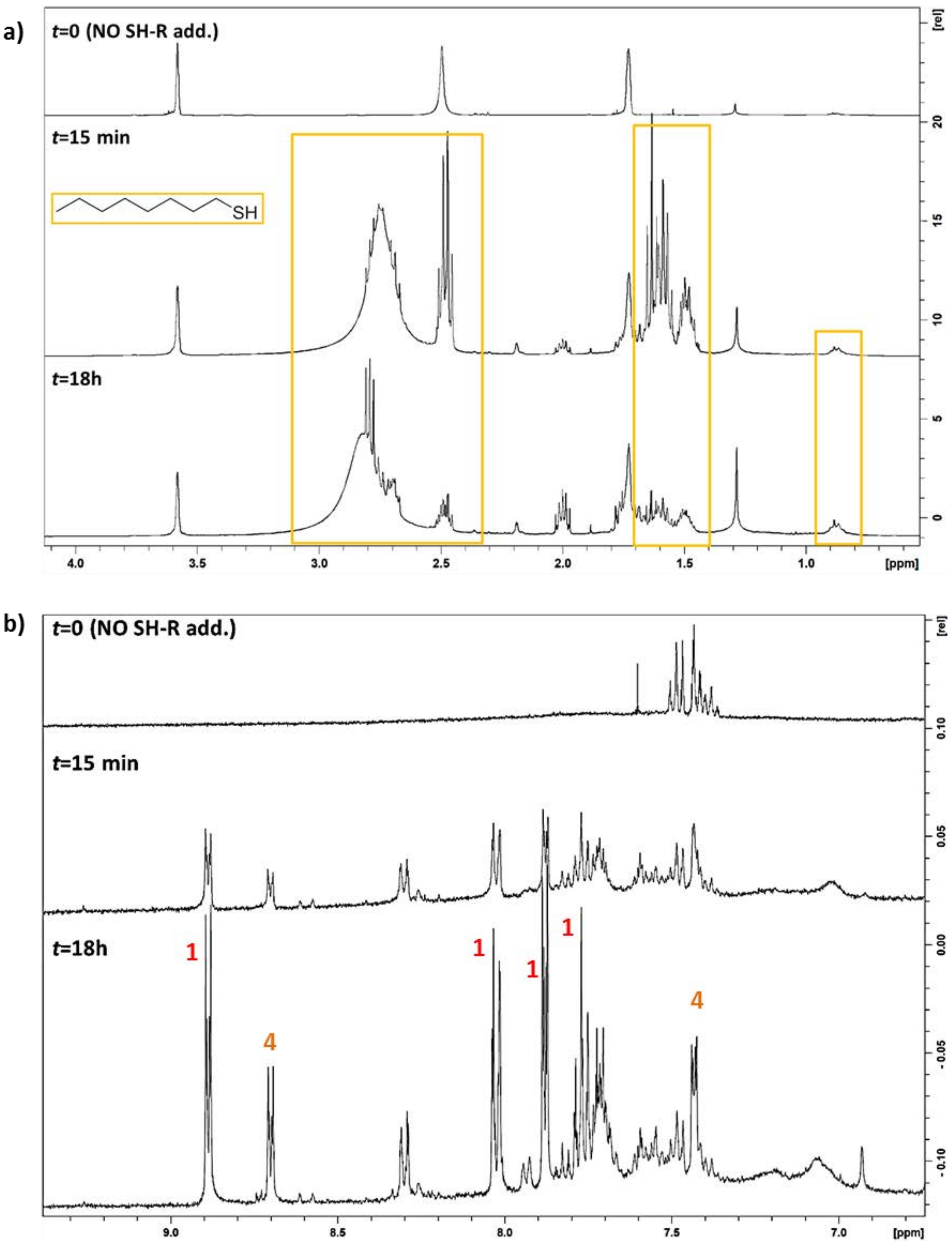

Figure 13. ^{1}H-NMR spectra of ligand exchange experiment with 1-pentanethiol recorded at *t*=0, *t*=15 min and *t*= 18 h. a) Aliphatic region and b) aromatic region.

Again, the signals of the thiol are visible 18h after 1-pentanethiol addition due to the excess added (Figure 13a, *t*=0). In the aromatic region, in this case even before the thiol addition (Figure 13b, *t*=0), the spectra show the presence of signals at 7-7.3 ppm. This can be explained by a partial decoordination of the PP ligand due to the exposure of the particles under air that led to partial oxidation of the metal surface. As a result, the coordination of the PP ligand is probably through *N*-donating of the pyridyl group instead of π-stacking interactions by the two aromaric groups of the ligand (the signals from the pyridyl group are not present at *t*=0). However, after the addition of 1-

pentanethiol, the **PP**-signals appeared again together with other peaks that we were not able to assign. This second exchange experiment thus confirmed the presence of **PP** ligand at the metal surface with that of other molecules.

In conclusion, despite the fact that the composition of surface ligands could not be fully elucidated, we found evidence that non-hydrogenated **PP** ligand is present on the surface of the NPs as well as partially hydrogenated or broken groups.

3B.2.6 Oxidation studies

In order to have at disposal nanomaterials to evaluate as catalysts for the water oxidation reaction, various oxidation methods have been tested to transform the Ru^0-NPs into RuO_2 ones. One main objective of these oxidation studies was to define reaction conditions allowing this transformation in a controlled way, meaning with no or only a limited sintering of the particles, in order to preserve the advantage of the small size of the initial particles that offers a large surface area for catalysis. The diverse oxidation methods employed are hereafter detailed and the results summarized in Table 6. The conditions applied were inspired by previous results in the group,[16] from the RuNPs samples either in the solid state or in an aqueous or organic suspension. The reaction conditions mainly consist in a soft treatment by air exposure at room temperature (Method A), or more drastic treatments as a high temperature treatment in a furnace (Method B) or the addition of an oxidative agent at room or higher temperature (Methods C to E).

- **Method A: One-week air exposure.** As a first essay, the RuNPs in the solid state were simply exposed to the ambient air during one week, by opening a WAXS capillary just after a first analysis indicating the presence of ruthenium in the metallic state (Figure 8). After this soft treatment on the **Ru-0.2PP** NPs, a new WAXS measurement indicated a slight evolution of the Ru pattern (Figure 14a) to the formation of some RuO_2, as evidenced by the shoulders appearing at $\theta \approx 15$ and 25°. In the case of **Ru-0.05MPT** sample, an amorphisation of the hcp phase can be observed due to the less sharp peaks, which could be due to a moderate oxidation but metallic Ru is still present (Figure 14b).

  To a purified sample which was exposed to the air after the washing procedure, CO coordination (Figure 16) and hydride titration analysis were done. TEM images previous to the analysis confirmed the small size was maintained, although some agglomeration was noticed (Figure 15).

  Regarding the hydrogenation of norbornene with **Ru-0.2PP**, no evolution was observed by gas chromatography with the absence of any signal from norbornane, suggesting that the conditions applied led to the elimination of Ru-H species from the surface.

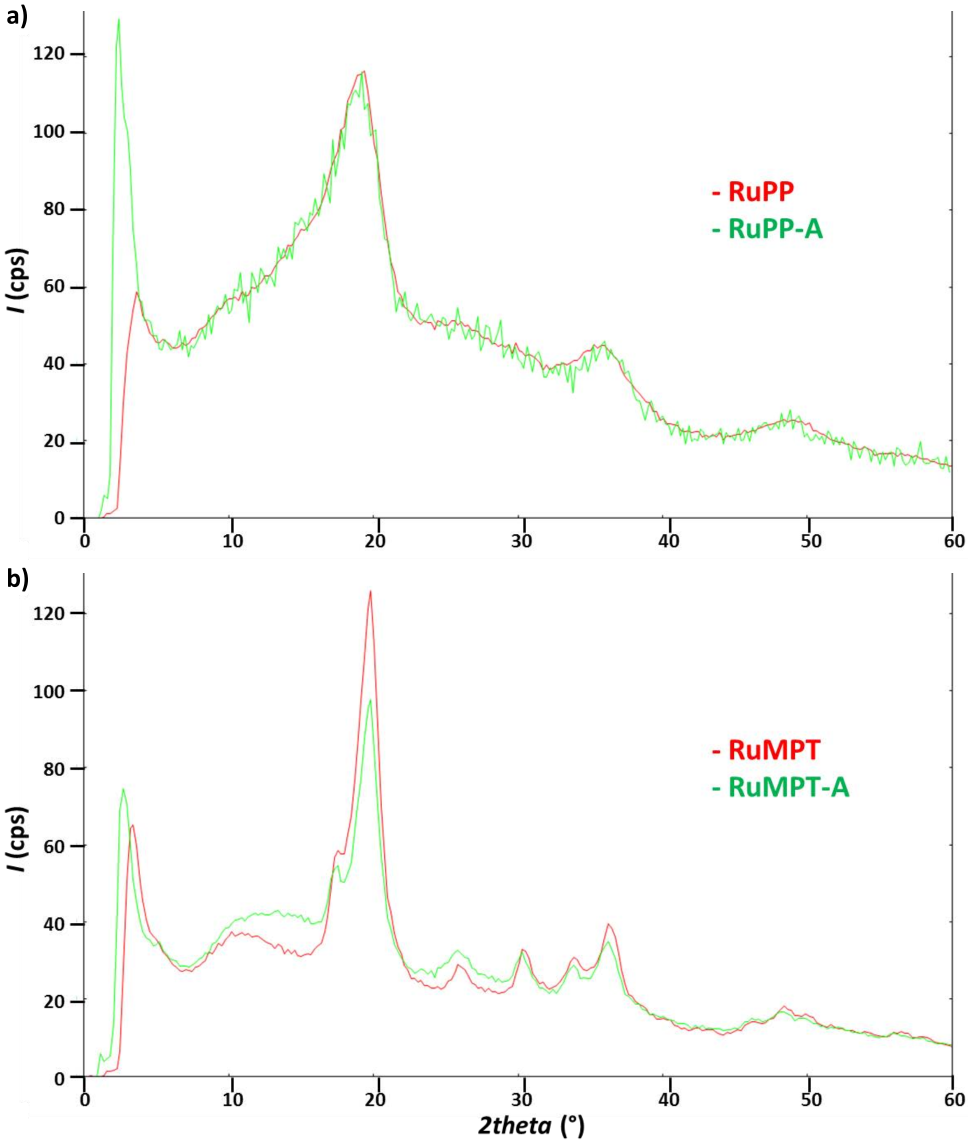

Figure 14. WAXS analysis of a) **Ru-0.2PP** and b) **Ru-0.05MPT** NPs after air exposure at room temperature for 1 week.

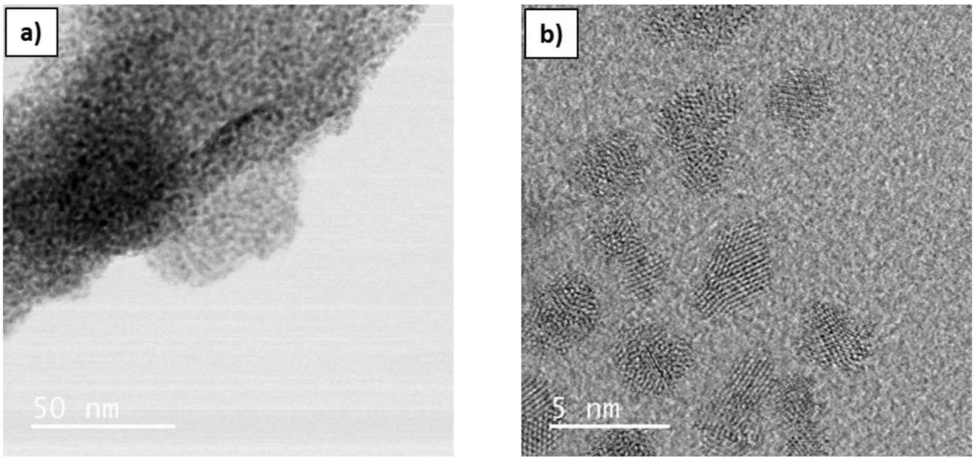

Figure 15. TEM images of **Ru-0.2PP** after air exposure.

In order to determine if the coordination of CO at the NP surface was feasible after the air exposure due to the partial oxidation, the **Ru-0.2PP** and **Ru-0.05MPT** samples have been exposed to 1 bar of CO in a Fisher-Porter reactor overnight. On Figure 16, the FTIR spectra allow to compare the ability of RuNPs to coordinate CO before and after air exposure. It can be seen that in all cases, both signals from terminal (2040 cm^{-1}) and bridging (1950 cm^{-1}) CO are observed after reacting with CO, and that the RuNPs are able to coordinate this molecule even after being air exposed. In the case of **Ru-0.05MPT** sample (Figure 16a) the intensity of the CO bands is lower than for the RuNPs not exposed to air. These results indicate that Ru sites are still present and able to coordinate CO in the NPs exposed to air at room temperature, but probably in a lower quantity than for the fresh RuNPs given the lower intensity of the CO bands observed. This could derive from the partial oxidation of the surface of the NPs, as suggested by the WAXS analysis. It is important to note the presence of a shoulder on the vibration band corresponding to bridging CO on the IR spectrum of the sample exposed to air. This was already observed for metallic **Ru-0.2PP** sample, and it was attributed to the two possible coordination bridging modes. This indicates that two bridging coordination modes are still possible on the NP surface. Thus, the partial oxidation could be located on a specific position of the NP, leaving the other coordination mode still available for CO interaction.

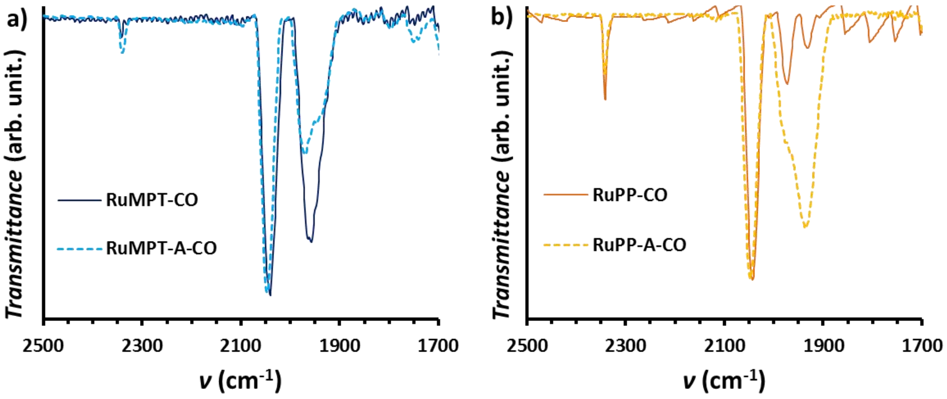

Figure 16. IR analysis of the CO coordination to **Ru-0.05MPT** (a) and **Ru-0.2PP** (b) oxidized samples (RuMPT-A-CO and RuPP-A-CO) under air, in contrast to the metallic ones (RuMPT-CO and RuPP-CO).

In the case of **Ru-0.2PP** (Figure 16b), the two peaks at 1950 cm^{-1} and 2040 cm^{-1} are present as well, but the ratio terminal/bridging has strongly changed in contrast to the fresh RuNPs with a increase of the bridging CO signals. This suggests that the oxidation took place on the available apexes/edges sites, as the faces are covered by the ligand. Moreover, the signals from the two bridging modes observed for the metallic **Ru-0.2PP** NPs also modified their ratio, increasing its intensity the one at lower frequencies.

In summary, full and crystalline RuO_2 could not be obtained by simply expose the samples at ambient air even after a full week. Such stability to air despite the small size of the particles can be attributed to the presence of the ligands at their surface which protect them and allow only a partial oxidation.

- **Method B: Thermal treatment in a furnace at 200 and 400 °C for 2h.** An air treatment of the **Ru-0.2PP** and **Ru-0.05MPT** NPs under thermal conditions at 200 °C and 400 °C for 2h inside a furnace, allowed to get highly oxidized nanomaterials as shown by WAXS analysis (Figure 17). As the obtained results are comparable for the two samples and the two temperatures tested, for simplifying only the observations for **Ru-0.05MPT** at 400 °C will be discussed. Hence, the presence of RuO_2 nanomaterials in the rutile crystalline phase has been observed by WAXS (Figure 17b), although metallic Ru presence is also revealed in Figure 17a.

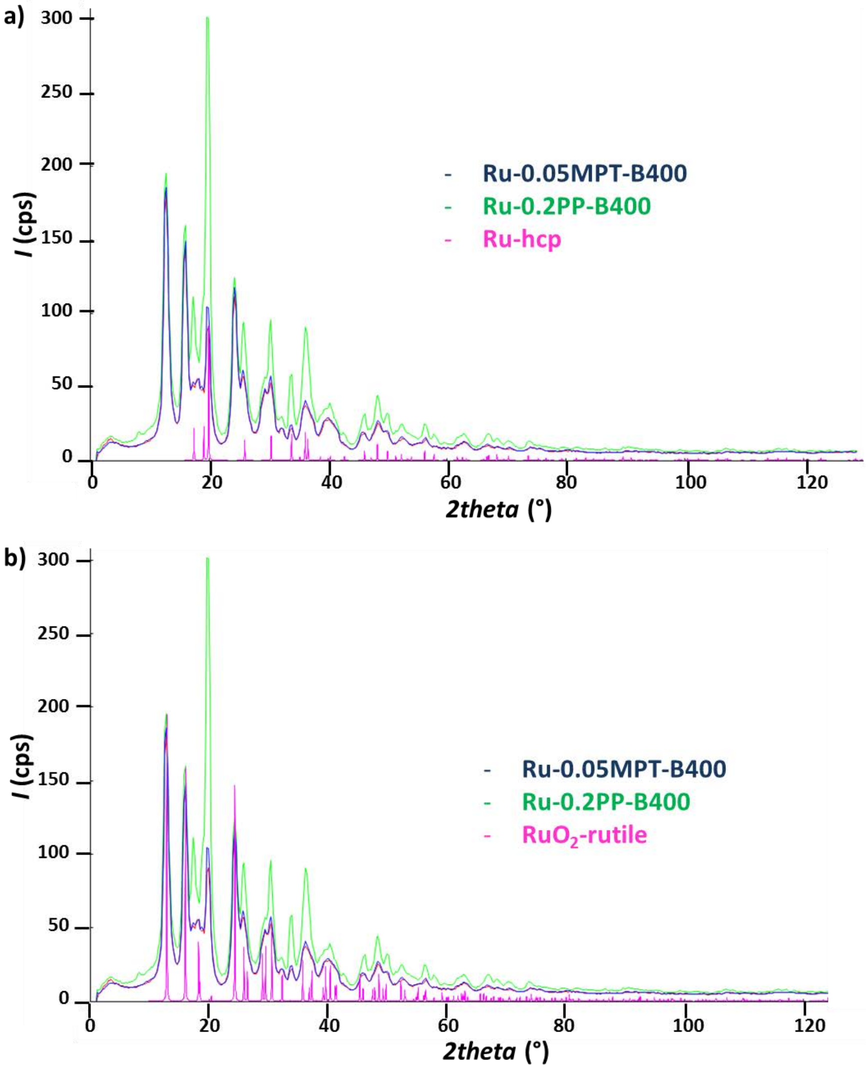

Figure 17. WAXS analysis of **Ru-0.2PP** and **Ru-0.05MPT** NPs after after air exposure at (400 °C). Comparison with a) Ru-hcp and b) RuO_2 reference phases.

In addition, the WAXS data suggest a coalescence of the particles which was clearly seen on TEM images (Figure 18 and Table 6). The fact that there is some remaining Ru even after air exposure in thermal conditions can result from an agglomeration process taking place while the oxidation is happening. This could stabilize big particles displaying a metallic core surrounded by a RuO_2 shell.

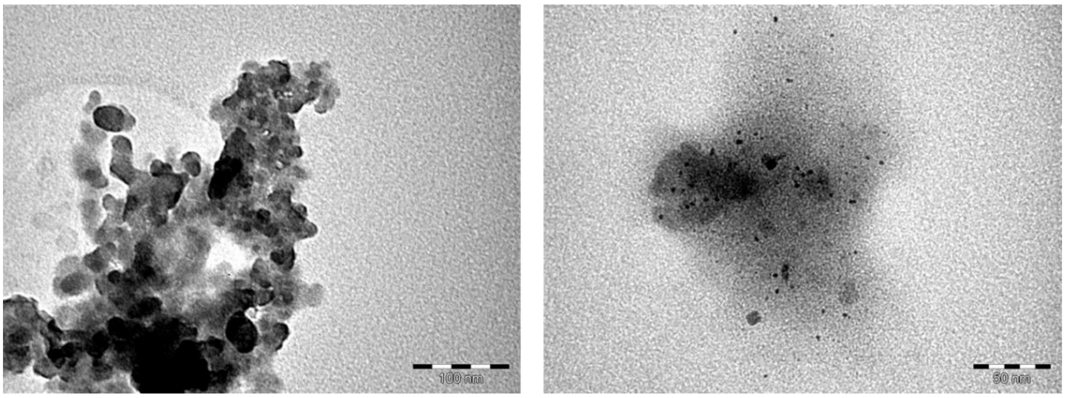

Figure 18. TEM images of **Ru-0.05MPT** sample after thermal treatment at 400 °C for 2h.

- **Method C: O_2-treatment at room temperature for three days of a THF-suspension of Ru-0.05MPT NPs.** To thermally treat the NPs under less harsh conditions and trying to avoid the particles coalescence during the oxidation procedure, a sample of **Ru-0.05MPT** NPs has been re-dispersed in a degassed THF solution. The so-obtained suspension has then been exposed to 3 bar of O_2 and left reacting at r.t. during three days. After isolation, the particles were analyzed by TEM (Figure 20) and WAXS (Figure 20). From WAXS analysis, it can be concluded that this oxidation treatment did not modify the oxidation state of the NPs which are still made of metallic Ru. TEM analysis has revealed agglomeration and some coalescence of the particles but a lot of small individual NPs are still present.

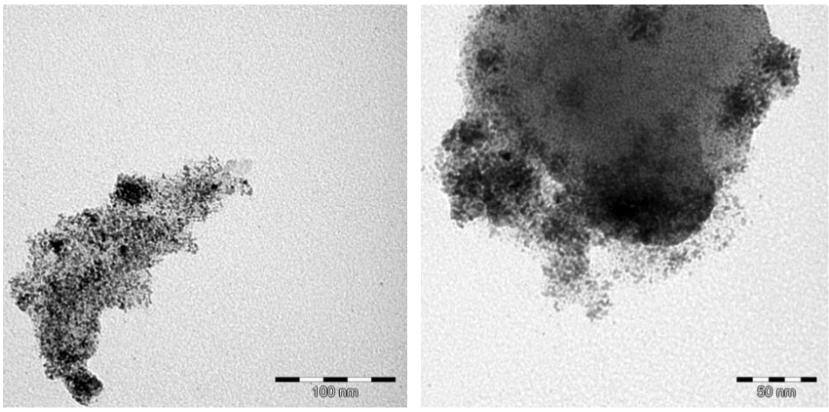

Figure 19. TEM images of **Ru-0.05MPT** sample after treatment of a THF suspension with O_2.

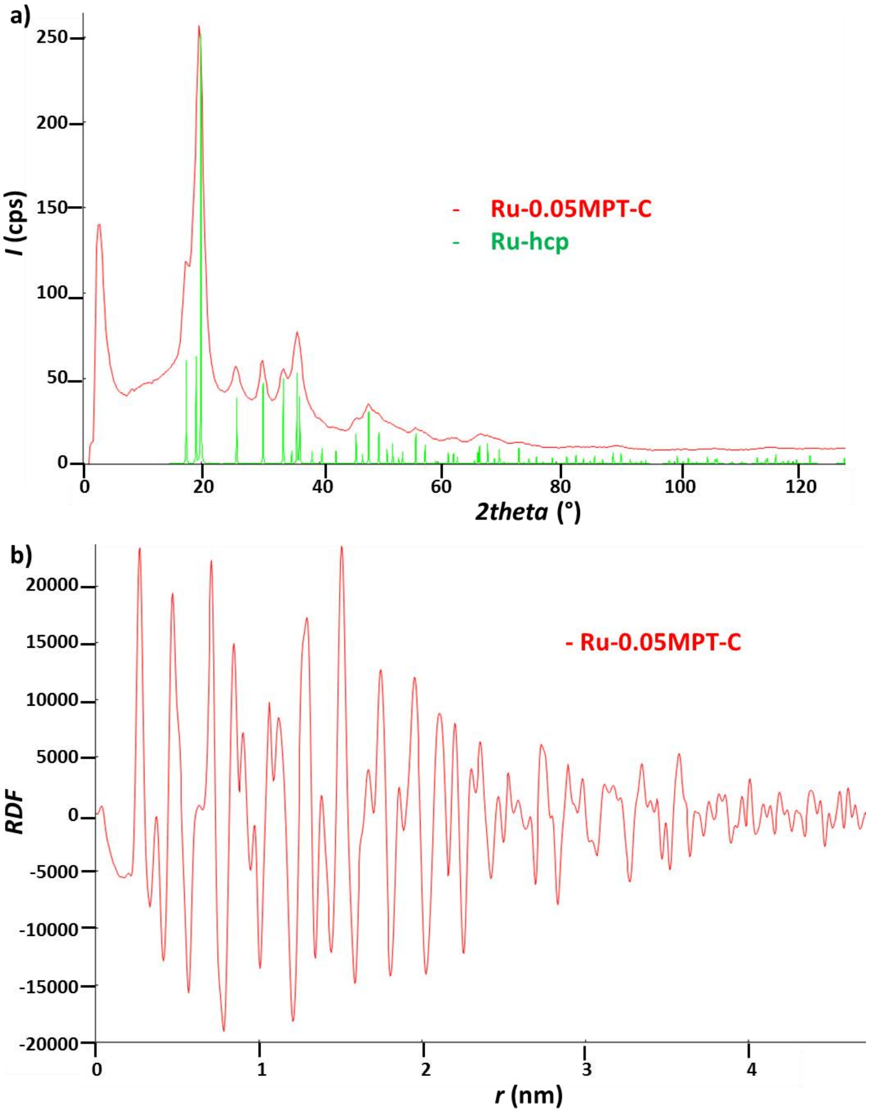

Figure 20. a) WAXS and b) RDF analysis of **Ru-0.05MPT** NPs after exposure of a THF-suspension to 3 bar O_2 at room temperature during 3 days. Comparison with Ru-hcp data.

- **Method D: O_2-treatment of a THF-suspension of Ru-0.05MPT NPs at room temperature for three days.** Similarly to the previous oxidation treatment, a THF-dispersion of **Ru-0.05MPT** NPs has been exposed to 3 bar of O_2 at 50 °C for 3 days. Again, as revealed by WAXS analysis, mainly metallic RuNPs have been observed (Figure 21), keeping the nanometric size shown before the treatment (≈4 nm, RDF in Figure 21b). It seems that THF has protected the NPs against oxidation.

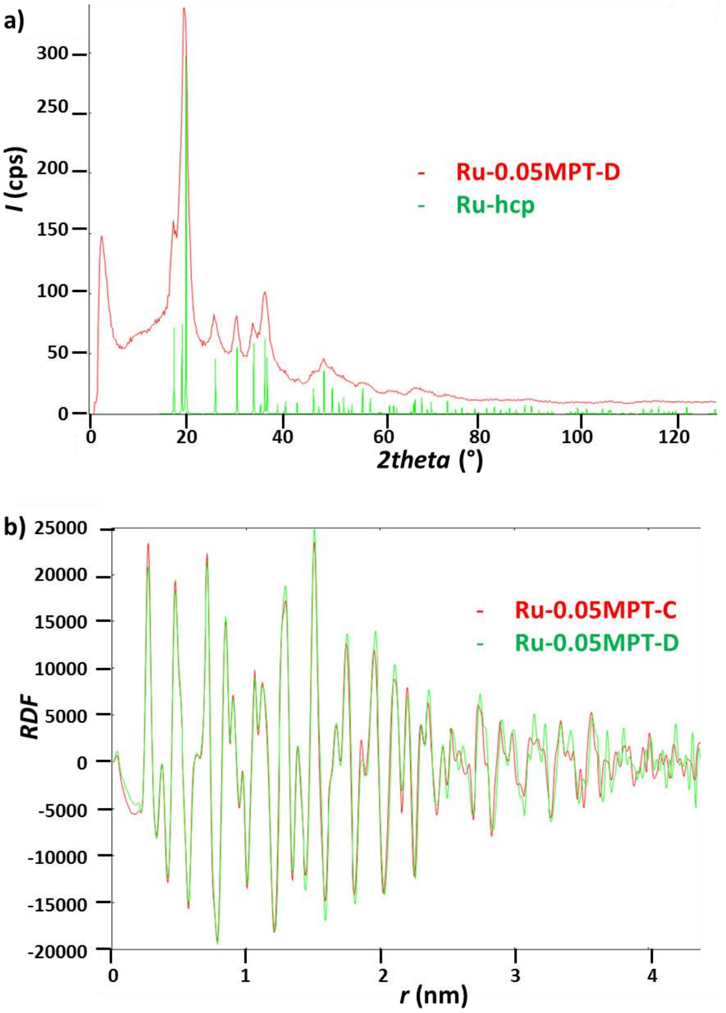

Figure 21. a) WAXS and b) RDF analysis of **Ru-0.05MPT** NPs after exposure of a THF-suspension to 3 bar O_2 at 50°C during 3 days. Comparison with Ru-hcp (a) and Ru-0.05MPT-C (b).

- **Method E: O_2-treatment of an aqueous dispersion of Ru-0.05MPT at 95 °C overnight.** The last methodology tried has consisted in refluxing a suspension of **Ru-0.05MPT** NPs in water at 95 °C overnight. The choice of these thermal conditions has been governed by the fact that the electrocatalytic experiments are performed in an aqueous medium. Thus we thought that oxidizing the NPs in water could be beneficial for their further catalytic performance. TEM analysis revealed the presence of almost only agglomerates but individual NPs can be distinguished inside (Figure 22). WAXS analysis indicated the presence of both Ru and RuO_2 and an amorphisation phenomenon (Figure 23). The rutile phase seems here more pronounced than with the other methods (A-C-D). Surprisingly, the RDF in this case gives a coherence length of 1.8 nm. This could only be attributed to a splitting of the particles during the treatment.

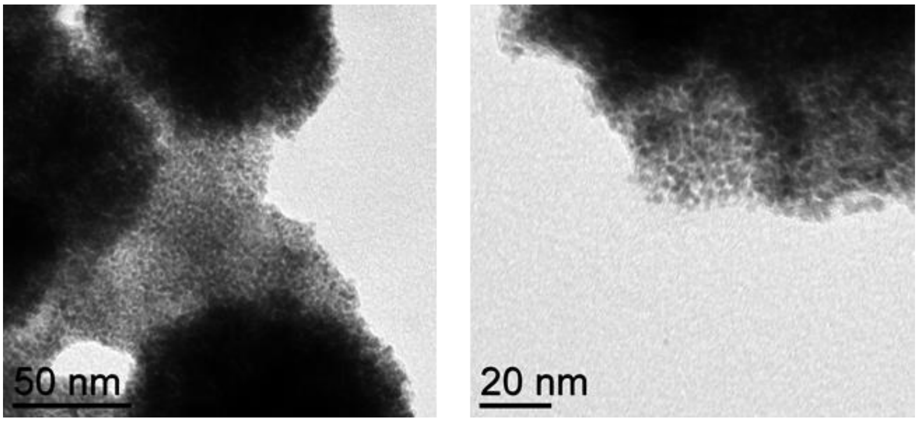

Figure 22. TEM images of **Ru-0.05MPT** sample after treatment of a H_2O suspension at 95 °C overnight under air conditions.

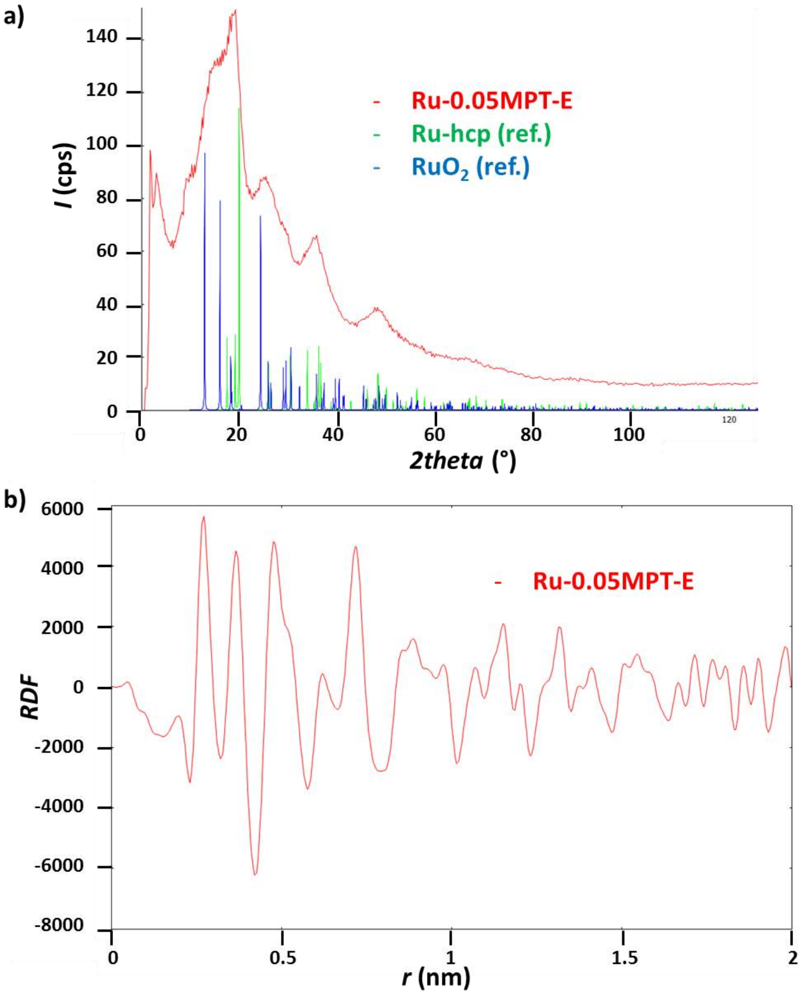

Figure 23. a) WAXS and b) RDF analysis of **Ru-0.05MPT** NPs after exposure of an aqueous-suspension to 3 bar O2 at 95 °C overnight.

To summarize (Table 6), among the five oxidation protocoles tested, the highest RuO_2 content was achieved with the thermal treatment in solid state, but this method led to sintering ending up with big particles and thus possibly less surface area. The last method (exposure of an aqueous suspension of **Ru-0.05MPT** NPs to 3 bar O_2 at 95°C for one night) led also to, a WAXS pattern with a high RuO_2/Ru^0 ratio. TEM analysis revealed the presence of agglomerated particles into large superstructures but appearing still individual. If it was not possible to estimate the mean size of the individual particles observed on TEM images, a coalescence length of ca. 1.8 nm could be determined from WAXS data, thus evidencing the presence of small objects. These results thus show that the surface area of the nanomaterial is probably still important in this case.

Table 6. Summary of the results achieved with the different applied oxidation methods.

Method ***Mean size (nm)***	***TEM image***	***Oxidation state &*** ***observations***
Ru-0.2PP (initial) 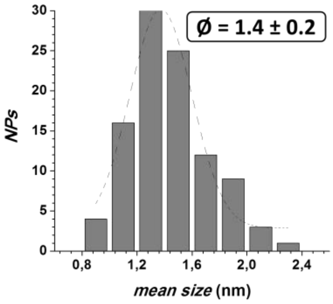	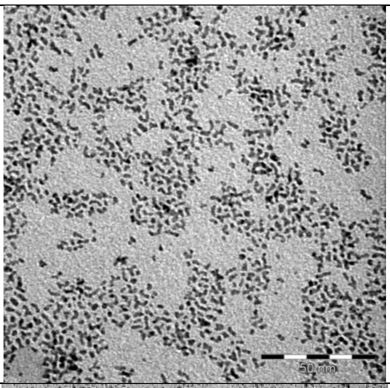	Ru^0 Small, well-dispersed and homogeneous in size NPs
A: air exposure in solid state -	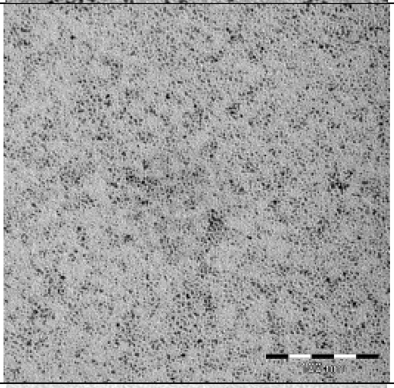	Mainly Ru^0 No change observed (slight agglomeration by RDF-WAXS)
B: thermal treatment at 200-400 °C in solid state -	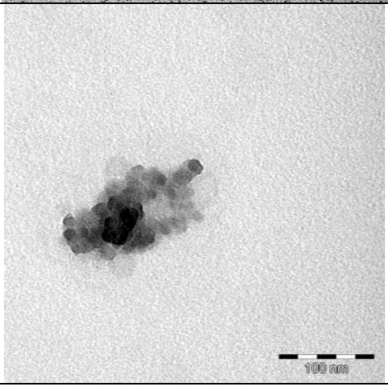	Ru^0/RuO_2 Both metallic and oxide phase are observed, but sintering is achieved at 200-400 °C

C: O_2 addition in a THF dispersion at r.t. for 3 days 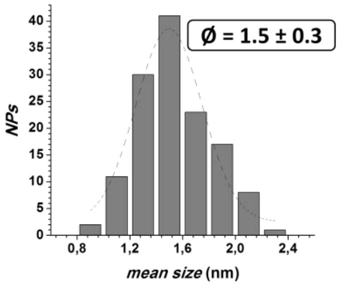 	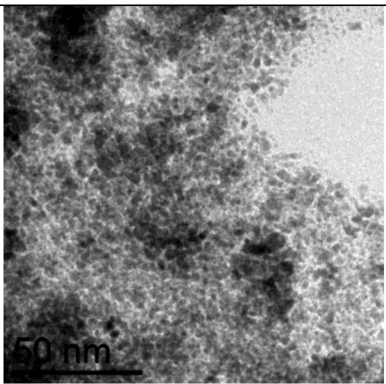 	Mainly Ru^0 No oxidation observed but particles coalescence and agglomeration
D: O_2 addition in a THF dispersion at 50 °C for 3 days 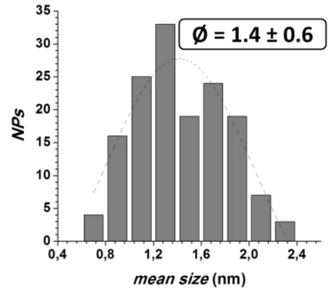 	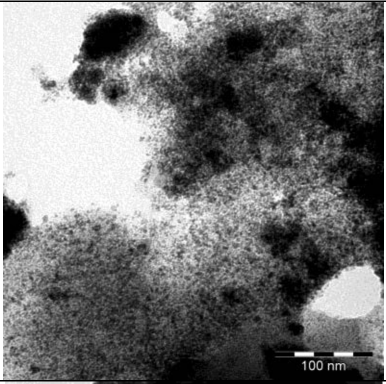 	Mainly Ru^0 Broad size distribution with no oxidation observed, agglomerated NPs
E: Air exposure in an aqueous suspension at 95 °C overnight 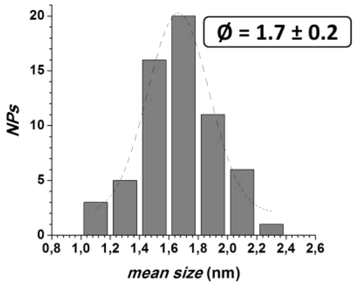 	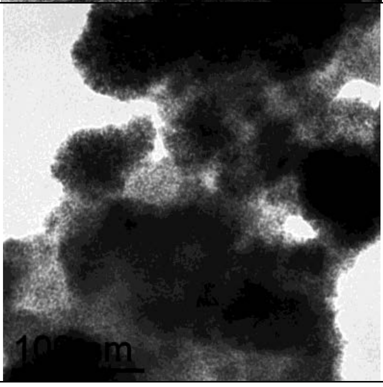 	Ru^0/RuO_2 Metallic and oxide phases are present. NPs grow bigger in size and agglomerate in a continuous matrix.

In conclusion of this part, it appears that the different reaction conditions tested did not allow to fully oxidize the **Ru-0.2PP** and **Ru-0.05MPT** NPs into controlled RuO_2 nanomaterials while keeping their small size. This can result from the strong coordination of **PP** and **MPT** ligands at their surface that can limit the oxidation to the core in soft conditions. Indeed a passivation of the surface has been observed but not a total oxidation into controlled RuO_2 NPs. In more drastic conditions namely a thermal treatment at 200 and 400°C, a fast sintering has been observed which could be the reason why Ru cores were maintained. Today, the controlled oxidation of these RuNPs remains a blocking point for their evaluation as water oxidation catalysts.

3B.3 Electrocatalytic HER studies

In order to test the electrocatalytic performance of **Ru-0.05MPT** and **Ru-0.2PP** NPs in the hydrogen evolution reaction, a 2 mg·mL^{-1} dispersion of each sample in THF was deposited onto the surface of a rotating disk glassy carbon electrode (RDE/GC), and the new supported materials tested as HECs in a three electrode configuration, together with a Pt grid and a saturated calomel electrode (SCE, KCl sat.) as counter (CE) and reference (RE) electrodes, respectively. The polarization curves of both **Ru-0.05MPT** (purple) and **Ru-0.2PP** (dark red) in 1 M H_2SO_4 solution are shown in Figure 24. They display a change on the current density at η_0 = 60 mV and η_0 = 0 mV, respectively, at which they start reducing protons to H_2.

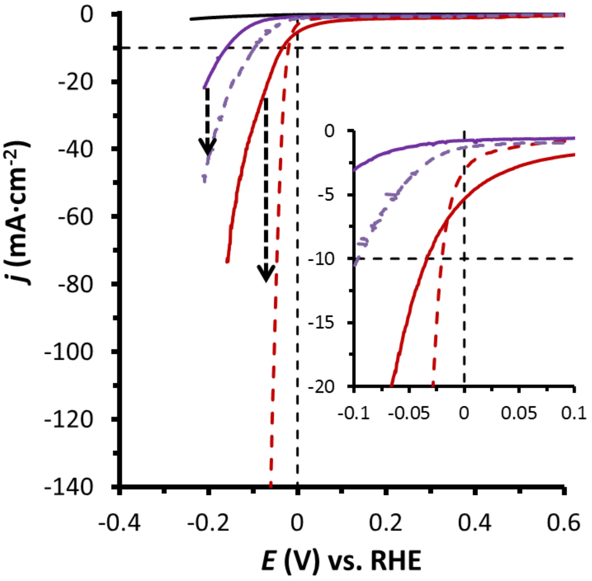

Figure 24. Polarization curves of **Ru-0.05MPT** (purple) and **Ru-0.2PP** (dark red) systems before (bold) and after (dashed) a 20 minutes bulk electrolysis at *j* = -10 mA·cm^{-2} in 1 M H_2SO_4. Inset, enlargement of the onset overpotential zone.

After 20 min at fixed *j* = -10 mA·cm^{-2}, both systems show a change on the subsequent LSV as depicted on the dashed curves (Figure 24). This behavior is attributed to a change on the surface oxidation state of the NPs. Since the particles get partially oxidized on the surface when exposed to air, as demonstrated in section 3B.2.6 method A, when applying a reductive potential the surface is reduced again to form Ru^0. This species is far more active than the passivating RuO_2 layer, displaying a huge increase on the current density at low overpotentials in contrast to the partially oxidized material. This process is further described and the species involved characterized in the following Chapter 3.C, for **Ru-0.2PP** system which afforded the highest electrocatalytic results.

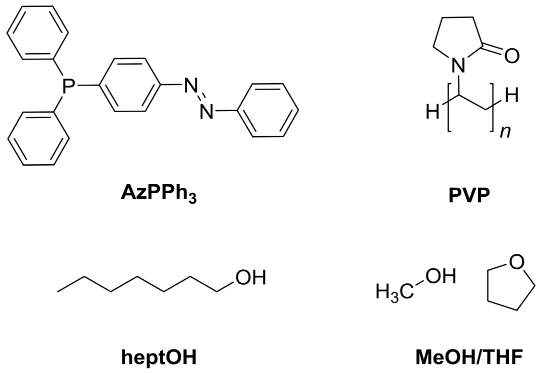

Figure 25. STAG used for the synthesis of other RuNPs (AzP = (*E*)-(4-(diphenylphosphanyl)azobenzene),[17] PVP = polyvinylpyrrolidone, heptOH = heptanol, and MeOH/THF).

Together with the pyridine-stabilized NPs, other cathodes were prepared with different RuNPs synthesized in the laboratory and in the presence of various stabilizing agents (STAG) including a polymer (PVP) as shown in Figure 25. The STAGs used for the stabilization of RuNPs are: AzP = (*E*)-(4-(diphenylphosphanyl)azobenzene),[17] PVP = polyvinylpyrrolidone, heptOH = heptanol, and MeOH/THF (**Ru-GC** in Ch. 3A). The mean sizes of all the NPs and their corresponding electrocatalytic data in 1 M H_2SO_4 are summarized in Table 7. For comparison purpose, electrochemical data for Ru-black and 60% Pt/C commercial products are also reported in Table 7. LSV curves of the different electrodes are given in Figure 26.

Table 7. Main electrochemical data of the different Ru-based stabilized NPs tested as HECs.

Entry	***System of NPs***	***NPs' mean size* (nm)**	**η_0 (mV)**	**η_{10} (mV)**	***b* (mV·dec.$^{-1}$)**
1	**Ru-0.05MPT**	1.2 ± 0.3	20	93	106
2	**Ru-0.2PP**	1.3 ± 0.3	0	20	29
3	**Ru-MeOH/THF**	21 ± 2	40	83	46
4	**Ru-heptOH**	3	35	80	109
5	**Ru-PVP**	1.1	75	>250	235
6	**Ru-AzP**	3	150	>250	170
7	**Rub**	-	70	150	65
8	**Pt/C**	-	0	27	32

It is worth mentioning that, for RuNPs prepared with stabilizers different from the pyridine-based ones, we did not observe any activation process when applying a reductive potential. This can be rationalized as:

- First, the particles hardly get oxidized when exposed to air due to the effect of the ligand stabilizing lower oxidation states, thus leading to a bare change in activity after several minutes under reductive potentials. This could be the case of Ru-MeOH/THF or Ru-heptOH, according to the high activities recorded and the reducing ability of alcohols.

- Alternatively, if the particles get severely oxidized and the recovery of the metallic phase is not possible electrochemically, the NPs would always display the same activity under HER conditions, resulting from the Ru^0/RuO_2 mixture as soon as they are exposed to air. Ru-PVP and Ru-AzP might be part of this group, considering the low current densities displayed.

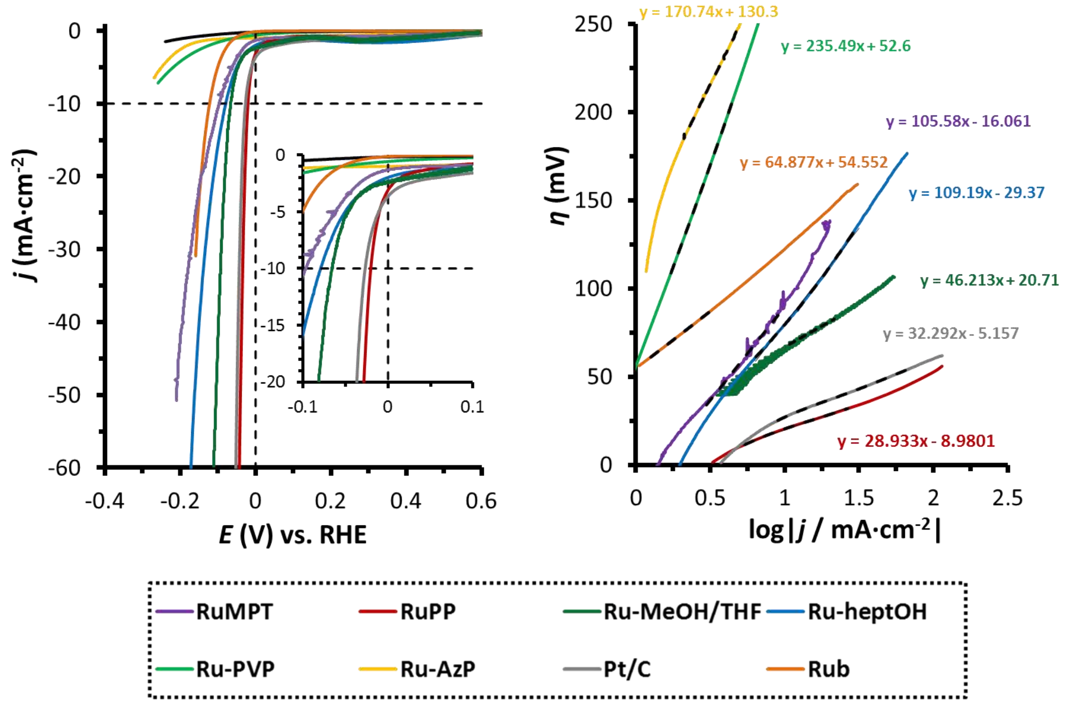

Figure 26. Left, polarization curves of the different tested systems in 1 M H_2SO_4; right, Tafel plots of those systems.

From the LSV curves we can conclude several points. First, the values obtained with **Ru-0.05MPT** and **Ru-0.2PP** systems are the best electrocatalytic results, the latter displaying current densities similar or even better than the state-of-the-art Pt/C electrocatalyst for HER. This confirms that pyridine-based ligands are efficient stabilizing agents providing a huge catalytic activity to the Ru-based NPs. Secondly, **Ru-MeOH/THF** (from chapter 3A) and Ru-heptOH also show interesting intermediate results: they achieved η_{10} values higher than **Ru-0.2PP** but lower than **Ru-0.05MPT**. These results state thus that NPs' stabilization with alcohols is also a favoring parameter to catalyze the reduction of protons. The reducing capacity of alcohols could play a major role on the stabilization of the metallic oxidation state, and also in assisting the HE-catalytic performance of the NPs.

Finally, Ru-AzP and Ru-PVP systems display much worse results. In the first case, one can expect that the phosphine based ligand is strongly coordinated at the NP surface, considering that both P and Ru are soft species (as described by Pearson). In the P-Ru bond, a strong π-back bonding can diminish the particles' surface electron density and thus weaken the metal capacity towards the reduction of protons,[18] slowing down the M-H group formation through the Volmer reaction. The last nanocatalyst, Ru-PVP, has been previously used for several catalytic reactions such as Fischer-Tropsch[19a] or double-bond and arene hydrogenation.[19b,20] However, being PVP a hydrophilic polymer, on one side it could get dissolved in the reaction aqueous solution, leaving the NPs' surface naked. As previously mentioned, on the other side it could get vigorously oxidized due to the low stabilization PVP induces, as no coordination is present between Ru and PVP. Additionally, PVP can diminish the electron transfer between the electrode and the NPs, lowering down the catalytic activity of the system. An example of photocatalytic hydrogen evolution using Ru-PVP NPs was reported by S. Fukuzumi in 2011.[21] But, those particles were obtained by ligand substitution of previously synthesized RuNPs stabilized with tri-n-octylamine, what suggests that both PVP and amine might be present on the surface of the particles, thus giving rise to slightly different surface properties than directly synthesized Ru-PVP NPs. They studied how some reaction conditions (such as NPs' mean size, pH or concentration) affected on the catalytic behavior, as already described in Ch. 1.

Another parameter widely used for electrocatalysts' comparison is the Tafel slope (*b,* mV·dec^{-1}). From the Tafel plot (Figure 26, right) we can extract *b*, which gives information on the kinetics of the catalyst and the rate determining step (rds). **Ru-0.2PP** and Pt/C systems present a Tafel slope close to 30 mV·dec^{-1}, suggesting the Tafel step as rds, which is the recombination of two M-H species to form H_2. **Ru-MeOH/THF** and Rub are closer to *b* = 40 mV·dec^{-1}, typical from catalysis where the rds is the Heyrovsky step, consisting on the H_2 electrodesorption with a proton from the solution. Ru-heptOH and **Ru-0.05MPT** are very close to 120 mV·dec^{-1}, being the adsorption of a H^+ to form the M-H species (Volmer step) the rds. Finally, Ru-PVP and Ru-AzP have both very high Tafel slopes (> 150 mV·dec^{-1}), what could mean that even the H^+ adsorption is extremely slow, and stating those species as uncompetitive electrocatalysts.

It is interesting to highlight the different kinetic behaviors observed between the two best systems of study (**Ru-0.2PP** and **Ru-0.05MPT**), illustrated by their Tafel slopes. While **PP**-stabilized NPs have the smallest *b* comparable to Pt/C with the Tafel step as rds, **Ru-0.05MPT** has a slope of 105 mV·dec^{-1}, with the formation of the M-H as the slowest path in the HER process. As both ligands have a similar chemical nature (pyridine-phenyl structure), the different configurations suggests a different interaction with the particles, what is finally transferred to the catalytic response of the systems. This is promising for future studies, as varying the capping ligands can help to understand the parameters ruling the catalytic behavior on the surface of the NPs, and thus to rationally design new active species.

3B.4 Conclusions & perspectives

The use of different characterization techniques allowed getting information about the structure, ligand coordination, Ru oxidation state and H/CO interaction with the surface of RuNPs. This study is interesting when comparing NPs with different characteristics such as the above mentioned ones or even being stabilized by different ligands. Using characterization techniques with different systems during HE catalysis can be of interest for unraveling the effect of those properties onto the final catalytic activity.

In this specific case, we have found synthetic conditions with **MPT**/**PP** ligands that lead to the formation of small and homogeneous-in-size RuNPs, as observed in the TEM images. We also demonstrated by WAXS that partial oxidation is observed when slow O_2 diffusion was applied to the powder material, although the mean size was kept after this process. **PP** ligand was demonstrated to remain present after the reducing conditions applied on the NPs' synthesis (3 bar H_2 overnight), although some hydrogenated or broken species were also detected by NMR spectroscopy. Even after the formation of this Ru^0/RuO_2 the ligand was still coordinated on the surface of the particles, as proven by TGA, EA and NMR spectroscopy. Finally, total oxidation of the particles to form RuO_2 for its evaluation as OEC could not be achieved, either due to particles agglomeration upon the applying of vigorous thermal conditions, or due to passivation of the surface by a RuO_2 layer which prevents further oxidation of the core.

The good catalytic results obtained with the set of RuNPs stabilized with organic ligands of different natures, open a door towards the correlation of nanocatalysts properties and their electrocatalytic performance. Our results confirmed that the coordination properties of ligands and their influence at NP surface need to be explored in more detail in order to produce more effective catalysts. As perspectives, several studies could be performed in order to try to better understand the electronic, structural or morphological characteristics inducing a change on the activity of the NPs, as follows:

- ✓ Considering **PP**-stabilized RuNPs, we can envisage to modify the synthetic conditions with the aim to obtain RuNPs displaying the same chemical environment but with different sizes (namely from 1 nm to 50 nm). This would help to check the size-effect on the catalytic properties.

- ✓ Changing the oxidation state of the NPs without modifying the mean size would permit to have a series of particles from Ru^0 to RuO_2 and intermediate mixtures of oxidation states, what could be useful to attribute the real activity of each phase in the presence/absence of the other.
- ✓ The choice of ligand has been demonstrated to be of paramount importance. Thus having in hands a library of particles with the same diameter and oxidation state but stabilized with a different ligand, could help attributing an activity trend to the electronic properties and coordinating capacity of the capping ligands on facilitating one or another mechanistic step depending on the ligand-metal interaction. This is very ambitious but if feasible, it should lead to precious information.
- ✓ Ru-based catalysts have been used already in several catalytic reactions. Thus, these NPs could be tested in other catalysis, such as electrocatalytic CO_2 reduction into C-based fuels or other chemicals (CO, formic acid, formaldehyde, methanol, ...).[22]
- ✓ Photocatalytic HE/OE catalysis following the reported results by S. Fukuzumi *et al.* would be highly desired.
- ✓ Finally, applying all the knowledge from the other points, other metals could be essayed, avoiding second-row scarce and expensive metals.

3B.5 Experimental part

Reagents. All operations for the synthesis of the ligand-capped Ru nanoparticles were carried out using standard Schlenk tubes, Fisher–Porter bottle techniques or in a glove-box (MBraun) under argon atmosphere. Solvents (THF and pentane) were purified before use, by filtration on adequate column in a purification apparatus (MBraun) and handled under argon atmosphere. Solvents were degassed before use according to a freeze–pump–thaw process. The ruthenium precursor, [Ru(cod)(cot)], was purchased from Nanomeps-Toulouse. Hydrogen gas (Alphagaz) was purchased from Air Liquide. 4-Phenylpyridine (**PP**) and 4'-(4-methylphenyl)-2,2':6',2"-terpyridine (**MPT**) used as a stabilizers were purchased from Sigma-Aldrich and used as received. High purity deionized water was obtained by passing distilled water through a nanopore Milli-Q water purification system.

Synthesis of RuNPs. The synthesis of **Ru-0.2PP** is hereafter described as typical example. [Ru(cod)(cot)] (120 mg, 0.38 mmol) and (12 mg, 0.08 mmol) of 4-phenylpyridine were dissolved under argon in 120 mL of THF in a Fisher porter reactor inside a Glove-box. After pressurization of the reactor with 3 bar of H_2 at room temperature (r.t.), the initial yellow solution turned dark brown in a few minutes. A vigorous magnetic stirring and the H_2 pressure were maintained for 16 h. After this reaction time, the H_2 pressure was evacuated and a drop of the colloidal solution was deposited onto a carbon-covered copper grid for TEM analysis. The Ru nanomaterial was isolated as a dark grey powder after precipitation by pentane addition and evaporation to dryness under vacuum.

Characterization. The crude colloidal solution has been characterized by Transmission Electron microscopy (TEM), High resolution electron microscopy (HRTEM) and the isolated solid by Wide-angle X-Ray scattering (WAXS), X-Ray photoelectron spectroscopy (XPS), Elemental analysis (EA), ThermoGravimetric Analysis (TGA) Fourier Transform InfraRed (FTIR) spectroscopy.

Transmission Electron Microscopy (TEM) and High resolution TEM (HRTEM). Samples for transmission electron microscopy (TEM) analyses were prepared by slow evaporation of a drop of the crude colloidal solution deposited onto a carbon-covered copper grid. Samples for high-resolution transmission electron microscopy (HRTEM) analyses were prepared by the same way from purified NPs redispersed in THF. TEM and HRTEM analyses were performed at the "Centre de Microcaractérisation Raymond Castaing" in Toulouse (UMS-CNRS 3623), on a MET JEOL JEM 1011 microscope operating at 100 kV with a point resolution of 0.45 nm and a JEOL JEM-ARM 200F microscope working at 200 kV with a point resolution lower of 0.19 nm, respectively. TEM allowed to evaluate the particle size, size distribution and morphology. Enlarged micrographs were used for treatment with ImageJ software to obtain a statistical size distribution and the nanoparticle mean diameter. FFT treatments of HRTEM images were carried out with Digital Micrograph Version 1.80.70 to determine the crystalline structure of the material.

Wide-angle X-Ray scattering (WAXS). Measurements were performed at CEMES-CNRS in Toulouse. Samples were measured in 1.0 mm diameter Lindemann glass capillaries. The samples were irradiated with graphite monochromatized molybdenum Kα (0.071069 nm) radiation and the X-Ray scattering intensity measurements were performed using a dedicated two-axis diffractometer. Radial distribution functions (RDF) were obtained after Fourier transformation of the corrected and reduced data.

X-Ray Photoelectron Spectra (XPS). Measurements were performed at the Catalan Institute of Nanoscience and Nanotechnology (ICN2) in Barcelona with a Phoibos 150 analyzer (SPECS GmbH, Berlin, Germany) in ultra-high vacuum conditions (base pressure $5E^{-10}$ mbar) with a monochromatic aluminium Kalpha X-Ray source (1486.74 eV). The energy resolution was measured by the FWHM of the Ag $3d^{5/2}$ peak for a sputtered silver foil was 0.62 eV.

ThermoGravimetric Analysis (TGA). Thermogravimetric analysis was performed in a Perkin Elmer TGA 7 analyzer. Measurements were carried out in a 30-500 °C temperature range in continuous heating regimes (2 °C/min) under Ar atmosphere.

The percentage of ligand in the sample was calculated as follows. From the experiment carried out on the ligand alone we could attribute the beginning of the ligand loss at 140 °C. So, the value of loss noticed at this temperature was taken as initial value. For the final ligand loss point, the value observed at the change of the slope was taken. The latter was then subtracted from the former to obtain the ligand percentage on each sample.

Elemental analysis (EA). EA was performed at the Laboratoire de Chimie de Coordination (LCC), Toulouse, on a Perkin-Elmer 2400 series II analyzer.

PP/Ru calculation. Number of mol (n) of PP was calculated from N wt.% obtained by EA and Ru wt.% was estimated from a) remaining wt.% after TGA's drop in the 130-250 °C range, attributed to organics and b) remaining wt.% subtracting organics (CHN) from EA results. Then, dividing n(**PP**) by n(Ru) gave rise to comparable ligand-to-metal ratios through calculations from both TGA/EA data.

Fourier Transform InfraRed spectroscopy. FTIR Spectra were recorded on a Perkin-Elmer GX2000 spectrometer in the range 4000–400 cm^{-1} at the LCC in Toulouse. All the samples were prepared as KBr pellets.

Electrochemical measurements. All the electrochemical experiments were performed in a BioLogic SP-150 potentiostat. Rotating disk electrode (RDE) was rotated at 3000 rpm in order to ensure complete removal of *in*-situ formed H_2 bubbles. The solutions were degassed previous to the electrochemical analysis with a N_2 flow. Ohmic potential (IR) drop was automatically corrected at 85 % using the Biologic EC-Lab software for cyclic voltammetry and chronoamperometry. For chronopotentiometry experiments IR drop was manually corrected ($E_{mod} = E_{meas} + E_{IR}$, mod=modified and meas=measured) at 85% by adding the corresponding potential value $E_{IR} = i_{exp}$ x (R_{mes} *x 0.85)*, where i_{exp} is the applied current in A and R_{mes} is the measured resistance in Ω. 1 M H_2SO_4 solution was prepared by mixing 56.1 mL of 95-97 % H_2SO_4 in 1 liter of Mili-Q water. 1 M NaOH solution was prepared by mixing 4 g in 100 mL of Mili-Q water.

A glassy carbon rotating disk electrode (RDE, ϕ = 0.3 cm, S = 0.07 cm^2) was used as working. A Pt grid was used as counter electrode (CE) and a Standard Calomel Electrode (SCE, Hg/Hg_2Cl_2, KCl sat.) electrode was used as a reference electrode (RE), and electrochemical data transformed to RHE by adding +0.24 V.

Electrode Preparation. A 2 $mg \cdot mL^{-1}$ dispersion was prepared by adding 1 mg of RuNPs in 500 µL of THF and sonicating for 30 min. Then, an aliquot of 5 µL (for GC_d and RDE) was added on the surface of the GC (S = 0.07 cm^2), and dried with a N_2 flow. This procedure was repeated three times to obtain GC-supported RuNPs. For Pt/C and Rub, dispersions ensuring a similar metal mass loading on the RDE than for GC-supported RuNPs.

Example of ligand, THF and hydride quantification from **Ru-0.05MPT** EA analysis results:

1. Mols of **MPT** from N wt.% (for 100 mg of **Ru-0.05MPT**):

$$1.72\%(N) \times \frac{1mol(N)}{14g(N)} \times \frac{1mol(MPT)}{3mol(N)} = 0.04mol(MPT)$$

2. Remaining C wt.%:

$$13.69\%(C) - \left(0.04mol(MPT) \times \frac{22mol(C)}{1mol(MPT)} \times \frac{12g(C)}{1mol(C)}\right) = 2.91\%(C)$$

3. Mols of THF from C wt.% (for 100 mg of **Ru-0.05MPT**):

$$2.91\%(C) \times \frac{1mol(C)}{12g(C)}) \times \frac{1mol(THF)}{4mol(C)} = 0.06mol(THF)$$

4. Remaining H wt.%:

$$1.26\%(H) - \left(0.04mol(MPT) \times \frac{17mol(H)}{1mol(MPT)} \times \frac{1g(H)}{1mol(H)}\right) - \left(0.06mol(THF) \times \frac{8mol(H)}{1mol(THF)} \times \frac{1g(H)}{1mol(H)}\right) = 0.1\%(H)$$

5. Mols of hydrides from H wt.% (for 100 mg of **Ru-0.05MPT**):

$$0.1\%(H) \times \frac{1mol(H)}{1g(H)}) \times \frac{1mol(hydride)}{1mol(H)} = 0.1mol(hydride)$$

6. Total of organics:

$$16.66\%(total) + \left(0.06mol(THF) \times \frac{1mol(O)}{1mol(THF)} \times \frac{16g(O)}{1mol(O)}\right) = 17.62\%(total)$$

7. Ru wt.% from total organics (for 100 mg of **Ru-0.05MPT**):

$$100\% - 17.62\% = 82.38\%(Ru)$$

From the two signals in the gas chromatography spectrum, we can calculate that the area of norbornane signals I 6.4% from the total area (norbornane + norbornene). Thus:

$$90mg(norbornene) \times \frac{1mmol(NNE)}{94.16mg(NNE)} \times 0.064 = 0.061mmol(norbornane)$$

$$0.061mmol(norbornane) \times \frac{2mmol(hydride)}{1mmol(NNA)} = 0.0122mmol(hydride)$$

3B.6 References

---

1 a) K. P. In *Organometallic Ruthenium Nanoparticles and Catalysis*, P. Lignier, B. Chaudret, in *Ruthenium in catalysis* **2014**, C. Bruneau and P.H. Dixneuf (Eds), Wiley VCH, Weinheim, **2014**, Top. Organomet. Chem. **2014**, *48*, 319-370; b) C. Amiens, B. Chaudret, D. Ciuculescu-Pradines, V. Collière, K. Fajerwerg, P. Fau, M. Kahn, A. Maisonnat, K. Soulantica, K. Philippot, *New J. Chem.* **2013**, *37*, 3374-3401.

2 S. Drouet, J. Creus, V. Collière, C. Amiens, J. García-Antón, X. Sala, K. Philippot, *Chem. Commun.* **2017**, *53*, 11713-11716.

3 R. Bofill, J. García-Anton, L. Escriche, X. Sala, A Llobet, *Comprehensive Inorganic Chemistry II* **2013**, *8*, 505-523.

4 a) J. Mahmood, F. Li, S. Jung, M. S. Okyay, I. Ahmad, S. Kim, N. Park, H. Y. Jeong, J. Baek, *Nature Nanotech.* **2017**, *12*, 441-446; b) Y. Zheng, Y. Jiao, Y. Zhu, L. H. Li, Y. Han, Y. Chen, M. Jaroniec, S. Qiao, *J. Am. Chem. Soc.* **2016**, *138*, 16174-16181; c) 4 J. Q. Chi, W. K. Gao, J. H. Lin, B. Dong, K. L. Yan, J. F. Qin, B. Liu, Y. M. Chai, C. G. Liu, *ChemSusChem* **2018**, *11*, 743-752; d) R. Ye, Y. Liu, Z. Peng, T. Wang, A. S. Jalilov, B. I. Yakobson, S. H. Wei, J. M. Tour, *ACS Appl. Mater. Interfaces* **2017**, *9*, 3785-3791.

5 I. Favier, S. Massou, E. Teuma, K. Philippot, B. Chaudret, M. Gómez, *Chem. Commun.* **2008**, *0*, 3296-3298.

6 a) J. Lee, S. A. S. Shah, P. J. Yoo, B. Lim, *Chem. Phys. Lett.* **2017**, *673*, 89-92; b) T. E. Lister, Y. V. Tolmachev, Y. Chu, W. G. Cullen, H. You, R. Yonco, Z. Nagy, *J. Electroanal. Chem.* **2003**, *554/555*, 71-76; c) J. Cheng, H. Zhang, H. Ma, H. Zhong, Y. Zou, *Electrchim. Acta* **2010**, *55*, 1855-1861; d) T. Bhowmik, M. K. Kundu, S. Barman, *ACS Appl. Mater. Interfaces* **2016**, *8*, 28678-28688.

7 a) E. A. Paoli, F. Masini, R. Frydenal, D. Deiana, C. Schlaup, M. Malizia, T. W. Hansen, S. Horch, I. E. L. Stephens, I. Chorkendorff, *Chem. Sci.* **2015**, *6*, 190-196; b) T. Reier, M. Oezaslan, P. Strasser, *ACS Catal.* **2012**, *2*, 1765-1772; c) S. Jung, C. C. L. McCrory, I. M. Ferrer, J. C. Peters, T. F. Jaramillo, *J. Mater. Chem. A* **2016**, *4*, 3068-3076; d) R. Matheu, L. Francàs, P. Chernev, M. Z. Ertem, V. Batista, M. Haumann, X. Sala, A. Llobet, *ACS Catal.* **2015**, *5*, 3422-3429.

8 K. Pelzer, O. Vidoni, K. Philippot, B. Chaudret, V. Colliere, *Adv. Funct. Mater.* **2003**, *13*, 118-126.

---

9 M. Guerrero, J. García-Antón, M. Tristany, J. Pons, J. Ros, K. Philippot, P. Lecante, B. Chaudret, *Langmuir* **2010**, *26*, 15532-15540.

10 a) M. Guerrero, A. Roucoux, A. Denicourt-Nowicki, H. Bricout, E. Monflier, V. Collière, K. Fajerwerg, K. Philippot, *Catal. Today* **2012**, *183*, 34-41; b) L. M. Martínez-Prieto, C. Urbaneja, P. Palma, J. Cámpora, K. Philippot, B. Chaudret, *Chem. Commun.* **2015**, *51*, 4647-4650.

11 F. Novio, K. Philippot, B. Chaudret, *Catal. Lett.* **2010**, *140*, 1-7.

12 a) M. Guerrero, Y. Coppel, N. T. T. Chau, A. Roucoux, A. Denicourt-Nowicki, E. Monflier, H. Bricout, P. Lecante, K. Philippot, *ChemCatChem* **2013**, *5*, 3802-3811; b) E. Bresó-Femenia, B. Chaudret, S. Castillón, *Catal. Sci. Technol.* **2015**, *5*, 2741-2751; c) X. Cui, A. Surkus, K. Junge, C. Topf, J. Radnik, C. Kreyenschulte, M. Beller, *Nature Communications* **2016**, *7*, Article number: 11326; d) Y. Morioka, A. Matsuoka, K. Binder, B. R. Knappett, A. E. H. Wheatley, H. Naka, *Catal. Sci. Technol.* **2016**, *6*, 5801-5805; e) A. D. Dwivedi, R. K. Rai, K. Gupta, S. K. Sin, *ChemCatChem* **2017**, *9*, 1930-1938.

13 a) A. C. Yang, C. W. Garland, *J. Phys. Chem.* **1957**, *61*, 1504-1512; b) B. L. Mojet, S. D. Ebbesen, L. Lefferts, *Chem. Soc. Rev*. **2010**, *39*, 4643-4655.

14 L. M. Martínez-Prieto, B. Chaudret, *Acc. Chem. Res.* **2018**, *51*, 376-384.

15 J. García-Antón, M. R. Axet, S. Jansat, K. Philippot, B. Chaudret, T. Pery, G. Buntkowsky, H.-H. Limbach, *Angew. Chem. Int. Ed.* **2008**, *47*, 2074-2078.

16 a) S. Jansat, K. Pelzer, J. García-Antón, R. Raucoules, K. Philippot, A. Maisonnat, B. Chaudret, Y. Guari, A. Medhi, C. Reyé, R. J. P. Corriu, *Adv. Funct. Mater.* **2007**, *17*, 3339-3347; b) V. Matsura, Y. Guari, C. Reyé, R. J. P. Corriu, M. Tristany, S. Jansat, K. Philippot, A. Maisonnat, B. Chaudret, *Adv. Funct. Mater.* **2009**, *19*, 3781-3787.

17 M. D. Segarra-Maset, P. W. N. M. van Leeuwen, Z. Freixa, *Eur. J. Inorg. Chem.* **2010**, 2075-2078.

18 S. Fukuzumi, Y. Yamada, *J. Mater. Chem.* **2012**, *22*, 24284-24296.

19 a) L. M. Martínez-Prieto, S. Carenco, C. H. Wu, E. Bonnefille, S. Axnanda, Z. Liu, P. F. Fazzini, K. Philippot, M. Salmeron, B. Chaudret, *ACS Catal.* **2014**, *4*, 3160-3168; b) E. Bresó-Femenia, C. Godard, C. Claver, B. Chaudret, S. Castillón, *Chem. Commun.* **2015**, *51*, 16342-16345.

20 S. Noël, D. Bourbiaux, N. Tabary, A. Ponchel, B. Martel, E. Monflier, B. Léger, *Catal. Sci. Technol.* **2017**, *7*, 5982-5992.

21 Y. Yamada, T. Miyahigashi, H. Kotani, K. Okubo, S. Fukuzumi, *J. Am. Chem. Soc.* **2011**, *133*, 16136-16145.

22 Q. Lu, F. Jiao, *Nano Energy* **2016**, *29*, 439-456.

3C. Hydrogen Evolution Catalysis with Ru-0.2PP NPs: Study of the Fate of the NPs in Catalysis

3C.1 Introduction

As already discussed, nano-sized catalysts present several attractive properties compared to molecular complexes,[1] already proven for numerous catalytic reactions[2,3] and more recently for water-splitting[4] as also described in sections 3A-3B. More specifically, in Chapter 3A a porous Ru nanomaterial prepared by the organometallic approach synthetic method gave rise to high electrocatalytic performance and excellent durability for HER.[5] Additionally, in the previous section 3B we described and structurally studied systems **Ru-0.05MPT** and **Ru-0.2PP**, with the latter showing impressive current densities when tested as HEC.

In this section we will report a more detailed evaluation in the HER of on the **Ru-0.2PP** catalyst (from now named **Ru1**). This nanomaterial is constituted of 1.5 nm RuNPs capped with the 4-phenylpyridine ligand. As shortly presented in section 3.B.3, this nanomaterial showed very low overpotentials (*η*), fast kinetics (Tafel slope and TOF) and excellent durability in both acidic and basic electrolytes, clearly outperforming commercial Ru black and being competitive to commercial Pt/C under the same reaction conditions. The catalytic performance of this new cathode is benchmarked with the state-of-the-art HER electrocatalysts and the factors controlling its activity are unraveled by combining spectroscopic and electrochemical techniques.

3C.2 Synthesis & characterization of Ru1

As already presented in the previous section 3B, **Ru1** was synthesized following the organometallic approach (Scheme 1) by decomposing the [Ru(cod)(cot)] (cod = 1,5-cyclooctadiene; cot = 1,3,5-cyclooctatriene) complex under H_2 atmosphere (3 bar) and at room temperature (r.t.), using THF as solvent and 4-phenylpyridine (**PP**) as stabilizing agent ([**PP**]/[Ru]= 0.2 molar equivalent). By this way, only the ligand voluntarily added as stabilizing agent (here the 4-phenylpyridine) is present on the metal surface, in addition to some THF and hydrides. A black colloidal dispersion was obtained from which the RuNPs were isolated under the form of a black powder, after precipitation by addition of pentane and drying under vacuum.

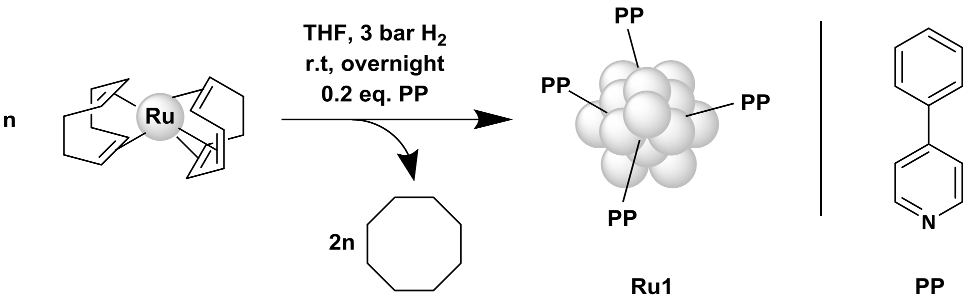

Scheme 1. Synthesis of **Ru1** with **PP** ligand chemical structure.

Transmission electron microscopy (TEM) analysis carried out from the crude colloidal solution after deposition of a drop on a carbon-covered copper grid, revealed the presence of very small NPs (Figure 1a), well-dispersed on the TEM grid, and displaying an average diameter of 1.5 ± 0.3 nm with a narrow size distribution (Figure 1b). Considering the standard deviation and other characterization such as TGA, EA and WAXS, **Ru1** and **Ru-0.2PP** from Ch. 3B are considered as the same system. At higher magnification (Figure 1c), some NPs close to each other or even coalesced are observed and various crystalline plans are visible. Electron diffraction patterns on a purified sample confirmed its crystalline character and allowed to measure interplanar distances (Figure 1d) as 0.2050, 0.1590, 0.1343 and 0.1142 nm, values in agreement with those of the (101), (102), (110) and (112) planes of the hexagonal compact crystalline (hcp) structure of bulk ruthenium.

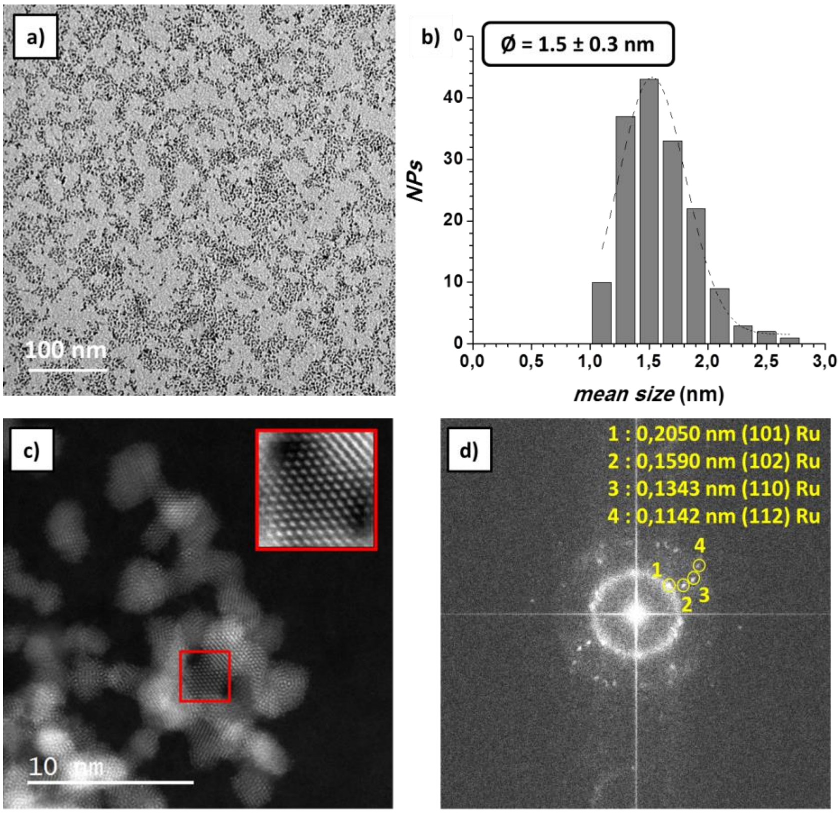

Figure 1. TEM image of **Ru1** at a) low magnification and b) corresponding size histogram); c) STEM-HAADF image and d) corresponding FFT diffraction pattern of **Ru1.**

Wide-Angle X-Ray Scattering (WAXS) analysis also confirmed the metallic character of the RuNPs and their hcp structure (see Figure 8b in Chapter 3B). A coherence length of ca. 1.5 nm could be determined (RDF, Figure 8c in Ch. 3B) in good agreement with the TEM data. Elemental (EA; Table 1) and thermogravimetric (TGA; red curve in Figure 2) analyses of **Ru1** led in both cases to an organic content in the sample of ca. 15% and so a high Ru content of ca. 85%. As commented in Ch. 3B, this Ru nanomaterial burned spontaneously when exposed to the air in solid state, a behavior that was previously observed with other RuNPs of similar sizes and stabilized with different ligands,[1] and also with **Ru-0.05MPT**. This phenomenon reveals a high reactive metal surface, which is assumed to derive from the small size of the NPs and the accessibility of their surface, although being coated by the **PP** ligand.

Table 1. Elemental composition calculated from TGA/EA results.

	Org. wt. % (TGA)	Org. wt.% (EA)	PP/Ru ratio
Ru1	14	16	0.14
Ru2	16	19	0.13

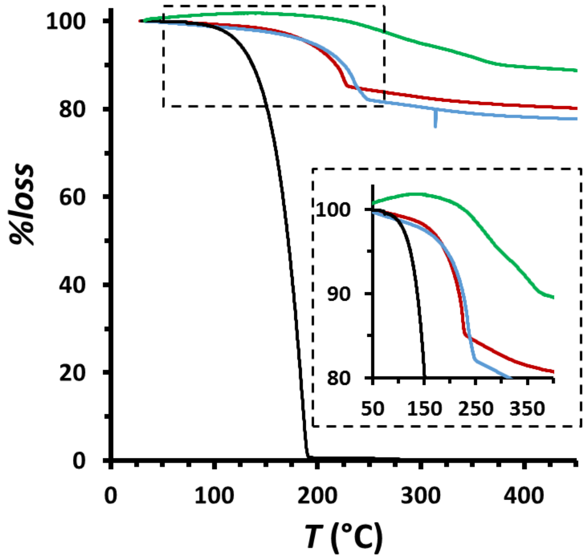

Figure 2. TGA of **Ru1** (red), **Ru2** (blue), **Ru1** after 20min bulk electrolysis at *j* = -10 mA·cm^{-2} (green) and **PP** ligand (clack).

Given the high reactivity of the **Ru1** nanomaterial when exposed to air, a protection appeared necessary to preserve its morphology before the electrocatalysis studies, which are performed in air and aqueous solutions. For this purpose **Ru1** was treated in the solid state by slow oxygen diffusion at r.t., leading to the **Ru2** nanomaterial (see Scheme 3 in the conclusions). The effect of this treatment on the oxidation state of the RuNPs was characterized by WAXS (Figure 14a in Ch. 3B), HRTEM-EDX (Figure 3a and b) and X-Ray Photoelectron Spectroscopy (XPS, Figure 3c). The three techniques indicated the presence of a mixture of Ru metal and Ru oxide in **Ru2**. This evidences a non-total oxidation of the particles that probably took place only at their surface, passivating them and avoiding an irreversible degradation.

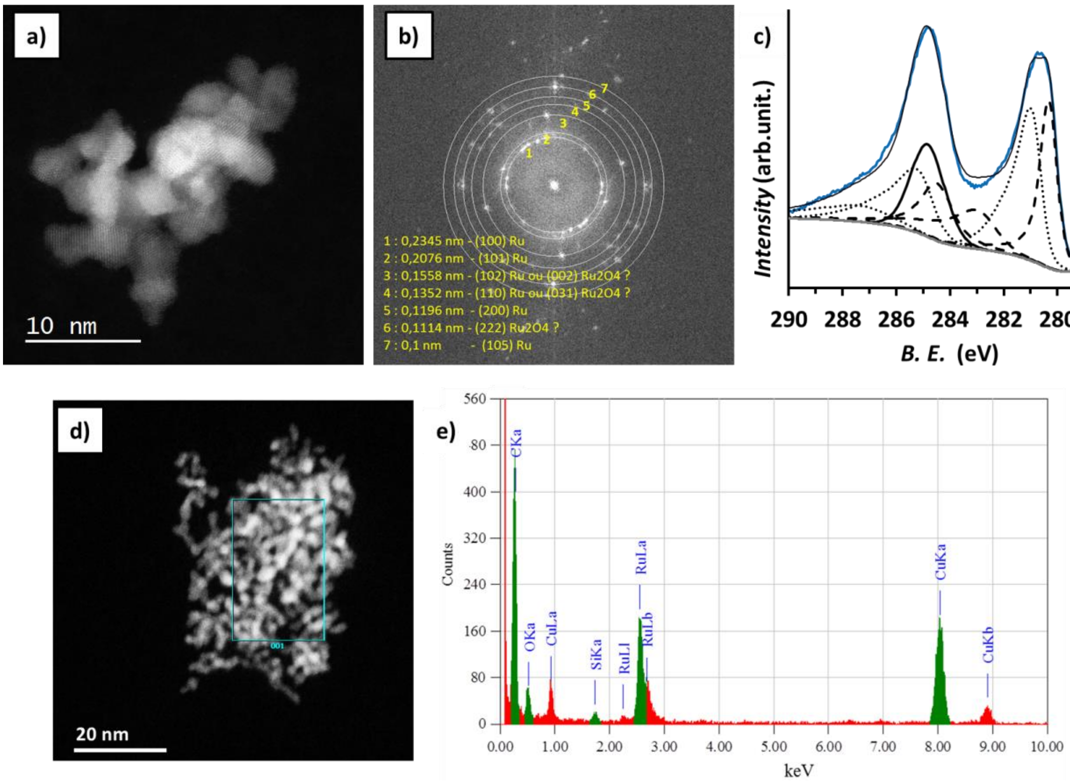

Figure 3. a) STEM-HAADF image and b) corresponding FFT diffraction pattern of **Ru2**. c) Powder XPS analysis of **Ru2** (blue). Fit of the signals: in dashed line, signals for metallic Ru (Ru $3d_{5/2}$-279.8, Ru $3d_{3/2}$-284.0 and satelite-283.2); in dotted line, signals for RuO_2 (Ru $3d_{5/2}$-280.8, Ru $3d_{3/2}$-285.0 and satelite-286.9); in thin black, envelope; in bold, carbon; in grey, background. d) STEM-HAADF image and e) corresponding EDX analysis of **Ru2**.

TGA and EA data (Figure 2 and Table 1, respectively) for **Ru1** and **Ru2** show similar % of organic content in both samples, as well as an invariable **PP**/Ru ratio, thus confirming the presence of the **PP** ligand also after passivation.

3C.2.1 Ligand coordination studies through DFT calculations

The coordination of the **PP** ligand onto the surface of the NPs (Ru_{surf}) was studied by Density Functional Theory (DFT) in order to unravel the most energetically favored configuration of the different coordination modes of the ligand. DFT calculations performed on a bare 1nm model and on its $1.2H/Ru_{surf}$ hydrogenated counterpart (simulating the results obtained for hydride titration in Ch. 3B, section 3B.2.4; $1.1H/Ru_{surf}$),[6] attested of the coordination of **PP** ligand at the Ru surface through two coordination modes. There is a competition between a vertical adsorption mode, ruled out by the σ-donation of the nitrogen lone pair (Figure 4a, **1σ$_{tip}$** mode) and an aromatic π-to-metal surface interaction, with a flat-lying configuration of **PP** where each aromatic cycle exhibits the well-known μ_3:η^2:η^2:η^2 face-capping mode of benzene (Figure 4b, **$1\pi_{001}$** mode).[7]

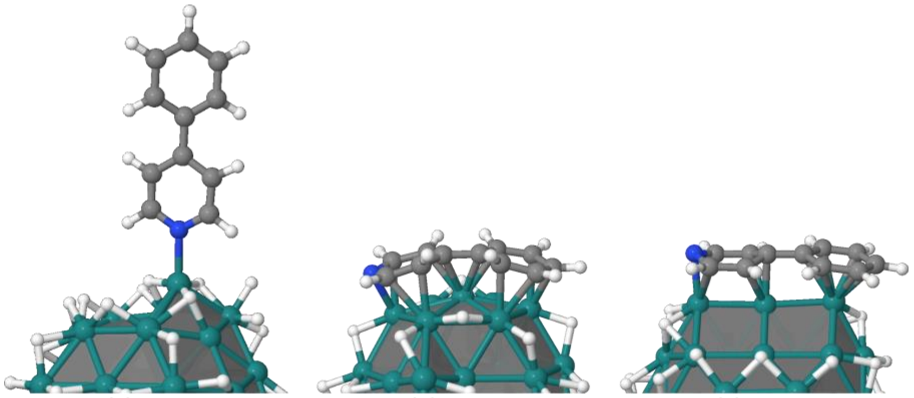
(a) $1\sigma_{tip}$ (b) $1\pi_{001}$ (c) $1\pi_{edge}$

Figure 4. σ (a) and π (b and c) coordination modes of **PP** on the $Ru_{55}H_{53}$ model (the faceting of the metal surface is highlighted. Geometries of **PP** and of the grafting metal site on the bare Ru_{55} model are very similar).

The π coordination of a single **PP** on one (001) facet of the bare RuNP model (Figure 4b) is stable by -83.2 kcal.mol^{-1}, whereas the σ bond (Figure 4a) is weaker by 49.8 kcal.mol^{-1} (see Table 2). Whilst the geometry of a σ-adsorbed **PP** is not different from the free species, with a ≈36° twist angle between the aromatic rings, it is significantly distorted in **$1\pi_{001}$**, since the two rings lie approximately in the same plane, with a pyramidalization of some C atoms. **PP**, which involves a lifting of the metal surface in the **$1\pi_{001}$** model, even exhibits a slightly curved shape. These moderate to strong adsorption energies are expected to be lowered for hydrogenated NPs, both owing to unfavorable electronic effects associated to the saturation of the metal adsorption sites by ligands, to slight distortions of the metal network, and to the steric hindrance involved by the saturation of the surface that overrides stabilization effects. Electronic effects are usually assessed through the so-called *d*-band center[8] of the metal core, which gets stabilized with respect to the Fermi energy upon ligand coverage, thus making further adsorption processes less favorable from a thermodynamic point of view.[6] To illustrate this, we considered a hydrogenated Ru_{55} model with 1.2H per surface Ru atom ($Ru_{55}H_{53}$), which accounts well with the 1.1H/Ru_{surf} experimental evidence (see section 3B.2.4 in sub-chapter 3B for experimental calculation).[9]

Table 2. Average adsorption energies of **PP** ligands (in kcal.mol^{-1}) on a bare Ru_{55} cluster model and on a hydrogenated counterpart, $Ru_{55}H_{53}$ (1.2H/Ru_{surf}). The average adsorption energy per **PP** ligand is calculated as E_{ads} = [E(nPP*) − E(RuNP) − nE(PP)]/n, where **PP*** designates an adsorbed **PP** ligand. Geometries are shown for the $Ru_{55}H_{53}$ model. All adsorption schemes considered on the $Ru_{55}H_{53}$ model have not been systematically evaluated on the bare model.

number of PP* (n)	adsorption mode	E_{ads} per PP		
		Ru_{55}	$Ru_{55}H_{53}$ (A)	
1	**1σ**[a]	-33.4	-32.1	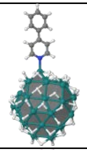
1	**1π**[b]	-83.2	-48.8	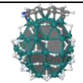
1	**1π**[c]	-63.6	-59.0	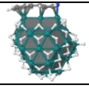
4	**4σ**	-	-24.2	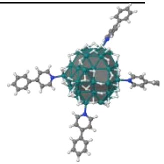
4	**4π**	-	-36.0	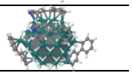
8	**8σ**	-	-22.3	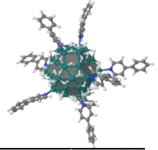
8	**4σ, 4π**	-	-25.7	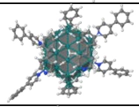
11	**9σ, 2π**	-	-24.1	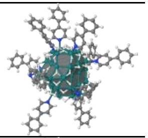
12	**12σ**	-	-20.3	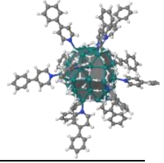

[a]: adsorption on the B_5 tip; [b]: adsorption on the 001 surface; [c]: adsorption on an edge

Whereas the σ adsorption strength is very little affected by the presence of surface H atoms (**1σ$_{tip}$**: -32.1 kcal.mol^{-1} on $Ru_{55}H_{53}$ *vs* -33.4 kcal.mol^{-1} on the naked RuNP), the π interaction becomes significantly less competitive (**1π$_{001}$**: -48.8 kcal.mol^{-1} vs. -83.2 kcal.mol^{-1}). This noticeable difference is both related to a stabilization of the *d*-band center of the 44 surface Ru atoms in $Ru_{55}H_{53}$ (2.9 eV *vs*. 2.6 eV for Ru_{55}) and to the sterically discomforted 53 hydrides on the remaining Ru surface area. The adsorption strength of **PP** on an edge was also evaluated, with an η^6-benzene ring and a μ:η^3:η^3-pyridine (**1π$_{edge}$** mode, see Figure 4c). Interestingly, it involves a weaker segregation of the H atoms than the **1π$_{001}$** mode does. As a consequence, the adsorption energy is similar to the bare NP case (**1π$_{edge}$**: -59.0 kcal.mol^{-1} vs. -63.6 kcal.mol^{-1}), and again a π coordination mode is significantly more stable than the σ grafting.

Let us now qualitatively evaluate the optimal number of **PP** ligands that the $Ru_{55}H_{53}$ model can accommodate. The co-adsorption properties of hydrides and **PP** ligands on the RuNP model could be theoretically evaluated within first-principles thermodynamics,[10] as it was recently applied to RuNPs in equilibrium with syngas,[6] but it is beyond the scope of the present study, and we only considered some trends with the same 1.2H/Ru$_{surf}$ RuNP model ($Ru_{55}H_{53}$). What is obvious from Figure 4 is that from a geometrical point of view it is possible to graft more σ-coordinated PPs than π-coordinated **PP**s within a unit surface area. We have also seen that to some extent the segregation of hydrides involved by the π coordination penalizes such mode on planar facets of RuNPs. Moreover, on the basis of electronic effects only, the higher the surface coverage, the lower the *d*-band center of the metal core and the weaker the adsorption strength of new ligands. As a consequence, several effects are expected to counterbalance. Firstly, the adsorption of one π-**PP** is stronger than the adsorption of two σ-**PP**s within the same surface area. Secondly, above a given surface coverage threshold, the segregation of H atoms involved by π-**PP**s adsorbed on planar or corrugated RuNP facets will become too high, thereby promoting σ-**PP**s upon π-**PP**s.

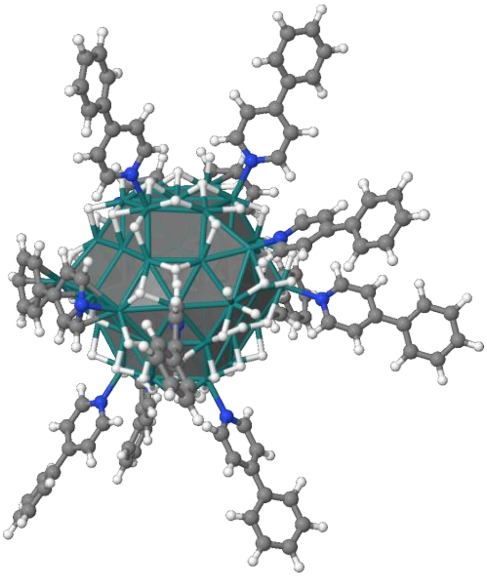

Figure 5. PP-protected 1 nm RuNP ($Ru_{55}H_{53}σPP_9πPP_2$).

With these simple ideas in hand, higher **PP** coverages were then considered on $Ru_{55}H_{53}$ (see Table 2). 4 π-**PP**s adsorb more strongly on the $Ru_{55}H_{53}$ model than 4 σ-**PP**s by ~12 kcal.mol^{-1}/PP (-36.0 kcal.mol^{-1}/**PP** vs. -24.2 kcal.mol^{-1}/**PP**). This large energy difference is significantly reduced when adding 4 new σ-**PP**s to these two configurations, the 8 σ-**PP**s geometry being stabilized by -22.3 kcal.mol^{-1}/**PP** whereas the (4 π-**PP**s, 4 σ-**PP**s) geometry is stabilized by -25.7 kcal.mol^{-1}/**PP**. The co-adsorption of 9 σ-**PP**s and 2 π-**PP**s (see Figure 5) is more stable than the adsorption of 12 σ-**PP**s (-265.2 kcal.mol^{-1} *vs.* -

243.4 kcal.mol^{-1}). It is also worth mentioning that an equilibrium between π-grafting and H_2-desorption may occur for the benefit of π-**PP**s on planar facets, given that, for example, the equilibrium reaction $Ru_{55}H_{53}$ + **PP** = $Ru_{55}H_{49}$**PP**(**1π$_{001}$**) + $2H_2(g)$ is exothermic by -12 kcal.mol^{-1}. All these results suggest that 1st) the saturation is reached around 12 **PP**s on this model (*i.e.* 0.27 **PP**/Ru_{surf} with this fixed 1.20 H/Ru_{surf} composition); and 2nd) the two σ and π grafting modes are expected to both occur on a given RuNP, with a versatile and rather strong π coordination.

In summary, DFT calculation allowed to demonstrate that **PP** ligand may be coordinated onto the NPs' surface in two possible configurations, namely σ-coordination from the pyridylic-N and π-interaction through the two aromatic rings, and that both of them probably coexist in a single NP.

3C.3 Electrocatalytic HER studies in 1 M H_2SO_4

The HER catalytic performance of **Ru2** was evaluated in 1 M H_2SO_4. A THF dispersion of **Ru2** was drop-casted onto a glassy carbon rotating disk electrode (RDE/GC) (see the Experimental part and Scheme 2 for further details on electrode preparation), to generate the **Ru2-GC** working electrode, which was introduced in a three-electrode cell together with a SCE (Saturated Calomel Electrode, KCl sat.) and a Pt grid as reference (RE) and counter (CE) electrodes, respectively.

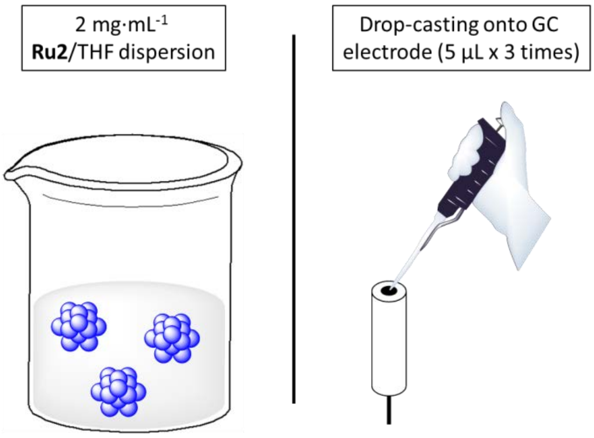
2 mg·mL^{-1}
Ru2/THF dispersion
Drop-casting onto GC electrode (5 µL x 3 times)

Scheme 2. Electrode preparation. Left, NPs dispersion in THF; right, drop-casting onto GC electrode.

For comparison purposes, the performances of commercial Pt/C and Ru black (Rub) were tested under the same experimental conditions, and the WE prepared using the same protocol and metal loading. The representative hydrogen evolution polarization curves of the three systems at 10 mV·s^{-1} scan rate and 3000 rpm (RDE rotation speed), are given in Figure 6a. In 1 M H_2SO_4 solution, both **Ru2-GC** and Pt/C (Figure 6, blue and grey curves, respectively) show a small onset overpotential (η_0) close to 0 mV, much lower than that of Rub (70 mV, orange curve). Together with η_0, another benchmarking parameter to compare the performance of heterogeneous catalysts is the overpotential value needed to achieve a current density of j = -10 mA·cm^{-2} (η_{10}).[11,12] **Ru2-GC** reaches this current density at η_{10} = 35 mV against 27 mV and 150 mV for Pt/C and Rub, respectively.

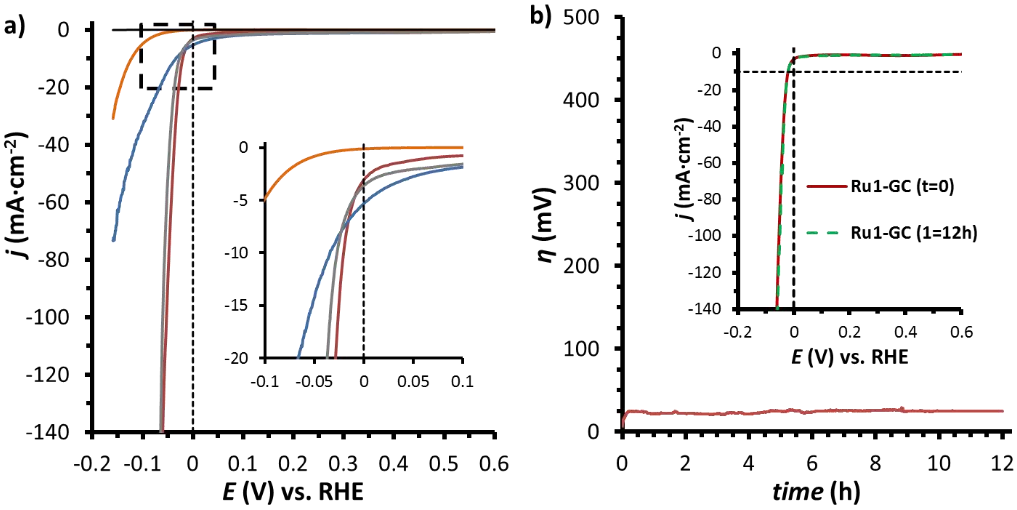

Figure 6. a) Polarization curves of **Ru1-GC** (red), **Ru2-GC** (blue), **Rub** (orange), commercial **Pt/C** (grey) and bare **RDE** (black) in 1 M H_2SO_4 solution; b) 12-hour bulk electrolysis experiment at j = -10 mA·cm^{-2} of **Ru1-GC** in 1 M H_2SO_4 solution. Inset, LSV experiment before and after bulk electrolysis.

The obtained η_0 and η_{10} values situate **Ru2-GC** within the best Ru-based systems in the literature (see Table A1 in Annex 1 for a comparison between the state-of-the-art HER electrocatalysts in acidic electrolytes), also very close to Pt/C. The catalytic performance of the system in 1 M aqueous H_2SO_4 solution can be significantly improved when submitted to a current-controlled bulk electrolysis at j = -10 mA·cm^{-2} for 20 minutes. As presented in Figure 6a (dark red), the resulting reduced system (**Ru1-GC**) shows a η_{10} of 20 mV, that is 7 and 130 mV less than Pt/C (27 mV) and Rub (150 mV), respectively, and reaches current densities as high as 1 A·cm^{-2} at an overpotential of only 120 mV, stating it as one of the best HECs reported so far.

Long-term stability is a key parameter for a catalyst to be potentially useful in the HER. Thus, **Ru1-GC** (1 M H_2SO_4) electrode was hold at a constant current density of j = -10 mA·cm^{-2} in a current-controlled experiment for 12h monitoring the change on the required overpotential. As shown in Figure 6b, **Ru1-GC** showed negligible change for η_{10} and identical LSV polarization curves before and after catalytic turnover. In addition, a Faradaic efficiency of 95% was determined by quantifying the amount of H_2 generated during an electrolysis using an H_2-probe (Figure 7a, red), and comparing it with the maximum amount of H_2 calculated from the total charge passed through the electrode (Figure 7a, black). This confirms the production of H_2 as the sole reaction taking place. Interestingly, after catalytic turnover the RuNPs are still visible on TEM images, indicating the high stability of our nanocatalyst.

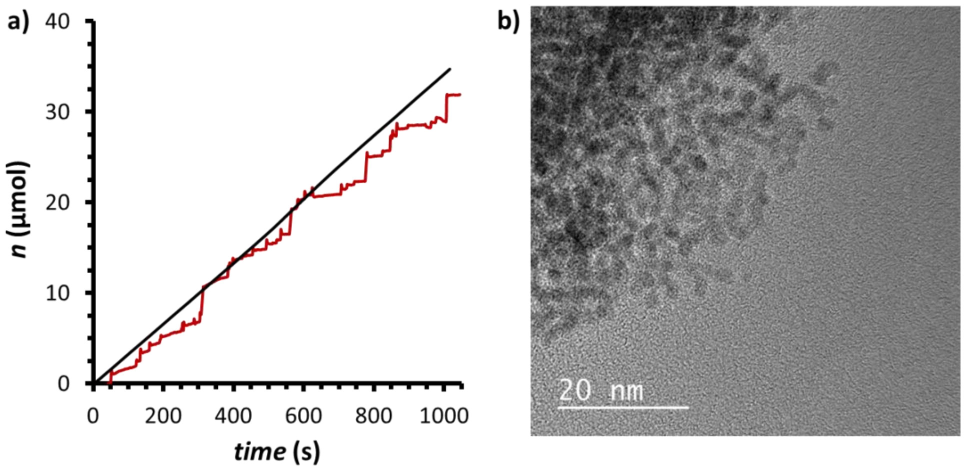

Figure 7. a) H_2-monitored (dark red) current-controlled bulk electrolysis (black) of **Ru1-GC** at *j* = -10 mA·cm^{-2} in 1 M H_2SO_4. The production of H_2 was monitored in the gas phase by the use of a Clark electrode. Faradaic efficiency ($\mathcal{E}$) = 95%. b) TEM images of **Ru1-GC** after 20 min bulk electrolysis at fixed *j* = -10 mA·cm^{-2} in 1 M M H_2SO_4.

In order to shed light on the nature of the new species formed in 1 M H_2SO_4 under reductive conditions, both **Ru2-GC** and **Ru1-GC** were analyzed by XPS (Figure 8a and b, respectively). As already mentioned for **Ru2**, a mixture of metallic Ru and RuO_2 is analogously observed for the **Ru2-GC** electrode with Ru $3d_{5/2}$ peaks centered at 279.8 eV (metallic Ru) and 280.8 eV (RuO_2).[13] For the **Ru1-GC** electrode, a total disappearance of the Ru $3d_{5/2}$ peak at 280.8 eV is noticed, thus indicating the reduction of superficial Ru^{IV} to metallic Ru under catalytic conditions.

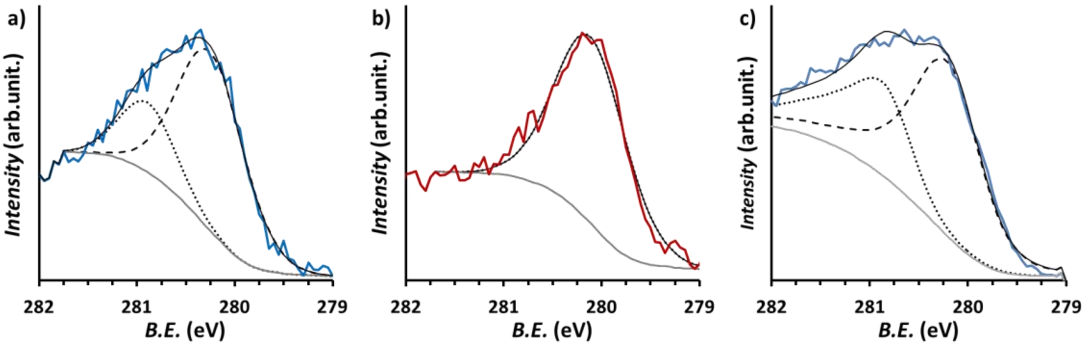

Figure 8. XPS analysis of a) **Ru2-GC** (blue), b) **Ru1-GC** (red) after 20 minutes bulk electrolysis at *j* = -10 mA·cm^{-2} in 1 M H_2SO_4, and c) **Ru2-GC** (blue) after 20 minutes bulk electrolysis at *j* = -10 mA·cm^{-2} in 1 M NaOH. Background (grey), metallic-Ru component (Ru $3d_{5/2}$-279.8, dashed black), RuO_2-component (Ru $3d_{5/2}$-280.8, dotted-black), envelope (bold).

After the reductive treatment, some material was recovered from the electrode in order to check the presence of **PP** ligand under those conditions, by performing TGA analysis (green curve in Figure 2). Material recovered from **Ru1-GC** showed similar organic content than its partially oxidized counterpart, thus confirming the presence of the **PP** ligand in the nanomaterial after reductive treatment.

As shown in Figure 9a, the passivation process of **Ru1-GC** can be monitored electrochemically by dipping this electrode in an aerated 1 M H_2SO_4 solution and recording LSV polarization curves at different times. As surface metallic Ru in **Ru1-GC** gets oxidized and RuO_2 is formed (see XPS data in Figure 8a), a progressive decrease of the catalytic current associated to the HER is observed, with LSV-4h (Figure 9a) finally resembling the electrochemical signature of **Ru2-GC**.

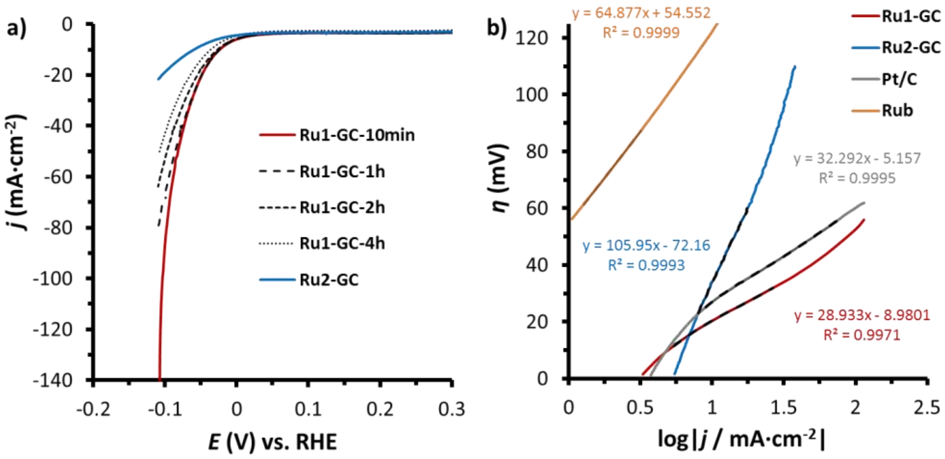

Figure 9. a) Polarization curves of **Ru1-GC** (after 10 minutes, electrode and electrochemical set-up preparation time) and subsequent curves, and **Ru2-GC** (blue) in 1 M H_2SO_4. b) Tafel plot of **Ru1-GC** (dark red), **Ru2-GC** (blue), Pt/C (grey) and Rub (orange) in 1 M H_2SO_4.

The different nature and catalytic performance of **Ru1-GC** and **Ru2-GC** in 1 M H_2SO_4 are evidenced through their corresponding Tafel plots (see Figure 9b). **Ru1-GC** shows a very low Tafel slope (29 $mV·dec^{-1}$), inferior to that of Pt/C (32 $mV·dec^{-1}$) and Rub (65 $mV·dec^{-1}$) under the same reaction conditions and metal loading, thus pointing to a Tafel-Volmer mechanism where the rate-determining step is the formation and desorption of molecular H_2 at the catalyst surface by the recombination of two metal-hydride species.[14] The low Tafel slope also indicates that **Ru1-GC** is able to reach high current densities at low overpotentials, a critical characteristic in order to attain practical applications. Contrarily, the 106 mV Tafel slope observed for **Ru2-GC** indicates a Tafel-Heyrovsky mechanism, in this case through the interaction of a M-H species with a H^+ on the media. This change on the mechanism devoted to the presence of RuO_2 species on the surface of the RuNPs, could be attributed to a longer distance between two M-H species, which would hinder their interaction and thus the Volmer step.

3C.4 Electrocatalytic HER studies in 1 M NaOH

The HER performance of **Ru2-GC** in 1 M NaOH is also remarkable (Figure 10a), with η_0 of ca. 0 mV and η_{10} of 25 mV, values lower than those of Pt/C (5 and 35 mV, respectively) and Rub (50 and 125 mV, respectively), under the same reaction conditions. These values situate **Ru2-GC** within the best Ru-based systems reported so far in basic media (see Table A2 in Annex 1 for a comparison between the state of the art HER catalysts in basic electrolytes).

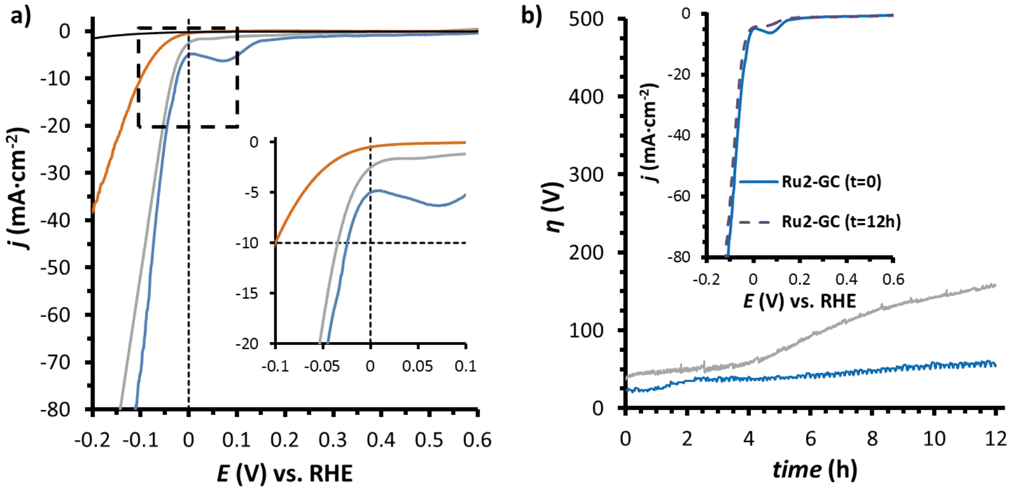

Figure 10. a) Polarization curves of **Ru2-GC** (blue), **Rub** (orange), commercial **Pt/C** (grey) and bare **RDE** (black) in 1 M NaOH solution at a 10 mV·s^{-1} scan rate and inset of the onset overpotential zone. b) 12-hour bulk electrolysis experiment at j = -10 mA·cm^{-2} of **Ru2-GC** (blue) and Pt/C (grey) in 1 M NaOH solution; inset, LSV experiment of **Ru2-GC** before (bold) and after (dashed) bulk electrolysis.

In contrast to its behavior in 1 M H_2SO_4, **Ru2-GC** does not evolve under reductive conditions (current-controlled bulk electrolysis at j = -10 mA·cm^{-2} for 20 minutes) in 1 M NaOH, showing identical electroactivity before and after the reductive treatment, even after 12h (Figure 10b, inset). These results confirm, as expected, the higher stability of the RuO_2 phase under basic conditions that is further corroborated by XPS analysis of the electrolyzed sample (Figure 8c). Comparison of Figure 8a and Figure 8c evidences a similar nature for both species, and the stability of the RuO_2 phase present at the surface of **Ru2-GC** under reductive basic conditions.

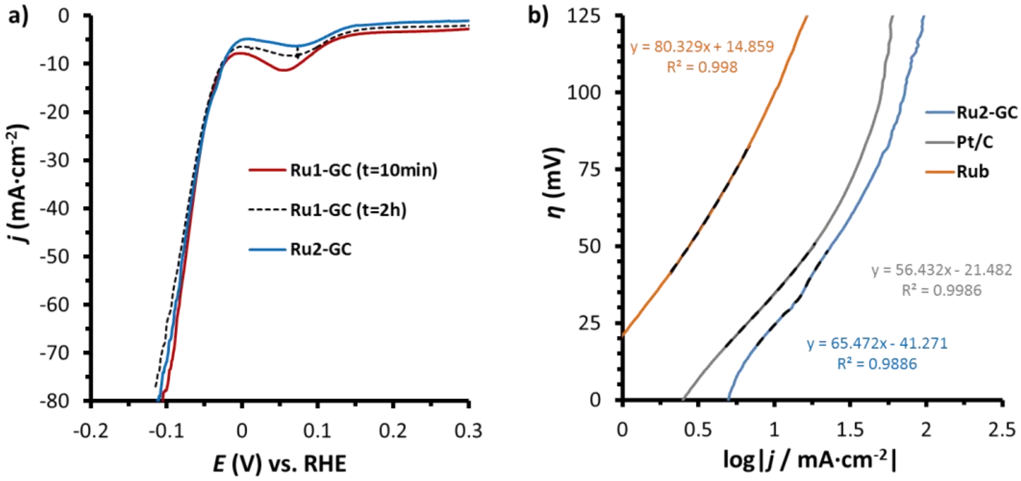

Figure 11. a) Polarization curves of **Ru1-GC** (dark red, after 10 minutes, electrode and electrochemical set-up preparation time) and at t=2h (dashed black), and **Ru2-GC** (blue) in 1 M NaOH. b) Tafel plot of **Ru2-GC** (blue), Pt/C (grey) and Rub (orange) in 1 M NaOH.

Analysis of the Tafel plot in 1 M NaOH solution (Figure 11b) shows a slope of 65 mV·dec^{-1} for **Ru2-GC**, 56 mV·dec^{-1} for Pt/C and 80 mV·dec^{-1} for Rub which as in the case of acidic media, could be associated to a Tafel-Heyrovsky mechanism where the rds is the H_2 formation and desorption.

Long-term stability current-controlled bulk electrolysis experiment at j = -10 mA·cm^{-2} was also performed in the case of **Ru2-GC** (1 M NaOH), which shows as well good stability, with η_{10} increasing in only 25 mV over the 12h electrolysis (Figure 10b). The notorious long-term stability of **Ru2-GC** in basic media was further evidenced by comparison with that of Pt/C under the same conditions, where η_{10} increased in more than 250 mV over the 12h electrolytic test.

Again, a Faradaic efficiency of 95% was determined by quantifying the amount of H_2 generated during electrolysis (Figure 12a), confirming the production of H_2 as the sole reaction taking place. In this case the RuNPs are also still visible on TEM images, indicating the high stability of our nanocatalysts (Figure 12b).

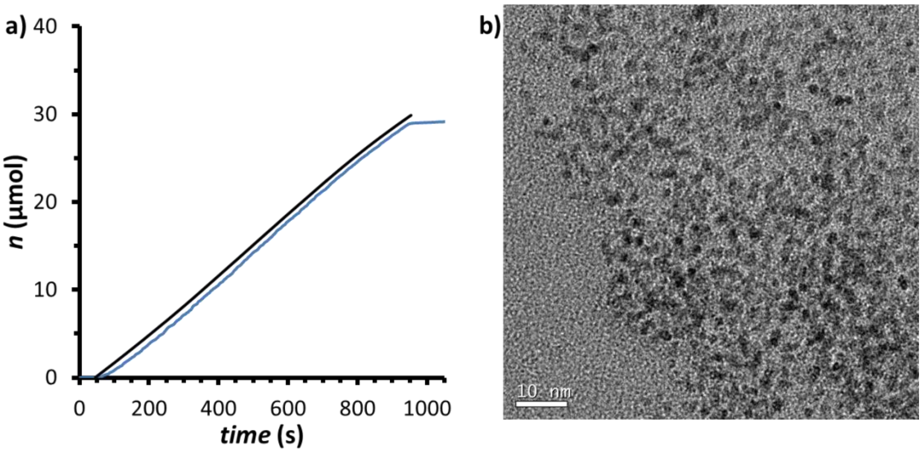

Figure 12. a) H_2-monitored (blue) current-controlled bulk electrolysis (black) of **Ru2-GC** at j = -10 mA·cm^{-2} in 1 M NaOH. The production of H_2 was monitored in the gas phase by the use of a clark electrode. Faradaic efficiency ($\mathcal{E}$) = 97%. b) TEM images of **Ru2-GC** after 20 min bulk electrolysis at fixed j = -10 mA·cm^{-2} in 1 M NaOH.

The excellent durability of our catalytic system in acidic and basic conditions indicates both, good mechanical stability of the cathode (no need of polymeric gluing agents between RuNPs and GC) and no aggregation of the RuNPs under turnover conditions. We believe these findings result from the presence of the **PP** capping agent that allows maintaining the nanostructured character of the material.

3C.5 Electrocatalytic performance benchmarking

The electrocatalytic performance and short-term stability of **Ru1-GC** (1 M H_2SO_4) and **Ru2-GC** (1 M NaOH) was further compared with that of other electrocatalysts following the benchmarking methodology reported by Jaramillo *et al.*[15] From the capacitive current in a non-Faradaic zone, which is only associated with double-layer charging, the double-layer capacitance (C_{DL}) was estimated (see Experimental part for calculation details). Then, the electrochemically active surface area (ECSA) of both electrodes was calculated from the C_{DL} (Figure 13).

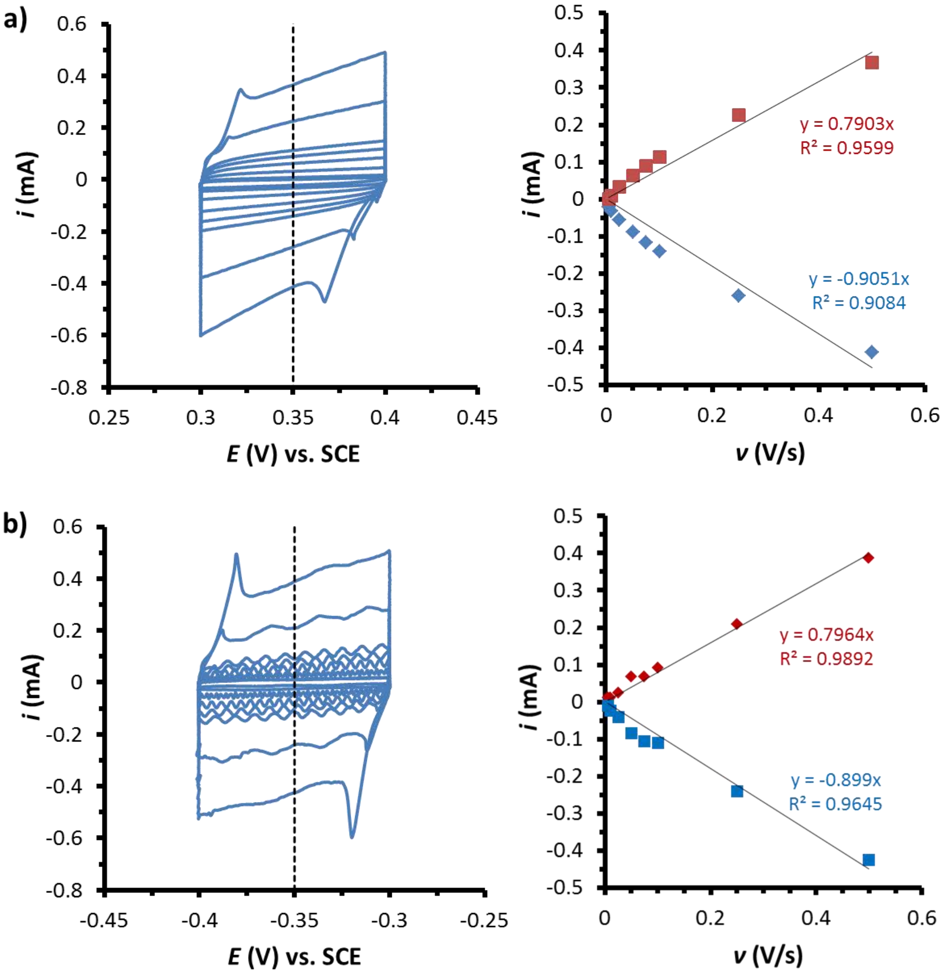

Figure 13. Left, representative multi CV experiment at different scan rates for C_{DL} determination in, and right, plot of current values at -0.35 V (vs. SCE) for the different scan rates, for C_{DL} determination, in a) 1 M H_2SO_4 and b) 1 M NaOH.

The roughness factor (RF) was calculated by dividing the estimated ECSA by the geometric area of the electrode (S = 0.07 cm^2). The ECSA value allows calculating the specific current density (j_S) of the electrode (current density per “real” electroactive area of the system) at a given overpotential. The obtained values of η_{10} at time = 0 and time = 2h and j_S at η = 100 mV ($j_{s(\eta=100)}$) are reported in Tables A3-A4 and plotted in Figure 14, together with those reported for selected HER catalysts benchmarked with the same methodology in acidic 1 M H_2SO_4 (η_{10} < 100 mV) and basic 1 M NaOH (η_{10} < 150 mV) solutions.

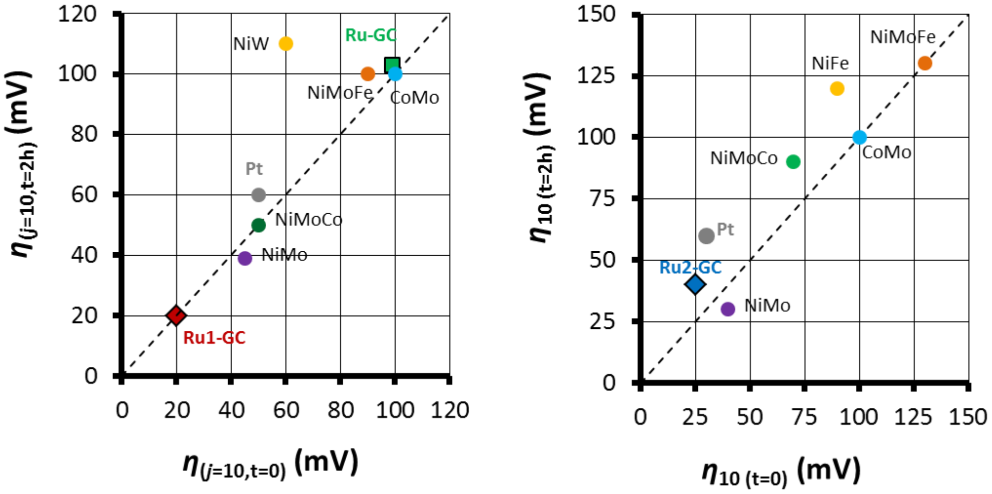

Figure 14. Graphical representation comparison of HEC by Jaramillo's methodology in 1 M H_2SO_4 (left) and 1 M NaOH (right).

Both **Ru1-GC** (acidic conditions) and **Ru2-GC** (basic conditions) show the lowest η_{10} (20 and 25 mV, respectively) among the reported systems (see Tables A3-A4). Thus, **Ru1-GC** and **Ru2-GC** outperform Pt in both electrolytes, which shows η_{10} of 50 (**Ru1-GC,** 1M H_2SO_4) and 30 mV (**Ru2-GC**, 1 M NaOH) and an increase to 60 mV in both media after 2h of electrolysis. The specific current density values observed at η = 100 mV (0.55 mA·cm^{-2} for **Ru1-GC** in acidic media and 0.19 mA·cm^{-2} for **Ru2-GC** in basic media) are between 2 and 137 times higher than those reported for all the benchmarked catalysts except Pt which, despite of the same order, shows superior values (see Tables A3-A4).

Further information about the intrinsic electrocatalytic activity of our Ru nanomaterials was obtained by calculating TOF values. This was made on the basis of estimated numbers of active sites determined through the underpotential deposition (UPD) of copper.[16,4] The method consists on applying a reductive potential to the WE in an electrochemical set-up with a 5 mM $CuSO_4$ solution, to electroreduce Cu^{2+} in the form of Cu^0 only on the Ru^0-active sites. The subsequent polarization curve towards oxidative potentials in a Cu-free H_2SO_4 solution, displays an oxidative wave devoted to the re-oxidation of Cu^0 to Cu^{2+}, with the area below the curve proportional to the number of electrons used for the oxidation and thus proportional to the deposited Cu and Ru-active species. Figure 15 shows the resulting curves for a) **Ru1-GC**, b) **Ru2-GC**, c) Pt/C and d) Rub, in acidic solution. As can be seen, **Ru2-GC** (Figure 15b) shows almost no Cu oxidation after the UPD process, confirming the passivation of the NPs' surface and thus the decrease on the number of Ru^0 surface species.

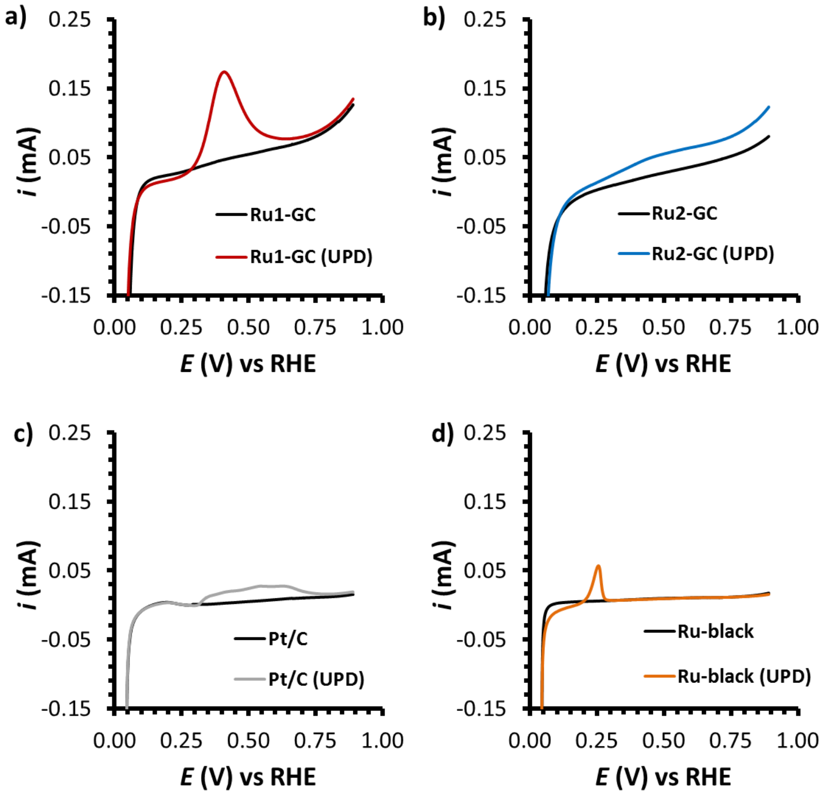

Figure 15. Copper UPD in 1 M H_2SO_4 solution before (black line) and after (colorful line) of a) **Ru1-GC**, b) **Ru2-GC**, c) **Pt/C** and d) **Ru-black**.

The calculated TOF values for **Ru1-GC** in 1 M H_2SO_4 at 25, 50 and 100 mV (vs. RHE) are 0.55, 3.06 and 17.38 s^{-1}, respectively, which are of the same order than those of Pt/C (1.65, 5.60 and 23.36 s^{-1}) under the same reaction conditions (Table A1 and Figure 16), and significantly higher than those of Rub. Tables A1-A2 allow to compare these TOF values with those reported for other relevant electrocatalysts for a wide set of transition metals, which highlights the fast kinetics of **Ru1-GC**, which outperforms the other systems.

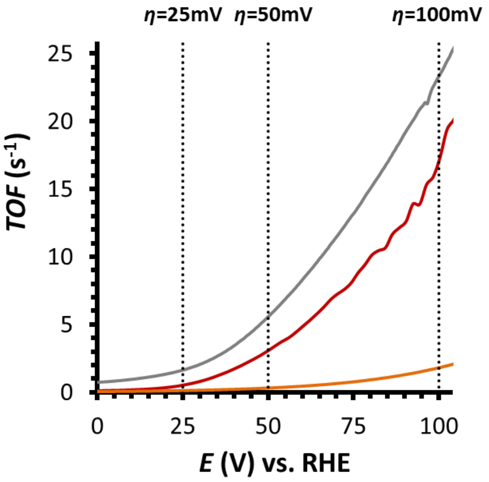

Figure 16. TOF vs. *E* (V) graph of **Ru1-GC** (red), **Pt/C** (grey) and **Rub** (orange) systems in 1 M H_2SO_4. Data obtained by dividing current intensity *i* = [mA] by the charge under the Cu-UPD wave in each case.

3A.6 Conclusions & perspectives

In summary, the application of the organometallic approach as synthetic method allowed obtaining very small and homogeneous-in-size, 4-phenylpyridine-capped RuNPs that are highly active for the HER in both acid and basic media. After partial surface oxidation, the catalytic activity of the resulting GC-deposited nanomaterial (**Ru2-GC**) in 1 M H_2SO_4 solution is highly dependent on the oxidation state of the NPs' surface, being metallic Ru sites clearly more active than RuO_2 ones. Maximization of the former's from the starting Ru/RuO_2 mixture while preserving the stabilizing ligand (**Ru1-GC**) is achieved through a short reductive treatment in the acidic electrolyte. In 1 M H_2SO_4 **Ru1-GC** beats commercial Ru black and is competitive or even superior to commercial Pt/C. It works at very low overpotentials ($\eta_0 \approx 0$ mV, $\eta_{10} = 20$ mV), presents a particularly low Tafel slope (29 mV·dec^{-1}), achieves TOFs as high as 17 s^{-1} at η = 100 mV and high specific current densities at η = 100 mV of 0.55 mA·cm^{-2}, and is capable to produce a current density of j = -10 mA·cm^{-2} for at least 12h without any sign of deactivation, while preserving the original morphology of the nanocatalyst.

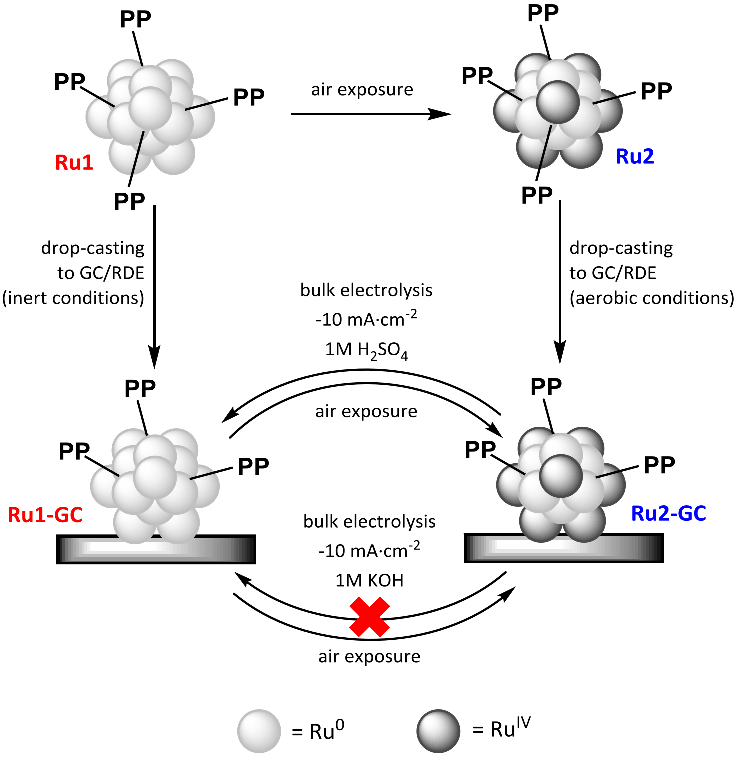
PP
PP
PP
PP
Ru1
air exposure
PP
PP
PP
PP
Ru2
drop-casting
to GC/RDE
(inert conditions)
drop-casting
to GC/RDE
(aerobic conditions)
bulk electrolysis
-10 mA·cm^{-2}
1M H_2SO_4
air exposure
PP
PP
PP
Ru1-GC
PP
PP
PP
Ru2-GC
bulk electrolysis
-10 mA·cm^{-2}
1M KOH
air exposure
= Ru^0
= Ru^{IV}

Scheme 3. Preparation strategy for the different Ru-NPs systems and electrodes used in this work. Grey spheres represent Ru atoms, while darker spheres represent oxidized Ru(IV) surface atoms.

In contrast, as evidenced by XPS, the original Ru/RuO_2 mixture present in **Ru2-GC** is preserved when 1 M NaOH is used as electrolyte, even under reductive catalytic conditions. The estimation of surface active sites and electroactive surface area by well stablished methods allowed benchmarking these new catalytic systems with other relevant catalysts in the literature, confirming them as two of the best HER electrocatalysts reported so far. Thus, in 1 M NaOH solution, **Ru2-GC** displays very low overpotentials ($\eta_0 \approx 0$ mV, $\eta_{10} = 25$ mV) and even better to those of commercial Pt/C and Rub. **Ru2-GC** in 1 M NaOH solution also fairly outperforms them in short and long-term stability tests by well preserving the RuNPs under catalytic turnover.

DFT calculations allowed unraveling which types of coordination may the ligand adopt onto the surface of the NP, the final configuration being proposed as a mixture of σ-coordination through the pyridylic-N group and π-coordination from the two aromatic groups. Further theoretical studies complemented by additional characterization may give information on a plausible change on the **PP** coordination after air exposure of the metallic NPs, and the corresponding surface oxidation. Depending on the available surface sites (considering the ligand coverage onto faces, edges or apexes) and comparing the studies with other RuNPs, the observed catalytic performance could be assigned to a specific position, being this information of paramount importance for the future development of new nanocatalysts.

All together, these results highlight the potential of designing and preparing ligand-stabilized nanocatalysts for the HER and, therefore, paves the way to the fine tuning of the catalytic properties of these nanocatalysts through the limitless strategy of ligand capping, as done for molecular catalysts.

In the perspective of gaining knowledge on the role of the **PP** ligand for achieving the high activities observed, the stabilization of RuNPs performed with similar molecules tas the **PP** could be beneficial. For example, the use of 4-cyclohexylpyridine or the incorporation of a bulky group on the phenyl moiety, both would allow understanding the contribution of this aromatic group on the stabilization and catalytic performance of the NPs. Additionally, the obtaining of **PP**-stabilized RuNPs of other sizes (namely 5, 10, 25 and 100 nm) by the modification of synthetic parameters, would allow on the adquisition of NPs with different characteristics (such as bigger faces or longer apexes), permitting a correlation of those properties with the corresponding associated catalytic activites.

This work will be submitted for publication in June 2018 (4-Phenylpyridine-capped Ru Nanoparticles as Efficient Electrocatalyst for the Hydrogen Evolution Reaction, J. Creus, S. Drouet, S- Suriñach, P. Lecante, V. Collière, R. Poteau, K. Philippot, J. García-Antón, X. Sala).

3A.7 Experimental part

Reagents. All operations for the synthesis of **Ru1** NPs were carried out using standard Schlenk tubes, Fisher–Porter bottle techniques or in a glove-box (MBraun) under argon atmosphere. Solvents (THF and pentane) were purified before use, by filtration on adequate column in a purification apparatus (MBraun) and handled under argon atmosphere. Solvents were degassed before use according to a freeze–pump–thaw process. The ruthenium precursor, [Ru(cod)(cot)], was purchased from Nanomeps-Toulouse. Hydrogen gas (Alphagaz) was purchased from Air Liquide. 4-Phenylpyridine (**PP**) used as a stabilizer was purchased from Sigma-Aldrich and used as received. High purity deionized water was obtained by passing distilled water through a nanopore Milli-Q water purification system.

Synthesis of Ru1. (120 mg, 0.38 mmol) of [Ru(cod)(cot)] and (12 mg, 0.08 mmol) of 4-phenylpyridine were dissolved under argon in 120 mL of THF in a Fisher porter reactor inside a Glove-box. After pressurization of the reactor with 3 bar of H_2 at room temperature (r.t.), the initial yellow solution turned dark brown in a few minutes. A vigorous magnetic stirring and the H_2 pressure were maintained for 16 h. After this reaction time, the H_2 pressure was evacuated and a drop of the colloidal solution was deposited onto a carbon-covered copper grid for TEM analysis. **Ru1** was isolated as a dark grey powder after precipitation by pentane addition and evaporation to dryness under vacuum.

Characterization. The crude colloidal solution has been characterized by Transmission Electron Microscopy (TEM), High Resolution TEM (HRTEM) and the isolated solid by Wide-Angle X-Ray Scattering (WAXS), X-Ray Photoelectron Spectroscopy (XPS), Elemental Analysis (EA) and ThermoGravimetric Analysis (TGA).

Transmission Electron Microscopy (TEM) and High resolution TEM (HRTEM). Samples for transmission electron microscopy (TEM) analyses were prepared by slow evaporation of a drop of the crude colloidal solution deposited onto a carbon-covered copper grid. Samples for high-resolution transmission electron microscopy (HRTEM) analyses were prepared by the same way from purified NPs re-dispersed in THF. TEM and HRTEM analyses were performed at the “Centre de Microcaractérisation Raymond Castaing” in Toulouse (UMS-CNRS 3623), on a MET JEOL JEM 1011 microscope operating at 100 kV with a point resolution of 0.45 nm and a JEOL JEM-ARM 200F microscope working at 200 kV with a point resolution lower of 0.19 nm, respectively. TEM allowed evaluating the particle size, size distribution and morphology. Enlarged micrographs were used for treatment with ImageJ software to obtain a statistical size distribution and the nanoparticle mean diameter. FFT treatments of HRTEM images were carried out with Digital Micrograph Version 1.80.70 to determine the crystalline structure of the material. The analyses were done by assuming that the nanoparticles are spherical. Nanoparticle sizes are quoted as the mean diameter ± the standard deviation.

Wide-angle X-Ray scattering (WAXS). Measurements were performed at CEMES-CNRS in Toulouse. Samples were measured in 1.0 mm diameter Lindemann glass capillaries. The samples were irradiated with graphite monochromatized molybdenum Kα (0.071069 nm) radiation and the X-Ray scattering intensity measurements were performed using a dedicated two-axis diffractometer. Radial distribution functions (RDF) were obtained after Fourier transformation of the corrected and reduced data.

X-Ray Photoelectron Spectra (XPS). Measurements were performed at the Catalan Institute of Nanoscience and Nanotechnology (ICN2) in Barcelona with a Phoibos 150 analyzer (SPECS GmbH, Berlin, Germany) in ultra-high vacuum conditions (base pressure $5E^{-10}$ mbar) with a monochromatic aluminium Kalpha X-Ray source (1486.74 eV). The energy resolution was measured by the FWHM of the Ag $3d^{5/2}$ peak for a sputtered silver foil was 0.62 eV.

ThermoGravimetric Analysis (TGA). Thermogravimetric analysis was performed in a Perkin Elmer TGA 7 analyzer. Measurements were carried out in a 30-500 °C temperature range in continuous heating regimes (2 °C/min) under Ar atmosphere.

The percentage of ligand in the sample was calculated as follows. From the experiment carried out on the ligand alone we could attribute the beginning of the ligand loss at 140 °C. So, the value of loss noticed at this temperature was taken as initial value. For the final ligand loss point, the value observed at the change of the slope was taken. The latter was then subtracted from the former to obtain the ligand percentage on each sample.

Elemental analysis (EA). EA was performed at the Laboratoire de Chimie de Coordination (LCC), Toulouse, on a Perkin-Elmer 2400 series II analyzer.

PP/Ru calculation. Number of mol (*n*) of **PP** was calculated from N wt.% obtained by EA and Ru wt.% was estimated from a) remaining wt.% after TGA's drop in the 130-250 °C range, attributed to organics and b) remaining wt.% subtracting organics (CHN) from EA results. Then, dividing *n*(PP) by *n*(Ru) gave rise to comparable ligand-to-metal ratios through calculations from both TGA/EA data.

Electrochemical measurements. All the electrochemical experiments were performed in a BioLogic SP-150 potentiostat. Rotating disk electrode (RDE) was rotated at 3000 rpm in order to ensure complete removal of *in*-situ formed H_2 bubbles. The solutions were degassed previous to the electrochemical analysis with a N_2 flow. Ohmic potential (IR) drop was automatically corrected at 85 % using the Biologic EC-Lab software for cyclic voltammetry and chronoamperometry. For chronopotentiometry experiments IR drop was manually corrected ($E_{mod} = E_{meas} + E_{IR}$, mod=modified and meas=measured) at 85% by adding the corresponding potential value $E_{IR} = i_{exp}$ x (R_{mes} *x 0.85)*, where i_{exp} is the applied current in A and R_{mes} is the measured resistance in Ω. 1 M H_2SO_4 solution was prepared by mixing 56.1 mL of 95-97 % H_2SO_4 in 1 liter of Mili-Q water. 1 M NaOH solution was prepared by mixing 4 g in 100 mL of Mili-Q water.

Either a glassy carbon disk (GC$_d$, ϕ = 0.3 cm, S = 0.07 cm^2), a rotating disk electrode (RDE, ϕ = 0.3 cm, S = 0.07 cm^2) or a Fluorine-dopped Tin Oxide electrode (FTO, 20 mm x 10 mm x 180 µm), were used as working electrodes (WE). In the case of FTO the surface dipped in the electrochemical solution was 1 cm^2. For GC$_d$ and FTO electrodes the experiment was magnetically stirred with a stirring bar.

A Pt grid was used as counter electrode (CE) and a Saturated Calomel Electrode (SCE, Hg/Hg_2Cl_2, KCl sat.) was used as a reference electrode (RE), except for the hydrogen-monitored bulk electrolysis that a Ag/AgCl (KCl sat.) was used as RE. All data was transformed to RHE by adding +0.24 V and +0.20 V for SCE and Ag/AgCl, respectively.

Electrode Preparation. A 2 mg·mL^{-1} dispersion was prepared by adding 1 mg of RuX (X=1, 2) in 500 µL of THF and sonicating for 30 min. Then, an aliquot of 5 µL (for GC$_d$ and RDE) was added on the surface of the GC (S = 0.07 cm^2), and dried with a N_2 flow. This procedure was repeated three times to obtain RuX-GC (X=1, 2). For FTO WE, a dispersion aliquot of 25 µL was added to the surface of the FTO (S = 1 cm^2), and dried with N_2. See Scheme 2 for schematic representation. For Pt/C and Rub, dispersions ensuring a similar metal mass loading on the RDE than for RuX-GC were prepared.

Double-layer capacitance (C_{DL}) and electrochemically active surface area (ECSA) determination. C_{DL} was estimated by CV. A non-Faradaic region was chosen from the LSV (typically a 0.1 V window about OCP), where no redox process takes place and all the measured current is due to double-layer charging (versus SCE, 0.35 V for 1 M H_2SO_4 and -0.35 V for 1 M NaOH). Based on this assumption, the charging current (i_c) can be calculated as the product of the electrochemical double-layer capacitance (C_{DL}) and the scan rate (v), as shown in Eq. 1:

$$i_c = vC_{DL} \qquad \text{Eq. 1}$$

Plotting i_c as a function of v yields a straight line with slope equal to C_{DL}. In this way, 8 different scan rates were used (5, 10, 25, 50, 75, 100, 250 and 500 mV/s), holding the working electrode at each potential vertex for 10 seconds prior to the next step.

ECSA was obtained by dividing the calculated capacitance to a tabulated value (specific capacitance, C_S) that depends on the material used and solution (for C, in 1M H_2SO_4 C_S=13-17 µF·cm^{-2}, in 1 M NaOH C_S= 40 µF·cm^{-2}):

$$ECSA[cm^2] = \frac{C_{DL}}{C_S} \qquad \text{Eq. 2}$$

$$RF = \frac{ECSA}{S} \qquad \text{Eq. 3}$$

Roughness factor (RF) was calculated by dividing the ECSA by the geometrical surface area (*S*).

Copper Under potential Deposition (UPD). Q_{Cu} and *n* were calculated from copper under potential deposition method (UPD). In a 20 mL cell containing a Pt grid as CE and a SCE as RE, a 1 M H_2SO_4 was prepared with 5 mM $CuSO_4$ concentration, and a bulk electrolysis at 0.24 V was applied for 100s. A LSV was performed before and after the bulk electrolysis in a clean 1 M H_2SO_4 solution without any presence of Cu (E_i = 0.04 V, E_f = 0.89 V, 10 mV/s), and a new wave devoted to the oxidation of deposited Cu appeared at *E* = 0.41 V.

The area under the oxidative wave, or Cu-UPD stripping charge (Q_{Cu}, Cu_{UPD}), was determined and used for the calculation of the number of active sites (*n*):

$$Cu_{\mathrm{UPD}} \rightarrow Cu^{2+} + 2\bar{e} \qquad \text{Eq. 4}$$

$$n[mol] = \frac{Q_{Cu}}{2F} \qquad \text{Eq. 5}$$

, where F is the Faraday constant (96485 C·mol^{-1}).

TOF (s^{-1}) calculations. TOF where calculated as follows:

$$TOF(s^{-1}) = \frac{I}{2Fn} = \frac{I}{Q_{Cu}} \qquad \text{Eq. 6}$$

where *I* is the current intensity on the LSV measurement, F is the Faradaic constant, and *n* the number of active sites obtained by the UPD method.

3C.8 References

---

1 K. Philippot and P. Serp, in *Nanomaterials in Catalysis* P. Serp and K. Philippot (Eds.), Wiley-VCH, Weinheim, 2013, Chapter 1, 1-54.

2 D. Astruc (Ed.), Nanoparticles and Catalysis, Wiley-VCH, Weinheim, 2008.

3 G. Schmid (Ed.), Clusters and Colloids. From Theory to Applications, Wiley- VCH, Weinheim, 1994.

4 J. Mahmood, F. Li, S. Jung, M. S. Okyay, I. Ahmad, S. Kim, N. Park, H. Y. Jeong, J. Baek, *Nature Nanotech.* **2017**, *12*, 441-446.

5 S. Drouet, J. Creus, V. Collière, C. Amiens, J. García-Antón, X. Sala, K. Philippot, *Chem. Commun.* **2017**, *53*, 11713-11716.

6 L. Cusinato, L. M. Martinez-Prieto, B. Chaudret, I. del Rosal, R. Poteau, *Nanoscale*, **2016**, *8*, 10974-10992.

7 B. F. G. Johnson, J. Lewis, C. Housecroft, M. Gallup, M. Martinelli, D. Braga, F. Grepioni, *J. Mol. Catal.*, **1992**, *74*, 61-72.

---

8 B. Hammer, J. K. Nørskov, *Surf. Sci*., **1995**, 343, 211-220.

9 J. García-Antón, M. R. Axet, S. Jansat, K. Philippot, B. Chaudret, T. Pery, G. Buntkowsky, H.-H. Limbach, *Angew. Chem. Int. Ed.* **2008**, *47*, 2074-2078.

10 K. Reuter, C. Stampfl, M. Scheffler, *Springer*. **2005**, *1*, 149-194.

11 M. G. Walter, E. L. Warren, J. R. McKone, S. W. Boettcher, Q. Mi, E. A. Santori, N. S. Lewis, *Chem. Rev.*, **2010**, 110, 6446–6473.

12 Y. Gorlin, T. F. Jaramillo, *J. Am. Chem. Soc.*, **2010**, 132, 13612–13614.

13 D. J. Morgan, *Surf. Interf. Anal.* **2015**, 47, 1072-1079.

14 T. Shinagawa, A. T. Garcia-Esparza, K. Takanabe, *Sci. Rep*., **2015**, 5, 13801-13821.

15 C. C. McCrory, S. Jung, I. M. Ferrer, S. M. Chatman, J. C. Peters, T. F. Jaramillo, *J. Am. Chem. Soc.*, **2015**, 137, 4347–4357.

16 C. L. Green, A. Kucernak, *J. Phys. Chem. B* **2002**, *106*, 1036-1047.

4

Ruthenium Nanoparticles Supported onto Carbon-based materials as Water Splitting Catalysts

Chapter 4 deals with the synthesis of supported RuNPs by adapting the organometallic solution synthetic methodology to the use of two different carbon-based supports: carbon nano-tubes (CNTs) and carbon fibers (CFs). Since the techniques available for the characterization of the obtained materials are more limited than for non-supported RuNPs (for instance WAXS or NMR cannot be used), TEM-HRTEM, XPS, ICP and TGA were applied to get information on the structure and composition of the carbon-supported particles. The obtained nanomaterials have been electrochemically tested in the reduction of protons and water oxidation catalysis.

4.0 Preface

In catalysis, the investigation of molecular complexes has been highly useful for the mechanistic understanding and the rational development of new catalysts,[1] allowing the improvement on catalytic performances.[2] However, the main issue with molecular catalysts relays on the long-term stability under catalytic conditions, leading to catalyst decomposition and formation of particles or films.[3] A good way to circumvent this problem and get more robust catalysts is the rough grafting of the metal complexes onto electrodes surface, leading to supported catalytic systems. But even when immobilized onto a supporting material, molecular species can decompose through ligand degradation, and such decomposition can lead to the formation of nano-sized species which are active in the best of the cases.[3a]

The use of nanoparticles (NPs) has already been proven as an advantageous alternative to molecular species in electrocatalysis, given their higher stability at strong pH and electrochemical conditions and also the high surface/volume ratio they display.[4] However, electron transfer in colloidal solutions is not as good as it is with homogeneous species. However, this issue can be solved by the immobilization of the particles onto solid supports and electrodes, as e.g. highly-conductive carbon-based materials (such as CNTs or CFs),[5,6] oxides (e.g. SiO_2, TiO_2),[7] or even directly to glassy carbon (GC) electrodes.[8] The immobilization of a nanoparticulate catalysts onto a support allows to 1st) decrease its aggregation at the same time as 2nd) increase the exposure of the catalyst surface and, consequently, its catalytic activity; moreover fixing a catalyst onto a supporting material may also 3rd) positively influence on its stability and 4th) facilitate its recyclability. In the case of NPs, for example, it may avoid their sintering into bigger particles under catalytic conditions.

Carbon-based supports are becoming common for catalytic applications due to their robustness, chemical inertness and availability in a large range of well-defined shapes and sizes.[9] Compared to inorganic metal-based materials, carbon nano-structures can be manufactured on a large scale with a lower production cost. Additionally, for electrocatalytic applications, they enhance the electron transfers between the electrode and the nanocatalyst, thus improving the efficiency of the latter. Their structure and morphology can be also of paramount importance due to the existence of direct metal-support interactions. Moreover, it is worth noting that both the immobilization[10] and the catalytic performance of the final hybrid materials can be influenced by the heteroatoms that are typically present on the surface of carbon-based supports. Diverse modifications of the chemical structure on the carbon-supports can be carried out to favor their anchoring properties or/and tune the metal-support interactions.

Concerning the use of C-based materials for catalytic HER, a few reports have appeared in the last three years that highlight their function as both support and activity enhancer for Ru-nanosized catalysts, leading to active systems for the reduction of protons in a wide range of conditions (see Ch. 1 for further details).[5,6,7,8a,11] Those C-supported Ru-based catalysts are prepared through complex synthetic protocols such as the condensation of organic precursors that direct the nucleation/growth of the RuNPs and subsequent annealing to generate a conductive carbon matrix from the organic part, or the direct assembly of a metal precursor ($RuCl_3$) in a hierarchically-ordered carbon-based electrode followed by an annealing step. These kind of methodologies, where the presence of counter ions (e.g. Cl^-, Na^+) is notorious as well as the use of drastic conditions (microwave radiation at 200 °C for 10 min), do not permit an accurate tuning of the active sites of the final structures, thus hindering a correlation between these parameters and the catalytic performance of the obtained materials. It is thus necessary to find methods to circumvent these difficulties and achieve more controlled materials in order to study the structure/catalytic performance relationships. In this sense, the organometallic approach is an attractive alternative as it allows to produce small-in-size and surface-controlled NPs.[12,13] The interest of this synthetic approach has been already shown in Chapter 3, where RuNPs displaying a good performance as hydrogen evolution catalysts (HECs) were described, with a control on the size, structure and surface of the material.

This chapter is divided into two sections following the nature of the supporting material employed. The use of multi-walled carbon nanotubes is described in sub-chapter 4A, while carbon fibers are treated in sub-chapter 4B. The fact to have supported RuNPs allowed their oxidizing into RuO_2 without dramatic sintering, giving rise to catalytic nanomaterials active towards both HER and OER.

4A. Carbon Nanotube-supported Ru Nanoparticles as catalyst for Oxygen Evolution and Hydrogen Evolution reactions: oxidation state-dependent activity

4A.1 Introduction

Carbon nanotubes (CNT), first discovered in 1991 by S. Iijima,[14,15] are graphene-like structures rolled up in a hollowed tubular way, which are mainly obtained by electrochemical arc discharge or laser ablation. Their fully-aromatic structure gives them specific chemical properties, as high stability and electron richness, and their nanometric size provides a high surface area. CNTs are basically divided into two main families: Single-Walled Carbon-Nanotubes (SWCNTs) and Multi-Walled CNTs (MWCNTs), being the latter more often employed due to their higher chemical resistance and stability although they are less structurally defined. Furthermore, multi-walled CNTs are easier and cheaper to produce than their single counterparts and their electronic structure is always metallic-like, regardless of their diameter or chirality. In contrast SWCNTs, depending on their characteristic diameter or chirality, can present either metallic or semiconducting electronic structures.[9] MWCNTs exhibit high conductivity, large surface area and resistance to corrosion, properties that make them highly suitable for electrocatalytic applications.[16] CNTs have some irregularities on the surface consisting in sp^3 carbon atoms functionalized with oxidized C-species, such as –OH, –C=O, –CHO and –COOH.[17] Those groups may be relevant for the stabilization of metallic species onto the nanotubes, and could electronically interact onto the catalytic performance of these systems.

In terms of HER catalysis, there are not many examples using CNT-supported Ru-based catalyst for this reaction. R. B. Dandamudi *et al.* successfully developed CNT-supported RuNPs as active catalyst towards the HER,[18a] by the direct assembly of a metal precursor ($RuCl_3$) in a pre-formed carbon-based material in the presence of CH_3COONa followed by a reductive annealing step, similar to those that other authors have previously reported.[11]

In OER, few CNT-based nanosystems have been reported so far,[19] most of them working under alkaline conditions (where the oxidation of water is favored). A surprising example is the work of J. Ma *et al.*,[19a] who reported a metal-free CNT material as active catalyst for the oxidation of water. The peculiarity of this system is the use of N-doped mesoporous carbon nanosheets (N-MCN), obtained from the pyrolysis of glucose/urea/CNTs. The CNTs are present inside the matrix enhancing the electron transfer, and the formed N-MCN reaches values as high as the best metal-based CNT-supported systems ($\eta_0 \approx 270$ mV and $\eta_{10} = 320$ mV, $b = 55$ mV·dec^{-1}). Being

IrO_2 the state-of-the-art species as WOC, the publication of C. Li *et al.* that describes an IrO_2@CNT system active in acidic media will be hereafter taken as reference for electrocatalytic performance benchmarking ($\eta_0 \approx 220$ mV and $\eta_{10} = 293$ mV, $b = 67$ mV·dec^{-1}).[19b]

In order to develop high surface area nanomaterials to be used as catalysts for the evolution of O_2 and H_2 from water splitting, and possessing a high number of active sites while being stable enough, the use of multi-walled carbon nanotubes (MWCNTs) as nanoparticle support appears to be an excellent choice.[18] Hence, in the following part, the synthesis of Ru and RuO_2 nanoparticles that are supported onto multi-walled carbon nanotubes (from now on abbreviated as CNTs) will be presented. The organometallic approach has been applied for the *in-situ* synthesis of RuNPs in the presence of CNTs, and without any additional stabilizing agent. The obtained nanostructures were then thermally oxidized to get RuO_2, which is known to be an efficient HE catalyst as demonstrated by B. Lim and S. Barman in very recent contributions.[20,5] RuO_2-based materials are also able to catalyze the oxidation of water at acceptable overpotentials.

4A.2 Synthesis and characterization of Ru@CNT and RuO_2@CNT

As shown in Scheme 1, **Ru@CNT** nanomaterial has been prepared by decomposition of a THF solution of the [Ru(cod)(cot)] (cod = 1,5-cyclooctadiene; cot = 1,3,5-cyclooctatriene) complex under H_2 atmosphere (3 bar), at room temperature (r.t.) and in the presence of Multi-Walled Carbon NanoTubes (Nanostructured & Amorphous Materials, Inc., O.D. = 50-80 nm, length = 10-20 µm, 99.9% purity) as a support without any other stabilizing agent ([CNT]/[Ru]= 10/7 weight equivalent), in a similar way to previous studies in the laboratory.[10] The CNTs act both as supporting material and stabilizer thanks to the above mentioned functionalities present on the CNTs' surface (e.g. -OH, -COOH) and the electron-richness of their aromatic structure.[17]

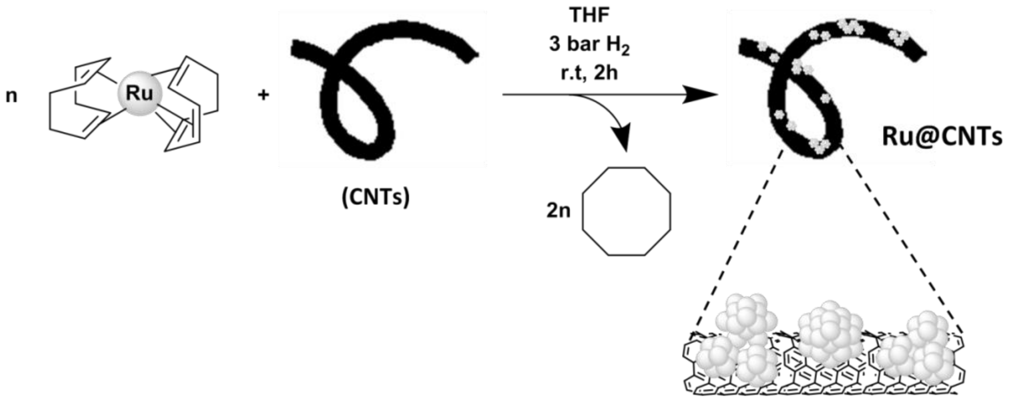

Scheme 1. Synthesis of CNT-supported RuNPs.

Transmission electron microscopy (TEM) analysis carried out from the crude suspension after deposition of a drop on a carbon-covered cupper grid, revealed the presence of very small nanoparticles that are well-dispersed on the surface of the carbon nanotubes (Figure 1a and b) and displaying an average size of 1.9 ± 0.6 nm. The presence of particles out of the CNTs' surface has not been detected.

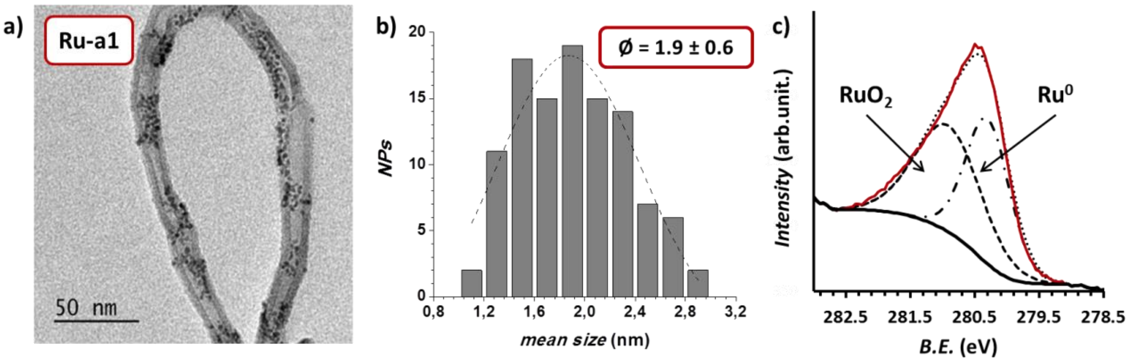

Figure 1. a) TEM picture, b) corresponding size histogram and c) XPS spectrum of partially oxidized **Ru@CNT** sample.

In Chapters 3B-3C, **Ru-0.05MPT** and **Ru-0.2PP** showed up to burn spontaneously when exposed to open air in the solid-state. However, after slow oxygen diffusion the NPs were partially oxidized at their surface, which limited their agglomeration and maintained a metallic core. Taking advantage of this previous knowledge we performed a washing treatment using degassed pentane but in air conditions in order to protect the NPs from total degradation and to favor a slow oxidation of their surface. The obtained **Ru@CNT** nanomaterial could then be isolated by centrifugation leading to a black powder. Inductive-coupled plasma (ICP) analysis indicated an average Ru wt.% content of 5 ± 1 %.

X-Ray Photoelectron Spectroscopy (XPS) analysis on the isolated **Ru@CNT** sample (Figure 1c) indicated the presence of RuO_2, as expected after the oxidation treatment performed by slow O_2 diffusion. HRTEM images on the purified **Ru@CNT** sample evidenced the presence of crystalline NPs (Figure 2), corresponding to both metallic and oxide phases (Ru^0/RuO_2). Electron diffraction patterns obtained after Fast Fourier Transform treatment allowed to measure interplanar distances, as follows: 1) 0.205, 0.230 and 0.215 nm that correspond to (101), (110), (102) planes of the hexagonal compact crystalline (hcp) structure of bulk ruthenium, and 2) distances of 0.114, 0.1283, 0.152 and 0.200 nm that are in agreement with (310), (131), (002) and (120) planes of the rutile structure as for RuO_2.

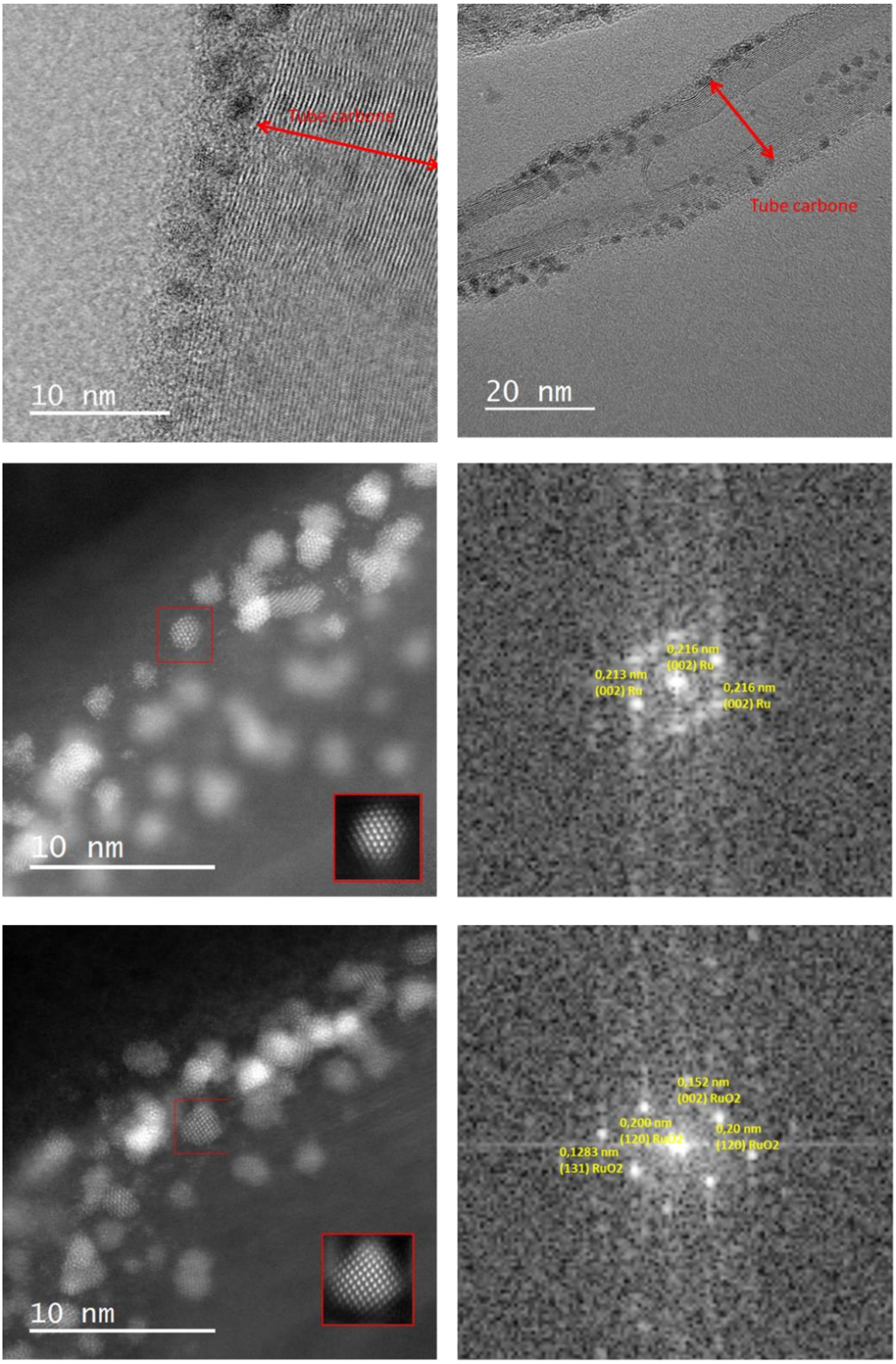
Tube carbone
10 nm
Tube carbone
20 nm
10 nm
0,216 nm
(002) Ru
0,213 nm
(002) Ru
0,216 nm
(002) Ru
10 nm
0,152 nm
(002) RuO2
0,200 nm
(120) RuO2
0,20 nm
(120) RuO2
0,1283 nm
(131) RuO2

Figure 2. HRTEM images and corresponding FFT patterns of partially oxidized **Ru@CNT** sample.

Energy Dispersive X-ray spectroscopy (EDX) on different regions of a HRTEM picture where RuNPs were observed confirmed the presence of Ru metal (Figure 3), and its absence on the non-modified zones of the CNTs as well as outside the CNTs. Furthermore, EDX analysis confirmed the presence of oxygen, specifically in the 003 region (Figure 3, bottom-left), that can be attributed to the presence of oxidized Ru, namely RuO_2.

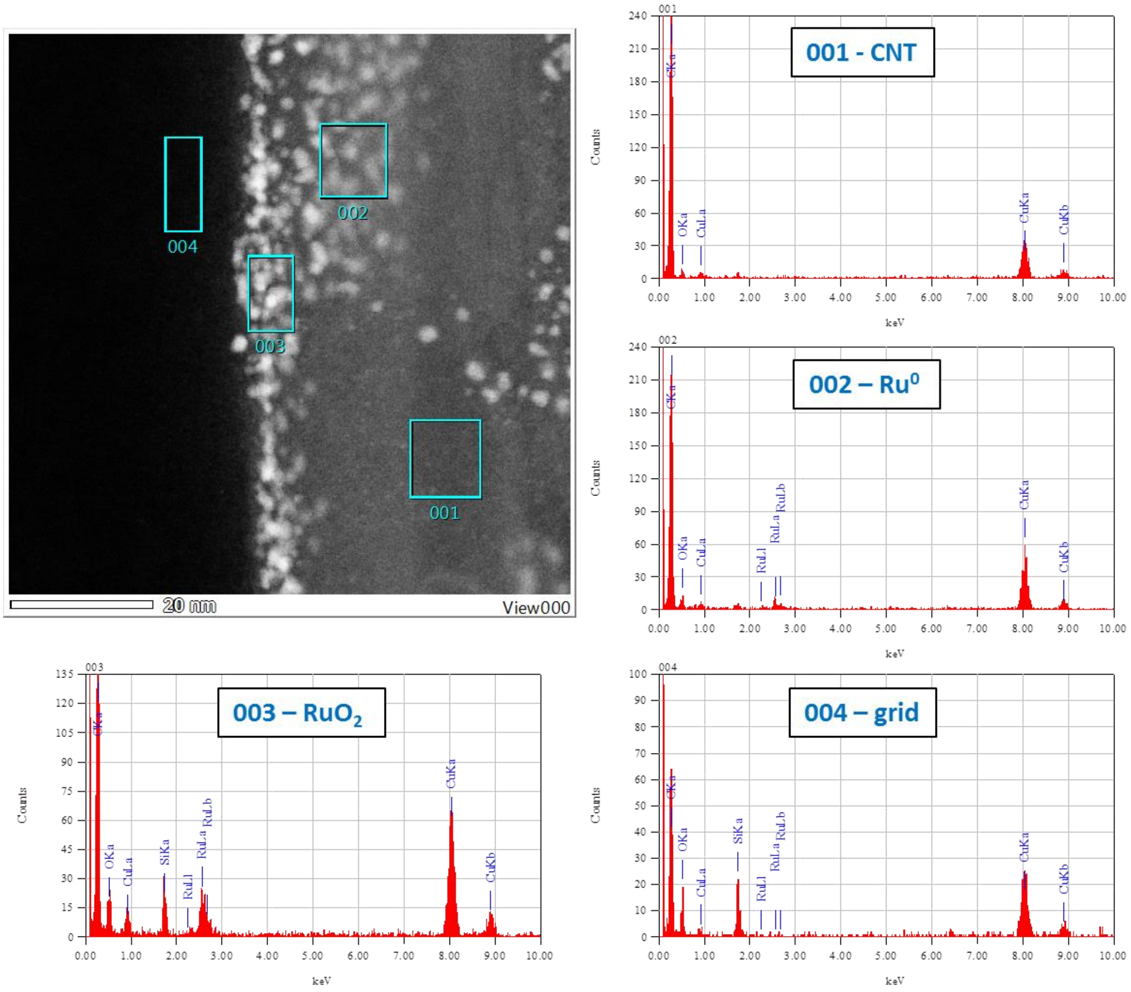

Figure 3. EDX analysis of partially oxidized **Ru@CNT** sample.

In a second step, partially oxidized **Ru@CNT** material has been treated in a furnace at 250 or 300 °C under air for 2 h. By this way, **$RuO_2$250@CNT** and **$RuO_2$300@CNT** nanomaterials were obtained, as evidenced by XPS analysis (Figure 4c).

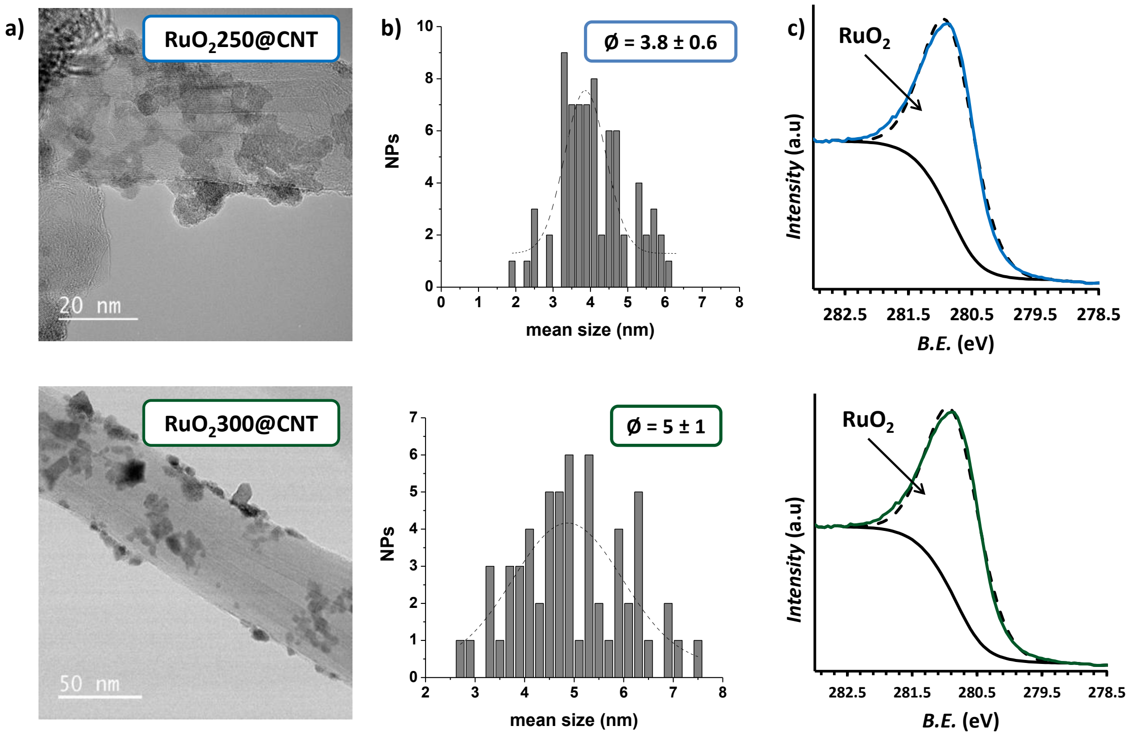

Figure 4. a) TEM pictures, b) corresponding size histograms and c) XPS spectra of **RuO$_2$250@CNT** (top) and **RuO$_2$300@CNT** (bottom).

TEM, HRTEM and EDX analyses performed after the heating treatment (from dispersion of the materials in THF) revealed the presence of large and crystalline objects, together with agglomerates of NPs and also individual NPs (Figure 4-Figure 6). Size histograms of **RuO$_2$250@CNT** and **RuO$_2$300@CNT** (Figure 4b, top and bottom, respectively) show wide size distributions with mean sizes of 3.8 ± 0.6 and 5 ± 1 nm, respectively, that are over the double of the main size observed in the case of the **Ru@CNT** nanomaterial. These observations indicate a sintering phenomenon undergone by the samples when thermally treated at 250 and 300°C. Similar results were previously observed by P. Serp *et al.* when annealing CNT-supported RuNPs at different temperatures (under reductive conditions), and also in Chapter 3B for non-supported **Ru-0.05MPT** and **Ru-0.2PP** NPs.[10b] Moreover, the higher mean size observed for **RuO$_2$300@CNT** in contrast to **RuO$_2$250@CNT** indicates that this sintering process is influenced by the temperature. The formation of bigger crystals being thermodynamically favored at higher temperature, the sintering phenomenon seems to increase with the increasing of temperature.

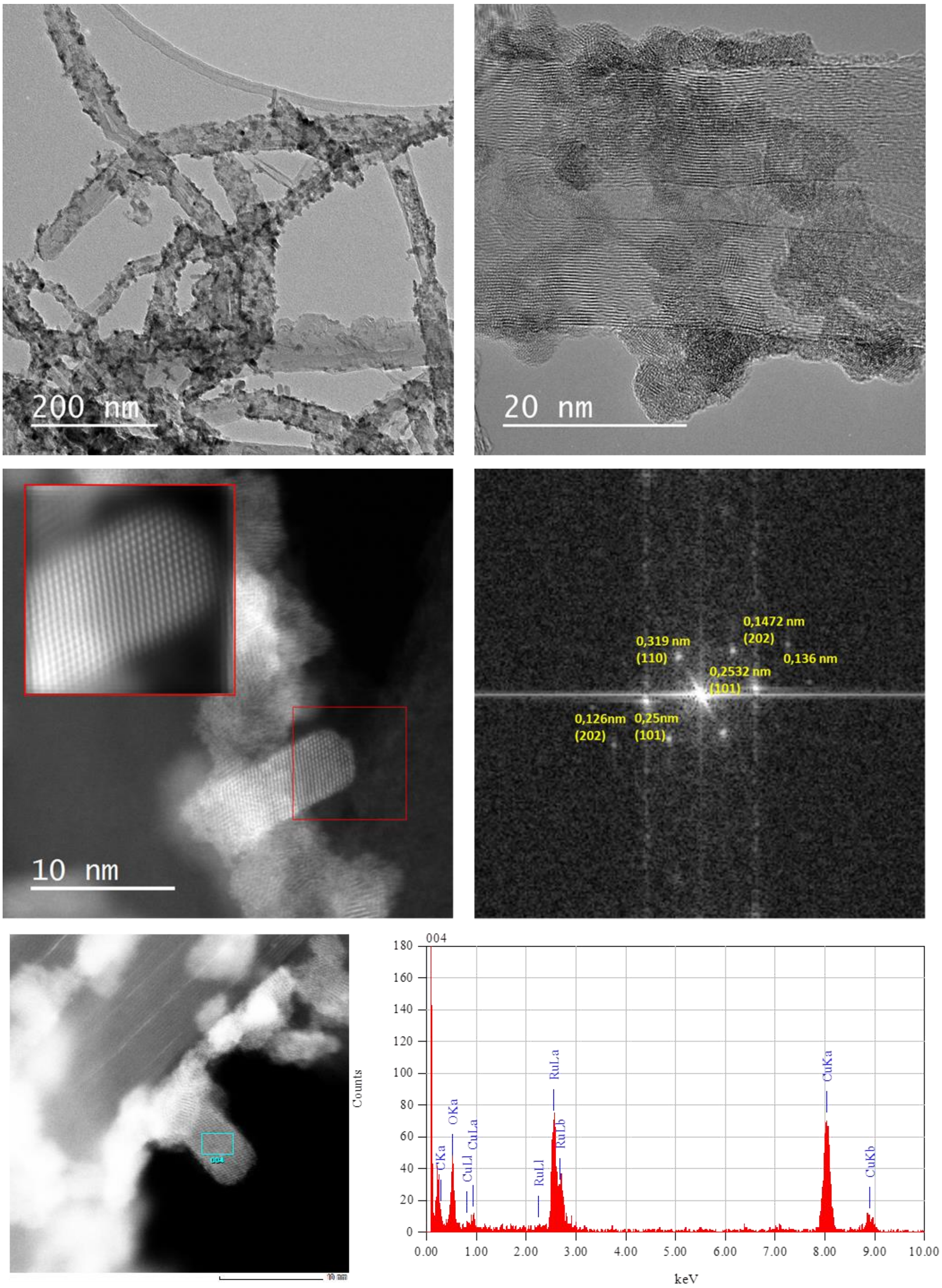
200 nm
20 nm
10 nm
0,1472 nm
(202)
0,319 nm
(110)
0,136 nm
0,2532 nm
(101)
0,126nm
(202)
0,25nm
(101)
004
Counts
CKa
OKa
CuLl
CuLa
RuLl
RuLa
RuLb
CuKa
CuKb
keV
0.00
1.00
2.00
3.00
4.00
5.00
6.00
7.00
8.00
9.00
10.00
0
20
40
60
80
100
120
140
160
180

Figure 5. HRTEM images, FFT patterns and EDX analysis of **$RuO_2$250@CNT** sample.

As expected, EDX analysis confirmed the presence of ruthenium and oxygen in high contents, as the result of the formation of mainly RuO_2. Moreover FFT patterns of HRTEM images (Figure 5-Figure 6) allowed to measure interplanar distances and by this way confirm the presence of mainly RuO_2 phase onto the CNTs.

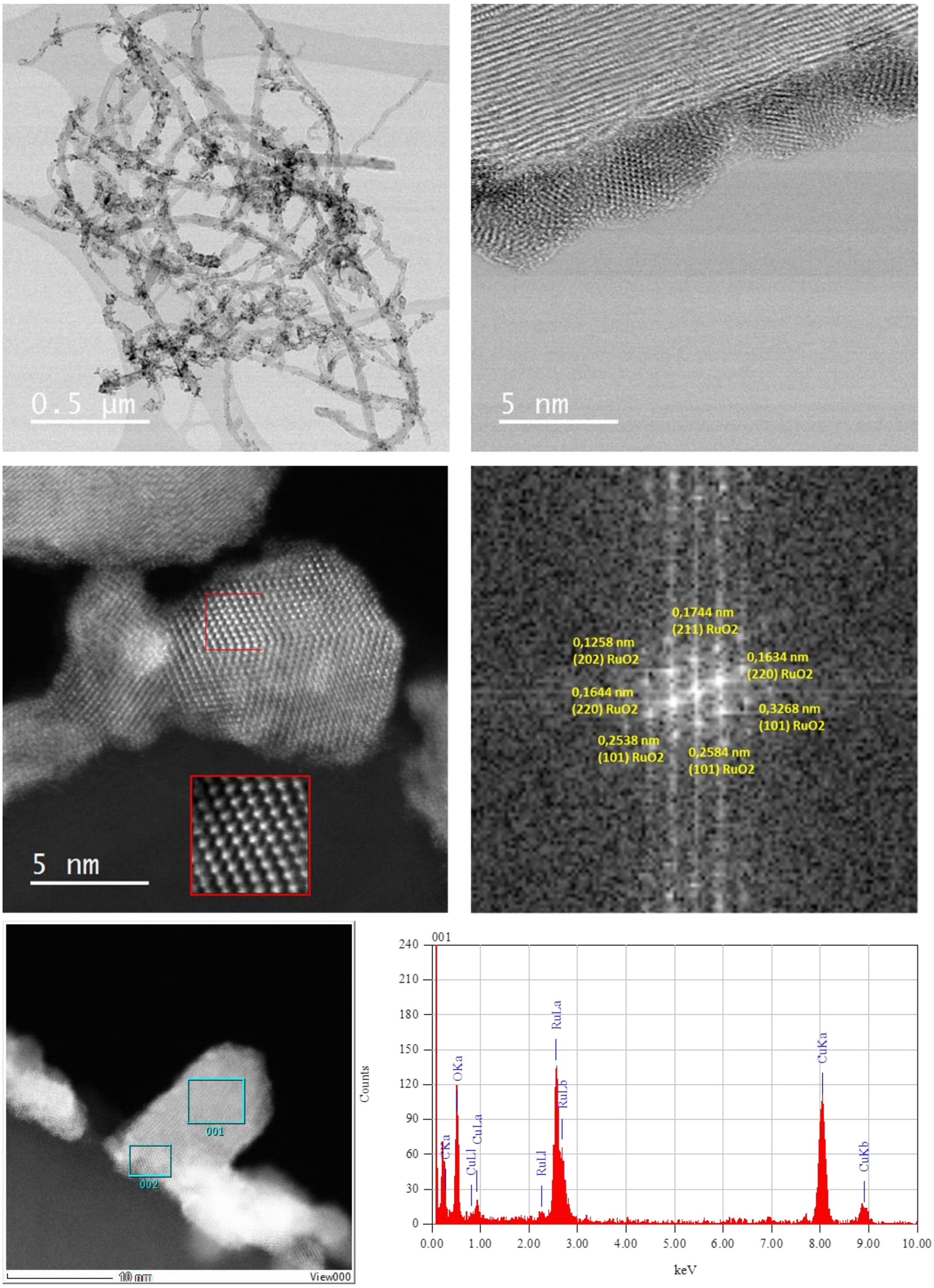

Figure 6. HRTEM images, FFT patterns and EDX analysis of **$RuO_2$300@CNT**.

4A.3 Electrocatalytic hydrogen evolution catalysis

The three CNT-supported Ru-based nanomaterials previously described (**Ru@CNT**, **$RuO_2$250@CNT** and **$RuO_2$300@CNT**) were suspended in THF (2 mg·mL^{-1}), drop-casted onto the surface of a glassy carbon rotating disk electrode (RDE/GC), and led dry under air for HER studies. The so-obtained electrodes were called as **Ru@CNT@GC**, **$RuO_2$250@CNT@GC** and **$RuO_2$300@CNT@GC**. They were tested as working electrodes (WE) in 1 M H_2SO_4 degassed solution, in a three-electrode configuration with a Pt-mesh as counter (CE) and a saturated calomel (SCE) as reference (RE) electrodes.

First, polarization curves under reductive potentials were recorded for the three systems (Figure 7-Figure 8). NPs' mean size determined by TEM analysis together with the composition of the NPs, namely Ru, RuO_2 or a mixture of both, are summarized in Table 1, where electrochemical benchmarking parameters as the onset overpotential (η_0), overpotential at $|j|$ = 10 mA·cm^{-2} (η_{10}) and Tafel slope (b) are also given. From the literature, it is generally accepted for a good HE catalyst to display both, η_0 and η_{10} <100 mV, and the smallest possible b. Thus, Pt/C e.g., has a $\eta_0 \approx 0$ mV and $\eta_{10} < 50$ mV, depending on the loading, with b = 30 mv·dec^{-1}. From Table 1 it can be seen that the three modified WE show high HER overpotentials (both η_0 and η_{10}, entries 1, 3 and 5) with η_0 already >100 mV. However, a shift on the polarization curves was observed for the three electrodes after performing a bulk electrolysis experiment at fixed j = -10 mA·cm^{-2} (Entries 2, 4 and 6 in Table 1).

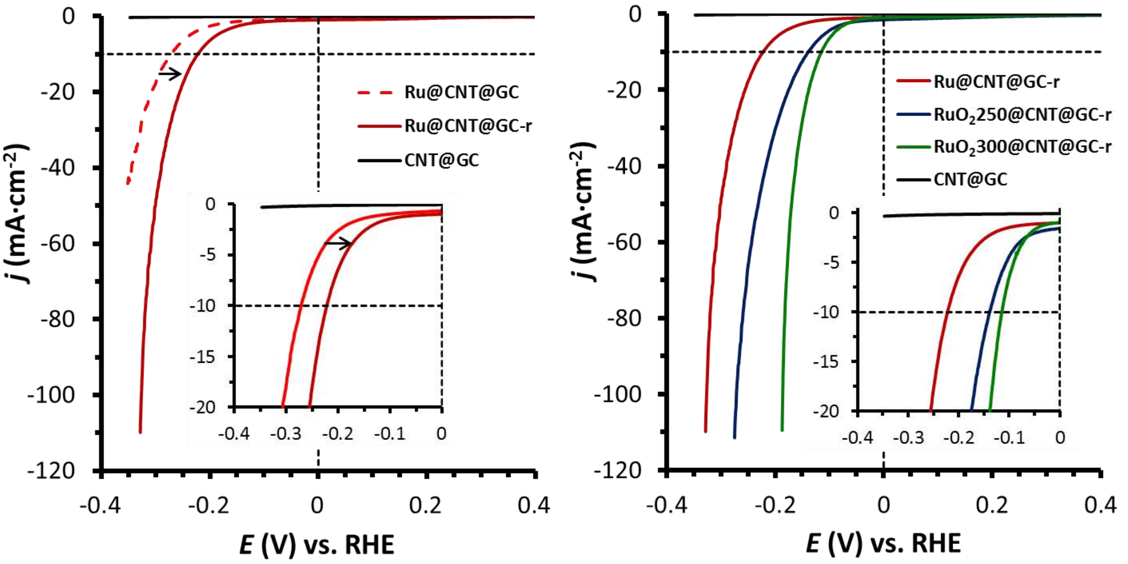

Figure 7. Left, polarization curves of **Ru@CNT@GC** (dashed red) and **Ru@CNT@GC-r** (dark red) before and after reductive process at j = -10 mA·cm^{-2} in 1M H_2SO_4, respectively; right, **Ru@CNT@GC-r** (dark red), **$RuO_2$250@CNT@GC-r** (blue) and **$RuO_2$300@CNT@GC-r** (green) after reductive process at j = -10 mA·cm^{-2} in 1M H_2SO_4.

Table 1. Main physico-chemical and electrochemical data of the CNT-supported RuNPs for HER.

Entry	*System*	*NPs' mean size* (nm)	*NPs' composition*	η_0 (mV)	η_{10} (mV)	*b* (mV·dec^{-1})
1	**Ru@CNT@GC**	1.9 ± 0.6	RuO_2-Ru	200	270	116
2	**Ru@CNT@GC-r** [i]		Ru [ii]	150	220	115
3	**$RuO_2$250@CNT@GC**	3.8 ± 0.6	RuO_2	125	240	200
4	**$RuO_2$250@CNT@GC-r** [i]		Ru-RuO_2 [ii]	80	140	110
5	**$RuO_2$300@CNT@GC**	5 ± 1	RuO_2	130	320	270
6	**$RuO_2$300@CNT@GC-r** [i]		Ru-RuO_2 [ii]	50	115	80

[i] These samples were treated under reductive conditions (j = -10 mA·cm^{-2}) for 20 minutes. [ii] The oxidation state being not yet analyzed, it is an assumption given literature data as well as previous observations in the lab.

Indeed a decrease of 50 mV on both the η_0 and the η_{10} is observed after the reductive bulk electrolysis experiment, leading to 150 and 220 mV, respectively, for **Ru@CNT@GC-r** (entry 2 in Table 1). It is worth mentioning that an analogous trend has been already observed using **Ru1** nanomaterial (see Chapter 3C). In that case, XPS analysis evidenced the presence of only metallic Ru after bulk electrolysis, thus indicating the reduction of the passivating RuO_2 layer in the applied electrocatalytic conditions. Given that, we can assume that a similar reduction happened here also and led to a Ru^0-based nanomaterial. Such a phenomenon can explain the enhancement observed on the HER activity.

Concerning **$RuO_2$250@CNT@GC** and **$RuO_2$300@CNT@GC**, higher shifts are visible after the reductive electrolysis (see entries 3/4 and 5/6 in Table 1, respectively), this being especially pronounced for **$RuO_2$300@CNT@GC**. With those nanomaterials that are initially mainly composed of RuO_2, the activity enhancement observed after reductive bulk electrolysis may derive from the formation of a metallic Ru layer on the surface of the RuO_2-NPs during the reductive process. If we compare with the data achieved with the full Ru^0 nanomaterial ($\eta_0 \approx 150$ mV and $\eta_{10} = 220$ mV, entry 2), the values obtained with the reduced **$RuO_2$250@CNT@GC-r** electrode ($\eta_0 \approx 80$ mV and $\eta_{10} = 140$ mV, entry 4) indicate a higher activity. Such a difference can be attributed to 1st) the formation of Ru^0 species at the surface of the RuO_2-based nanomaterial under reductive conditions, giving rise to a core/shell-like RuO_2/Ru^0 structure; and 2nd) the increase on the exposed surface derived from the formation of Ru^0-species, which introduces irregularities on the crystalline structure. A similar behavior has been already reported by H. You *et al.* in 2003,[21] who studied the change on the catalytic activity induced by the formation of Ru^0 sites on RuO_2 (1 1 0) and (1 0 0) single crystal surfaces, after cathodic polarization. Indeed, they observed an increase on the current density while cycling their electrochemical set-up under reductive potentials that they correlated to a change of the crystalline structure evidenced by synchrotron X-Ray surface scattering, and thus suggested the reduction of the oxide surface as the driving force of the enhanced HER activity.

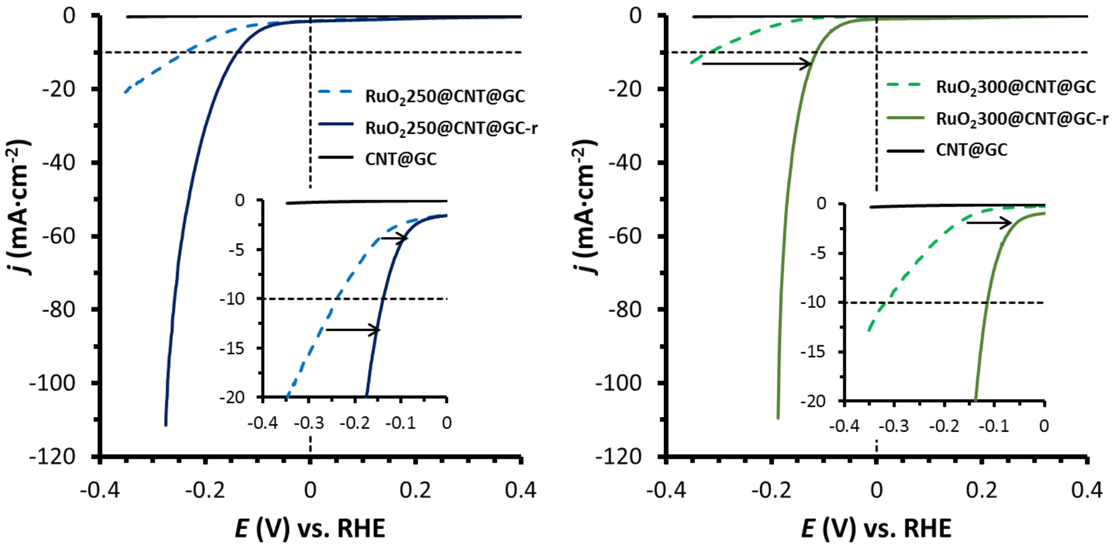

Figure 8. Polarization curves of **RuO_2@CNT** systems before and after reductive process at $|j|$ = 10 $mA\cdot cm^{-2}$ in 1 M H_2SO_4. Left, **$RuO_2$250@CNT@GC** (dashed blue) and **$RuO_2$250@CNT@GC-r** (dark blue); right, **$RuO_2$300@CNT@GC** (dashed green) and **$RuO_2$300@CNT@GC-r** (dark green).

A similar catalytic behavior has been noticed with the **$RuO_2$300@CNT@GC** system. In that case η_0 and η_{10} of 130 and 320 mV are first observed, respectively (entry 5). After reduction treatment (entry 6), lower $\eta_0 \approx 50$ mV and $\eta_{10} = 115$ mV are reached, indicating a higher activity, as the result of the formation of Ru metal active sites and thus structure modification at the material surface. The values achieved are better than those previously obtained with **$RuO_2$250@CNT-GC-r** electrode. In addition to the formation of Ru^0-species on the surface of RuO_2-crystals, the improving on the catalytic activity of RuO_2-based materials compared to the Ru^0-NPs precursor may rely on another parameter. The modification of both, the particles but also CNTs, may improve the electron transfer from the electrode to the active sites, thus increasing the electrocatalytic performance of the cathodic system.

Figure 9 (left) presents the Tafel plots obtained for the three electrodes after reductive treatment. The Tafel slope (*b*) allows defining the rate determining step (rds) of the catalytic reaction as described in Ch. 1. **Ru@CNT@GC-r** (dark red) shows a Tafel slope of 115 $mv\cdot dec^{-1}$, typical for catalysts having the Volmer step as rds (hydride adsorption on the surface of the NP, typically $b \approx 120$ $mv\cdot dec^{-1}$). **$RuO_2$250@CNT@GC-r** (dark blue) and **$RuO_2$300@CNT@GC-r** (dark green) present Tafel slopes of 109 and 77 $mv\cdot dec^{-1}$, respectively, that reveal for both electrodes a situation in between the Volmer and Heyrovsky steps as rds (Heyrovsky step: H_2 electrodesorption with a proton from the solution presents values of $b \approx 40$ $mv\cdot dec^{-1}$).

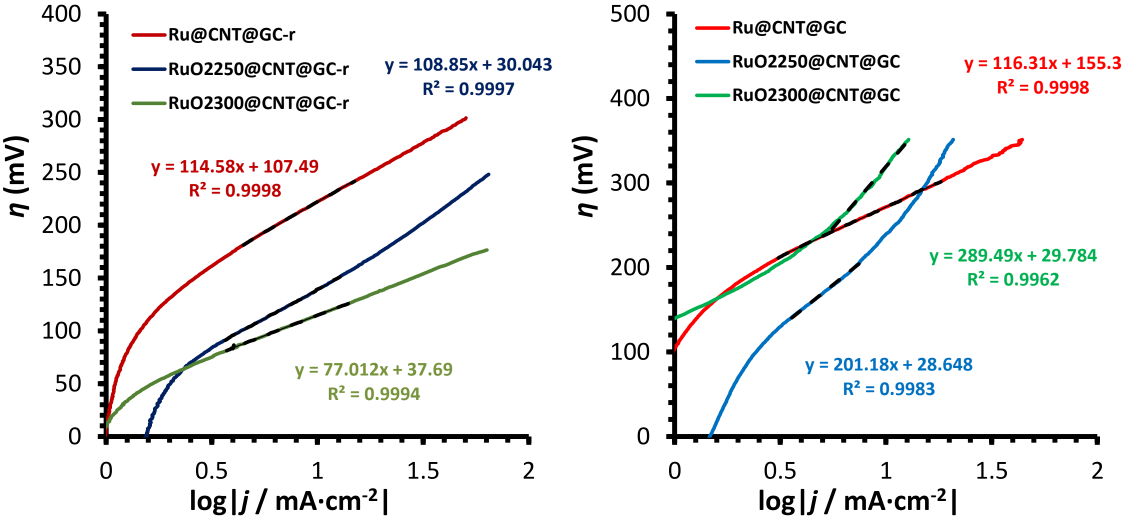

Figure 9. Tafel plot of left, **Ru@CNT@GC-r** (dark red), **$RuO_2$250@CNT@GC-r** (dark blue) and **$RuO_2$300@CNT@GC-r** (dark green), and right, **Ru@CNT@GC** (red), **$RuO_2$250@CNT@GC** (light blue) and **$RuO_2$300@CNT@GC** (light green), in 1 M H_2SO_4.

Tafel plots of non-reduced systems **Ru@CNT@GC** (red), **$RuO_2$250@CNT@GC** (light blue) and **$RuO_2$300@CNT@GC** (light green), are shown in the right part of Figure 9 for comparison with those of the reduced systems. For both **$RuO_2$250@CNT** and **$RuO_2$300@CNT**, an important decrease on the Tafel slope after the reduction process can be thus observed, as expected for Ru^0-species which are more active towards the HER than RuO_2. In contrast, $b \approx 115$ mv·dec^{-1}, almost does not change in the case of **Ru@CNT@GC**. This can be explained by the fact that for **Ru@CNT@GC** before the reduction process, the activity is already attributed to Ru^0 species that were not passivated when exposed to air, thus maintaining the kinetics after the modification of the superficial RuO_2 to Ru^0. In contraposition, **$RuO_2$250@CNT** and **$RuO_2$300@CNT** improve their kinetics due to the Ru^0-species formation, and presumably due to the enhancement on the electron transfer.

In comparison to other electrocatalytic studies with Ru^0/RuO_2-based materials,[5,6,7] the data reached with **$RuO_2$300@CNT@GC-r** electrode show this material is the best system in this work and that its results are among the best ones reported so far ($\eta_0 \approx$ 50 mV, η_{10} = 115 mV and b = 80 mv·dec^{-1}), being even superior than those of Rub material presented in Chapter 3C (see Table A1 in the Annex part). In terms of η_0, 50 mV is a small value, but the slow kinetics reflected by the high Tafel slope (further evaluated in the following paragraph) leads to a relatively high η_{10} value. If we compare these results with **Ru-GC** (from Chapter 3A; **Ru-MeOH/THF** system) and **Ru1** (from Chapter 3C; **Ru-0.2PP** system), we can see that a similar η_0 is observed as for **Ru-GC** (40 mV in that case), but the higher Tafel slope (46 mV·dec^{-1} for **Ru-GC**) leads also to a higher η_{10} (83 mV vs. 115 mV). This demonstrates that **$RuO_2$300@CNT@GC-r** is not far from the MeOH/THF stabilized RuNPs. Nevertheless **Ru1** outstands these values, confirming to be a better catalyst as the result of the influence of the pyridine-based stabilizing ligand.

4A.4 Electrocatalytic studies in OER

Ru@CNT@GC-r, **RuO$_2$250@CNT@GC** and **RuO$_2$300@CNT@GC** electrodes were also evaluated in the OER, and the obtained results are summarized in Table 2. For **Ru@CNT** only the reduced system **Ru@CNT@GC-r** was tested, to ensure the presence of only Ru^0 phase and not RuO$_2$-Ru^0 mixture, in order to evaluate a one-phase nanomaterial. Thus, when using **Ru@CNT@GC-r** as WOC (Figure 10a) in acidic conditions, almost no current was observed with overpotentials as high as η = 420 mV, even for the first voltammetry experiment. From previous works in the literature,[20,22] it has been stated that metallic Ru is more active than RuO$_2$ for OER. Nevertheless, its low stability towards RuO$_4$ formation under OER conditions prevents its use as WOC.[22a,d] In the work of T. Reier, P. Strasser *et al.*, carbon-supported (Vulcan XC 72R) Ru^0-NPs presented an irreversible oxidation wave at 1.5 V (versus RHE), the same point where OER starts for bulk Ru, attributed to a fast corrosion of Ru under the electrocatalytic conditions.[22d] Thus, depending on the catalytic system, high current densities are observed on the first voltammetry rapidly decreasing on the subsequent ones, or very low current can be already displayed on the first LSV due to faster decomposition. The behavior of **Ru@CNT@GC-r** corresponds to the 2nd case, showing a very low current density and a fast deactivation after 3 consecutive LSVs (Figure 10a) in the applied conditions, with the same irreversible oxidation wave at 1.5 V.

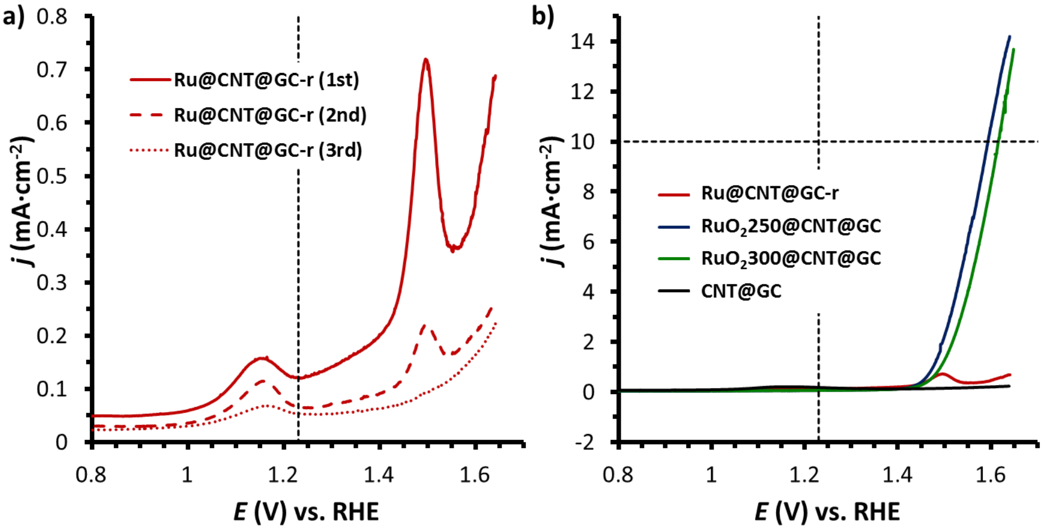

Figure 10. a) Consecutive polarization curves of **Ru@CNT@GC-r** under OER condition in 1 M H_2SO_4 solution. b) Polarization curves of **Ru@CNT@GC-r** (dark red), **RuO$_2$250@CNT@GC** (blue), **RuO$_2$300@CNT@GC** (green) and bare GC (black).

In contrast, as shown in Figure 10b, the oxidized **$RuO_2$250@CNT@GC** and **$RuO_2$300@CNT@GC** nanomaterials display a sharp change on the curve slope at around 220-230 mV overpotentials due to the oxidation of water (Table 2, entries 2 and 3, η_0), achieving j = 10 mA·cm^{-2} at η_{10} = 364 mV and 385 mV, respectively.

Table 2. Main physico-chemical and electrochemical data of the CNT-supported Ru-based systems for OER.

Entry	*System*	*NPs' mean size* (nm)	*NPs' composition*	η_0 (mV)	η_{10} (mV)	*b* (mV·dec.$^{-1}$)
1	**Ru@CNT@GC-r** [i]	1.9 ± 0.6	Ru [ii]	-	-	-
2	**$RuO_2$250@CNT@GC**	3.8 ± 0.6	RuO_2	220	364	66
3	**$RuO_2$300@CNT@GC**	5 ± 1	RuO_2	230	385	78
4	**$RuO_2$300@CNT@GC-r** [i]		Ru-RuO_2 [ii]	230	300	64

[i] These samples were treated under reductive conditions (|j| = 10 mA·cm^{-2}) for 20 minutes. [ii] The oxidation state being not yet analyzed, it is an assumption given previous literature data as well as observations from other experiments in the research group.

For comparison purposes, the activity of **$RuO_2$300@CNT@GC-r** nanomaterial was also evaluated under OER conditions (Figure 11).

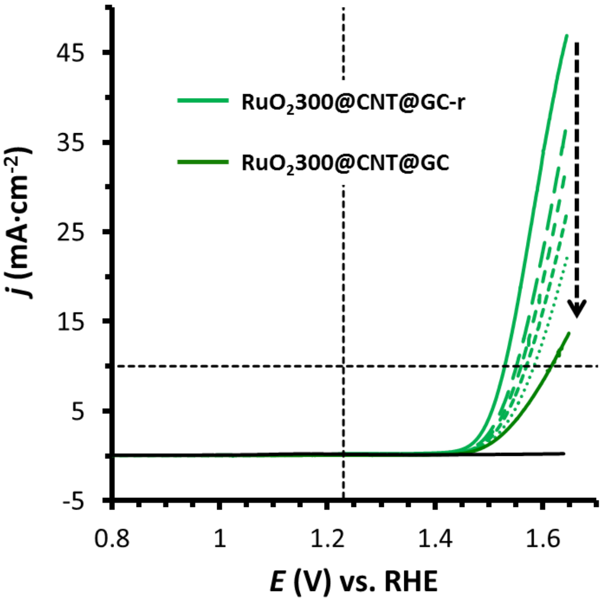

Figure 11. Successive LSV curves obtained for **$RuO_2$300@CNT@GC-r** in 1 M H_2SO_4 (1st light green, subsequent dashed/dotted green), and **$RuO_2$300@CNT@GC** (dark green) previous to electroreduction.

Initially, the activity of the reduced **$RuO_2$300@CNT@GC-r** is superior to that of to the fully oxidized **$RuO_2$300@CNT@GC** system (η_0 ≈230 mV, η_{10} = 300 mV, b = 64 mV·dec^{-1}). These results evidence that a higher activity is achieved in the presence of metallic Ru. However, after several consecutive cyclic voltammetries (dashed and dotted light green lines) the current density decreased, what can be attributed to Ru^0 decomposition into RuO_4, as previously reported by I. Chorkendorff and T. Reier.[22a,d] The final activity of this system appeared similar to that of **$RuO_2$300@CNT@GC** before the reductive process (dark green line). This suggests first, the formation of a metallic layer at the surface of the RuO_2 NPs due to the reduction process, and second the direct oxidation of the metallic layer into RuO_4 in OER conditions, leading thus to a similar activity as for **$RuO_2$300@CNT@GC** after the whole redox stress.

Tafel plots of **$RuO_2$250@CNT@GC**, **$RuO_2$300@CNT@GC** and **$RuO_2$300@CNT@GC-r** species are shown in Figure 12. The Tafel slope values obtained at small overpotentials (Table 2, entries 2-4, *b*) are higher than those expected for mechanisms where the rds is the recombination step (the reaction of two Cat-OH groups to form an Cat-O and H_2O; b = 30 mV·dec^{-1}), and slightly closer to those where the rds is the second electron transfer (Cat-OH releases "$1H^+$+$1\bar{e}$" to form Cat-O; 40 mV·dec^{-1}), both steps corresponding to the "Cat-O" species formation from a Cat-OH (see Chapter 1 for more details).[20,23]

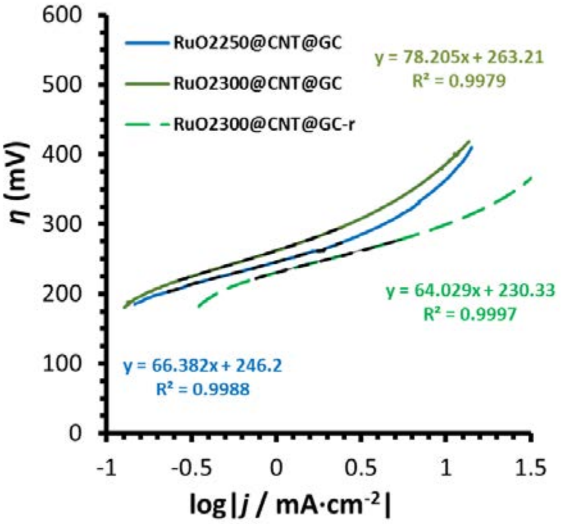

Figure 12. Tafel plot of **$RuO_2$250@CNT@GC** (blue), **$RuO_2$300@CNT@GC** (dark green) and **$RuO_2$300@CNT@GC-r** (dashed pale green) systems in 1 M H_2SO_4.

Being Ir a scarce and highly-expensive metal which is widely used in the OER as for example in commercial PEM electrolyzers, the results obtained for **$RuO_2$300@CNT@GC-r** (being the best ones achieved in this work) were compared with those of the IrO_2@CNT system reported by C. Li *et al.*[19b] **$RuO_2$300@CNT@GC-r** starts catalyzing the oxidation of water at similar overpotentials than IrO_2@CNT ($\eta_0 \approx$ 230 mV vs. $\eta_0 \approx$ 220 mV, respectively), and has also a similar Tafel slope (b= 64 vs. 67 mV·dec^{-1}), leading thus to a similar η_{10} (η_{10} = 300 vs. 293 mV). However, its low stability makes this system unsuitable for OER catalysis under acidic conditions, analogously to what happened with Ru/RuO_2 Chorkendorff's system.[22a] In contrast, **$RuO_2$250@CNT@GC** presents a similar onset and Tafel slope than those two systems ($\eta_0 \approx$ 220 mV and b =

66 mV·dec^{-1}), and despite the slightly higher η_{10} ≈ 364 mV, **$RuO_2$250@CNT@GC**'s stability is much more remarkable than **$RuO_2$300@CNT@GC-r** one, stating it as a suitable candidate for replacing Ir-based catalysts.

4A.5 Influence of the oxidation state of the NPs

In both proton reduction and water oxidation catalysis with CNT-supported Ru-based nanomaterials, we have observed changes on the electrocatalytic activity, which are attributed to modifications of the catalyst surface state and more precisely the oxidation state of Ru. As already mentioned, a partial oxidation of the NPs' surface was observed for **Ru1** sample when exposed to slow O_2 diffusion, leading to a core/shell structure where Ru^0-core is surrounded by a RuO_2 layer (see Chapter 3C). This oxidation was proven to be reversible when applying reduction conditions of HER.

In the present case, the partially oxidized and initially isolated **Ru@CNT@GC** nanomaterial (Table 1, entry 1) has been reduced to Ru^0 under reductive conditions leading to **Ru@CNT@GC-r** (see Scheme 2), which reaches moderate activities in HER (η_0 ≈ 150 mV and η_{10} = 220 mV) as the result of presenting more metallic Ru sites at the surface of the catalyst (Table 1, entry 2).

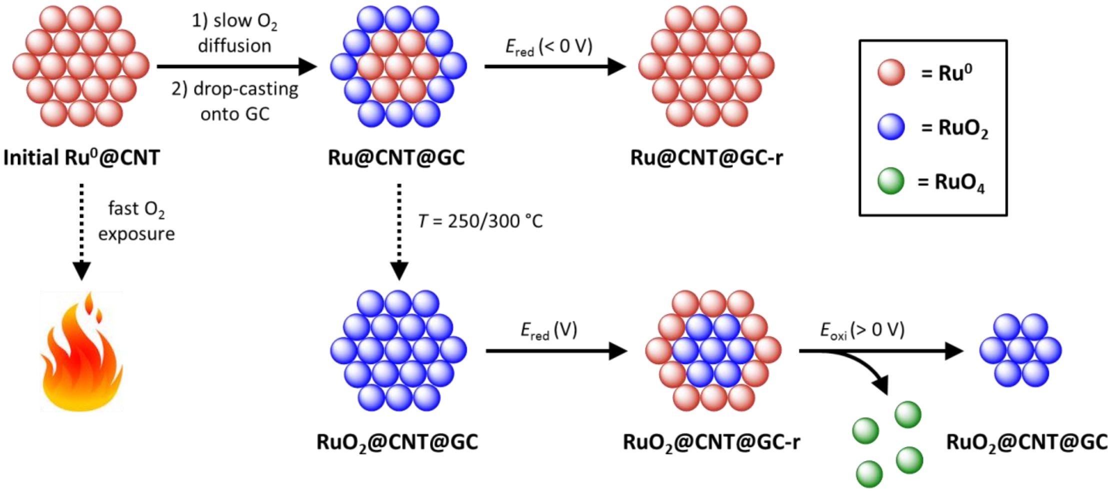

Scheme 2. Proposed scenario for the oxidation/reduction processes happening at the surface of CNT-supported Ru and RuO_2-NPs during electrocatalysis.

An analogous trend was observed for **$RuO_2$250@CNT@GC** and **$RuO_2$300@CNT@GC** samples when these systems were tested as HECs (Table 1, entries 3 and 5). After applying a reduction potential for 20 min an "activation" was observed on the subsequent LSV experiment (Figure 8, Table 1, entries 4 and 6), probably due to partial electroreduction of the surface (**$RuO_2$250@CNT@GC-r** / **$RuO_2$300@CNT@GC-r**). This led to the formation of a RuO_2/Ru^0 core/shell-like materials (Scheme 2) that display HER activities higher than Ru^0 itself (η_0 ≈ 50 mV and η_{10} = 115 mV for

$RuO_2$300@CNT@GC-r), as the result of this dual structure. Additionally, the thermal treatment could induce changes also on the CNTs, which together with RuO_2-crystals formation, could facilitate the electron transfer from the electrode to the active species, thus displaying higher intensities and kinetics than the **Ru@CNT@GC-r**.

In the OER, thermally oxidized **$RuO_2$250@CNT@GC** and **$RuO_2$300@CNT@GC** (Table 2, entries 2 and 3) showed up to be good catalysts for the OER with small overpotentials ($\eta_0 \approx 230$ mV and $\eta_{10} = 385$ mV for **$RuO_2$300@CNT@GC**) and no apparent deactivation (Figure 10b). In contrast, the best activities were displayed by the electroreduced **$RuO_2$300@CNT@GC-r** (Table 2, entry 4; $\eta_0 \approx 230$ mV and $\eta_{10} = 300$ mV), with a RuO_2/Ru^0 core/shell-like structure. However, the low stability of Ru^0 species under OER conditions led to a fast decrease on the activity until reaching the same current densities as **$RuO_2$300@CNT@GC** (Figure 11), attributed to a fast oxidation of the surface metallic atoms directly into RuO_4, which is volatile and so might be leached in in solution. A similar behavior was observed with the full metallic **Ru@CNT@GC-r** when tested as WOC (Table 2, entry 1), which displayed very small current intensities that dramatically decreased at each LSV (Figure 10a), probably due to its fast oxidation into RuO_4 in the applied conditions.

4A.6 Conclusions & perspectives

Several conclusions can derive from the findings obtained in the electrocatalytic water splitting using CNT-supported ruthenium based materials as catalysts:

- ✓ The *in-situ* synthesis of CNT-supported RuNPs was easily performed in the absence of any extra stabilizer. The good dispersion and stability of the Ru-NPs is attributed to the interaction between the NPs and the CNTs.
- ✓ Thermal oxidation of the supported RuNPs allowed to get completely oxidized crystalline RuO_2-NPs. A slight sintering was observed but with all the particles maintaining in the nano-size range. This confirmed the positive influence of the support which limits the sintering of the particles and favors the oxidation process. Interestingly, similar oxidation treatments applied to non-supported **Ru1** NPs (see Chapter 3C for further details), led to agglomeration of the particles which prevented their full oxidation, even at 400 °C for 2 h.
- ✓ Both metallic and oxidized RuNPs showed activity in the HER. This activity was enhanced after an electroreductive treatment, presumably due to the reduction of the superficial-RuO_2 to Ru^0. This behavior was already observed for **Ru2-GC** to **Ru1-GC** in Chapter 3C, and also reported in other works involving RuO_2.[21] The low overpotential values achieved by **$RuO_2$250@CNT@GC-r** and **$RuO_2$300@CNT@GC-r** ($\eta_0 \approx 50$ mV and $\eta_{10} = 115$ mV for the latter) are

attributed to the RuO_2/Ru^0 core/shell structure formed after the reductive process, as well as to the enhancement of the electron transfer from the electrode to the active species. The results obtained place these nanomaterials among the most outstanding nano-sized HEC in the literature.

- ✓ The catalytic activity of the CNT-supported nanomaterial was also tested in OER, with the RuO_2-based materials displaying very small overpotentials ($\eta_0 \approx$ 220 mV and η_{10} = 364 mV for **$RuO_2$250@CNT@GC**). An influence of the surface state of the NPs is believed as a) direct Ru^0 oxidation to RuO_4 with corresponding decrease in the catalytic activity; b) good stability of RuO_2 under the OER conditions.

To complete this work, long-term stability studies under both HE and OE reaction conditions are required, as well as the determination of Faradaic efficiencies, to obtain the roughness of the nanomaterials under the catalytic conditions. Complementary XPS and HRTEM analysis will help to confirm the influence of the surface oxidation state on the activation/deactivation process.

The modification of the surface composition of the CNTs appears as an interesting perspective to tune the catalytic properties and maybe enhance the stability of our nanocatalyst. We have performed preliminary essays in this direction, using different molecules as follows:

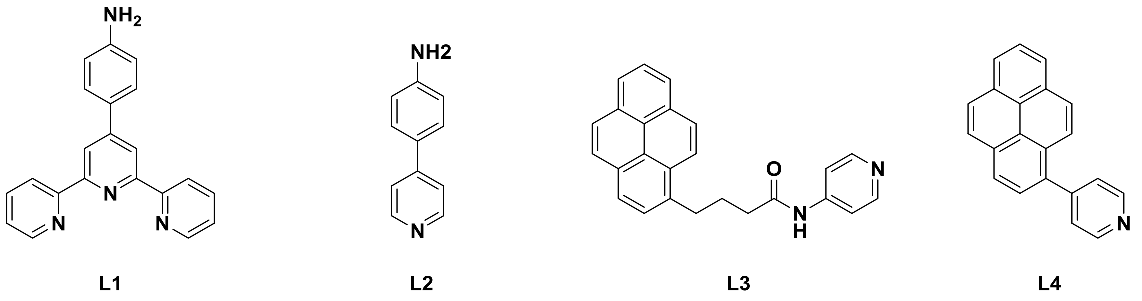

Figure 13. Ligands Lx (x=1-4) used for the functionalization of MWCNTs.

- In order to tune the CNTs' surface we have envisaged to covalently attach pyridine-based ligands on the CNTs by an electroreduction process. Such a modification on the CNTs' surface is expected to play a key role both on the nucleation/stabilization of the particles during the synthesis and on the catalytic performance of the obtained materials due to the electronical properties of the pyridine-N. Two modified supports have already been synthesized by electrografting through the electroreduction of an *in-situ*-formed diazonium salt (Scheme 3),[24] starting up from ligands **L1** and **L2** (see Figure 13) and characterized by TGA (Figure 15):

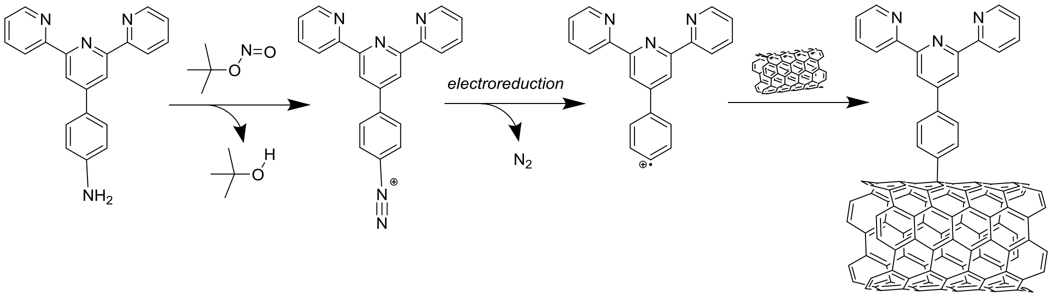

Scheme 3. Electrografting process taking part between ligand **L1** and a CNT through the electroreduction of an *in-situ*-formed diazonium salt.

- Additionally, π-stacking "connection" is considered as a clean way to functionalize carbon materials, as no chemical reaction is involved for the anchoring procedure and so no poisoning species expected on the final product.[25] Thus, analogous to the previous point, two pyridine/pyrene-based ligands (**L3** and **L4** in Figure 13) have been used to modify the CNT's surface by anchoring them through π-stacking interactions. These molecules present different connections between pyrene and pyridine moieties. In **L3**, there is an aliphatic chain with an amide function, in contrast to a direct connection between the two groups for **L4**. **L3** and **L4** were previously synthesized in the lab to anchor metal complexes onto CNTs.[2]

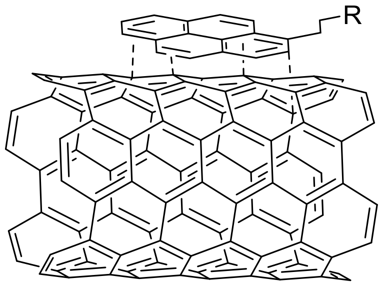

Figure 14. Representation of π-stacking interactions between a CNT and a pyrene group.

As seen in Figure 15, TG analysis of the modified **Lx@CNT** (x=1,2,3,4) materials in 50-800 °C shows a weight loss in the 50-550 °C region attributed to the decomposition of anchored ligands **L1-L4** on the surface of the CNTs. For ligands **L1**-**L2** a weight loss of ≈4% is observed, whereas for **L3**-**L4** it is of ≈6%. A main difference is present in the coordination mode of the ligands: covalent bond for **L1** and **L2** and π-stacking for **L3** and **L4**. The higher range of temperatures at which the ligands are decomposed is due to the anchoring (from previous works, e.g. Chapter 3B, we know that this kind of ligands degrade at 350-450 °C).

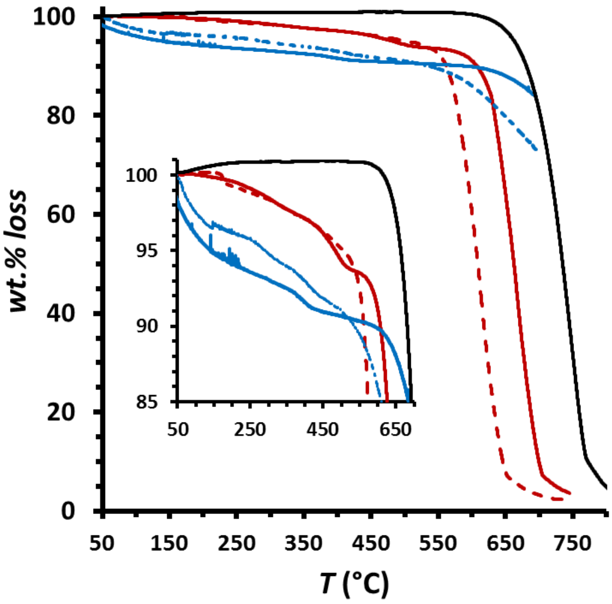

Figure 15. TGA of the modified CNTs with ligands Lx: in red, electrografted **L1@CNT** and **L2@CNT** (dashed), and in blue, "π-stacked" **L3@CNT** and **L4@CNT** (dashed).

Future comparison studies based on the synthesis of RuNPs onto these new supports and the evaluation of their electrocatalytic performance should provide interesting results about the influence of these two modes of anchoring onto both the stability and catalytic activity of the obtained nanomaterials.

4A.7 Experimental part

Reagents. All operations for the synthesis of **Ru@CNT** samples were carried out using standard Schlenk tubes, Fisher–Porter bottle techniques or in a glove-box (MBraun) under argon atmosphere. Solvents (THF and pentane) were purified before use by distillation under N_2 atmosphere with a drying agent (sodium+benzophenone and CaH_2, respectively) and degassed according to a freeze–pump–thaw process. The ruthenium precursor, [Ru(cod)(cot)] was purchased from Nanomeps-Toulouse. Hydrogen gas was purchased from Abelló Linde, S.A. MWCNTs were purchased from Nanostructured & Amorphous Materials, Inc. (Texas, USA) with 99.9% purity and an OD: 50-80 nm and 10-20 µm length. High purity deionized water was obtained by passing distilled water through a nanopore Milli-Q water purification system.

Synthesis of Ru@CNT. In a Fisher Porter reactor, 20 mg of MWCNTs were dispersed in 20 mL of dried and degassed THF in an ultrasound bath for 30 min. Then 5 mg (0.032 mmol) of [Ru(cod)(cot)] were added in the reaction medium inside a Glove-box. After pressurization of the reactor with 3 bar of H_2 at room temperature (r.t.), the initial yellow solution turned dark brown in a few minutes. A vigorous magnetic stirring and the H_2 pressure were maintained for 2 h. After this reaction time, the H_2 pressure was evacuated. A drop of the colloidal suspension was deposited onto a carbon-covered copper grid for TEM analysis, and the Ru nanomaterial was isolated as a black powder by centrifugation and washing with THF and pentane and drying under vacuum.

$RuO_2$250@CNT and **$RuO_2$300@CNT. Ru@CNT** sample was oxidized at 250 or 300 °C inside a furnace during 2 h in aerobic conditions. The furnace was pre-heated at the desired temperature previous to sample introduction

Characterization. The crude suspension has been characterized by Transmission Electron Microscopy (TEM), and the isolated solid by High Resolution TEM (HRTEM) coupled with Energy-Dispersive X-ray spectroscopy (EDX), X-Ray Photoelectron Spectroscopy (XPS), Inductive-Coupled plasma (ICP) and ThermoGravimetric Analysis (TGA).

Transmission Electron Microscopy (TEM) and High resolution TEM (HR-TEM). TEM was performed at the “Servei de Microscopia de la UAB” using a JEOL JEM 2010 electron microscope, and HRTEM at the “Centre de Microcaractérisation Raymond Castaing” in Toulouse (UMS-CNRS 3623) on a JEOL JEM-ARM 200F microscope working at 200 kV with a point resolution 0.19 nm. Samples for transmission electron microscopy (TEM) analyses were prepared by slow evaporation of a drop of the crude dispersion deposited onto a holey carbon-covered copper grid. Samples for high-resolution transmission electron microscopy (HRTEM) analyses were prepared by the same way from purified samples redispersed in THF. TEM allowed evaluating the particle’s mean size, size distribution, dispersion and morphology. Enlarged micrographs were used for treatment with ImageJ software to obtain a statistical size distribution and the nanoparticles’ mean diameter. The analyses were done assuming that the NPs are spherical. NPs sizes are quoted as the main diameter ± the standard deviation. FFT treatments of HRTEM images were carried out with Digital Micrograph Version 1.80.70 to determine the crystalline structure of the material. The analyses were done by assuming that the nanoparticles are spherical. Nanoparticle sizes are quoted as the mean diameter ± the standard deviation.

X-Ray Photoelectron Spectra (XPS). Measurements were performed at the Catalan Institute of Nanoscience and Nanotechnology (ICN2) in Barcelona with a Phoibos 150 analyzer (SPECS GmbH, Berlin, Germany) in ultra-high vacuum conditions (base pressure $5E^{-10}$ mbar) with a monochromatic aluminium Kalpha X-Ray source (1486.74 eV). The energy resolution was measured by the FWHM of the Ag $3d^{5/2}$ peak for a sputtered silver foil was 0.62 eV.

Inductively Coupled Plasma Optical Emission Spectrometry (ICP-OES). Measurements were performed on an Optima 4300DV Perkin-Elmer system. Samples were prepared by taking 5 mg of the NP powders and digesting them with aqua regia under microwave conditions followed by a dilution of the mixture with HCl 1% (v/v).

ThermoGravimetric Analysis (TGA). Thermogravimetric analyses were performed by Prof. S. Suriñach in the Materials Physics Department of UAB. They were carried out in a Perkin Elmer TGA 7 analyzer. Measurements were carried out in a 30-750 °C temperature range in continuous heating regimes (2 °C/min) under Ar atmosphere. The samples were pre-treated for 30 min at 150°C under vacuum in order to remove any solvent residues.

The percentage of ligand in the sample was calculated as follows. From the ligand experiment we attribute the beginning of the ligand loss at 140 °C, so the value at this temperature was taken as initial value. For the final ligand loss point, the value on the change of the slope was taken. The latter was subtracted from the former to obtain the ligand percentage on each sample.

Electrochemical measurements. All the electrochemical experiments were performed using a BioLogic SP-150 potentiostat. Rotating disk electrode (RDE) was rotated at 3000 rpm in order to ensure complete removal of *in-situ* formed gas bubbles. The solutions were degassed previous to the electrochemical analysis with a N_2 flow. Ohmic potential (IR) drop was automatically corrected at 85 % using the Biologic EC-Lab software for cyclic voltammetry and chronoamperometry. For chronopotentiometry experiments IR drop was manually corrected ($E_{\mathrm{mod}} = E_{\mathrm{meas}} + E_{\mathrm{IR}}$, mod=modified and meas=measured) at 85% by adding the corresponding potential value $E_{\mathrm{IR}} = i_{\mathrm{exp}} \times (R_{\mathrm{mes}} \times 0.85)$, where i_{exp} is the applied current in A and R_{mes} is the measured resistance in Ω. 1 M H_2SO_4 solution was prepared by mixing 56.1 mL of 95-97 % H_2SO_4 in 1 liter of Mili-Q water.

Either a glassy carbon disk (GC_d, ϕ = 0.3 cm, S = 0.07 cm^2) or a rotating disk electrode (RDE, ϕ = 0.3 cm, S = 0.07 cm^2) were used as working electrodes (WE). A Pt grid was used as counter electrode (CE) and a Saturated Calomel Electrode (SCE, KCl sat.) was used as a reference electrode (RE). All data were transformed to RHE by adding +0.24 V.

Electrode Preparation. A 2 $mg \cdot mL^{-1}$ dispersion was prepared by adding 1 mg of sample in 500 µL of THF and sonicating for 30 min. Then, a 5 µL aliquot (for GC_d and RDE) of this dispersion was added on the surface of the GC (S = 0.07 cm^2), and dried with a N_2 flow.

Linear Seep Voltammetry (LSV). For LSV a 20 mL vial was used as an electrochemical cell. For HER experiments, the system was scanned from E_i = 0.640 V to E_f = -0.360 V at a scan rate of 10 mV/s unless otherwise stated, and from E_i = 0.240 V to E_f = 1.640 V for OER experiments, at a scan rate of 10 mV/s unless otherwise stated.

4A.8 References

---

1 a) S. W. Gersten, G. J. Samuels, T. J. Meyer, *J. Am. Chem. Soc.* **1982**, *104*, 4029-4030; b) J. R. McKone, S. C. Marinescu, B. S. Brunschwig, J. R. Winkler, H. B. Gray, *Chem. Sci.* **2014**, *5*, 865-878.

2 J. Creus, R. Matheu, I. Peñafiel, D. Moonshiram, P. Blondeau, J. Benet-Buchholz, J. García-Antón, X. Sala, C. Godard, A. Llobet, *Angew. Chem. Int. Ed.* **2016**, *55*, 15382-15386

3 a) R. Matheu, L. Francàs, P. Chernev, M. Z. Ertem, V. Batista, M. Haumann, X. Sala, A. Llobet, *ACS Catal.* **2015**, *5*, 3422-3429; b) T. Abe, T. Goto, K. Ohzeki, M. Kaneko, *Electrochim. Acta* **2000**, *45*, 4009-4014.

4 M. Zheng, Y. Li, *J. Mater. Chem. A* **2015**, *3*, 14942-14962

5 T. Bhowmik, M. K. Kundu, S. Barman, *ACS Appl. Mater. Interfaces* **2016**, *8*, 28678-28688

6 a) J. Mahmood, F. Li, S. Jung, M. S. Okyay, I. Ahmad, S. Kim, N. Park, H. Y. Jeong, J. Baek, *Nature Nanotech.* **2017**, *12*, 441-446; b) J. Cheng, H. Zhang, H. Ma, H. Zhong, Y. Zou, *Electrchim. Acta* **2010**, *55,* 1855-1861; c) X. Kong, K. Xu, C. Zhang, J. Dai, S. N. Oliaee, L. Li, X. Zeng, C. Wu, Z. Peng, *ACS Catal.* **2016**, *6*, 1487-1492; d) Y. Zheng, Y. Jiao, Y. Zhu, L. H. Li, Y. Han, Y. Chen, M. Jaroniec, S. Qiao, *J. Am. Chem. Soc.* **2016**, *138*, 16174-16181; e) Z. Chen, J. Lu, Y. Ai, Y. Ji, T. Adschiri, L. Wan, *ACS Appl. Mater. Interfaces* **2016**, *8*, 35132-35137; f) J.-Q. Chi, W. K. Gao, J. H. Lin, B. Dong, K. L. Yan, J. F. Qin, B. Liu, Y. M. Chai, C. G. Liu, *ChemSusChem* **2018**, *11*, 743-752.

7 a) Y. Zhang, T. Ren, *Chem. Commun.* **2012**, *48*, 11005-11007; b) N. C. King, C. Dickinson, W. Zhou, D. W. Bruce, *Dalton Trans.* **2005**, *0*, 1027-1032; c) E. Demir, S. Akbayrak, A. M. Önal, S. Özkar, *ACS Appl. Mater. Interfaces* **2018**, *10*, 6299-6308; d) R. Ye, Y. Liu, Z. Peng, T. Wang, A. S. Jalilov, B. I. Yakobson, S. H. Wei, J. M. Tour, *ACS Appl. Mater. Interfaces* **2017**, *9*, 3785-3791.

8 a) S. Drouet, J. Creus, V. Collière, C. Amiens, J. García-Antón, X. Sala, K. Philippot, *Chem. Commun.* **2017**, *53*, 11713-11716; b) K. Magdić, K. Kvastek, V. Horvat-Radošević, *Electrochim. Acta* **2015**, *167*, 455-469.

9 N. Karousis, N. Tagmatarchis, D. Tasis, *Chem. Rev*. **2010***, 110*, 5366-5397.

10 a) E. Castillejos, P. Debouttière, L. Roiban, A. Solhy, V. Martinez, Y. Kihn, O. Ersen, K. Philippot, B. Chaudret, P. Serp, *Angew. Chem. Int. Ed.* **2009**, *48*, 2529-2533; b) B. F. Machado, M. Oubenali, M. R. Axet, T. T. NGuyen, M. Tunckol, M. Girleanu, O. Ersen, I. C. Gerber, P. Serp, *J. Catal.* **2014**, *309*, 185-198.

11 Z. L. Wang, K. Sun, J. Henzie, X. Hao, C. Li, T. Takei, Y. M. Kang, Y. Yamauchi, *Angew. Chem. Int. Ed.* **2018**, *57*, 5848-5852.

12 C. Amiens, B. Chaudret, D. Ciuculescu-Pradines, V. Collière, K. Fajerwerg, P. Fau, M. Kahn, A. Maisonnat, K. Philippot, *New J. Chem.* **2013**, *37*, 3374-3401.

13 K. Philippot, P. Lignier, B. Chaudret, in *Ruthenium in catalysis* **2014**, C. Bruneau and P.H. Dixneuf (Eds), Wiley VCH, Weinheim, **2014**, *Top. Organomet. Chem.* **2014**, 48, 319-370.

14 S. Iijima, *Nature* **1991**, *354*, 56-58.

15 P. Patidar, K. Kasera, M. K. Vijay, P. Diwan, *IJSRD* **2014**, *9*, 237-240.

16 X. Zhang, Y. Ye, H. Wang, S. Yao, *Radiat. Phys. Chem.* **2010**, *79*, 1058-1062.

17 P. Khalid, M. A. Hussain, V. B. Suman, A. B. Arun*, J. Environ. Nanotechnol.* Volume **2015**, *4*, 62-75.

18 a) B. Santosh, Z. Wu, R. S. Siddhartha, G. K. Prasad, S. S. Ramamurthy, S. Mitra, R. B. Dandamudi, *Int. J. Hydrogen Energy* **2016**, *41,* 23007-23014; b) J. Goel, S. Basu, *Int. J. Hydrogen Energy* **2014**, *39,* 15956-15966.

19 a) X. Li, Y. Fang, S. Zhao, J. Wu, F. Li, M. Tian, X. Long, J. Jin, J. Ma, *J. Mater. Chem. A* **2016**, *4*, 13133-13141; b) J. Guan, D. Li, R. Si, S. Miao, F. Zhang, C. Li, *ACS Catal.* **2017**, *7*, 5983-5986; c) T. H. Lu, C. J. Chen, Y. R. Lu, C. L. Dong, R. S. Liu, *J. Phys. Chem. C* **2016**, *120*, 28093-28099.

20 J. Lee, S. A. S. Shah, P. J. Yoo, B. Lim, *Chem. Phys. Lett.* **2017**, *673*, 89-92.

21 T. E. Lister, Y. V. Tolmachev, Y. Chu, W. G. Cullen, H. You, R. Yonco, Z. Nagy*, J. Electroanal. Chem.* **2003**, *554/555*, 71-7.

22 a) E. A. Paoli, F. Masini, R. Frydenal, D. Deiana, C. Schlaup, M. Malizia, T. W. Hansen, S. Horch, I. E. L. Stephens, I. Chorkendorff, *Chem. Sci.* **2015**, *6*, 190-196; b) I. C. Man, H. Y. Su, F. Calle-Vallejo, H. A. Hansen, J. I. Martínez, N. G. Inoglu, J. Kitchin, T. F. Jaramillo, J. K. Nørskov, J. Rossmeisl, *ChemCatChem* **2011**, *3*, 1159-1165; c) K. Maeda, R. Abe, K. Domen, *J. Phys. Chem. C* **2011**, *115*, 3057-3064; d) T. Reier, M. Oezaslan, P. Strasser, *ACS Catal.* **2012**, *2*, 1765-1772.

23 L. A. De Faria, J. F. C. Boodts, S. Trasatti, *J. Appl. Electrochem.* **1996**, *26*, 1195-1199.

24 D. Bélanger, J. Pinson, *Chem. Soc. Rev*. **2011**, 40, 3995-4048.

25 R. J. Chen, Y. Zhang, D. Wang, H. Dai, *J. Am. Chem. Soc.* **2001**, *123*, 3838-3839.

4B. Carbon Microfiber-Supported RuNPs as HECs: Stabilizing Effect of the Support & Surface Environment

4B.1 Introduction

In the previous sub-Chapter 4A, CNTs were used as catalyst support for Ru-based NPs, considering their well-known properties as, for example, high stability in a wide range of conditions and large surface area. Good overpotential and current intensity values have been obtained with Ru@CNTs for HER/OER, as reported for other CNT-based molecular systems.[1] However, to be applied as electrocatalysts for water splitting reactions, CNT-based species require to be deposited onto an electrode, what endangers the mechanical stability as there is no chemical bond in this immobilization. Additionally, when deposited onto small-surface-area electrodes, the absolute yields of produced H_2/O_2 are very low, which is a limiting factor for their applicability in scale-up devices.

Thus, another appropriate carbon-based material is needed for large-scale electrocatalytic HER applications and carbon fibers (CFs) appear as a material of choice to attend this objective. Indeed, carbon fibers are a low-cost carbon-based material that presents high surface area, high chemical and thermal stability and also a remarkable electric conductivity. In addition, CFs are highly flexible and portable, being able to bent, twist or fold in any direction while being able to easily restore their original shape.[2] Moreover, CFs are an electrode itself, thus avoiding their immobilization onto other conductive supports (as in the case of CNTs) being directly used as working electrodes for electrocatalytic experiments.

In the literature, only a few HE-nanocatalysts based on the use of CFs as both the catalyst support and electrode (or derivatives such as CF cloth or CF paper) have been developed so far.[3] They are mainly made of low-cost and highly-abundant first-row transition metals, such as Ni[4] or Co.[5] Moreover, when bare CFs were tested as potential-HECs without any further modification and no additional species they showed catalytic activity and a good robustness.[6] However, the lack of homogeneity in benchmarking the results does not allow a proper comparison of the described catalysts. Nevertheless, CFs seems to be an ideal support in order to achieve a more efficient HER nanocatalyst through a symbiotic-type interaction. The immobilization of RuNPs can lead to an enhancing of the current intensities in comparison with those of the bare support, and a higher stability and recyclability of the particles can be achieved.

In the following part, we will describe the preparation and characterization of a cathodic system for HER based on RuNPs supported onto carbon microfibers (CFs) which are composed by a pyridyl-based structure (see Figure 1-left). These CFs-electrodes were provided by Dr. R. Mas-Ballesté from the Universidad Autónoma de Madrid. As previously proven when using pyridine-type ligands as stabilizers of RuNPs (Ch. 3B-3C), pyridyl groups can enhance the activity of the catalytic material. In the present case we can also expect an improvement of the nanoparticle grafting efficiency on the carbon fibers. Additionally and for comparison purposes, CFs modified under oxidative treatment were also provided, which contain carboxylate groups on the pyridyl-based structure, in the form of nicotine-like species. The NPs have been obtained through the organometallic approach,[7] by decomposing *in-situ* the [Ru(cod)(cot)] precursor in the presence of the CFs. In addition, **Ru-0.2PP** nanomaterial (**Ru1** in Ch. 3C) has been deposited onto the same CFs in order to compare the electrocatalytic performances of this other CF-supported Ru nanocatalyst with those of *in-situ* prepared Ru@CF systems. As it will be shown, our studies allowed to demonstrate that the use of functionalized / non-functionalized CFs as well as the different stabilization of the NPs play a key role in the HER activity attained, but even more importantly, on the stability of the hybrid nanomaterial.

4B.2 Synthesis & characterization of CF-supported RuNPs

Four different CF-supported RuNPs systems have been prepared for comparison purposes in catalysis. First, two different supports were provided by Dr. R. Mas-Ballesté: non-modified pristine carbon fibers (**pCF**, Figure 1 and Figure 2a and b) and functionalized CFs (**fCF**, Figure 1 and Figure 2c and d).[6] **pCF**/**fCF** are composed by pyridyl groups in a graphene-like structure with a clean surface, but XPS proves that they are less structured than the “highly oriented pyrolytic graphite” reference material, as described in a previous publication by R. Mas-Ballesté *et al*. **fCF** have been obtained by surface oxidation of **pCF** in a 1:1 mixture of H_2SO_4/H_2O_2 at r.t. (see Figure 1, left), to obtain carboxylate groups on the pyridyl moieties in the form of nicotine-like species. In this oxidative process the graphitic regions of the carbon fibers were not altered and therefore, electric conductivity is preserved.

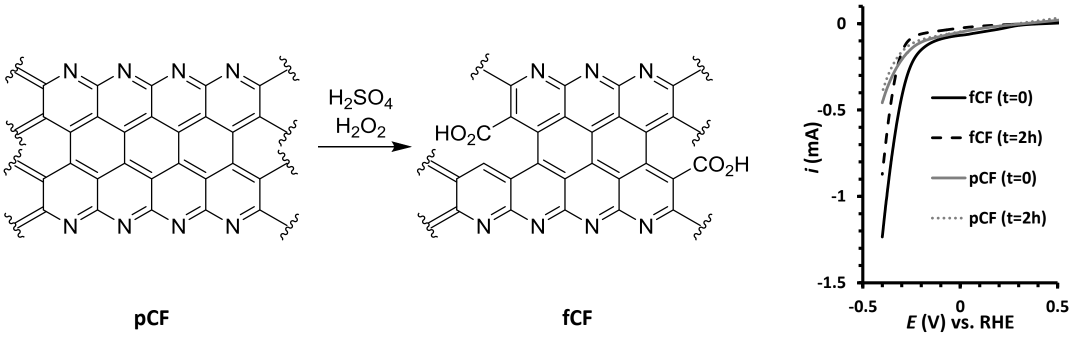

Figure 1. Left, preparation of **fCF** from **pCF**. Right, LSV experiment of **pCF** and **fCF** in 1 M H_2SO_4 before and after a 2 h bulk electrolysis at *j* = -10 mA·cm^{-2}.

Those modified fibers (**fCF**) have been demonstrated to be electroactive catalysts towards HER, as the result of the presence of carboxylated moieties in their pyridyl-based carbon structure (Figure 1, right).[6] Additionally, when acting as a support for nanoparticles, such a functionalization is expected to have influence on both the grafting and chemical stabilization of the NPs, and consequently on the stability towards modification of their oxidation state during catalysis investigation. In the same Figure 1-right, we can observe that **pCF** display much worse activity towards HER. Previous to modification with RuNPs, the CF-filaments were joined in ≈21000-fibers bunches and cut in 6-cm long electrodes, each weighting ≈90 mg (see Experimental part for more details).

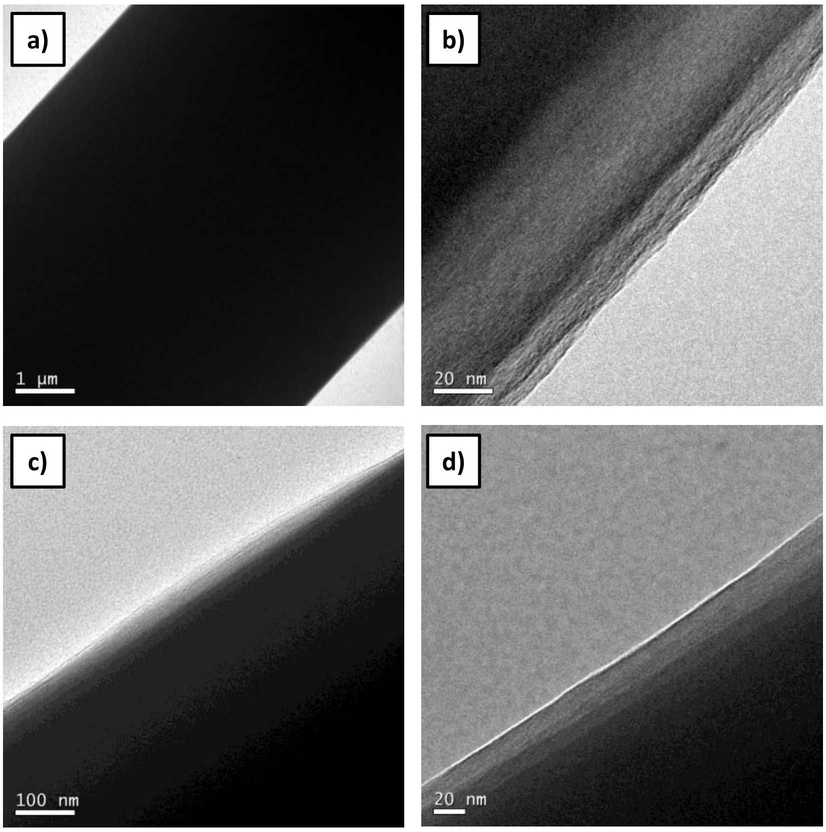

Figure 2. TEM pictures of non-modified **pCF** (a and b) and **fCF** (c and d) at different magnifications.

The deposition of RuNPs on the **pCF** and **fCF** electrodes has been performed by two different ways based on the organometallic approach.[7] On one hand (1st method), an *in-situ* synthesis of RuNPs has been carried out by decomposing 10 mg of [Ru(cod)(cot)] (cod: 1,5-cyclooctadiene; cot: 1,3,5-cyclooctatriene) in the presence of the CF electrodes (90 mg) in THF, at r.t. under 3 bar of H_2. Two electrodes (one **pCF** and one **fCF**) were placed in the reaction vessel to ensure same reaction conditions for the two new species, meaning a Ru/CF ratio of ≈ 1.8 wt.% in each reaction. By this way naked metal atoms released from the decomposition of the Ru precursor nucleated directly on the carbon-based surface, as represented in Scheme 1. In these conditions, only the carbon surface of the support, which is based on a pyridylic structure and carboxylic groups functionalities when present (**fCF**), and THF used as solvent can contribute to the stabilization of the RuNPs.

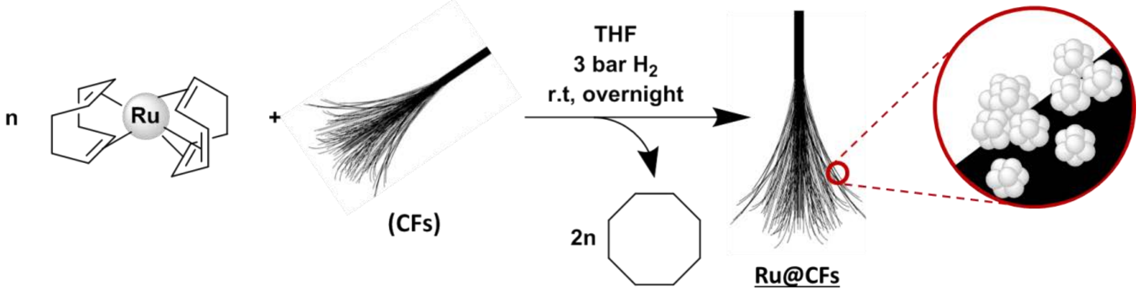

Scheme 1. *In-situ* synthesis of CF-supported Ru-NPs.

On the other hand (2nd method), pre-synthesized **Ru-0.2PP** nanoparticles as previously described in Chapter 3B-3C were immobilized on the CFs by soaking xCF (x=p,f) into a crude colloidal dispersion of **Ru-0.2PP**. In this case, the RuNPs have been first stabilized by the **PP** ligand and in a second step deposited on the CFs by a simple immersion of the support in the colloidal dispersion stirring at r.t. overnight. The idea was here to study the influence of the presence of both a stabilizing ligand and the CF supports onto the catalytic properties. It is important to note that, when supported on a glassy carbon disk electrode (Ch. 3B-3C), **Ru-0.2PP** NPs showed large current intensities at low overpotentials for the electrocatalytic reduction of protons, with excellent stability after 12h catalyzing the evolution of H_2 under strong acidic (**Ru1-GC**) and basic (**Ru2-GC**) conditions (1 M H_2SO_4 and 1 M NaOH, respectively).

The combination of the two different CFs supports (**pCF** & **fCF**) and two synthetic methodologies (1st & 2nd method, *in-situ* & *ex-situ*, respectively) has led to obtain 4 different CF-supported RuNPs systems: **Ru@pCF** and **Ru@fCF** (1st method), and **RuPP@pCF** and **RuPP@fCF** (2nd method). After purification by rinsing with pentane, these nanomaterials have been characterized by TEM, XPS and ICP analysis. Figure 3 shows representative TEM pictures recorded for the 4 CF-supported RuNPs systems. One can detect in each case the presence of very small particles onto the surface of the carbon fibers. Even if a few agglomerates of very small NPs have been also observed, they are mostly organized into a homogeneous layer standing along the fibers, except for **Ru@fCF** system which repeatedly showed more NPs' agglomeration. This is important to note as it can have an important effect on the electrocatalytic performance, as less NPs' surface and consequently less catalytic sites might be exposed.

High particle-loading on the CFs' surface and very small particles' dimension are visible characteristics on the TEM images. The bad contrast caused by the fibers and the small diameter of the particles made difficult to measure the mean sizes, which appears to be in the 1-2 nm range in the 4 cases (Figure 3-right for size histograms and Table 1).

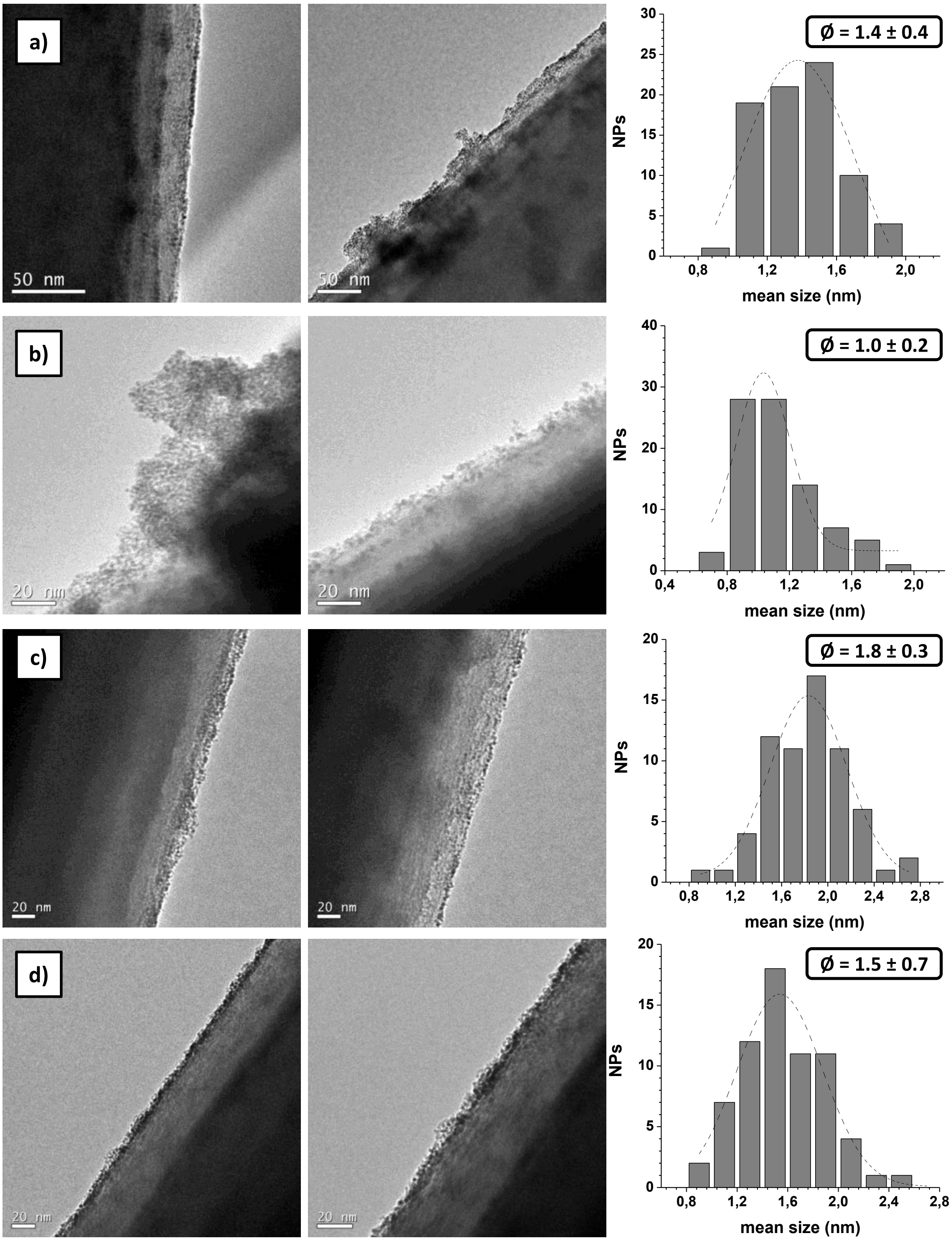
a)
50 nm
50 nm
Ø = 1.4 ± 0.4
NPs
mean size (nm)
b)
20 nm
20 nm
Ø = 1.0 ± 0.2
NPs
mean size (nm)
c)
20 nm
20 nm
Ø = 1.8 ± 0.3
NPs
mean size (nm)
d)
20 nm
20 nm
Ø = 1.5 ± 0.7
NPs
mean size (nm)

Figure 3. Representative TEM images of a) **Ru@pCF**, b) **Ru@fCF**, c) **RuPP@pCF** and d) **RuPP@fCF** CF-supported RuNPs systems.

We can note a slight difference in mean size between the materials **RuPP@pCF** and **RuPP@fCF**, namely 1.5±0.3 against 1.8±0.7 nm, while no difference is expected as the same batch of preformed NPs has been used in these two cases. Nevertheless, we can consider that it is not significant given the large standard deviation observed in the second case and due to the difficulties of the measurements. Further, when comparing the **Ru@pCF** and **Ru@fCF** systems, it seems that the presence of carboxylic acids groups on the carbon fibers has no influence on the RuNPs mean size (1.2±0.4 against 1.0±0.2 nm, respectively) but here also the difficulties in measurements cannot allow us to conclude unambiguously.

As already observed in Chapter 3C, XPS analyses show that the RuNPs contain two phases, metallic Ru and RuO_2, due to a partial oxidation of the NPs' surface (Figure 4).

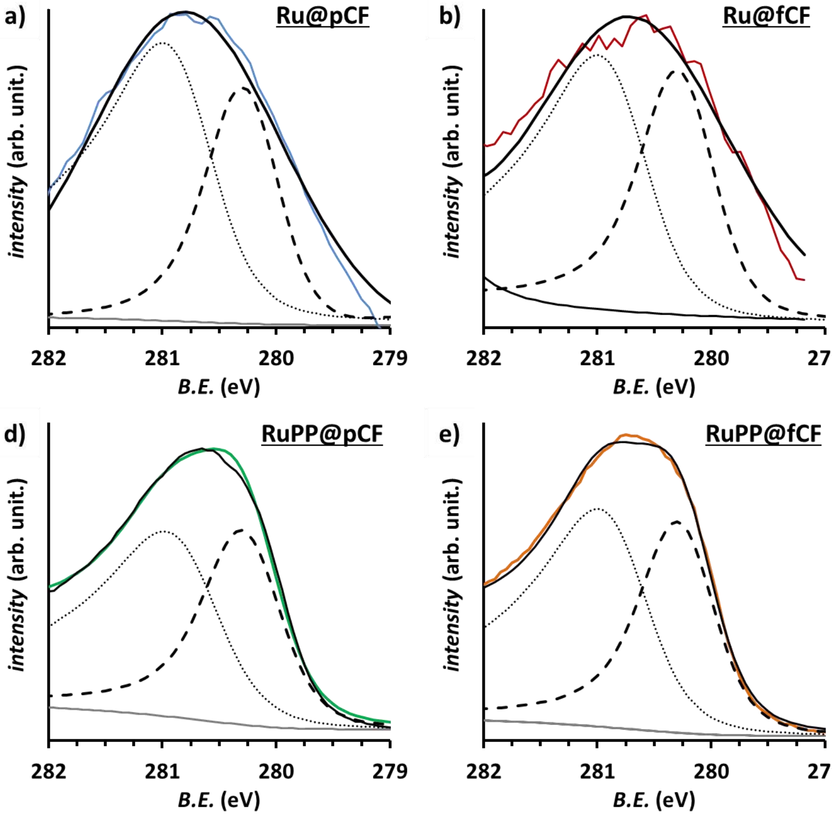

Figure 4. XPS analysis of a) **Ru@pCF** (blue), b) **Ru@fCF** (red), c) **RuPP@pCF** (green) and d) **RuPP@fCF** (orange). Background (grey), metallic-Ru component (Ru $3d_{5/2}$-279.8, dashed black), RuO_2-component (Ru $3d_{5/2}$-280.8, dotted-black), envelope (bold).

Finally, ICP analysis results of the 4 nanomaterials slightly vary from one sample to the other. The measured Ru content is in the 0.4-1.1% range in all the cases. This low loading could be expected as the fibers' thickness is 8 µm, which implies a high C content. However, considering the initial Ru/CF ratio present in the reaction vessel (≈1.8 Ru wt.%), the values confirm an effective immobilization by the two methodologies.

4B.3 Electrocatalytic HER studies

Having in hands 4 different CF-supported RuNPs systems, they have been investigated in electrocatalytic proton reduction catalysis. In order to limit electrochemical reproducibility issues caused by fibers' self-attaching, electrodes were built using 1 mg of each sample for electrocatalytic evaluation (see Experimental part for electrode preparation). In addition, when H_2 is being produced it forms big bubbles that block the electrode surface altering the electrochemical response, being this phenomenon diminished by using the 1mg-samples. The electrodes were tested in a two-compartment cell in 1 M H_2SO_4 under reductive potentials. First, a change on the current intensity has been observed at reductive potentials < 0 V vs. RHE, which is the thermodynamic potential for H^+ reduction reaction (E_{therm}). The current intensity, which is referenced per mg of material, i_{cat} = [$\text{mA·mg}_{\text{cat}}^{-1}$], has been also normalized by the Ru wt.% in each case, in order to be able to compare the catalytic activity between samples with different loadings, and the new values were labeled as i_{Ru} = [$\text{mA·g}_{\text{Ru}}^{-1}$].

Table 1. Main data describing the electrochemical performance of **Ru@pCF**, **Ru@fCF**, **Ru0.2PP@pCF** and **Ru0.2PP@fCF** at 1M H_2SO_4. RuNPs' mean size (Ø), onset overpotential (η_0), overpotential at i_{cat} = 10 mA·mg^{-1} (η_{10}), Ru wt. % in the sample, overpotential at $|i_{\text{Ru}}|$ = 1 A·mg^{-1}, percentage of current intensity at η=200 mV after a 2h electrolysis.

System	**Ø (nm)**	***η_0*** **(mV)**	***η_{10}*** **(mV, i_{cat} = 10 mA·mg^{-1})**	***Ru wt.%***	***η*** **(mV, $\lvert i_{\text{Ru}}\rvert$ = 1 A·mg^{-1})**	**% i_{cat} (t = 2 h)***
pCF	-	220	-	-	-	-
fCF	-	180	-	-	-	-
Ru1	1.5 ± 0.3	0	20 (j = 10 mA·cm^{-2})	85	90	-
Ru@pCF	1.4 ± 0.4	70	265	0.57	240	34
Ru@fCF	1.0 ± 0.2	30	235	0.65	210	16
RuPP@pCF	1.8 ± 0.3	5	225	0.47	150	99
RuPP@fCF	1.5 ± 0.7	0	180	1.10	190	40

* %i_{cat} calculated by dividing i_{cat} (η=200 mV) at t=2 h by the value at t=0 as short-term stability data.

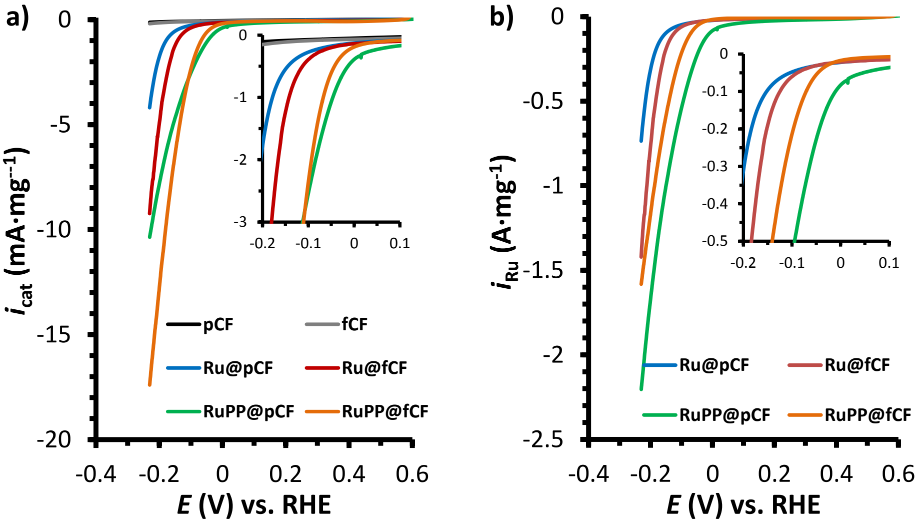

Figure 5. Polarization curves of **Ru@pCF** (blue), **Ru@fCF** (red), **Ru0.2PP@pCF** (green), **Ru0.2PP@fCF** (orange), **pCF** (black) and **fCF** (grey) at 1 M H_2SO_4 normalized by mg of material (left) and by mg of Ru (right).

Observing Table 1 and Figure 5, we can conclude that the two factors, namely a) fibers' nature and b) NPs' surface environment, both play a key role on the activity and stability of the CF-supported RuNPs hybrid systems. On one hand, *ex-situ* synthesized **RuPP**-systems (**RuPP@pCF** and **RuPP@fCF**) reach higher intensities at smaller overpotentials than *in-situ* Ru-based ones (**Ru@pCF** and **Ru@fCF**). This behavior confirms the positive effect of the 4-phenylpyridine ligand interaction with the particles on their catalytic performance, as observed in Chapter 3B-3C with non-supported **Ru-0.2PP**/**Ru1-GC** NPs. Indeed, η_0 is close to 0 mV for **RuPP@pCF** and **RuPP@fCF**, confirming a similar behavior than that of **Ru1-GC**, and thus no influence of the carbon support in this parameter. In contrast, **Ru@pCF** and **Ru@fCF** show higher η_0 (30 and 70 mV, respectively) than RuPP@xCF, comparable with those in the literature for C-supported RuNPs.[8]

On the other hand, higher currents are observed for **Ru@fCF** and **RuPP@fCF** in contrast to their **pCF** counterparts (**Ru@pCF** and **RuPP@pCF**). This result suggests a positive influence of the functionalized support on the catalytic activity, possibly due to the ē-donor ability of the carboxylate groups formed on the pyridyl structure after the treatment with H_2SO_4/H_2O_2.

For stability studies, overpotentials equal to 350 mV and 250 mV were applied for systems Ru@xCF and RuPP@xCF respectively (x=p,f), in order to reach a $|i_{cat}| \approx 10$ $mA \cdot mg_{cat}^{-1}$ but avoiding the use of abusive reduction potentials. Table 1 summarizes the electrochemical performances of the four different systems displayed in Figure 6. The last column in Table 1, % i_{cat} (t=2h) defined as the remaining current percentage at a specific η = 200 mV after 2 h at 250-350 mV reductive potential, gives an idea of the stability of the system during catalysis (graphical data in Figure 6). While **Ru@fCF** diminishes its i_{cat} to >1/5th in <2h (i_{cat} = -5.0 mA (*t*=0) vs. -0.8 mA (*t*=90min)), **Ru@pCF** still keeps 1/3rd i_{cat} after a similar time (i_{cat} = -1.8 mA (*t*=0) vs. -0.4 mA (*t*=2h)), requiring 5h to lose the same percentage of activity. Similar to that, **RuPP@fCF** requires 2h to lose 60% of the i_{cat} (i_{cat} = -14.5 mA (*t*=0) vs. -5.7 mA (*t*=2h)), still more stable than Ru@xCFs systems. Impressively, **RuPP@pCF** is almost unaltered after 2h (i_{cat} = -8.6 mA (*t*=0) vs. -7.7 mA (*t*=2h), with 40% i_{cat} remaining after 18h. Therefore, the stability decreases as:

RuPP@pCF > **RuPP@fCF** > **Ru@pCF** > **Ru@fCF**

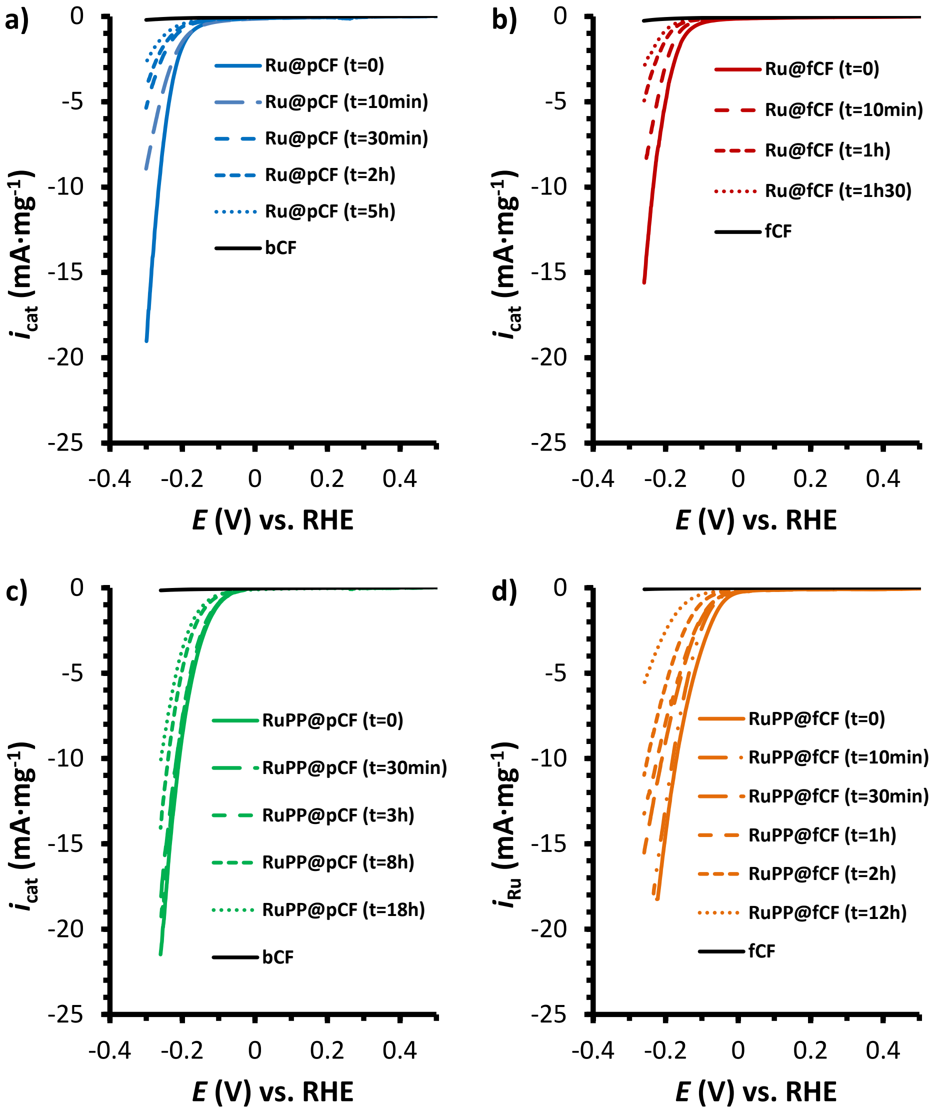

Figure 6. LSV curves of A) **Ru@pCF**, B) **Ru@fCF**, C) **RuPP@pCF** and D) **RuPP@pCF**, along a bulk electrolysis experiment at 1M H_2SO_4 pH=0. An E_{app}=250 mV was used for Ru@xCF systems to reach i_{cat}≈10 mA·mg during the electrolysis, and E_{app}=150 mV for RuPP-based systems.

According to these results, concerning the use of **pCF** or **fCF** as supports, although **fCF** is able to reach higher current densities with the two types of NPs (*in-situ* vs. *ex-situ*), **pCF** provides a higher stability than the **fCF** counterpart (either for the *in-situ* and for the *ex-situ* **Ru1**). This suggests that the carboxylate groups present in the functionalized **fCF** play a negative role on the stabilization of the particles under catalytic conditions, deteriorating the stability provided by the pyridyl-based structure of both CFs. Also, the use of ex-situ pre-synthesized **Ru1** NPs vs. the *in-situ* obtained ones strongly enhances the robustness of the hybrid materials, being the **Ru1**-based systems more stable than any of the two Ru@xCFs' electrodes. It is also worth mentioning that a higher reduction potential was required for Ru@xCFs to reach $|i_{cat}|$ ≈ 10 mA·mg_{cat}^{-1}. This difference is attributed to the absence of the **PP** ligand on the surface of the Ru@xCFs' samples which, as proved in Ch. 3B-3C, is a key factor on the catalytic performance of the RuNPs. Moreover, **Ru@fCF** TEM pictures showed more agglomerates of small NPs than the other systems, an effect that could be also influencing its low stability.

To unravel the causes influencing the stability of the four systems and further consequences, TEM analyses of the modified CFs after the 2h bulk electrolysis experiment were performed. The presence/absence of Ru in solution was checked by ICP. Comparing TEM images in Figure 7, there is visual evidence that the *in-situ* prepared Ru@xCFs systems leach a high amount of the initial NPs during the catalytic process, leaving a cleaner CFs' surface for both **Ru@pCF** and **Ru@fCF** (Figure 7a and b, respectively) with some agglomerates also formed during the catalytic reaction. This trend is confirmed by EDX analysis on the surface of **Ru@pCF** and **Ru@fCF** (Figure 8a and b, respectively) showing almost no presence of Ru, what is in agreement with the electrocatalytic results.

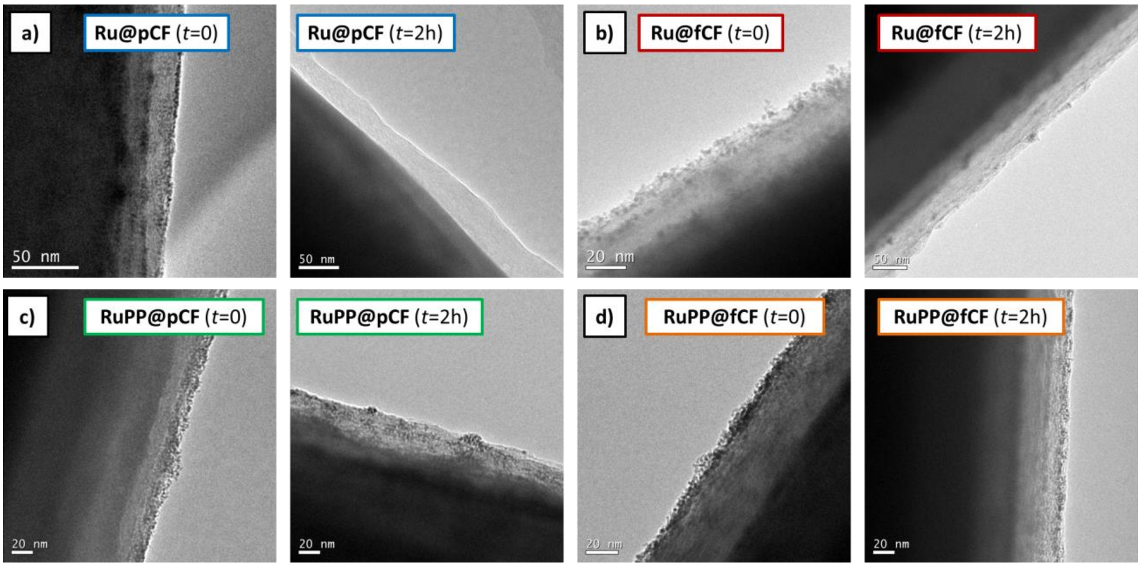

Figure 7. Representative TEM images of a) **Ru@pCF**, b) **Ru@fCF**, c) **RuPP@pCF** and d) **RuPP@fCF** at *t*=0 and *t*=2h after bulk electrolysis in 1 M H_2SO_4 at η =250 and 350 mV for Ru@xCF and RuPP@xCF, respectively.

In contrast, the two **Ru1**-based systems (**RuPP@pCF** and **RuPP@fCF**) showed similar loading on the surface of the fibers before and after catalysis (Figure 7c and d, respectively), with very small NPs along the CFs' surface and almost no agglomeration observed. EDX analyses (Figure 8c and d, respectively) confirm in this case the presence of Ru throughout the surface. Two possibilities may justify the NPs' leaching from the surface of the electrode. On the one hand, the evolution of the material under catalytic conditions may form molecular species that get solved in the reaction media. Considering the stability results obtained in the other parts of this manuscript and the lack of literature supporting this hypothesis, this process is not likely expected. On the other hand, mechanical instability can suppose a continuous loss of NPs, which may settle down on the bottom of the reaction vessel as detached NPs.

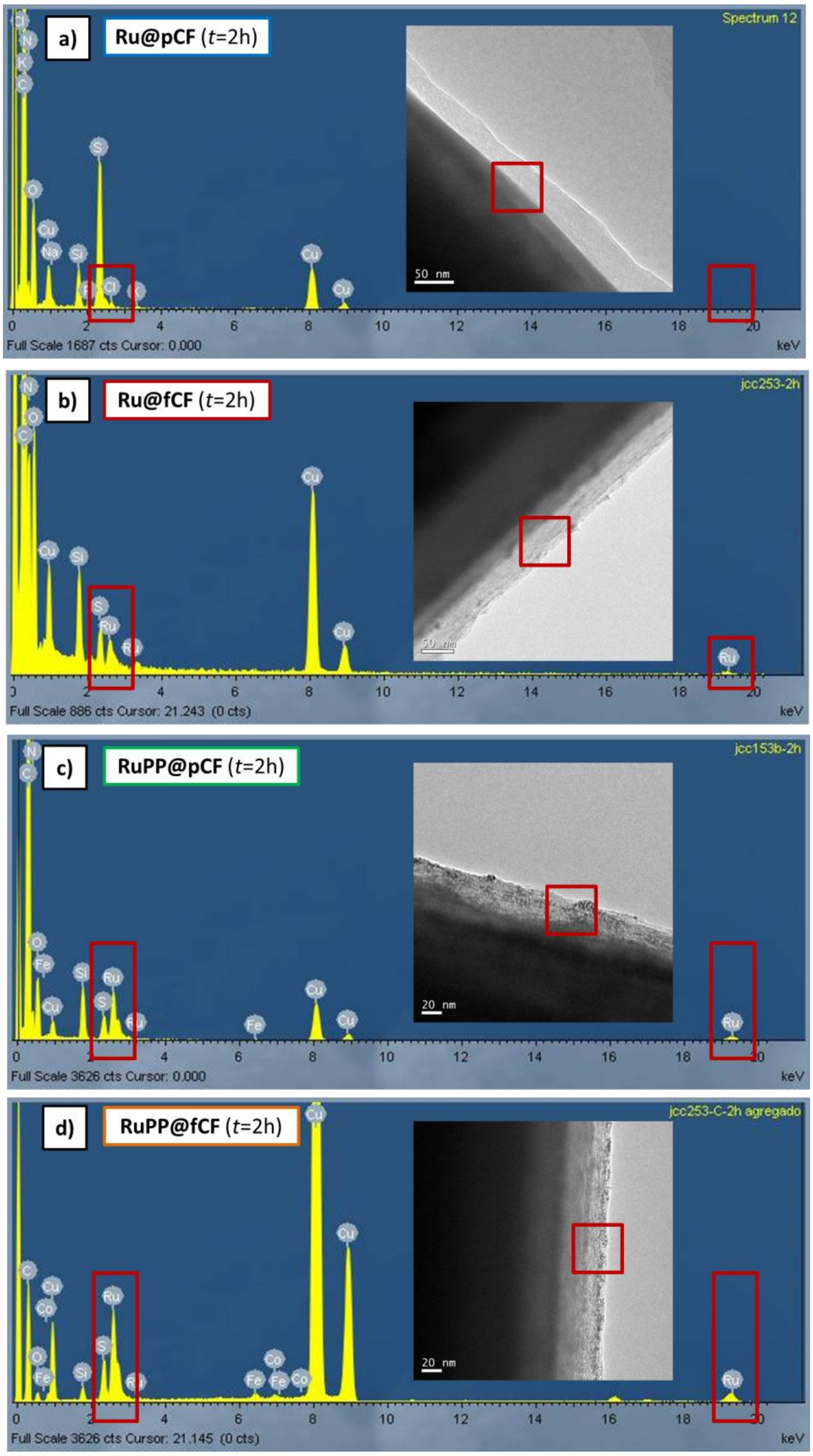

Figure 8. TEM/EDX analysis of a) **Ru@pCF**, b) **Ru@fCF**, c) **RuPP@pCF** and d) **RuPP@fCF** at *t*=2h after bulk electrolysis in 1 M H_2SO_4 at η =250 and 350 mV for Ru@xCF and RuPP@xCF, respectively.

In this sense, ICP-OES analyses were performed from the reaction solution (1 M H_2SO_4) after 2h bulk electrolysis. The results showed a small quantity of Ru for the four systems (<0.1 mg·L^{-1}, ≈5% out of the total Ru in the samples) very close to the detection limit and to the reference sample (1 M H_2SO_4 used as blank solution). Thus, as expected, the instability problem does not seem to be caused by dissolution of new

Ru-species but by mechanically detaching of the NPs from the CFs' surface. By this way, the particles could remain on the bottom of the reaction vessel, and thus not being taken for ICP analysis. Further studies need to be performed to confirm this hypothesis.

In order to test the Faradaic efficiency (FE, %) of the systems, 10-min bulk electrolysis experiment were performed with a H_2-clark sensor *in-situ* detecting the H_2 generation and storage on the gas phase. The charge passed through the system was transformed, first to moles of electrons by the Faradaic constant (96485 C·mol^{-1}), and second to theoretical H_2 moles, taking into account that the formation of every hydrogen molecule requires two electrons ($2H^+ + 2\bar{e} \rightarrow H_2$). The experimental data were extracted from the clark sensor: they were transformed to hydrogen moles by calibrating the electrochemical signal (mV) with different amounts of 99% pure H_2 and extrapolating the obtained data. The FE was estimated by dividing the sensor value by the charge value at the end of the experiment, confirming that almost quantitative amount of electrons were specifically devoted to the reduction of protons and not to other side processes (see Figure 9).

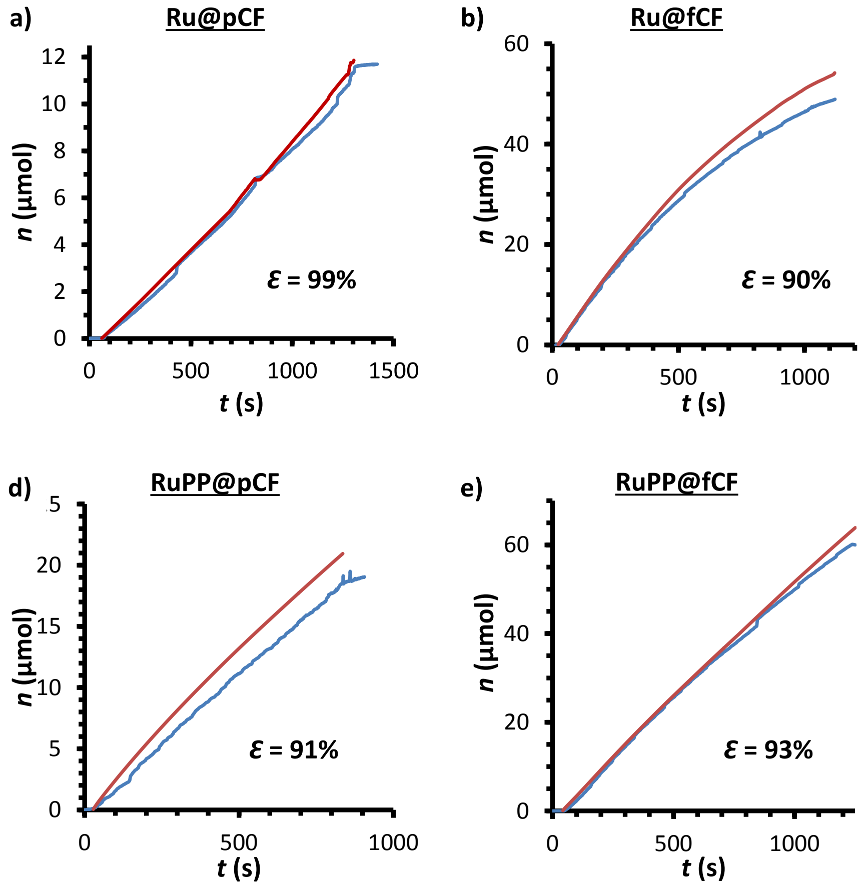

Figure 9. H_2-monitored bulk electrolysis experiments for Fadaraic efficency (FE) determination. For **Ru@pCF/Ru@fCF** and **RuPP@pCF/RuPP@fCF** an E_{app} of 350 and 250 mV were respectively applied.

Although the HER is obviously favored in acidic conditions due to the higher H^+ concentration, photoelectrochemical devices tend to work in basic media. This is because the oxidative semi-reaction (OER), which is more complex, is favored in alkaline solutions, where the release of protons for the PCET mechanism is much easier. Additionally, metal-based catalysts are usually unstable in strong acidic conditions, better tolerating high pH ranges. In view of this, **Ru@pCF** was tested at different pHs, to study the effect of this parameter on its catalytic performance. It is known from Chapter 3C that **Ru1** is very active and presents long-term stability at extreme pH conditions (1 M H_2SO_4 and 1 M NaOH).

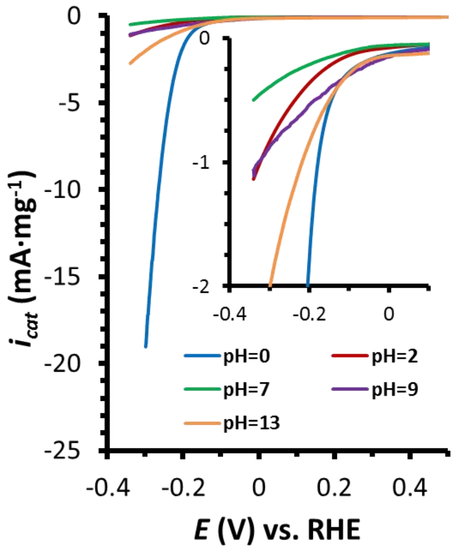

Figure 10. LSV curves of **Ru@pCF** at different pH conditions: 1 M H_2SO_4 pH=0 (blue), BBS pH=2 (maroon), PBS pH=7 (green), BBS pH=9 (purple) and 1M NaOH pH=14 (orange).

Polarization curves at pH= 0, 2, 7, 9 and 13 show a very similar trend as **Ru1**. Current densities decrease in medium-range pHs, with the worst results displayed at pH=7, but a high i_{cat} is achieved at pH=13, although it is lower than the activity observed at pH=0.

In order to benchmark the catalytic activity with other systems on the literature, activity normalization was carried out for our best system **RuPP@pCF** by the calculation of the double-layer capacitance (C_{DL}), electrochemically active surface area (ECSA) and specific activity at η = 100 mV ($j_{S(\eta=100)}$), as proposed in Jaramillo's methodology (Figure 11a and b).[9] An ECSA = 91.6 cm^2 was obtained, in the same range as the one calculated for **Ru1-GC** in 1 M H_2SO_4 (57 cm^2). This value leads to a $j_{S(\eta=100)}$ = 0.028 mA·cm^{-2}, which is within the same range than some of the electrocatalysts reported on Table A3 in Annex1 (NiW: 0.014 mA·cm^{-2}; NiMoCo: 0.043 mA·cm^{-2}), but lower than **Ru-GC** and **Ru1-GC** (0.067 and 0.550 mA·cm^{-2}, respectively) from Ch. 3A and 3C, respectively.

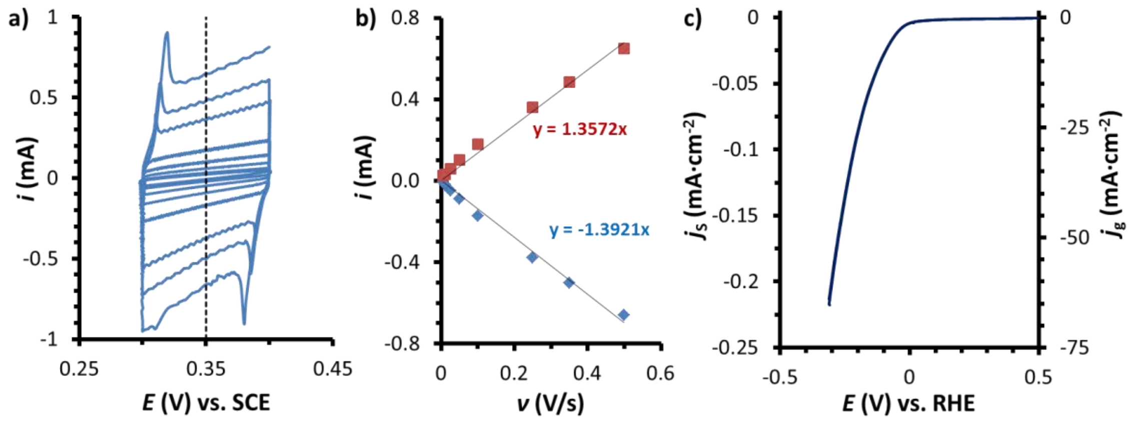

Figure 11. ECSA calculation through the electrochemical method described by Jaramillo *et al.* (a and b),[9] and c) LSV curve normalized by ECSA (left axis) and by the estimated surface area S = 0.3 cm^2 (right axis) in 1 M H_2SO_4.

On the literature, CFs-based nanocatalysts normalize their C_{DL} values by the electrode geometrical surface area, a parameter that we could not analyze. As an estimation from studies made by R. Mas-Ballesté *et al.*,[6] we assume that our 1-mg build electrodes have a geometrical surface area of 0.3 cm^2 (for further details see Experimental part). Considering this value, a normalized C_{DL} of 4.57 mF·cm^{-2} is obtained for **RuPP@pCF**, being that result among the best ones reported for CFs' supported HECs (Table 2).

Table 2. Comparison of different CF-supported HECs. Parameters: onset overpotential (η_0, mV), overpotential at j = -10 mA·cm^{-2} (η_{10}, mV), double-layer capacitance per surface unit (C_{DL}/S, mF·cm^{-2}).

Ref.	**System**	**Media**	**η_0 (mV)**	**η_{10} (mV, $\|j\|$= 10 mA·cm^{-2})**	***C_{DL}/S (mF·cm^{-2})***
4a	*Ni_3N/CMFs/ Ni_3N*	1 M KOH	28	115	221.1 (1 M KOH)
4b	*NiO-NRs/FCP*	1 M KOH	60	110	-
4c	*NiWS/CF*	0.5 M H_2SO_4	150	56	596.2
4d	*NiP/CP*	0.5 M H_2SO_4	75	98	-
5a	*PANI/CoP HNWs-CFs*	0.5 M H_2SO_4	20	55	113.4
5b	*Fe-Co_9S_8 NSs/CCF*	0.5 M H_2SO_4	100	65	373.19 (1 M KOH)
5c	*CoP/CFP-H*	0.5 M H_2SO_4	100	128	2.29
3	*WSe_2 NF/CF*	0.5 M H_2SO_4	225	375	-
This work	**RuPP@pCF**	1 M H_2SO_4	0	110 (0.3cm^2)	4.57 (ECSA=91.6cm^2)

Additionally, from the estimated S = 0.3 cm^2, a η_{10} of 110 mV was calculated, which is an acceptable value in comparison to those reported by other CFs-based electrocatalysts (see Table 2). Although S = 0.3 cm^2 is an estimated value, it was the only way to benchmark our results with those on the literature. This is because neither the ECSA nor $j_{S(\eta=100)}$ are provided for any of the reported electrocatalysts, thus limiting the proper catalysts comparison.

4B.4 Conclusions & perspectives

To sum up, we have prepared four different cathodes based on Ru nanoparticles deposited onto carbon fibers as a support, varying either the functionalization state of the carbon-based support or the synthetic procedure for the deposition of the particles, and consequently the surface environment. When tested as working electrodes in an electrochemical set-up for the proton reduction reaction, the four systems showed different activity and stability behaviors:

1) **Ru@fCF** and **RuPP@fCF** show both higher currents than their **pCF**-counterparts, confirming a positive trend of the presence of carboxylic groups on the CFs structure, on the catalytic activity of the RuNPs.
2) However, **pCF**-based electrodes display a higher stability than **fCF**-ones, meaning that those carboxilated functionalities present on the **fCF** electrodes play a negative role on the catalytic stability of the NPs.
3) **PP**-stabilized systems show higher current densities at lower overpotentials than Ru@xCF, confirming the positive effect of the **PP** ligand on the catalytic performance of the NPs, as already observed in Chapters 3B-3C.

As a future work, long-term stability should be deeply studied. In the case that the activity loss is caused by mechanical instability, the use of a fixing polymer (such as nafion or poly(methyl methacrylate), PMMA) could be beneficial to increase this parameter. It is worth checking other catalysis media (pH = 3-14) with **RuPP@pCF**, to study how the activity of **Ru-0.2PP** NPs changes (from Ch. 3B-3C) once supported in a carbon-based material depending on the pH.

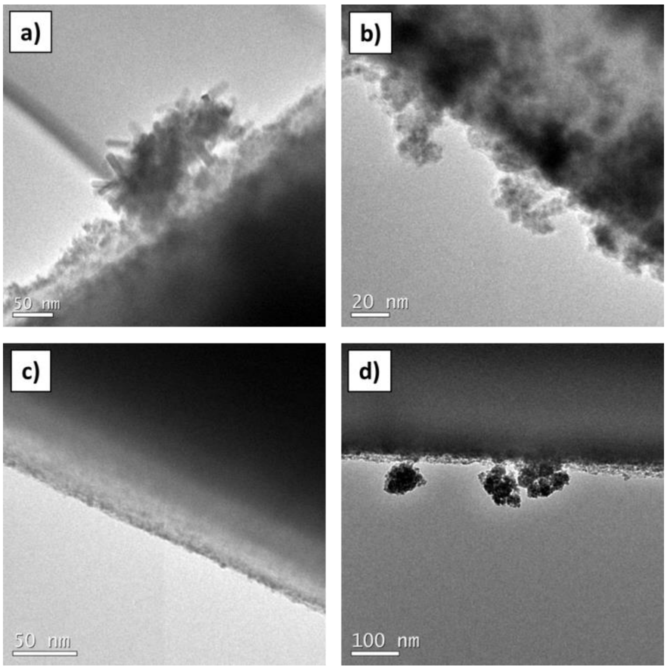

Figure 12. Representative TEM images of a) **$RuO_2$250@pCF**, b) **$RuO_2$300@pCF**, c) **$RuO_2$250@fCF** and d) **$RuO_2$300@fCF** CF-supported RuNPs systems.

In view of the results here described, as well as those previously shown in Chapter 4A with CNT-supported RuNPs, we also propose to oxidize the RuNPs to form RuO_2 and test the catalytic activity towards HER and OER. First oxidation tests with **Ru@pCF** and **Ru@fCF** at two temperatures (250 and 300 °C) resulted in the formation of mainly RuO_2 particles (as suggested by preliminary XPS analysis), some of them keeping small size but others getting agglomerated during the thermal process (see TEM pictures in Figure 12).

Then, electrocatalytic HE has been tested with the four oxidized materials and results are summarized in Figure 13 and Table 3:

Table 3. Main electrochemical parameters of RuO_2@xCF systems. Parameters: onset overpotential (η_0, mV) and overpotential at i_{cat} = 10 mA·mg^{-1} (η_{10}).

System	**η_0 (mV)**	**η_{10} (mV, $\lvert i_{cat}\rvert$ = 10 mA·mg^{-1})**
RuO_2(250)@pCF	40	240
RuO_2(300)@pCF	60	205
RuO_2(250)@fCF	60	250
RuO_2(300)@fCF	25	230

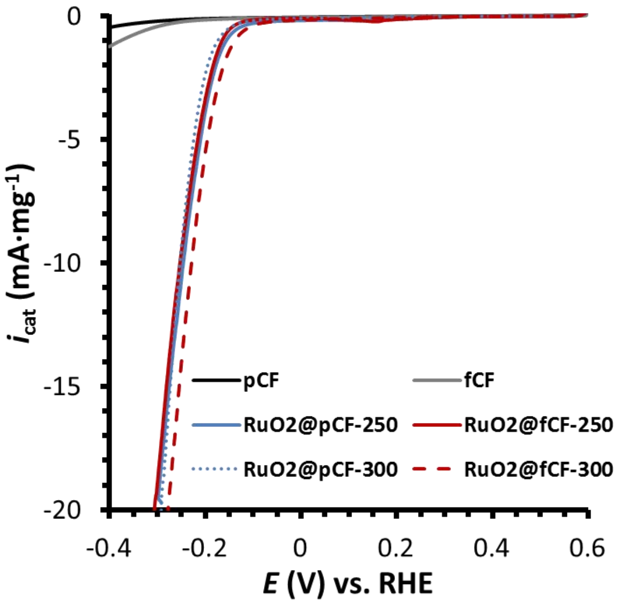

Figure 13. Polarization curves of **RuO_2(250)@pCF** (blue), **RuO_2(300)@pCF** (dashed-blue), **RuO_2(250)@fCF** (red), **RuO_2(300)@fCF** (red), bare **pCF** (black) and **fCF** (grey).

The preliminary results show that the electrochemical behavior of the four samples is similar in terms of overpotentials. Thus, the oxidation temperature (250-300 °C) and the nature of the support (**pCF** vs. **fCF**) do not seem to have a huge effect on the short-term catalytic performance of the formed RuO_2 NPs.

According to these results, it would be interesting to oxidize RuPP@xCF systems to RuO_2 to see whether the ligand and the support are essential to the catalytic behavior and roughness of the hybrid systems.

4B.5 Experimental part

Reagents. All operations for the synthesis of the CF-supported RuNPs were carried out using standard Schlenk tubes, Fisher–Porter bottle techniques or in a glove-box (MBraun) under argon atmosphere. Solvents (THF and pentane) were purified before use, by filtration on adequate column in a purification apparatus (MBraun) and handled under argon atmosphere. Solvents were degassed before use according to a freeze–pump–thaw process. The ruthenium precursor, [Ru(cod)(cot)] was purchased from Nanomeps-Toulouse. Hydrogen gas (Alphagaz) was purchased from Air Liquide. Phenylpyridine used as stabilizer was purchased from Sigma-Aldrich and used as received. High purity deionized water was obtained by passing distilled water through a nanopore Milli-Q water purification system. Carbon fibers (CFs) electrodes were were provided by Dr. R. Mas-Ballesté from Universidad Autónoma de Madrid (UAM).

Electrode preparation. The carbon fiber electrodes were hand-made prepared using a short copper wire, ≈50 cm long carbon fibers and some Teflon tape to tight everything together. The CFs electrodes contain 7 bundles **(1)** of 3000 filaments (21000 filaments) of 5-8 μm of diameter and 6 cm length each. The fibers are bended **(2)** as if each electrode contained the double of the filaments (42000), but only 2 cm were exposed for NPs' synthesis and electrode usage **(3)**. Those electrodes are approximately 90 mg weight.

After deposition of the NPs but previous to electrochemical evaluation, those electrodes were cut in 3-cm-long filaments (half fiber), and 1-mg-samples were sticked in a Cu tape together with a Cu-wire **(4)**, still ensuring 2 cm length for catalysis evaluation.

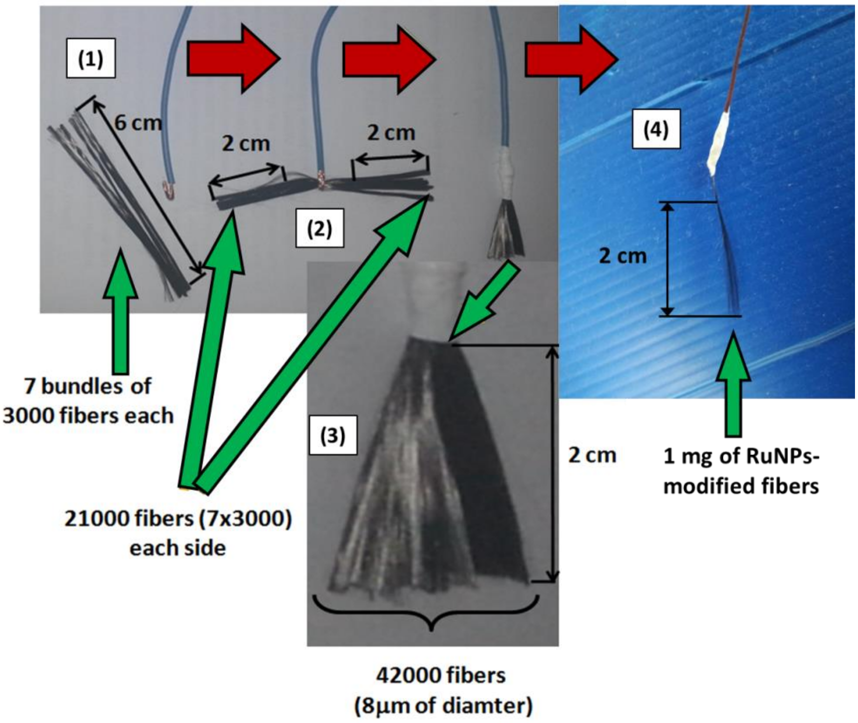
(1)
6 cm
2 cm
2 cm
(2)
(3)
(4)
2 cm
2 cm
7 bundles of
3000 fibers each
21000 fibers (7x3000)
each side
42000 fibers
(8μm of diamter)
1 mg of RuNPs-
modified fibers

Figure 14. Steps to make a CF brush. Figure adapted from reference 6.

Ru@xCF, x = pristine (p) or functionalized (f). 2 cm of xCFs were soaked in a 10 mL THF solution containing the [Ru(cod)(cot)] (10 mg, 0.026 mmol) inside a Fisher-Porter bottle. 3 bar of H_2 were added and the reaction mixture was stirred at r.t. overnight. After depressurization, the volatiles were evacuated under vacuum and the solvent removed through cannula. The resulting CF materials were rinsed with pentane and dried under vacuum.

Ru@pCF. TEM: Ø = 1.4 ± 0.4 nm. ICP(Ru%) = 0.57 %.

Ru@fCF. TEM: Ø = 1.0 ± 0.2 nm. ICP(Ru%) = 0.65 %.

RuPP@xCF, x = pristine (p) or functionalized (f). 2 cm of xCFs electrodes were soaked overnight in a THF (10 mL) crude dispersion of **Ru-0.2PP** NPs (or **Ru1**) inside a Fisher-Porter bottle. Then, the supernatant was removed through cannula and the resulting CF materials were rinsed with pentane (3x10 mL) and dried under vacuum.

RuPP@pCF. TEM: Ø = 1.8 ± 0.3 nm. ICP(Ru%) = 0.47 %.

RuPP@pCF. TEM: Ø = 1.5 ± 0.7 nm. ICP (Ru%): Ru@fCF = 1.10 %.

Characterization

Transmission Electron Microsopy (TEM) & High-Resolution Electron Microscopy (HREM). TEM and HREM observations were performed at the "Centre de

Microcaractérisation Raymond Castaing” in Toulouse (UMS-CNRS 3623) and at the “Servei de Micoscòpia” of the UAB. Samples for transmission electron microscopy (TEM) analyses were prepared by slow evaporation of a drop of the crude colloidal solution deposited onto a holey carbon-covered copper grid. Samples for high-resolution TEM (HRTEM) analyses were prepared by the same way from purified NPs redispersed in THF. TEM and HR-TEM analyses were performed on a MET JEOL JEM 1011 microscope operating at 100 kV with a resolution point of 0.45 nm and a JEOL JEM-ARM 200F microscope working at 200 kV with a resolution point lower of 0.19 nm, respectively. TEM allowed to evaluate the particle size, size distribution and morphology. Enlarged micrographs were used for treatment with ImageJ software to obtain a statistical size distribution and the nanoparticle mean diameter. The analyses were done by assuming that the nanoparticles are spherical. Nanoparticle sizes are quoted as the mean diameter ± the standard deviation.

Inductive-Coupled Plasma (ICP-OES). ICP-OES measurements were performed at the “Servei d’Anàlisis Químic” (SAQ) in the UAB, on an Optima 4300DV Perkin-Elmer system. Solid samples were prepared by digesting 1 mg with *aqua regia* under microwave conditions followed by a dilution of the mixture with HCl 1% (v/v). Liquid samples were directly diluted with HCl 1% (v/v).

X-ray Photoelectron Spectroscopy (XPS). Measurements were performed at the Catalan Institute of Nanoscience and Nanotechnology (ICN2) in Barcelona with a Phoibos 150 analyzer (SPECS GmbH, Berlin, Germany) in ultra-high vacuum conditions (base pressure 5E^{-10} mbar) with a monochromatic aluminium Kalpha x-ray source (1486.74 eV). The energy resolution was measured by the FWHM of the Ag 3d$^{5/2}$ peak for a sputtered silver foil was 0.62 eV.

Electrochemical measurements. All the electrochemical experiments were performed using a BioLogic SP-150 potentiostat. Solutions were degassed previous to the electrochemical analysis with a N_2 flow. IR drop was automatically corrected at 85 % using the Biologic EC-Lab software for cyclic voltammetry and chronoamperometry. 1 M H_2SO_4 solution was prepared by mixing 56.1 mL of 95-97 % H_2SO_4 in 1 liter of Mili-Q water. A Pt grid was used as a counter electrode (CE) and an Ag/AgCl (KCl sat.) electrode was used as a reference electrode (RE). All data were transformed to RHE by adding +0.20 V. A 10 mL two-compartment cell with a separation membrane between the two compartments was used. Both compartments were filled with 8 mL of 1 M H_2SO_4 solution and both compartments were equipped with a stirring bar. Prior to each measurement, both compartments were purged with N_2 for 15 min. For H_2-monitored bulk electrolysis an Unisense H2-NP clark electrode was used to measure hydrogen evolution in the gas phase and to calculate the Faradaic efficiency. The clark electrode was calibrated by adding different volumes of 99 % pure hydrogen at the end of the experiment. The CE was placed in one compartment and the other was provided with WE, RE and Clark electrode.

Linear Seep Voltammetry (LSV). The system was scanned from E_i = 0.6 V to E_f = -0.4 V at 10 mV/s scan rate unless otherwise stated.

Chronoamperometry. Controlled potential chronoamperometric experiments were performed at E_{app} = 0.25 V and 0.35 V for Ru- and RuPP-CF based systems, respectively.

Electrode surface area estimation. Considering that a full brush electrode weights 90 mg and has a maximum surface area of 40 cm^2, and that we build 1 mg electrodes with only $2/3^{rds}$ of the surface used in electrochemical experiments, this leads to a maximum electrode geometrical surface of 0.3 cm^2.

4B.6 References

---

1 J. Creus, R. Matheu, I. Peñafiel, D. Moonshiram, P. Blondeau, J. Benet-Buchholz, J. García-Antón, X. Sala, C. Godard, A. Llobet, *Angew. Chem. Int. Ed.* **2016**, *55*, 15382-15386

2 X. Han, X. Tong, G. Wu, N. Yang, X. Y. Guo, *Carbon* **2018**, *129*, 245-251.

3 D. A. Henckel, O. M. Lenz, K. M. Krishnan, B. M. Cossairt, *Nano Lett.* **2018**, *18*, 2329-2335.

4 a) T. Liu, M. Li, C. Jiao, M. Hassan, X. Bo, M. Zhou, H. L. Wang, *J. Mater. Chem. A* **2017**, *5*, 9377-9390; b) T. Zhanga, M. Y. Wua, D. Y. Yana, J. Maoa, H. Liua, W. B. Hua, X. W. Dua, T. Linga, S. Z. Qiao, *Nano Energy* **2018**, *43*, 103-109; c) S. S. Lu, X. Shang, L. M. Zhang, B. Dong, W. K. Gao, F. N. Dai, B. Liu, Y. M. Chai, C. G. Liu, *App. Surf. Sci.* **2018**, *445*, 445-453; d) X. Wang, W. Li, D. Xiong, D. Y. Petrovykh, L. Liu, *Adv. Funct. Mater* **2016**, *26*, 4067-4077.

5 a) J. X. Feng, S. Y. Tong, Y. X. Tong, G. R. Li, *J. Am. Chem. Soc.* **2018**, *140*, 5118-5126; b) K. Ao, D. Li, Y. Yao, P. Lv, Y. Cai, Q. Wei, *Electrochimica Acta* **2018**, *264*, 157-165; c) S. H. Yu, D. H. C. Chua, *ACS Appl. Mater. Interfaces* **2018**, *10*, 14777-14785.

6 O. González-del Moral, A. Call, F. Franco, A. Moya, J. A. Nieto-Rodríguez, M. Frias, J. L. G. Fierro, M. Costas, J. Lloret-Fillol, J. Alemán, R. Mas-Ballesté, *Chem. Eur. J.* **2018**, *24,* 3305-3313.

7 K. Philippot *et al.* in *Ruthenium in catalysis* **2014**, C. Bruneau and P.H. Dixneuf (Eds), Wiley VCH, Weinheim, **2014**, *Top. Organomet. Chem.* **2014**, *48*, 319

8 a) J. Mahmood, F. Li, S. Jung, M. S. Okyay, I. Ahmad, S. Kim, N. Park, H. Y. Jeong, J. Baek, *Nature Nanotech.* **2017**, *12*, 441-446; b) T. Bhowmik, M. K. Kundu, S. Barman, *ACS Appl. Mater. Interfaces* **2016**, *8*, 28678-28688; c) J. Cheng, H. Zhang, H. Ma, H. Zhong, Y. Zou, *Electrchim. Acta* **2010**, *55,* 1855-1861; d) X. Kong, K. Xu, C. Zhang, J. Dai, S. N. Oliaee, L. Li, X. Zeng, C. Wu, Z. Peng, *ACS Catal.* **2016**, *6*, 1487-1492; e) Y. Zheng, Y. Jiao, Y. Zhu, L. H. Li, Y. Han, Y. Chen, M. Jaroniec, S. Qiao, *J. Am. Chem. Soc.* **2016**, *138*, 16174-16181; f) Z. Chen, J. Lu, Y. Ai, Y. Ji, T. Adschiri, L. Wan, *ACS Appl. Mater. Interfaces* **2016**, *8*, 35132-35137.

9 a) C. C. K. McCrory, S. Jung, J. C. Peters, T. F. Jaramillo, *J. Am. Chem. Soc.* **2013**, *135*, 16977-16987; b) C. C. K. McCrory, S. Jung, I. M. Ferrer, S. M. Chatman, J. C. Peters, T. F. Jaramillo, *J. Am. Chem. Soc.* **2015**, *137*, 4347-4357.

5

General Conclusions

After describing the different subprojects performed in the frame of this PhD work centered on the development of novel nanocatalysts for the water splitting reaction, and taking into account the goals proposed in Chapter 2, this last part of the manuscript will resume the main conclusions that can be drawn from the obtained results in the synthesis, characterization, catalytic performance evaluation and comparison with the state-of-the-art data. Some perspectives will also be given.

5. Conclusions

In this PhD manuscript, the synthesis, characterization and electrocatalytic evaluation of Ru-based nanoparticles has been presented, with the focus fixed on the catalytic performance of each system influenced by the different structural properties. The use of the organometallic approach has permitted the obtaining of ligand-stabilized colloidal NPs and supported nanomaterials, which have been characterized by several techniques such as TEM, WAXS, XPS, XRD, TGA, ICP, EA among others, allowing a control on parameters such as surface environment, oxidation state or mean size. The nanomaterials have been tested in the water splitting process, mainly as hydrogen evolution catalysts (HECs).

In Chapter 3, the use of MeOH/THF, 4-phenylpyridine (**PP**) or 4’-(4-methylphenyl)-2,2’:6’,2”-terpyridine (**MPT**) has allowed to obtain NPs with different morphological properties which, when deposited onto a glassy carbon electrode, display distinct behavior as Hydrogen Evolution Catalysts (HECs). In the case of MeOH/THF-stabilized NPs, a porous nanomaterial of ca. 21 nm has been obtained, which is composed by very small NPs assembled in bigger groups. This porosity is responsible of achieving high active surface, reason why the nanomaterial show prominent activities in the proton reduction. On the other side, the use of pyridine-based ligands (**PP**/**MPT**) has allowed to obtain very small NPs (1-1.5 nm) with a high Ru-content (80-85%), which display activities as high as the state-of-the-art Pt/C. Those NPs suffer from surface oxidation when exposed to the air loosing catalytic activity, but their reduced counterpart can be simply recovered by an electroreduction process, as demonstrated by XPS, achieving very high current densities in the proton reduction reaction. In general terms, RuNPs stabilized by **PP**/**MPT** ligands displayed better performances on the electrocatalytic reduction of protons than MeOH/THF-stabilized system, supporting the positive influence of pyridine groups in Ru-based catalysis, either in molecular complexes or nanoparticles.

In a modification of the synthetic procedure, the incorporation of C-based supports (CNTs: Multi-Walled Carbon Nanotubes; CFs: Carbon microFibers) in the reaction mixture has allowed to obtain very small RuNPs dispersed on the material surface, as described in Chapter 4. The presence of a support is very promising when oxidizing the particles under thermal conditions: whereas colloidal NPs coalesce to form big agglomerates in solid state, onto the surface of the supports the NPs only slightly sinter, forming RuO_2 crystals on the nano-size range. High-surface CNTs modified with RuNPs appeared to be active species towards the H_2 evolution, as well as RuO_2@CNTs do. The systems also have an oxidation-state dependent HER-activity, being highly active after the formation of Ru^0-species on their surface. Additionally, RuO_2-based samples have shown to be active Water Oxidation Catalysts (WOCs), displaying activities similar to IrO_2-based electrodes, being the latter the state-of-the-art metal for this reaction. In the case of CF-supported RuNPs, thin homogenous films of nanoparticles have been observed by TEM on the surface of the fibers. Those hybrid systems are also active in the HER, but their performance is dependent on the nature of the support and the NPs' surface environment, being the best system the one based on the deposition of pre-synthesized **RuPP** NPs. The long-term stability of those systems is on top of the perspective work, expecting a hybrid material which is highly recyclable.

With all those results in hands and taking into account that the specific conclusions have been already given at the end of each chapter, some general observations will be hereafter detailed, considering the main results achieved in the whole PhD thesis:

- In chapter 3A, the synthesis of porous **Ru-MeOH/THF** by using a mixture of MeOH and THF as stabilizing agent has allowed to achieve a cathode with a very high surface area per Ru content (173.07 $m^2{\cdot}g^{-1}$), which showed high activities as HEC at a low Ru loading. The good performance obtained with this **Ru-MeOH/THF** nanocatalyst might be not only related to the porous character of this nanomaterial, but also to the mode of stabilization of the particles. Indeed, the alcohol is supposed to have an effect even on the catalytic properties but this has not been demonstrated yet. Nevertheless this hypothesis is supported by the prominent current densities displayed by the other Ru-alcohol system described in this work, the Ru-heptOH NPs described in Chapter 3B. It is thus believed that the reducing ability of alcohols present at the NP surface could assist their catalytic performance. This work has been published in Chemical Communications RSC-journal (*Chem. Commun.* **2017**, *53*, 11713-11716) and its catalytic performance is among the best systems in the literature.

- The deep characterization performed on ligand-stabilized NPs as described in Chapter 3B by using complementary techniques, allowed us to improve the understanding on the structure of the nano-sized systems. The results obtained evidenced that a fine study of a series of different NPs in terms of sizes, stabilizing agents, oxidation states, etc. is necessary to correlate those parameters with their catalytic performance, to be able afford real advancements. Such an investigation is extremely rare in the literature but it is strongly required in order to improve the rational development of active and rugged nano-sized catalysts. In this sense, the use of pyridine derivative ligands like **PP** and **MPT** to stabilize RuNPs showed up to be beneficial for the catalytic behavior in HER. Although with both **MPT** and **PP** ligands a passivation has been observed due to the formation of superficial RuO_2 species, a recovery of their initial surface state appeared possible through an electroreduction step after their deposition onto the electrode. The different activities observed with the two ligands might be induced by a different coordination mode, having both the possibility of σ-donation or π-stacking interactions which can vary depending on the structure/sterical hindrance of the ligands. **PP**-Stabilized RuNPs have been further studied in Chapter 3C and the fate of the nanocatalyst evaluated under the catalytic conditions. Preliminary DFT calculations allowed first to propose two **PP** coordination modes to the surface of the NPs being the final configuration proposed as a mixture of both, σ-coordination and π-interactions from the pyridyl-N and the aromatic groups, respectively. The results observed with **PP**-stabilized RuNPs as HEC are among the best reported so far, being in the range of Pt/C in acidic media and outstanding it under basic conditions. Thus, a manuscript is on preparation for submitting this work on a chemistry journal.

- In chapter 4, CNTs and CFs turned out to be efficient supports for the anchoring of RuNPs. The transformation of RuNPs into RuO_2 ones by thermal oxidation could be accomplished with both types of supports. Even if a slight sintering was associated in all the cases, the obtained RuO_2 particles have always been kept on the nanometric range. These results are very interesting as an analogous controlled oxidation process could not be achieved in the case of **MPT**/**PP**-stabilized colloidal NPs. Indeed, oxidation experiments in mild reaction conditions did not allow getting a complete oxidation of the NPs probably induced by the strong protection of the NPs due to the ligand coordination at their surface. Moreover, thermal oxidation treatments led to uncontrolled massive sintering of the particles.

- CNT-supported RuNPs, have displayed good results on the HER. The best results were achieved with electroreduced CNT-supported RuO_2 nanocrystals. A core/shell-like structure resulting from the formation of Ru^0 species at the surface of the RuO_2 cores seem to be responsible for this higher performance, as well as an improvement on the electrode-catalyst electron transfer due to a change on the structure. The CNT-supported RuO_2 nanocrystals also showed low overpotentials on catalyzing the OER. The activity is not only related on the crystallinity but also on the oxidation state. It has been proved that Ru^0 species are very active on the water oxidation, but rapidly decreasing the electrocatalytic intensities due to the formation and leaching of RuO_4. However, crystalline-RuO_2 NPs proved to be stable at a short-term catalysis, displaying similar results than IrO_2@CNT.

- The use of CFs as support has evidenced the strong influence of the support and of the surface environment of the particles onto their catalytic performance. On one side, we have shown that *in-situ* formed RuNPs in the presence of the CFs progressively decreased their electrocatalytic intensities reaching very small currents in a few hours. In contrast, the deposition of *ex-situ* prepared **PP**-stabilized RuNPs onto CFs led to catalysts displaying also low overpotentials but with higher stability. Preliminary studies suggest a mechanical leaching of the NPs in the *in-situ* systems, in contraposition to the evolution to soluble species under catalytic conditions This mechanical leaching could be improved by using polymers such as nafion or PMMA.

- Finally, the modification of CFs by an acidic treatment in order to have carboxylic acid functions at their surface appeared to be less efficient than expected for the stabilization of CF-supported RuNPs, maybe due to a less structured pyridine-based material surface.

Although in the literature there is an increasing number of publications concerning the use of nano-sized materials as catalysts for WS-reactions, the lack of homogeneity in the reported results as well as the scarcity on the understanding of the catalytic systems in a structural and mechanistic point of view, makes it extremely difficult to obtain any trend between structural properties and catalytic behavior. For this reason, full studies of the catalysts' properties and evolution before, during and after catalytic experiments, more specifically in the case of HECs are required. Those studies should permit an understanding of the processes taking place on the materials, being able to rationally design new species with better performances on the catalytic reactions, based on the gained knowledge regarding the correlation between catalyst properties / catalytic activity. In this sense, the results here obtained are not only important for the specific achievements on electrocatalysis, but they are opening new doors for the development and understanding of the chemistry surrounding the two reactions involved in water splitting with RuNPs-based catalysts.

6

Annexes

The Annex part is splitted in two sections. On the first one, Tables A1-A4 contain the state-of-the-art electrocatalysts based on supported NPs made of Ru and other transition metals, for the hydrogen evolution reaction. While in Tables A1-A2 (acid and basic media, respectively) the activity is compared through the kinetic TOF parameter (in the cases where it was calculated), Tables A3-A4 (acid and basic media, respectively) benchmark the catalytic performance of the species by T. F. Jaramillo's methodology, namely by the roughness factor. Data from new nanocatalysts reported in this manuscript are also provided in the tables.

Finally, the publication concerning the work described in Chapter 3A (Chem. Commun. ***2017****, 53, 11713) and another publication that has been developed during this PhD period (Angew. Chem. Int. Ed.* ***2016****, 55, 15382), have been added at the end of this Annex.*

Annex 1: Tables for Hydrogen Evolution Catalysts' Electrochemical Performance Benchmarking

Table A1. Comparison of different nanomaterials including Ru-based ones as HER electrocatalysts in acidic electrolytes. Parameters: mean diameter (Ø), onset overpotential (η_0, mV), overpotential at $j = -10$ mA·cm^{-2} (η_{10}, mV), Tafel slope (*b*, mV·dec^{-1}), exchange current density (j_0, mA·cm^{-2}), and turnover frequency (TOF, s^{-1}).

Entry (*Ref.*)	**Catalyst**	**Ø (nm)**	**η_0 (mV)**	**η_{10} (mV)**	***b* (mV·dec^{-1})**	**j_0 (mA·cm^{-2})**	**TOF (s^{-1})**
A1	RuO$_2$-C (Vulcan) [a]	5-8	≈ 0	≈ 15	26	-	-
A2	Ru/SiNWs [a]	42.9	≈ 140	200	81	0.48	-
A3	GCE-S-GNs-1000-CB-Ru (sulfur-dopped graphene + carbon black) [a]	35	65	80	61	0.541	-
A4	RuNPs-GC [a]	100	50	90	≈ 130	-	-
A5	Ru-2D-nanosheets [a]	50-80	0	20 (10 mA·mg^{-1})	46	-	-
A6	RuNPs-GLC (graphene layered carbon) [a]	2-5	3	35	46	-	-
A7	RuNPs-CNx [a]	1.5	40	156	70	-	-
A7	1D-RuO$_2$-CNwires [a]	length ≈ 100 Ø ≈ 10	14	93	40	0.22	-
A8	Ru/*g*-C$_3$N$_4$/C (graphitic carbon-nitride over C) [a]	2	≈ 15-20	≈ 70	-	-	≈ 4.85 (100 mV)
A9	Ru-C$_2$N [a]	1.6	9.5	22	30	1.9	0.67 (25 mV) 1.95 (50 mV)
A10	RuP$_x$@NPC [a]	4	25	50	46	-	-
A11	Ru/CeO$_2$	3.89 ± 1.24	33	47	41	0.61	0.8 (27 mV)
A12	Ru$_2$P/RGO-20 [a]	<7	≈ 0	22	29	2.2	-

A13	CoPS nanoplate ^{a}	5		48	57	0.98	-
A14	A-Ni-C ^{a}	10		34	41	1.20	-
A15	CoS|P/CNT ^{a}	10-20		64	55	1.14	-
A16	$WO_{2.9}$ ^{a}	100		70	50	0.40	8.04 (100 mV) 24.76 (200 mV)
A17	$MoS_2/CoSe_2$ ^{a}	-	11	68	36	0.07	-
A18	Pt-MoS_2 ^{a}	1-3		53	40	-	-
A19	Ni_5P_4 ^{b}	5-20		23	33	-	3.5 (100 mV) 9.8 (200 mV)
A19	Ni_2P-(b) ^{b}	-		42	38	-	0.015 (100 mV) 0.064(200 mV)
A20	Ni_2P-(a) ^{a}	17		≈ 100	46	2.70	0.015 (100 mV) 0.5(200 mV)
A21	Ni-Mo ^{a}	50-300		< 100	-	-	-
A22	Pt-CNs/RGO ^{a}	5.8 x 3.0	18	≈ 75	29	0.18	-
A23	$Ni_{43}Au_{57}$ ^{a}	10 ± 0.8	7	≈ 50	43	-	-
Ch. 3C	**Ru-black** ^{b}	**-**	**70**	**150**	**65**	**0.14**	**0.12 (25 mV)** **0.31 (50 mV)** **1.81(100 mV)**
Ch. 3C	Pt/C ^{b}	-	0	27	32	1.40	1.65 (25 mV) 5.60 (50 mV) 23.36 (100 mV)
Ch. 3A	**Ru-GC** ^{a} **(Ru-MeOH/THF)**	**20**	**0**	**83**	**46**	**0.36**	**0.07 (25 mV)** **0.10 (50 mV)** **0.87 (100 mV)**
Ch. 3C	**Ru2-GC** ^{b}	**1.5 ± 0.3**	**0**	**35**	**106**	**4.79**	**-**
Ch. 3C	**Ru1-GC** ^{b}	**1.5 ± 0.3**	**0**	**20**	**29**	**2.04**	**0.55 (25 mV)** **3.06 (50 mV)** **17.38 (100 mV)**

Electrolyte: (^{a}) 0.5 M H_2SO_4 and (^{b}) 1 M H_2SO_4.

Table A2. Comparison of different metal-based materials as HER electrocatalysts in basic electrolytes from literature data. Parameters: mean diameter (Ø), onset overpotential (η_0, mV), overpotential at *j* = -10 mA·cm^{-2} (η_{10}, mV), Tafel slope (*b*, mV·dec^{-1}), exchange current density (j_0, mA·cm^{-2}), and turnover frequency (TOF, s^{-1}).

Entry (*Ref.*)	**Catalyst**	**Ø (nm)**	**η_0 (mV)**	**η_{10} (mV)**	**b (mV·dec^{-1})**	**j_0 (mA·cm^{-2})**	**TOF (s^{-1})**
A7	1D-RuO$_2$-CNwires ^{ii}	length ≈ 100 Ø ≈ 10	16	95	70	0.28	-
A9	Ru-C$_2$N ^{iii}	1.6	-	17	38	-	0.76 (25 mV) 1.66 (50 mV)
A24-25	hydrous-RuO$_2$ ^{iii}	< 5	≈ 25	60	-	-	-
A26	cristalline-RuO$_2$ ^{iii}	-	≈ 25	74	-	-	-
A8	Ru/*g*-C$_3$N$_4$/C (graphitic carbon-nitride over C) ^{i}	2	≈ 15-20	79	-	-	4.2 (100 mV)
A26	Ru^0/NG-750 ^{iii}	5.8 ± 1.5	0	8	30	-	0.35 (100 mV)
A10	RuP$_x$@NPC ^{iii}	4	≈ 30	74	70	-	-
A12	Ru2P/RGO-20 ^{iii}	<7	≈ 0	13	56	-	-
A27	Ru@NC	1.6	15	26	36	-	0.83 (25 mV) 3.02 (50 mV) 10.8 (100 mV)
A28	np-CuTi ^{i}	-	≈ 0	47	110	-	-
A29	NiO-Ni-CNT ^{iii}	≈ 10	≈ 25	86	82	-	-
Ch. 3C	**Ru-black** ^{iii}	**-**	**50**	**125**	**80**	**0.65**	**0.42 (25 mV)** **1.04 (50 mV)** **3.70(100 mV)**
Ch. 3C	**Pt/C** ^{iii}		**5**	**35**	**56**	**2.40**	**1.50 (25 mV)** **4.20 (50 mV)** **11.80 (100 mV)**
Ch. 3C	**Ru2-GC** ^{iii}	**1.5 ± 0.3**	**0**	**25**	**65**	**0.19**	**-**

Electrolyte: (^{i}) 0.1 M KOH, (^{ii}) 0.5 M KOH and (^{iii}) 1 M KOH/NaOH.

Table A3. Comparison of different HECs by the Jaramillo's methodology in 1 M H_2SO_4. Parameters: roughness factor (RF), overpotential at j = -10 mA·cm^{-2} (η_{10}, mV) at t=0 and t=2h, current density at η=100 mV ($j_{(\eta=100)}$, mA·cm^{-2}) and specific current density at η=100 mV ($j_{S(\eta=100)}$, mA·cm^{-2}).

Entry (*Ref.*)	**Catalyst**	**RF**	**$\eta_{10\ (t=0)}$ (mV)**	**$\eta_{10\ (t=2h)}$ (mV)**	**$j_{(\eta=100)}$ (mA·cm^{-2})**	**$j_{S(\eta=100)}$ (mA·cm^{-2})**
A30	CoMo	1100 ± 600	100	100	4.6	0.004
A31	NiMo	1200 ± 500	45	39	91	0.074
A32	NiW	1200 ± 600	60	110	17	0.014
A33	NiMoCo	1200 ± 500	50	50	53	0.043
A34	NiMoFe	700 ± 200	90	100	10	0.014
A35	Pt-(b)	90 ± 20	50	60	220	2.500
Ch. 4B	**RuPP@pCF**	-	-	-	-	**0.028**
Ch. 3A	**Ru-GC (Ru-MeOH/THF)**	**645 ± 87**	**99**	**103**	**43.3**	**0.067**
Ch. 3C	**Ru1-GC**	**895 ± 95**	**20**	**20**	**496**	**0.550**

Table A4. Comparion of different HEC by the Jaramillo's methodology in 1M NaOH. Parameters: roughness factor (RF), overpotential at j = -10 mA·cm^{-2} (η_{10}, mV) at t=0 and t=2h, current density at η=100 mV ($j_{(\eta=100)}$, mA·cm^{-2}) and specific current density at η=100 mV ($j_{S(\eta=100)}$, mA·cm^{-2}).

Entry (*Ref.*)	**Catalyst**	**RF**	**$\eta_{10\ (t=0)}$ (mV)**	**$\eta_{10\ (t=2h)}$ (mV)**	**$j_{(\eta=100)}$ (mA·cm^{-2})**	**$j_{S(\eta=100)}$ (mA·cm^{-2})**
A31	CoMo	700 ± 400	100	100	2.3	0.002
A30-31	NiMo	800 ± 400	40	30	35	0.047
A36	NiFe	4000 ± 1000	90	120	2.6	0.002
A33	NiMoCo	900 ± 400	70	90	19	0.02
A34	NiMoFe	900 ± 400	130	130	3.2	0.003
A35	Pt-(b)	130 ± 50	30	60	70	0.540
Ch. 3C	**Ru2-GC**	320 ± 140	25	40	61	0.191

References

A1 J. Cheng, H. Zhang, H. Ma, H. Zhong, Y. Zou, *Electrchim. Acta* **2010**, *55,* 1855-1861.

A2 L. Zhu, Q. Cai, F. Liao, M. Shengb, B. Wub, M. Shao, *Electrochem. Commun.* **2015**, *52,* 29-33.

A3 R. K. Shervedani , A. Amini, *Carbon* **2015**, *93*, 762-773.

A4 K. Magdić, K. Kvastek, V. Horvat-Radošević, *Electrochim. Acta* **2015**, *167*, 455-469.

A5 X. Kong, K. Xu, C. Zhang, J. Dai, S. N. Oliaee, L. Li, X. Zeng, C. Wu, Z. Peng, *ACS Catal.* **2016**, *6*, 1487-1492.

A6 Z. Chen, J. Lu, Y. Ai, Y. Ji, T. Adschiri, L. Wan, *ACS Appl. Mater. Interfaces* **2016**, *8*, 35132-35137.

A7 T. Bhowmik, M. K. Kundu, S. Barman, *ACS Appl. Mater. Interfaces* **2016**, *8*, 28678-28688.

A8 Y. Zheng, Y. Jiao, Y. Zhu, L. H. Li, Y. Han, Y. Chen, M. Jaroniec, S. Qiao, *J. Am. Chem. Soc.* **2016**, *138*, 16174-16181.

A9 J. Mahmood, F. Li, S. Jung, M. S. Okyay, I. Ahmad, S. Kim, N. Park, H. Y. Jeong, J. Baek, *Nature Nanotech.* **2017**, *12*, 441-446.

A10 J. Q. Chi, W. K. Gao, J. H. Lin, B. Dong, K. L. Yan, J. F. Qin, B. Liu, Y. M. Chai, C. G. Liu, *ChemSusChem* **2018**, *11*, 743-752.

A11 E. Demir, S. Akbayrak, A. M. Önal, S. Özkar, *ACS Appl. Mater. Interfaces* **2018**, *10*, 6299-6308.

A12 T. Liu, S. Wang, Q. Zhang, L. Chen, W. Hu, C. M. Li, *Chem. Commun.* **2018**, DOI: 10.1039/C8CC01166D.

A13 M. Cabán-Acevedo, M. L. Stone, J. R. Schmidt, J. G. Thomas, Q. Ding, H. C. Chang, M. L. Tsai, J. H. He, S. Jin, *Nature Mater.* **2015**, *14*, 1245-1251.

A14 L. Fan, P. F. Liu, X. Yan, L. Gu, Z. Z. Yang, H. G. Yang, S. Qiu, X. Yao, *Nature Comm.* **2016**, *7*, 10667-10673.

A15 W. Liu, E. Hu, H. Jiang, Y. Xiang, Z. Weng, M. Li, Q. Fan, X. Yu, E. I. Altman, H. Wang, *Nature Comm.* **2016**, *7*, 10771-10779.

A16 Y. H. Li, P. F. Liu, L. F. Pan, H. F. Wang, Z. Z. Yang, L. R. Zheng, P. Hu, H. J. Zhao, L. Gu, H. G. Yang, *Nature Comm.* **2015**, *6*, 8064-8070.

A17 M. R. Gao, J. X. Liang, Y.-R. Zheng, Y. F. Xu, J. Jiang, Q. Gao, J. Li, S. H. Yu, *Nature Comm.* **2015**, *6*, 5982-5988.

A18 X. Huang, Z. Zeng, S. Bao, M. Wang, X. Qi, Z. Fan, H. Zhang, *Nature Comm.* **2013**, *4*, 1444-1451.

A19 A. B. Laursen, K. R. Patraju, M. J. Whitaker, M. Retuerto, T. Sarkar, N. Yao, K. V. Ramanujachary, M. Greenblatt, G. C. Dismukes, *Energy Environ. Sci.* **2015**, *8*, 1027-1034.

A20 E. J. Popczun, J. R. McKone, C. G. Read, A. J. Biacchi, A. M. Wiltrout, N. S. Lewis, R. E. Schaak, *J. Am. Chem. Soc.* **2013**, *135*, 9267-9270.

A21 J. R. McKone, B. F. Sadtler, C. A. Werlang, N. S. Lewis, H. B. Gray, *ACS Catal.* **2013**, *3*, 166-169.

A22 G. R. Xu, J. J. Hui, T. Huang, Y. Chen, J. M. Lee, *J. Power Sources* **2015**, *285*, 393-399.

A23 H. Lv, Z. Xi, Z. Chen, S. Guo, Y. Yu, W. Zhu, Q. Li, X. Zhang, M. Pan, G. Lu, S. Mu, S. Sun, *J. Am. Chem. Soc.* **2015**, *137*, 5859-5862.

A24 N. Kang, T. Yu, G. H. Lim, T. Koh, B. Lim, *Chem. Phys. Lett.* **2014**, *592*, 192-195.

A25 J. Lee, S. A. S. Shah, P. J. Yoo, B. Lim, *Chem. Phys. Lett.* **2017**, *673*, 89-92.

A26 R. Ye,Y. Liu, Z. Peng, T. Wang, A. S. Jalilov, B. I. Yakobson, S. H. Wei, J. M. Tour *ACS Appl. Mater. Interfaces* **2017**, *9*, 3785-3791.

A27 Z. L. Wang, K. Sun, J. Henzie, X. Hao, C. Li, T. Takei, Y. Yamauchi, *Angew. Chem. Int. Ed.* **2018**, *Angew. Chem. Int. Ed.* **2018**, *57*, 5848-5852.

A28 Q. Lu, G. S. Hutchings , W. Yu, Y. Zhou, R. V. Forest, R. Tao, J. Rosen , B. T. Yonemoto , Z. Cao, H. Zheng, J. Q. Xiao, F. Jiao, J. G. Chen, *Nature Comm.* **2015**, *6*, 6567-6574.

A29 M. Gong, W. Zhou, M. C. Tsai, J. Zhou, M. Guan , M. C. Lin, B. Zhang, Y. Hu, D. Y. Wang, J. Yang, S. J. Pennycook, B. J. Hwang, H. Dai, *Nature Comm.* **2014**, *5*, 4695-4700.

A30 C. Fan, D. L. Piron, A. Sleb, P. Paradis, *J. Electrochem. Soc.* **1994**, *141*, 382-387.

A31 E. Navarro-Flores, Z. Chong, S. Omanovic, *J. Mol. Catal. A: Chem.* **2005**, *226*, 179-197.

A32 I. A. Raj, K. I. Vasu, *J. Appl. Electrochem.* **1990**, *20*, 32-38.

A33 C. Fan, D. L. Piron, P. Paradis, *Electrochim. Acta* **1994**, *39*, 2715-2722.

A34 I. A. Raj, K. I. Vasu, *J. Appl. Electrochem.* **1992**, *22*, 471-477.

A35 D. J. Walton, L. D. Burke, M. M. Murphy, *Electrochim. Acta*, **1996**, *41*, 2747-2751.

A36 R. Solmaz, G. Kardas, *Electrochim. Acta* **2009**, *54*, 3726-3734.

ChemComm

COMMUNICATION

View Article Online
View Journal | View Issue

Published on 02 October 2017. Downloaded by Universitat Autonoma de Barcelona on 28/05/2018 12:20:58.

Check for updates

Cite this: *Chem. Commun.*, 2017, 53, 11713

Received 19th July 2017,
Accepted 29th September 2017

DOI: 10.1039/c7cc05615j

rsc.li/chemcomm

A porous Ru nanomaterial as an efficient electrocatalyst for the hydrogen evolution reaction under acidic and neutral conditions†

S. Drouet, *[ab] J. Creus,[abc] V. Collière,[ab] C. Amiens,[ab] J. García-Antón,[c] X. Sala[c] and K. Philippot *[ab]

A porous Ru nanomaterial exhibits high electrocatalytic performance and excellent durability for the hydrogen evolution reaction (HER) under both acidic and neutral conditions. It displays a low overpotential of 83 mV at a current density of 10 mA cm^{-2} and an excellent durability up to 12 h in 0.5 M H_2SO_4.

In view of depleting resources and increasing levels of greenhouse gases, the replacement of fossil fuels by a clean and renewable energy source is one of the most urgent and challenging issues our society is facing today.[1,2] Hydrogen is found to be an excellent candidate because it is a great energy carrier, and can be easily converted into electrical power without generating environmentally harmful by-products. Hydrogen can be produced from water through the water-splitting process which involves two successive reactions, namely oxygen evolution and hydrogen evolution reactions (OER and HER, respectively).[3] These two reactions need to be catalysed to make the whole process efficient, meaning that it can be operated at low overpotential and under fast kinetic conditions. The search for highly effective and stable electrocatalysts is thus extremely desirable for both reactions. With respect to the HER, among the various catalysts tested, Pt-based catalysts are considered to be the best systems for this reaction.[4,5] However the prohibitive price and scarcity of platinum make it unsuitable for large scale commercial applications. Therefore, the development of efficient and cheaper catalysts that can operate at low overpotential with high stability is highly required. Ruthenium has been one of the most studied transition metals used in the development of catalysts for the OER showing high electrocatalytic activity, but the performance of this metal for the HER has not been much investigated.[6–9] However, in the past few years, several works described Ru-based nanomaterials as efficient hydrogen evolution catalysts either under acidic or alkaline conditions.[10–13] For instance, Kong *et al.* reported the preparation and electrocatalytic performance in the HER of two-dimensional Ru nanostructures.[11] The observed improved kinetics of this system when compared to Ru black powder is attributed to the greater specific area of the former due to its 2D structure. This hypothesis is supported by the fact that materials possessing a large surface area should display more active sites. The use of such materials thus seems to be a promising strategy for enhancing the catalytic activity. In this regard, very recently, porous assemblies of Pd nanoparticles have been reported to be efficient catalysts for both the HER and oxygen reduction reaction (ORR).[14] This Pd nanomaterial exhibited high electrocatalytic activity for the HER with a low overpotential of *ca.* 80 mV, at a current density of 100 mA cm^{-2}, a small Tafel slope of 30 mV dec^{-1} and a long-term stability for at least 1000 consecutive cyclic voltammograms. These results provide evidence that using a material with a high surface area can be highly advantageous in electrocatalysis. However, notwithstanding its high catalytic performance, palladium is not a cheaper alternative to platinum catalysts since it is in the same order of price.

On the basis of the above results with Pd and of the possibilities offered by the organometallic approach to achieve nanostructured materials having a clean surface and high surface area as especially demonstrated for Ru,[15,16] we decided to evaluate the catalytic performance in the HER of Ru nanomaterials derived from an organometallic precursor. In the present work, we focused on a Ru nanomaterial which displays a porous morphology combined with a clean and reactive metal surface as shown previously in gas-phase hydrogenation catalysis.[17] Moreover, its synthesis is very simple and can be achieved under mild conditions.[18] As will be seen later, this Ru nanomaterial proved to be a very effective HER catalyst, exhibiting high electrocatalytic performance and excellent durability under both acidic and neutral conditions.

The Ru nanomaterial object of this study, and hereafter named Ru/MeOH/THF, was easily prepared by decomposition of the [Ru(cod)(cot)] (cod = 1,5-cyclooctadiene; cot = 1,3,5-cyclooctatriene) organometallic precursor under a H_2 atmosphere

---

[a] *Laboratoire de Chimie de Coordination du CNRS, 205 route de Narbonne, F-31077, Toulouse Cedex 04, France*
[b] *Université de Toulouse, UPS, INPT, LCC, F-31077 Toulouse Cedex 04, France. E-mail: samuel.drouet@lcc-toulouse.fr, karine.philippot@lcc-toulouse.fr*
[c] *Departament de Química, Facultat de Ciències, Universitat Autònoma de Barcelona, 08193 Bellaterra, Catalonia, Spain*

† Electronic supplementary information (ESI) available. See DOI: 10.1039/c7cc05615j

Published on 02 October 2017. Downloaded by Universitat Autonoma de Barcelona on 28/05/2018 12:20:58.

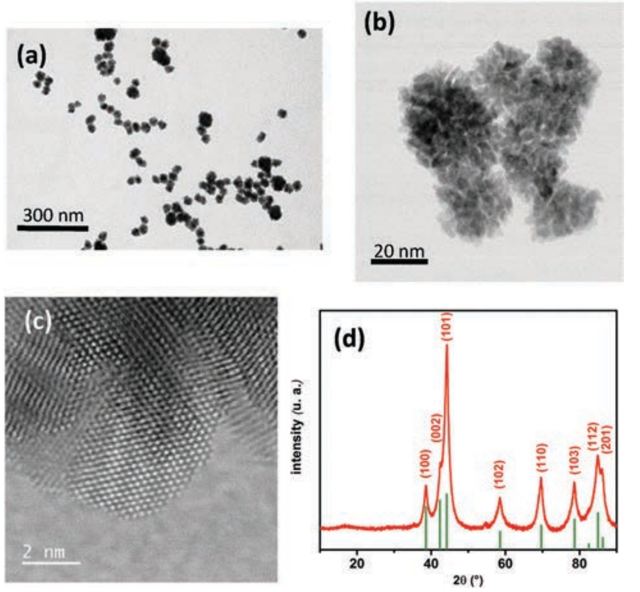

Fig. 1 (a and b) TEM images and (c) HR-TEM image of the Ru/MeOH/THF nanomaterial. (d) The theoretical pattern for hexagonal close packed (hcp) ruthenium (green) and the XRD pattern of the Ru/MeOH/THF nanomaterial (red).

(3 bar) in a MeOH/THF (5/95 in volume) solvent mixture in the absence of any other stabilizers, as previously reported.[18] In this way, a dark brown colloidal solution was obtained. TEM/HR-TEM (transmission electron microscopy at low and high resolution) analysis of the crude colloidal solution revealed the presence of nanoparticles of *ca.* 21.4 nm mean size (Fig. 1a). As also visible in the images, these nanoparticles display a sponge-like morphology and well-crystallized character (see Fig. 1b). The Fast Fourier Transformation (FFT) of the HR-TEM images (Fig. S2, ESI†) indicated the presence of the interplanar distances of 0.234, 0.203 and 0.158 nm corresponding to the crystalline (100), (101) and (102) planes of the hexagonal close-packed (hcp) structure of bulk Ru, respectively. The porous and polycrystalline aspect of the particles is attributed to an aggregation phenomenon of smaller individual particles during the synthesis process due to the composition of the reaction medium, particularly the absence of a strong stabilizer.

Nevertheless, the obtained colloidal solution is stable for a long period of time and the evaporation of the solvents under vacuum allowed the Ru nanomaterial to be obtained in the form of a black powder. Powder-XRD analysis (Fig. 1d) confirmed that the Ru particles adopt the hcp crystalline structure. X-ray photoelectron spectroscopy (XPS) of a sample deposited on a glassy carbon rod permitted the identification of the surface chemical composition and valence states of the Ru atoms (Fig. S3, ESI†). The results revealed the presence of both Ru(0) and RuO_2 (Fig. S3, ESI†). Ru(0) is evidenced by both peaks at 461.5 and 483.9 eV, corresponding to Ru $3p_{3/2}$ and $3p_{1/2}$ of Ru(0) while the shoulder observed at 279.9 eV close to the peak of Ru(0) 3d is attributed to RuO_2.[19] The presence of RuO_2 can be explained by the formation of an oxide passivation layer due to air exposure of the nanomaterial during XPS analysis. The formation of such a thin superficial oxide layer was previously observed.[18] Thus, this facile synthesis method allowed the acquisition of a Ru nanomaterial composed of *ca.* 21.4 nm porous nanoparticles which display a surface free of strongly coordinated stabilizers and a high surface area, which are two very attractive characteristics for application in catalysis. The catalytically active surface area (ECSA) of the Ru/MeOH/THF sample was estimated by an electrochemical method based on cyclic voltammetry measurements (Fig. S4, ESI†).[20] This method gives direct access to the double layer capacitance, which further permits the determination of the ECSA value by dividing the capacitance value by a general capacitance of 0.015 mF cm^{-2}, for a catalyst-free carbon electrode under the same conditions. For better accuracy, the experiment was repeated three times. A double capacitance value of 0.65 mF was found to lead to an ECSA value of 173.07 $m^2\ g^{-1}$. Compared to the value measured under the same conditions for Ru powder used as a reference in this work, which is 72.60 $m^2\ g^{-1}$, this result provides evidence that the Ru/MeOH/THF nanomaterial presents a very high active surface area. It is also important to note that 173.07 $m^2\ g^{-1}$ is a value higher than that reported by Kong *et al.* for 2D Ru nanostructures. The copper underpotential deposition method has been applied to determine the number of active sites and to calculate the turnover frequency (TOF) (ESI,† Fig. S5).[21] A TOF value of 0.87 s^{-1} at 100 mV of overpotential has been obtained.

The electrocatalytic activity of the Ru nanomaterial described above for the HER was first studied by linear sweep voltammetry (LSV) in 0.5 M H_2SO_4 solution. A relevant figure of merit for benchmarking the catalytic activity of heterogeneous catalysts is the overpotential value needed to achieve 10 mA cm_{geo}^{-2} (geometric area) current density, η (10 mA cm_{geo}^{-2}), which corresponds to the approximate current density expected for a 10% efficient solar-to-fuel conversion photoelectrochemical cell under 1 Sun illumination.[3,22] As shown in Fig. 2a, the Ru/MeOH/THF nanomaterial displays an efficient catalytic activity with a low overpotential at 10 mA cm^{-2} of 83 mV which is a lower value than that measured for commercial Ru powder (94 mV), but higher than the overpotential observed for the state of the art Pt/C (58 mV) catalyst. The electrocatalytic activity and stability of Ru/MeOH/THF were further compared with other electrocatalysts following the benchmark method published by Jaramillo *et al.*[5,23–27] The corresponding values of η (10 m cm_{geo}^{-2}) at time = 0 and time = 2 h are reported in Table S1 (ESI†) and plotted in Fig. S6 (ESI†). Tafel plot analysis allows evaluation of the rate determining step and therefore elucidation of the HER mechanism. It is known that the HER process may occur following two different mechanisms corresponding to a combination of two elementary steps, the Volmer–Tafel and the Volmer–Heyrovsky mechanism, respectively. In our study, a Tafel slope of 46 mV dec^{-1} has been determined from the low scan rate polarization curve performed with Ru/MeOH/THF (Fig. 2d). This value suggests that the HER follows the Volmer–Heyrovsky mechanism where the Heyrovsky step is the rate determining step of the overall reaction.[28] The Tafel slope value is also an intrinsic parameter in the evaluation of the catalytic performance of electrocatalysts. The Tafel slope of 46 mV dec^{-1},

This journal is © The Royal Society of Chemistry 2017

Published on 02 October 2017. Downloaded by Universitat Autonoma de Barcelona on 28/05/2018 12:20:58.

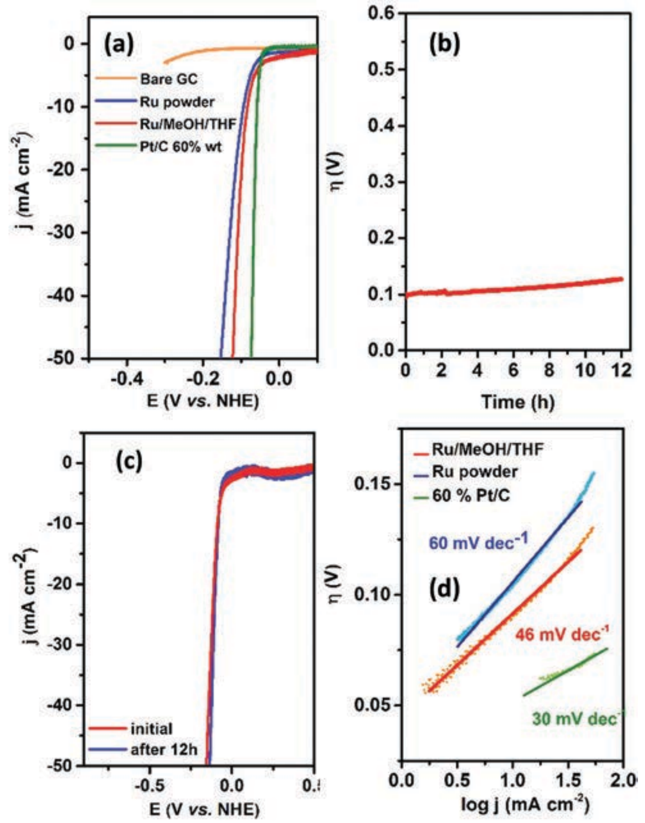

Fig. 2 (a) LSV curves of the Ru/MeOH/THF nanomaterial (red), Ru powder (blue) and Pt/C (green) in 0.5 M H_2SO_4 solution at 10 mV s^{-1}. The LSV curve of a bare GC electrode (orange). (b) Galvanostatic experiment of the Ru/MeOH/THF nanomaterial at a current density of 10 mA cm^{-2} in 0.5 M H_2SO_4, without ohmic drop compensation (c) LSV curves of the initial Ru/MeOH/THF nanomaterial (red) and after 12 h of galvanostatic experiment (blue) in 0.5 M H_2SO_4 solution at 10 mV s^{-1}. (d) Tafel plots of the Ru/MeOH/THF nanomaterial (red), Ru powder (blue) and Pt/C (green) in 0.5 M H_2SO_4 solution.

obtained for our Ru/MeOH/THF electrocatalyst, is a much lower value than that measured for commercial Ru powder, namely 60 mV (Table S2, ESI†). This result indicates that our Ru nanomaterial presents superior kinetic performance. The long-term durability of our Ru/MeOH/THF catalyst was studied by performing a galvanostatic experiment for over 12 h (Fig. 2b). At a current density of 10 mA cm^{-2}, a stable overpotential was observed over the time of the experiment without important variation (*i.e.* 30 mV). This behaviour is indicative of a good stability of the Ru/MeOH/THF nanomaterial. The small overpotential increase is attributed to the formation of copious H_2 bubbles that block and inhibit the catalyst surface. As shown in Fig. 2c the polarization curves/LSVs recorded before and after the galvanostatic experiment perfectly overlay, which provides evidence for the long-term stability of the Ru/MeOH/THF catalyst. To determine the nature of the catalytically active species, the XPS study was carried out after performing a controlled potential electrolysis at −0.05 V *vs.* NHE for 15 min. The XPS data presented in Fig. S3 (ESI†), clearly reveal only one peak in the 3d core-level region at 279.8 eV, suggesting Ru(0) to be the unique active species for the HER.

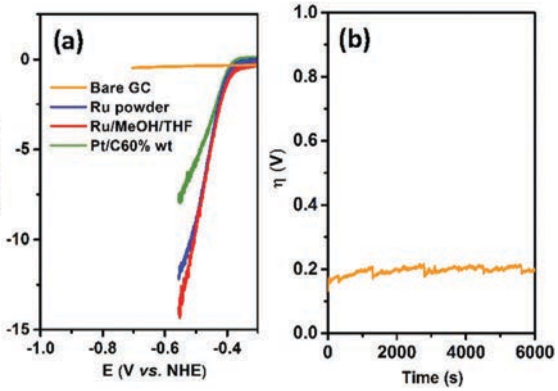

Fig. 3 (a) LSV curves of the Ru/MeOH/THF nanomaterial (red), Ru powder (blue) and Pt/C (green) in 0.1 M phosphate buffer solution at 1 mV s^{-1}. LSV curve of a bare GC electrode (orange) in 0.1 M phosphate buffer solution at 1 mV s^{-1}. (b) Galvanostatic experiment of the Ru/MeOH/THF nanomaterial at a current density of 10 mA cm^{-2} in 0.1 M phosphate buffer at pH 7, without ohmic-drop compensation.

In the perspective study on the Ru/MeOH/THF catalyst in a photocatalytic setup in combination with a molecular photosensitizer, such as porphyrins or polypyridine ruthenium complexes, which are used under neutral conditions,[29] electrocatalysis measurements were also performed at pH 7 (0.1 M phosphate buffer solution). As shown in Fig. 3a, it is worth noting that the Ru/MeOH/THF catalyst also exhibits high electrocatalytic activity under these neutral conditions with an overpotential η (10 mA cm$_{\text{geo}}^{-2}$) of 83 mV. A galvanostatic experiment performed at j = 10 mA cm^{-2} for 2 h demonstrated a stable catalytic activity (Fig. 3b). The stability was also verified by performing a LSV after 2 h of galvanostatic experiment. Fig. S7 (ESI†) shows that the final polarization curve exhibits similar catalytic current to the initial one. A Tafel slope of 80 mV dec^{-1} (Fig. S8, ESI†) was determined in this case, which is higher than the corresponding value obtained in acid solution, thus indicating slower kinetics for the HER under neutral than under acidic conditions. In order to evaluate the Faradaic yield of the Ru/MeOH/THF nanomaterial for the hydrogen production, a controlled potential electrolysis (CPE) was performed at a potential of −0.05 V *vs.* NHE (η = 50 mV) in 0.5 M H_2SO_4. Both, the stable current measured over the time of the experiment and the reproducibility of the polarization curves recorded before and after the catalytic process provide evidence for the high stability of the catalytic activity of the Ru nanomaterial (Fig. S9 and S10, ESI†). The latter control experiments also outline the high stability of the nanomaterial deposited at the electrode surface. The amount of hydrogen produced over the time of the CPE was quantified by means of a Clark electrode, giving a nearly quantitative faradaic yield of 97%.

In summary, we have reported the electrocatalytic performance of a porous Ru nanomaterial made of *ca.* 21.4 nm individual particles in the HER, in both acidic and neutral conditions, and in comparison with commercial Ru powder and Pt/C. This efficient electrocatalyst was easily prepared by an organometallic approach using only a mixture of methanol and THF as a stabilizer, which causes it to have a clean metal surface. Among the different

Published on 02 October 2017. Downloaded by Universitat Autonoma de Barcelona on 28/05/2018 12:20:58.

characteristics determined in electrocatalysis, a low overpotential of 83 mV at a current density of 10 mA cm^{-2} and an excellent durability up to 12 h in 0.5 M H_2SO_4 were obtained. Moreover, an onset overpotential close to 0 V in 0.1 M phosphate buffer solution was also observed. This remarkable behavior is attributed to the porous character of the nanomaterial coupled with a weakly coordinated stabilizer which gives rise to a highly accessible metal surface as demonstrated by the high electrochemically active surface area measured, namely 173 $m^2\ g^{-1}$.

We are grateful to IDEX UNITI Emergence (UFTMIP: 2015-209-CIF-D-DRD-127185) and CTP (no. 13/12/12.15) programs and CNRS and UPS for financial support. CNRS and UPS-Toulouse are also thanked for funding. We thank D. Ciuculescu-Pradines and A. Sournia-Saquet for helpful discussions and suggestions. L. Vendier is acknowledged for helping with powder-XRD analyses. X. Sala and J. García-Antón thank MINECO/FEDER CTQ2015-64261 for financial support. J. Creus thanks UAB and Euroregió Pirineus Mediterrània for predoctoral grants. J. García-Antón acknowledges the Serra Húnter Program.

Conflicts of interest

There are no conflicts to declare.

Notes and references

1 N. S. Lewis and D. G. Nocera, *Proc. Natl. Acad. Sci. U. S. A.*, 2006, **103**, 15729–15735.
2 T. R. Cook, D. K. Dogutan, S. Y. Reece, Y. Surendranath, T. S. Teets and D. G. Nocera, *Chem. Rev.*, 2010, **110**, 6474–6502.
3 M. G. Walter, E. L. Warren, J. R. McKone, S. W. Boettcher, Q. Mi, E. A. Santori and N. S. Lewis, *Chem. Rev.*, 2010, **110**, 6446–6473.
4 S. Trasatti, *J. Electroanal. Chem. Interfacial Electrochem.*, 1972, **39**, 163–184.
5 C. C. McCrory, S. Jung, I. M. Ferrer, S. M. Chatman, J. C. Peters and T. F. Jaramillo, *J. Am. Chem. Soc.*, 2015, **137**, 4347–4357.
6 E. A. Paoli, F. Masini, R. Frydendal, D. Deiana, C. Schlaup, M. Malizia, T. W. Hansen, S. Horch, I. E. L. Stephens and I. Chorkendorff, *Chem. Sci.*, 2015, **6**, 190–196.
7 Y. Lee, J. Suntivich, K. J. May, E. E. Perry and Y. Shao-Horn, *J. Phys. Chem. Lett.*, 2012, **3**, 399–404.
8 T. Reier, M. Oezaslan and P. Strasser, *ACS Catal.*, 2012, **2**, 1765–1772.
9 E. Tsuji, A. Imanishi, K.-i. Fukui and Y. Nakato, *Electrochim. Acta*, 2011, **56**, 2009–2016.
10 Z. Chen, J. Lu, Y. Ai, Y. Ji, T. Adschiri and L. Wan, *ACS Appl. Mater. Interfaces*, 2016, **8**, 35132–35137.
11 X. Kong, K. Xu, C. Zhang, J. Dai, S. Norooz Oliaee, L. Li, X. Zeng, C. Wu and Z. Peng, *ACS Catal.*, 2016, **6**, 1487–1492.
12 J. Mahmood, F. Li, S. M. Jung, M. S. Okyay, I. Ahmad, S. J. Kim, N. Park, H. Y. Jeong and J. B. Baek, *Nat. Nanotechnol.*, 2017, **12**, 441–446.
13 Y. Zheng, Y. Jiao, Y. Zhu, L. H. Li, Y. Han, Y. Chen, M. Jaroniec and S. Z. Qiao, *J. Am. Chem. Soc.*, 2016, **138**, 16174–16181.
14 S. Liu, X. Mu, H. Duan, C. Chen and H. Zhang, *Eur. J. Inorg. Chem.*, 2017, 535–539.
15 K. Philippot, P. Lignier and B. Chaudret, Organometallic Ruthenium Nanoparticles and Catalysis, in *Ruthenium in catalysis*, ed. C. Bruneau and P. H. Dixneuf, Wiley VCH, Weinheim, 2014, *Top. Organomet. Chem.*, 2014, **48**, 319–370.
16 C. Amiens, B. Chaudret, D. Ciuculescu-Pradines, V. Collière, K. Fajerwerg, P. Fau, M. Kahn, A. Maisonnat, K. Soulantica and K. Philippot, *New J. Chem.*, 2013, **37**, 3374.
17 K. Pelzer, K. Philippot, B. Chaudret, W. Meyer-Zaika and G. Schmid, *Z. Anorg. Allg. Chem.*, 2003, **629**, 1217–1222.
18 K. Pelzer, O. Vidoni, K. Philippot, B. Chaudret and V. Colliere, *Adv. Funct. Mater.*, 2003, **13**, 118–126.
19 M. A. Ernst and W. G. Sloof, *Surf. Interface Anal.*, 2008, **40**, 334–337.
20 S. Jung, C. C. L. McCrory, I. M. Ferrer, J. C. Peters and T. F. Jaramillo, *J. Mater. Chem. A*, 2016, **4**, 3068–3076.
21 C. L. Green and A. Kucernak, *J. Phys. Chem. B*, 2002, **106**, 1036–1047.
22 Y. Gorlin and T. F. Jaramillo, *J. Am. Chem. Soc.*, 2010, **132**, 13612–13614.
23 C. Fan, D. L. Piron, A. Sleb and P. Paradis, *J. Electrochem. Soc.*, 1994, **141**, 382–387.
24 E. Navarro-Flores, Z. Chong and S. Omanovic, *J. Mol. Catal. A: Chem.*, 2005, **226**, 179–197.
25 I. A. Raj and K. I. Vasu, *J. Appl. Electrochem.*, 1992, **22**, 471–477.
26 C. Fan, D. L. Piron and P. Paradis, *Electrochim. Acta*, 1994, **39**, 2715–2722.
27 I. A. Raj and K. I. Vasu, *J. Appl. Electrochem.*, 1990, **20**, 32–38.
28 T. Shinagawa, A. T. Garcia-Esparza and K. Takanabe, *Sci. Rep.*, 2015, **5**, 13801.
29 H.-C. Chen, D. G. H. Hetterscheid, R. M. Williams, J. I. van der Vlugt, J. N. H. Reek and A. M. Brouwer, *Energy Environ. Sci.*, 2015, **8**, 975–982.

This journal is © The Royal Society of Chemistry 2017

Water Oxidation Hot Paper

International Edition: DOI: 10.1002/anie.201609167
German Edition: DOI: 10.1002/ange.201609167

A Million Turnover Molecular Anode for Catalytic Water Oxidation

Jordi Creus+, Roc Matheu+, Itziar Peñafiel, Dooshaye Moonshiram, Pascal Blondeau, Jordi Benet-Buchholz, Jordi García-Antón, Xavier Sala,* Cyril Godard,* and Antoni Llobet**

Abstract: *Molecular ruthenium-based water oxidation catalyst precursors of general formula* $[Ru(tda)(L^i)_2]$ *(*tda^{2-} *is [2,2′:6′,2′′-terpyridine]-6,6′′-dicarboxylato;* $L^1 = $ *4-(pyren-1-yl)-N-(pyridin-4-ylmethyl)butanamide,* ***1b****;* $L^2 = $ *4-(pyren-1-yl)pyridine),* ***1c****), have been prepared and thoroughly characterized. Both complexes contain a pyrene group allowing ready and efficiently anchoring via π interactions on multi-walled carbon nanotubes (MWCNT). These hybrid solid state materials are exceptionally stable molecular water-oxidation anodes capable of carrying out more than a million turnover numbers (TNs) at pH 7 with an* $E_{app} = 1.45$ *V vs. NHE without any sign of degradation. XAS spectroscopy analysis before, during, and after catalysis together with electrochemical techniques allow their unprecedented oxidative ruggedness to be monitored and verified.*

Visible-light-induced water splitting to produce hydrogen fuel is one of the potential alternatives to fossil fuels.[1] To achieve this goal, powerful and stable water oxidation catalysts (WOCs) that can be anchored onto solid-state devices to facilitate water-splitting cell assembling and engineering are needed.[2] On the molecular front, it is imperative to have water-oxidation catalysts that can work under restricted translational mobility conditions,[2] and whose O–O bond formation step occurs via a "water nucleophilic attack" mechanism (WNA).[3] Molecular WOCs whose low energy O–O bond formation pathways in the homogeneous phase occur via an "interaction of 2 M–O units" (I2M) might still be able to carry out the catalytic water oxidation reaction at the surface of an electrode, but will need to proceed through higher energy pathways that can lead to catalyst degradation.[2b] Further, given the intrinsic high energy demands for the water oxidation catalysis, it is essential that the anchoring groups that act as an interface between the catalysts and surface are oxidatively resistant.

Herein, we report new hybrid materials consisting of molecular WOCs anchored onto multi-walled carbon nanotubes (MWCNTs) via π-stacking interactions.[2c] The resulting materials are extremely stable and allow the anchoring of a large amount of catalyst giving turnover numbers (TNs) over a million without apparent deactivation.

Recently,[4] we have reported the synthesis of complex $\{Ru^{II}(tda)(py)_2\}$ (**1a**; for a drawing of tda^{2-} see Scheme 1) and have shown that in its high oxidation states (IV) it acts as a precursor for the formation of $\{Ru^{V}(O)(tda)(py)_2\}^{+}$. This complex is the most powerful molecular water oxidation catalyst described to date, achieving turnover frequencies (TOF) in the range of 50000 s^{-1}. In addition, we showed that the rate determining step for the water oxidation reaction is the O–O bond formation, which in this case occurs via WNA, as evidenced by kinetics and further supported by DFT calculations.

Given the remarkable performance of $\{Ru^{V}(O)(tda)(py)_2\}^{+}$, we proceeded to anchor it on conductive solid supports with the aim of generating a powerful hybrid anode for the electrocatalytic oxidation of water to dioxygen, that could be potentially incorporated in water splitting devices. For this purpose, we used MWCNTs as support, given their high stability, conductivity and large electrochemically active surface area.[2c,5] MWCNTs were also selected because of their inertness as compared to oxides that can potentially block labile Ru-aqua groups and thus reduce or even suppress the activity of the catalyst.[6] Moreover, this anchoring approach avoids the use of phosphonate or carboxylate moieties that have a limited stability in water in the presence of a supporting electrolyte under irradiation.[7] To anchor our catalyst on MWCNTs, we prepared pyridyl type of ligands functionalized with the pyrenyl group (Scheme 1), so that they can be anchored on MWCNTs via π-stacking interactions without significantly modifying the intrinsic electronic and geometrical properties of the parent complex.[8] We synthesized ligand L^1 that contains an amide group as previously described,[2e] and a new ligand L^2 that contains a direct C–C bond between the pyridyl group and the pyrene moiety, see Supporting Information for details. This strategy

---

[*] J. Creus,[+] Dr. J. García-Antón, Dr. X. Sala, Prof. A. Llobet
Departament de Química
Universitat Autònoma de Barcelona
Carrer dels Til·lers s/n, 08193 Cerdanyola del Vallès (Spain)
E-mail: xavier.sala@uab.cat

J. Creus,[+] R. Matheu,[+] Dr. I. Peñafiel, Dr. C. Godard
Departament de Química Física i Inorgànica
Universitat Rovira i Virgili
Carrer Marcel·lí Domingo s/n, 43007 Tarragona (Spain)
E-mail: cyril.godard@urv.cat

R. Matheu,[+] Dr. J. Benet-Buchholz, Prof. A. Llobet
Institute of Chemical Research of Catalonia (ICIQ)
Barcelona Institute of Science and Technology (BIST)
Avinguda Països Catalans 16, 43007 Tarragona (Spain)
E-mail: allobet@iciq.cat

Dr. D. Moonshiram
Chemical Science and Engineering Division, Argonne National Laboratory
9700 S. Cass Avenue, Lemont, IL 60439 (USA)

Dr. P. Blondeau
Departament de Química Orgànica i Analítica
Universitat Rovira i Virgili
Carrer Marcel·lí Domingo s/n, 43007 Tarragona (Spain)
E-mail: pascal.blondeau@urv.cat

[+] These authors contributed equally to this work.

Supporting information and the ORCID identification number(s) for the author(s) of this article can be found under http://dx.doi.org/10.1002/anie.201609167.

© 2016 Wiley-VCH Verlag GmbH & Co. KGaA, Weinheim

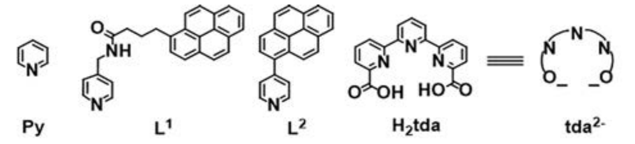

Complex-Material/Axial L	py	L^1	L^2
$[Ru^{II}(tda)L_2]$	**1a**	**1b**	**1c**
$[Ru^{II}(tda)L_2]$@MWCNT@GC	--	**2b**	**2c**
$[Ru^{IV}(tda)L_2]^{2+}$@MWCNT@GC	--	$\mathbf{2b}^{2+}$	$\mathbf{2c}^{2+}$
$[Ru^{IV}(O)(tda)L_2]$@MWCNT@GC	--	**3b**	**3c**

Scheme 1. Drawing of the ligands discussed herein (top) and complex labelling strategy (bottom).

avoids the use of easily oxidizing methylene groups, which is fundamental for the long-term performance of any molecular water oxidation catalysts.[9]

The synthesis of complexes $\{Ru(tda)(L^i)_2\}$ ($i = 1$, **1b**; $i = 2$, **1c**), is straightforward and similar to related complexes (see details of the synthesis in the Supporting Information).[2e,4] A single-crystal X-ray structure of **1b** is shown in Figure 1. It shows a distorted octahedral coordination around the Ru^{II} metal ion with the tda^{2-} ligand acting in a κ-N^3O fashion and leaving one of the carboxylate moieties uncoordinated. The axial positions are occupied by two pyridyl moieties from two L^1 ligands. Overall, the structure of **1b** shows a very similar first coordination sphere for the Ru center as reported for **1a**.[4] To further electronically and structurally characterize these complexes, X-ray absorption spectroscopy (XAS) was carried out for powders of **1a**, $\{Ru^{III}(tda)(py)_2\}(PF_6)$ (**1a**-(PF_6)), $\{Ru^{IV}(tda)(py)_2\}(PF_6)_2$ (**1a**$(PF_6)_2$), **1b**, and RuO_2 and the results are shown in Figure 2A and the Supporting Information. In all cases the half-edge energies obtained from X-ray absorption near edge structure (XANES) were consistent with the oxidation state assignment, and the metric parameters obtained by extended X-ray absorption fine structure (EXAFS) were very similar to those of related X-ray structures (Table S3 in the Supporting Information).[4]

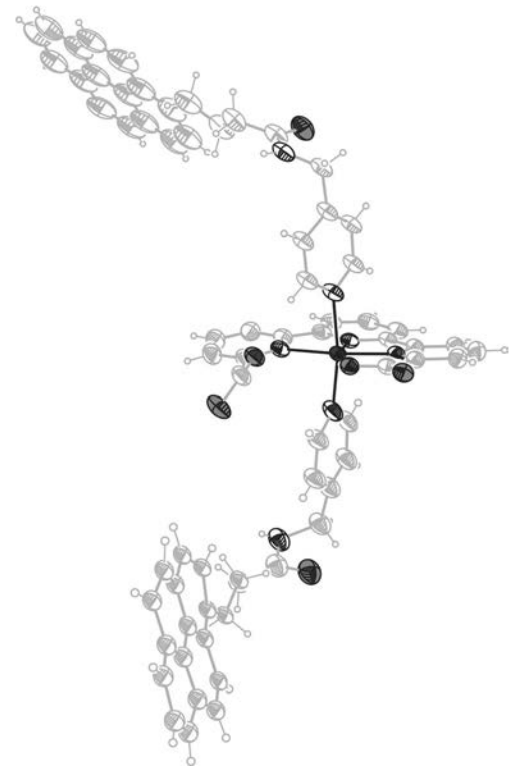

Figure 1. ORTEP plot of the catalyst precursor $\{Ru^{II}(tda)(L^1)_2\}$ (**1b**; thermal ellipsoids set at 50% probability). Black ellipsoid color codes: Ru black filling; O gray filling; N no filling. C gray ellipsoid with no filling. Small gray circles H.

Glassy carbon disks (GC_d, $S = 0.07\ cm^2$) were used as working electrodes (WE) for all the electrochemical work described herein, except when larger surface areas were needed, in which case, glassy carbon plates (GC_p, $S = 1\ cm^2$) were used. Further, a Pt disk and a $Hg/HgSO_4$ electrode were used as auxiliary and reference electrode respectively. All the potentials reported herein are converted into NHE by adding 0.65 V. Conductive electrode materials were prepared by depositing a few μL of a suspension of MWCNTs on the surface of glassy carbon electrodes. The solvent was then allowed to evaporate. The resulting materials are termed "MWCNT@GC". They were then soaked in a solution of the catalyst precursor **1b** or **1c** affording the hybrid anode materials "$\{Ru^{II}(tda)(L^i)_2\}$@MWCNT@GC" ($i = 1$, **2b**; $i = 2$, **2c**), that contained the catalyst precursor attached to the MWCNTs and were characterized by electrochemical techniques and XAS.

The amount of molecular complex deposited on the surface of the electrode turned out to be of $\Gamma_{2\mathbf{b}} = 6.35\ nmol\,cm^{-2}$ for **2b** and $\Gamma_{2\mathbf{c}} = 0.20\ nmol\,cm^{-2}$ for **2c**. Further, XAS was carried out for **2b** anchored on GC_p to additionally characterize the nature of these hybrid materials. Unfortunately, the lower catalyst loading obtained for **2c**, even supported in the GG_p electrode, prevented its XAS analysis. For **2b** it was found that the nature of the molecular species attached to the surface of the MWCNTs was identical to those of the precursor complexes, except that atmospheric oxygen had oxidized the initial Ru^{II} complex to Ru^{III} by 80%, as revealed by XANES and EXAFS (Figure 2B, Table S2). Additional evidence for this oxidation phenomenon was obtained by measuring the open circuit potential (OCP) as a function of time for a sample of **2b** in an open atmosphere (see Figure S30). We termed this partially oxidized material as $\mathbf{2b}^0$, and showed that its Ru κ-edge at half peak neatly correlates with oxidation state 2.8 and thus indicates that the sample $\mathbf{2b}^0$ contains 80% $\mathbf{2b}^+$ and 20% **2b** (Figure 2B, empty square marker). In addition, the simulated EXAFS experiments for $\mathbf{2b}^+$ ($\mathbf{2b}^0$–20% **1b**) also gives very good fits and thus further supports this point (see Figure 2D, Figure S33, Table S4 and Table S5). The EXAFS simulations were carried out assuming a coordination number of 6 (5N atoms, 1O atom) for Ru^{II} and assuming the typical pseudo-octahedral geometry expected for a Ru^{II} d^6 ion. On the other hand, for Ru^{III}, a coordination number of "6.5" was assumed (5N, 1O, 0.5O), with a distorted octahedral coordination containing an additional oxygen contact (Ru–O distance of 2.4 Å), in a similar manner as found in the X-ray structure of $\mathbf{1a}^+$

© 2016 Wiley-VCH Verlag GmbH & Co. KGaA, Weinheim

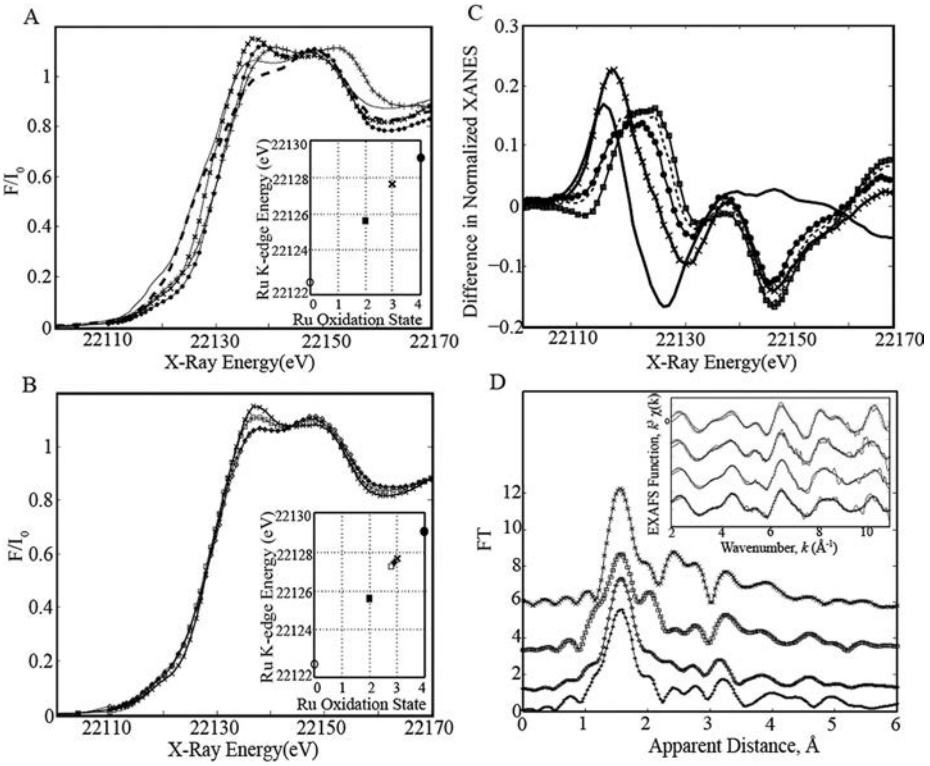

Figure 2. A) Normalized Ru K-edge XANES for **1a** (solid black), **1b** (dashed), **1a**$^+$ (cross), **1a**$^{2+}$ (plus), and RuO_2 (solid circle). Inset: Plot of half k-edge energy vs. oxidation state for Ru^0 metal (empty circle), **1a** and **1b** (black square), **1a**$^+$ (cross), and RuO_2 (solid circle). B) Normalized Ru K-edge XANES for **1a**$^+$ (cross), **2b**^{0} (empty square), **2b**′ (diamond) and **2b**″ (star). Inset: Plot of half k-edge energy vs. oxidation state (same symbols as in (A)) **2b**^{0} (empty square), **2b**′ and **2b**″ (star). C) Difference spectra for: **1b**–**1a**$^+$ (solid black), **1b**–RuO_2 (cross), **1a**$^+$–RuO_2 (dashed), **2b**–RuO_2 (square), and **2b“**–RuO_2 (solid circle). D) Fourier transforms of k^3-weighted Ru EXAFS for the Ru^{III} complexes from top to bottom, **1a**$^+$ (cross) and **2b**$^+$: (**2b**^{0}–20% **1b**) (empty square), (**2b**′–10% **1b**) (diamond), and (**2b**″–10% **1b**) (star). D) Back Fourier transformed experimental (solid lines) and fitted (with marker lines) $k^3\chi(k)$ from top to bottom for **1a**$^+$, **2b**$^+$: (**2b**^{0}–20% **1b**),(**2b**′–10% **1b**), and (**2b**″–10% **1b**). Experimental spectra were calculated for k values of 1.941–10.9 Å^{-1}.

(Figure S32, Table S4, fit 12).[4] The data fit obtained for **1a**$^+$ is very similar to that obtained for **2b**$^+$ reflecting their structural similarities.

To generate the active catalyst at the surface of the electrode material, a potential of 1.25 V was applied for 500 s under stirring at pH 12 to **2b** or **2c**. This process oxidizes the initial Ru^{II} complex to its oxidation state IV, where the coordination of a hydroxide anion occurs readily,[4] as indicated in the Equations (1) and (2) for **2b**.

$$\text{“}\underset{\mathbf{2b}}{\{\mathrm{Ru^{II}(tda)(L^1)_2}\}}\text{@MWCNT@GC”} - 2\,e^- \rightarrow \text{“}\underset{\mathbf{2b}^{2+}}{\{\mathrm{Ru^{IV}(tda)(L^1)_2}\}^{2+}}\text{@MWCNT@GC”} \tag{1}$$

$$\text{“}\underset{\mathbf{2b}^{2+}}{\{\mathrm{Ru^{IV}(tda)(L^1)_2}\}^{2+}}\text{@MWCNT@GC”} + OH^- \rightleftharpoons \text{“}\underset{\mathbf{3b}}{\{\mathrm{Ru^{IV}(O)(tda)(L^1)_2}\}}\text{@MWCNT@GC”} + H^+ \tag{2}$$

Once generated, the active hybrid materials were removed from the pH 12 solution, rinsed with water, and introduced in another solution at pH 7. Under these conditions, a mixture of **2b**$^{2+}$ and **3b** is generated with an approximate ratio of 5:1 that remains in equilibrium, as deduced from cyclic voltammetry (CV) experiments at pH 7 (See Figure 3 left).

Figure 3 shows that for the precursor material, waves for the III/II and IV/III couples are observed at 0.55 V and 1.10 V respectively, together with a large current density that appears at 1.3–1.4 V associated with the oxidation of the MWNCTs. On the other hand, on the CV of the **2b**$^{2+}$:**3b** mixture, additional small waves appear in the 0.6–0.9 V potential range associated with the electroactivity of the anchored $\{Ru^{IV}(O)(tda)(L^1)_2\}$ catalyst, **3b**, as we have earlier described for its homologue $\{Ru^{IV}(O)(tda)(py)_2\}$ in homogeneous phase.[4]

Finally, a very large electrocatalytic current due to the oxidation of water to dioxygen associated with the Ru^V/Ru^{IV} couple occurs at 1.2–1.3 V, manifesting the high activity of this catalytic hybrid material. Interestingly, current densities above 10 mA cm^{-2} are achieved that are assumed to be critical for the construction of a water splitting device.[10]

We quantified the performance of this new solid-state molecular-anode for water oxidation, comparing its performances with its homogeneous homologue by carrying out a foot-of-the-wave analysis (FOWA)[11] also at pH 7 (see Figure 3). A $TOF_{max} = 8935\ s^{-1}$ was obtained from the fitted data similar to that obtained for $\{Ru^{IV}(O)(tda)(py)_2\}$.[4] This is extremely important because it clearly shows that the activity of the catalyst anchored on a solid support, under translationally restricted mobility conditions, is maintained. It thus allows transferring the information obtained in homogeneous phase to the desired solid-state anode material, thanks to the WNA nature of the O–O bond formation step that occurs both in homogeneous phase and anchored. This is in sharp contrast with the related complex $\{Ru^{IV}(O)(bda)(4\text{-}Me\text{-}py)_2\}$ (bda^{2-} is 6,6′-dicarboxylate-2,2′-bypyridine), that mechanistically operates via a bimolecular I2M mechanism,[12] and once anchored needs to change its mechanism to a higher energy pathway that significantly decrease the TOF_{max} values and leads to degradation.

The activity of “$\{Ru^{IV}(O)(tda)(L^2)_2\}$@MWCNT@GC” (**3c**) at pH 7 was also evaluated in a similar manner as that of **3b**, giving a $TOF_{max} = 8076\ s^{-1}$. This is very similar to that obtained for **3b** (see Figure S24), further supporting the suitability of the chosen heterogenization strategy. The long-term stability of these new solid-state hybrid molecular

© 2016 Wiley-VCH Verlag GmbH & Co. KGaA, Weinheim

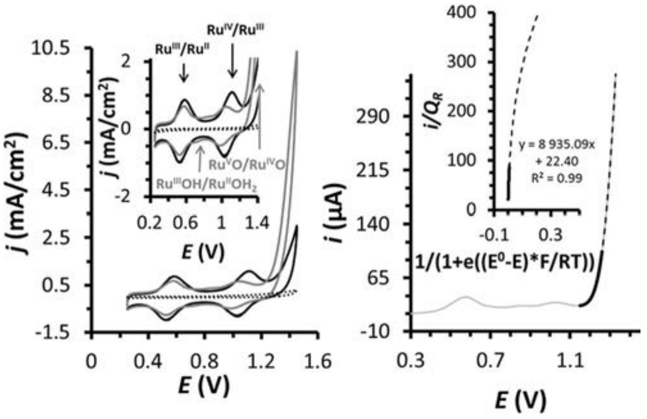

Figure 3. Left: black solid line, CV for **2b** in pH 7 solution at a scan rate of 100 mVs^{-1} from 0.25 to 1.45 V, with a surface coverage of $\Gamma_{2b} = 6.35$ nmol$\,$cm^{-2} using GC$_d$ as WE. Gray line, CV of a mixture of **2b**$^{2+}$:**3b** ($\Gamma_{2b^{2+}} = 2.66$ nmol$\,$cm^{-2} and $\Gamma_{3b} = 0.55$ nmol$\,$cm^{-2}) under the same conditions. In dashed black a blank for MWCNT@GC$_d$. Inset: enlargement of the 0.2–1.4 V potential zone. Right: linear sweep voltammetry at pH 7 for the **2b**$^{2+}$:**3b** mixture (gray solid line). Inset: plot of i/Q_R vs. [$1/(1+e((E^0\text{-}E)*F/RT))$]. The black dashed line in both cases represents the experimental data used for the FOWA analysis, and the black solid line shows the experimental data used for the extraction of TOF$_{max}$ = 8935 s^{-1} for **3b**.

anodes were evaluated at pH 7 based on repetitive CV, bulk electrolysis and XAS, shown in Figure 2 and Figure 4. The left and middle part of Figure 4 displays 1000 repetitive CV scans carried out at 100 mVs^{-1} for the anodes containing mixtures of **2b**$^{2+}$:**3b** and **2c**$^{2+}$:**3c**, between 0.25 and 1.45 V. For the case of **2b**$^{2+}$:**3b** (Figure 4, left), as the repetitive cycles proceed, both the intensity of the electrocatalytic current and the intensity of the waves arising from the catalyst precursor progressively decrease, until no electroactivity is observed. Thus as the catalytic reaction proceeds, the catalyst and catalyst precursor progressively disappear from the surface of the electrode, most likely due to the oxidation of the linker. In sharp contrast for the case of **2c**$^{2+}$:**3c** (Figure 4, middle), the intensity of the electrocatalytic current decreases by approximately 65 % of its initial value but the electroactivity of the precursor catalysts, **2c**$^{2+}$, remains intact as shown in Figure 4, right. The change in the intensity of the electrocatalytic current at 1.45 V is mainly attributed to a shift of the equilibrated species between precursor **2c**$^{2+}$, and the active catalytic species **3c** that occurs during long-term catalysis (see Figure S25 for an inset of the molecular peaks). Also, a small decrease of the intensity can be attributed to the partial detachment of the MWCNT due most likely to a mechanical friction effect.

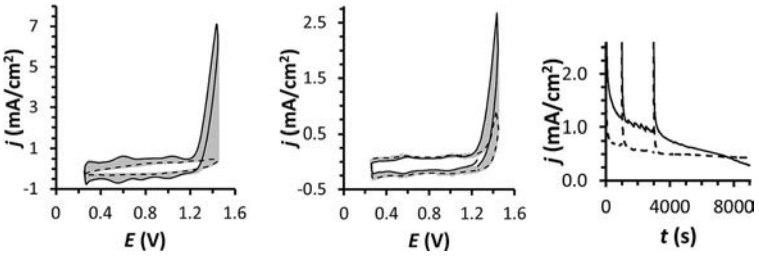

Figure 4. 1000 repetitive CV scans at pH 7 at a scan rate of 100 mVs^{-1} from 0.25 to 1.45 V for **2b**$^{2+}$:**3b** (left, $\Gamma_{2b^{2+}} = 2.07$ nmol$\,$cm^{-2} and $\Gamma_{3b} = 0.36$ nmol$\,$cm^{-2}) and **2c**$^{2+}$:**3c** (middle: $\Gamma_{2c^{2+}} = 0.13$ nmol$\,$cm^{-2} and $\Gamma_{3c} = 0.03$ nmol$\,$cm^{-2}) at GC$_d$. Black solid line is the first cycle, black dashed line is the 1000th cycle. In gray are 2nd–999th cycles. Right: bulk electrolysis of **2b**$^{2+}$:**3b** (solid black, $\Gamma_{2b^{2+}} = 2.10$ nmol$\,$cm^{-2} and $\Gamma_{3b} = 0.40$ nmol$\,$cm^{-2}) and **2c**$^{2+}$:**3c** (dashed black, $\Gamma_{2c^{2+}} = 0.11$ nmol$\,$cm^{-2} and $\Gamma_{3c} = 0.03$ nmol$\,$cm^{-2}) in a phosphate buffered solution at pH 7 at $E_{app} = 1.45$ V under stirring using GC$_d$ as WE. The experiments were stopped at 1000 s and 3000 s and then subsequently reinitialized. See Figure S29 for an analogous experiment on bare MWCNT@GC$_d$.

A similar trend is observed when bulk electrolysis experiments using GC$_d$ electrodes are carried out at pH 7 with an applied potential of 1.45 V as can be seen in Figure 4, right. For the system **2b**$^{2+}$:**3b** (solid black line), the initial current density reaches a value of 2 mA$\,$cm^{-2}, but as time elapses the current density progressively decreases to less than 0.25 mA$\,$cm^{-2} after 2.5 h. On the other hand, for the **2c**$^{2+}$:**3c** system (dashed black line) the initial current density is 1.5 mA$\,$cm^{-2}, and it decreases to 0.7 mA$\,$cm^{-2} at about 40 min and then remains constant. While the hybrid anode **2c**$^{2+}$:**3c** is extremely stable generating roughly 0.18 million TNs without apparent deactivation, **2b**$^{2+}$:**3b** slowly deactivates but still giving a remarkable final TNs of 0.67 million. TNs in the range of 1.2 million can be obtained for **2c**$^{2+}$:**3c** under similar conditions but by running the experiment for longer periods of time (12 h; see Figure S27). The strikingly different long-term performances of these two anode materials are associated with the different oxidative stability of their linking moieties as discussed above for the repetitive CV experiments.

These results manifest again the importance of ligand design for long-lasting anodes for water splitting applications that if properly designed can parallel the performance of related oxide based electroanodes. Finally, a bulk electrolysis experiment was performed in a GC$_p$ for **2b**$^{2+}$:**3b** under similar conditions, and the amount of O_2 generated was measured via a Clark electrode on the gas phase giving Faradaic efficiencies above 90 %, showing once more the ruggedness of the present system (Figure S28). The remaining current is basically used for the oxidation of the graphite electrode.

The structure of the hybrid material **2b**$^{2+}$:**3b** was also analyzed by XAS, using glassy carbon plates GC$_p$ and the results are reported in Figure 2, and Figures S32 and S33 and Tables S3 and S5. Two samples of the hybrid material **2b**$^{2+}$:**3b** ($\Gamma_{2b^{2+}} = 0.57 \pm 0.16$ nmol$\,$cm^{-2} and $\Gamma_{3b} = 0.64 \pm 0.24$ nmol$\,$cm^{-2}; $\Gamma_{2b^{2+}}:\Gamma_{3b} = 0.89 \pm 0.20$ nmol$\,$cm^{-2}) were exposed to a bulk electrolysis experiment at pH 7, with an applied potential of 1.45 V for 1000 s for the first sample and for 1 h for the second one.

Subsequently a CV was carried out with a final potential of 0.2 V that generated the catalyst precursor and the active catalyst at oxidation state II, that are labeled as **2b′** and **2b″** for the samples exposed to 1000 s and 1 h electrolysis, respectively, and left in open air for a week. As was also the case for **2b**^{0}, XANES spectra show half peak κ-edge energies that indicate that initial Ru^{II} complex is oxidized to Ru^{III} by 90 % in both cases

© 2016 Wiley-VCH Verlag GmbH & Co. KGaA, Weinheim

(see Table S2 and inset in Figure 2 B). In addition, the EXAFS (see Figures 2 D, S32, Table S3 and Table S5 (fits 4, 8 and 12)) point out that the samples before catalysis $\mathbf{2b}^0$ and after 1000 s and 1 h catalysis **2b“** and **2b**” respectively, are practically identical to $\mathbf{1a}^+$, after subtraction of their Ru^{II} contribution, and thus confirms the presence of $\mathbf{2b}^+$. This is a very important result since it shows that the nature of the catalyst remains intact after catalysis. In addition, XAS spectroscopy unambiguously shows the absence of any traces of RuO_2 after 1 h catalysis. This can be monitored by the specific peak at 22156 eV, nicely visualized through the difference spectra in Figure 2 C, that is highly characteristic of RuO_2 as well as by the absence of RuO_2 in the EXAFS spectral features shown in Figure 2 D and Figure S33. This is again very significant since it clearly demonstrates the molecular nature of the catalysis in heterogeneous phase, in sharp contrast with many instances where the original molecular catalyst is transformed to the corresponding metal oxide that ends up being the real active catalyst.[2b]

In conclusion, we report a million turnover molecular electroanode that consists of a molecular Ru catalyst anchored on the surface of MWCNTs via a pyrenyl functionality. The extraordinary unprecedented stability of the molecular catalyst is a result of a bottom-up approach that includes a thorough mechanistic understanding of the water oxidation catalyst steps involved in water nucleophilic attack events. XAS spectroscopy has been shown to be a very valuable tool in the solid state to monitor the long-term stability and molecular nature of the anchored water oxidation catalysts.

Acknowledgements

A.L., X.S., and J.G.-A. thank MINECO (CTQ-2016–80058-R, SEV-2013-0319; CTQ-2014–52974-REDC and CTQ2015-64261-R). J.C. and R.M. respectively thank UAB, “Euroregió Pirineus Mediterrània” and “La Caixa” for PhD grants. D.M. acknowledges support from the US DOE, Contract No. DE-AC02-06-CH11357. This research used resources of Sector 20 beamline at the Advanced Photon Source which is operated by the US DOE and the Canadian Light Source J.G-A. thanks Serra Hunter Program.

Keywords: electrocatalysis · redox properties · transition metal complexes · water oxidation catalysis · water splitting

How to cite: *Angew. Chem. Int. Ed.* **2016**, *55*, 15382–15386
Angew. Chem. **2016**, *128*, 15608–15612

---

[1] N. S. Lewis, *Science* **2016**, *351*, 19201–19209.

[2] a) L. Alibabaei, B. D. Sherman, M. R. Norris, M. K. Brennaman, T. J. Meyer, *Proc. Natl. Acad. Sci. USA* **2015**, *112*, 5899–5902; b) R. Matheu, L. Francàs, P. Chernev, M. Z. Ertem, V. Batista, M. Haumann, X. Sala, A. Llobet, *ACS Catal.* **2015**, *5*, 3422–3429; c) N. Karousis, N. Tagmatarchis, D. Tasis, *Chem. Rev.* **2010**, *110*, 5366–5397; d) G. Pastori, K. Wahab, A. Bucci, G. Bellachioma, C. Zuccaccia, J. Llorca, H. Idriss, A. Macchioni, *Chem. Eur. J.* **2016**, *22*, 13459–13463; e) F. Li, B. Zhang, X. Li, Y. Jiang, L. Chen, Y. Li, L. Sun, *Angew. Chem. Int. Ed.* **2011**, *50*, 12276–12279; *Angew. Chem.* **2011**, *123*, 12484–12487.

[3] a) X. Sala, S. Maji, R. Bofill, J. Garcia-Anton, L. Escriche, A. Llobet, *Acc. Chem. Res.* **2014**, *47*, 504–516; b) J. J. Concepcion, J. W. Jurss, J. L. Templeton, T. J. Meyer, *J. Am. Chem. Soc.* **2008**, *130*, 16462–16463.

[4] R. Matheu, M. Z. Ertem, J. Benet-Buchholz, E. Coronado, V. S. Batista, X. Sala, A. Llobet, *J. Am. Chem. Soc.* **2015**, *137*, 10786–10795.

[5] C. C. L. McCrory, S. Jung, I. M. Ferrer, S. M. Chatman, J. C. Peters, T. F. Jaramillo, *J. Am. Chem. Soc.* **2015**, *137*, 4347–4357.

[6] L. Francàs, C. Richmond, P. Garrido-Barros, N. Planas, S. Roeser, J. Benet-Buchholz, L. Escriche, X. Sala, A. Llobet, *Chem. Eur. J.* **2016**, *22*, 5261–5268.

[7] J. T. Hyde, K. Hanson, A. K. Vannucci, A. M. Lapides, L. Alibabaei, M. R. Norris, T. J. Meyer, D. P. Harrison, *ACS Appl. Mater. Interfaces* **2015**, *7*, 9554–9562.

[8] A. Maurin, M. Robert, *J. Am. Chem. Soc.* **2016**, *138*, 2492–2495.

[9] D. Hong, S. Mandal, Y. Yamada, Y.-M. Lee, W. Nam, A. Llobet, S. Fukuzumi, *Inorg. Chem.* **2013**, *52*, 9522–9531.

[10] M. G. Walter, E. L. Warren, J. R. McKone, S. W. Boettcher, Q. Mi, E. A. Santori, N. S. Lewis, *Chem. Rev.* **2010**, *110*, 6446–6473.

[11] C. Costentin, S. Drouet, M. Robert, J.-M. Savéant, *J. Am. Chem. Soc.* **2012**, *134*, 11235–11242.

[12] L. Duan, F. Bozoglian, S. Mandal, B. Stewart, T. Privalov, A. Llobet, L. Sun, *Nat. Chem.* **2012**, *4*, 418–423.

Received: September 19, 2016
Published online: November 7, 2016

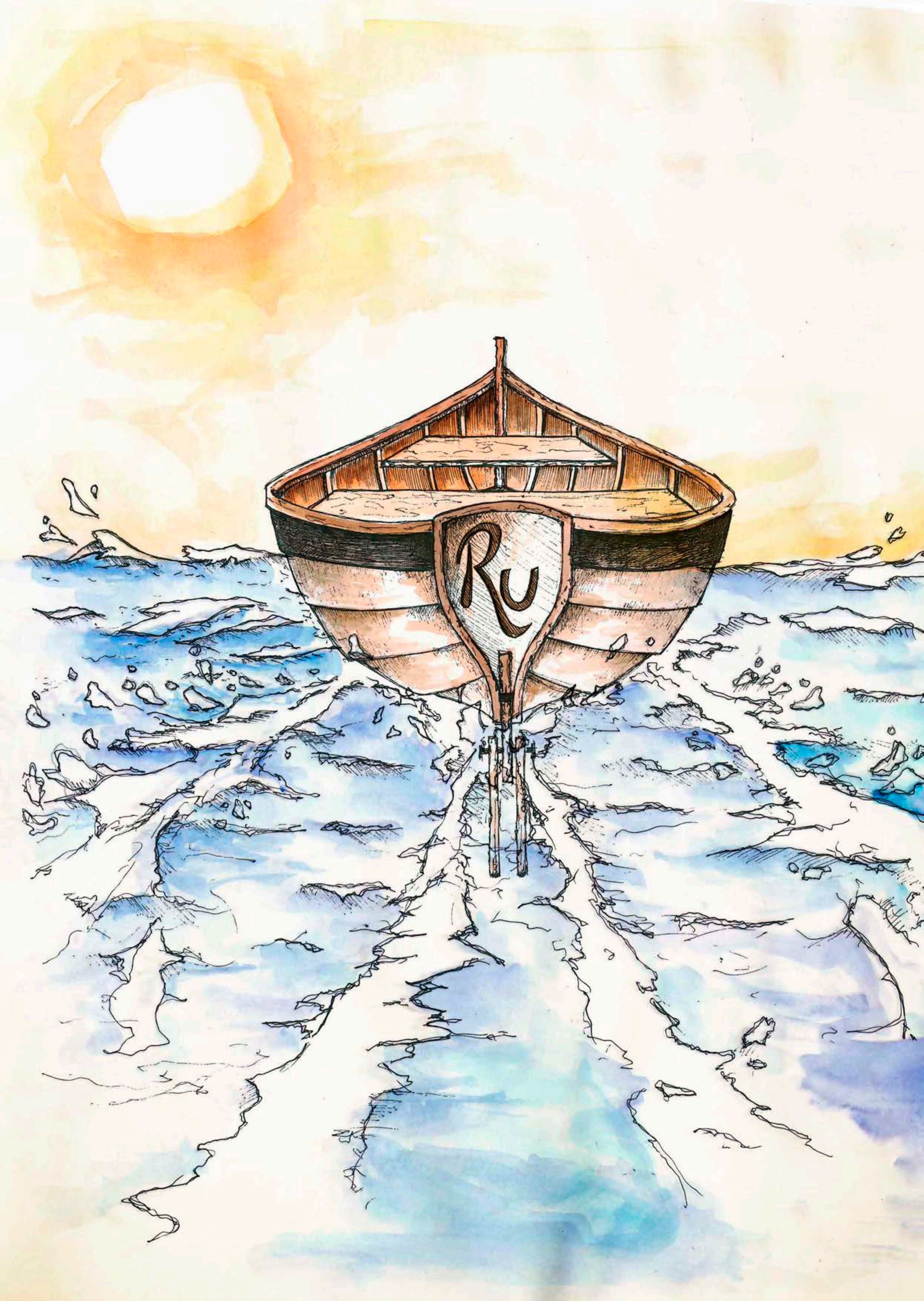
Ru